UNIVERSITY OF CALIFORNIA,
IRVINE

Envisioning and Designing a Renewable Future with Offshore Wind and Hydrogen in California

DISSERTATION

submitted in partial satisfaction of the requirements
for the

DOCTOR OF PHILOSOPHY

in Mechanical and Aerospace Engineering

by

Alejandra Hormaza Mejia

Dissertation Committee:
Professor Jack Brouwer, Chair
Professor David Copp
Professor Steven Davis

2023

DEDICATION

To my parents,
for making my dreams their own,
and for showing me boundless love
since day one.

TABLE OF CONTENTS

LIST OF FIGURES

LIST OF TABLES

ACKNOWLEDGEMENTS

One of the most important people for me to thank is my advisor, mentor, and friend, Professor Jack Brouwer. Jack Brouwer taught me a lot about research in thermodynamics, the theory of fuel cells and electrolysis, and experimentation. More importantly, Jack taught me about innovative thinking, generosity, kindness, perseverance, and patience. His contagious and enthusiastic energy for green energy and helping others is inspiring and influential. My most sincere thanks to Professor Jack Brouwer for giving me a chance as an undergraduate student researcher in 2015. I will always be grateful to him for this incredible opportunity, and I will always be a fan of the ways he is changing the world.

Many thanks to my committee members: Professor David Copp and Steven Davis. I would like to thank Professor David Copp for his support and collaboration on our offshore wind study. I would also like to thank Professor Steven Davis for his insightful feedback on my research. To Professor Natascha Buswell, I would like to express my gratitude for her mentorship in engineering education and life, encouragement, and friendship. I am forever thankful to her for opening up my eyes to the world of engineering education.

To my colleagues that helped me tremendously with the design and building of the experimental test stand: Jasper Yao and Bobby Lauviger. I would like to thank them for their creativity, enthusiasm, and time. I would also like to thank Chris Kim (Jun Yong Kim), for his insightful discussions that helped me develop my model. I am inspired by his impressive modelling knowledge. Many thanks to Luca Mastropasqua for his insight and support throughout my research.

To the rest of my APEP colleagues, thank you for being a part of such a formative period of my life. I am immensely grateful to have spent my PhD and (most of my 20's) in such an inspiring, welcoming, and friendly environment.

Lastly, I would like to thank my family and friends, for their unconditional love, patience, and support in helping me make this dream a reality.

VITA

Alejandra Hormaza Mejia

2014	Undergraduate Researcher Accelerator Mass Spectrometry Lab, University of California, Irvine
2015-2017	Undergraduate Researcher National Fuel Cell Research Center, University of California, Irvine
2017	B.S. in Chemical Engineering, University of California, Irvine, CA
2018	Teaching Assistant – Department of Mechanical and Aerospace Engineering University of California, Irvine
2019	Intern, California Energy Commission Sacramento, CA
2019	M.S. in Mechanical Engineering Advisor: Jack Brouwer University of California, Irvine Thesis: Why Hydrogen Leaks at the Same Rate as Natural Gas from Typical Low-Pressure Natural Gas Infrastructure?
2022	Intern, Environmental Defense Fund Austin, Texas
2022 - 2023	Fuel Cell Systems Engineering Consultant Hydroplane Ltd., Thousand Oaks, CA
2017-2023	Graduate Research Assistant National Fuel Cell Research Center, University of California, Irvine
2023	Ph.D. in Mechanical and Aerospace Engineering Advisor: Jack Brouwer University of California, Irvine

FIELD OF STUDY

Mechanical Engineering

PUBLICATIONS

Mejia, Alejandra Hormaza, Jacob Brouwer, and David Copp. "Case Study of the Performance and Dynamics of California Offshore Wind, Onshore Wind and Solar Power Production." Under review (2022).

Mejia, Alejandra Hormaza, Jacob Brouwer, and Michael Mac Kinnon. "Hydrogen Leaks at the Same Rate as Natural Gas in Typical Low-Pressure Gas Infrastructure." International Journal of Hydrogen Energy 45, no. 15 (2020): 8810-8826.

Mejia, Alejandra Hormaza, Masaya Yoshioka, Jun Yong Kim, and Jack Brouwer. "Impacts of Hydrogen-Natural Gas Mixtures on a Commercial Solid Oxide Fuel Cell System." ECS Transactions 96, no. 1 (2020): 133.

Stansberry, John, **Alejandra Hormaza Mejia**, Li Zhao, and Jack Brouwer. "Experimental Analysis of Photovoltaic Integration with a Proton Exchange Membrane Electrolysis System for Power-to-Gas." International Journal of Hydrogen Energy 42, no. 52 (2017): 30569-30583.

Copp, D. A., & **Hormaza Mejia, A.**, & Walter, M. E., & Buswell, N. T. (2020, June), Whom Are We Serving? An Exploration of Student Demographics in a Large Engineering Design Projects Ecosystem Paper presented at 2020 ASEE Virtual Annual Conference Content Access, Virtual Online. https://peer.asee.org/35511

Hormaza-Mejia, Alejandra and Brouwer, Jack. "Gaseous Fuel Leakage from Natural Gas Infrastructure" American Society of Mechanical Engineers 2018 15th International Mechanical Engineering Congress & Exposition, Pittsburgh, Pennsylvania, November 14, 2018

Hormaza-Mejia, **Alejandra**, Zhao, Li, and Brouwer, Jack. "SOFC Micro-CHP System with Thermal Energy Storage in Residential Applications." American Society of Mechanical Engineers 2017 15th International Fuel Cell Science, Engineering and Technology Conference, Charlotte, North Carolina, June 26, 2017. https://doi.org/10.1115/FUELCELL2017-3142

ABSTRACT OF THE DISSERTATION

Envisioning and Designing a Renewable Future with Offshore Wind and Hydrogen in California

by

Alejandra Hormaza Mejia

Doctor of Philosophy in Mechanical And Aerospace Engineering

University of California, Irvine, 2023

Professor Jack Brouwer Irvine, Chair

Accelerating towards a future that is sustained by green energy is essential to avoid a climate catastrophe. While solar, onshore wind, and batteries have become ubiquitous due to massive public funding and investments which have led to reduced costs and significant improvements in the technologies, achieving an energy system that is truly decarbonized across all sectors and net zero emissions requires a myriad of solutions to address the challenges associated with intermittent renewable energy.

Offshore wind has a tremendous potential to contribute to decarbonization due to its high capacity factors and recent developments in platform foundation technologies. In the last decade, offshore wind has become a flourishing source of energy with many countries investing and deploying this technology. Hydrogen may be used as a transmission and storage medium for offshore wind. Solid oxide electrolysis (SOE) may also play a vital role in hydrogen production and decarbonization due to its advantageous thermodynamic and kinetic operating conditions. While any source of electricity can be used to power SOE systems, green hydrogen made from a renewable power source represents the most substantial and sustainable pathway forward to achieve net zero emissions. The goal of this work is to explore and assess how offshore wind and

hydrogen can support a 100% renewable future in California. To achieve this, this work is divided into three main sections:

First, the benefits and challenges of offshore wind are analyzed in California using generation duration curves, correlation analyses, demand-based metrics, and the discrete Fourier transform to assess the feasibility of integrating this energy with the electrical grid.

Second, an SOE system coupled with offshore wind is designed and proposed, with an emphasis on modelling the thermodynamics of such a system. This work assesses the heat transfer, electrochemical efficiencies, and dynamics of an offshore platform. The results of this platform are compared with alternative electrolysis technologies including low temperature and high temperature proton exchange membrane systems.

Finally, this work experimentally assesses the potential impacts of using seawater as the water source for a high temperature SOE cell. Using a variety of electrochemical analysis methods and tools, including polarization curves, electrochemical impedance spectroscopy, distribution of relaxation times, and Scanning Electron Microscopy, this study finds strong evidence of salt precipitation on the cell which did not appear to negatively impact the performance of the cell in the duration of the experiment.

1 INTRODUCTION

There is a strong consensus among scientists that global average temperatures must not exceed 2°C above pre-industrial levels as stated in the Paris Agreement [1]. The escalating climate crisis must be addressed with urgent, coordinated efforts that address the intersectionality of this global emergency, including climate change adaptation, resilience and mitigation, social equity, and economic development [2]. An increasing global response to avert the present climate emergency and in anticipation of a progressively dangerous and harmful climate crisis, has led numerous governments and local municipalities throughout the world to enact laws and policies mandating swift transitions from fossil fuels to renewable energy conversion systems in the next few decades. The majority of these policies have been focused on achieving a future carbon-free electrical grid by electrification of various energy services including light-duty transportation, heating, cooling, and lighting [3]. While these efforts to decarbonize the electrical grid are worthwhile and the progress has been impressive, decarbonization of numerous high-polluting sectors is essential to stabilize global mean temperatures and to meet international climate targets [3]. These sectors include aviation, long-distance transportation, long-distance shipping, steel production, and cement production [3]. Decarbonizing various sectors, which have historically relied on direct use of fossil fuels for combustion, is necessary to address the entirety of this global climate calamity and to prevent global temperatures from exceeding 2°C above pre-industrial levels. The entire energy system that society relies on must be reimagined with net-zero emissions to avert the intensifying climate crisis.

Attempts to reduce emissions from these "difficult-to-decarbonize" sectors have been insufficient, and progress has been largely unnoticeable. The increasing emissions along with a rising demand for services from these sectors is extremely alarming: total CO_2 emissions from shipping increased 2.4% between 2013 and 2015 [4]; emissions from cement production have also been steadily increasing and it is considered the third largest source of anthropogenic CO_2 emissions [5]; CO_2 emissions from commercial aviation have increased 32% over the past five years [6]. Decarbonizing these hard-to-abate sectors is not only necessary for mitigating climate change, but also for the humanity and for the livelihood of many communities that deeply suffer the worst consequences of these emissions. These are some of the most polluting sectors that

disproportionally devastate and harm low-income and vulnerable communities, particularly communities of color, since many of these communities live in neighborhoods that are adjacent to ports, railyards, distribution centers, and freight corridors [7]. Therefore, it is absolutely essential to decarbonize these high-polluting sectors for the health, safety, and lives of the communities most harmed by these emissions.

A new paradigm is emerging across the shipping industry to radically reduce greenhouse gas emissions motivated by the Paris agreement that requires zero emissions in the shipping sector [8]. The maritime industry is a significant emitter of GHG emission and SOx, NOx, and particulate matter. Decarbonizing this capital-intensive industry with long-life assets and thin margins is complex and will require a holistic and coordinated collaboration among various key players [9]. While electrification has been used to decarbonize various forms of transportation, batteries alone cannot be used as a clean energy source in shipping due to weight and space restrictions and power requirements for trans-oceanic journeys [8]. Cleaner fuels may be a long-term solution to reducing emissions in the maritime industry. Studies suggest that renewably produced hydrogen is the most cost-effective solution to decarbonize the shipping system [8].

While policies have supported various renewable energy technologies to achieve carbon-free electricity, a diverse and innovative portfolio of renewable energy resources and sustainable storage and distribution methods are essential to fully decarbonize all energy sectors. The role of hydrogen will be critical in various sectors including road and rail transportation, international shipping and air transport [10]. Additionally, there is a growing need for long-duration energy storage to account for variation in renewable energy resources [11]. Hydrogen as a vector for energy storage is more suitable than batteries in applications that require long-duration backup power, such as meeting the power demand of remote, isolated communities [12]. Incorporating large-scale storage options is necessary to transfer excess electrical energy from the grid to other economic sectors [13]. Hydrogen is one possible solution to these storage challenges. The transition to a future that is entirely carbon free and zero-emissions across all sectors will require a variety of clean energy technologies including solar, on-shore and offshore wind, batteries, and hydrogen to be used strategically and collaboratively. A diverse portfolio of renewable energy resources results in various advantages. Reliance on a variety of renewables that are

geographically distributed will mitigate the intermittency and variability of any one particular resource at a time [10].

Additionally, the transition to cleaner energy presents an opportunity to enable energy equity in our society. For example, installing offshore wind farms in Northern California, may allow vulnerable communities in remote, isolated locations that are not connected to the grid to have access to reliable electricity. In the United States, there are hundreds of communities in Alaska and islanded territories that rely on diesel generators for their power requirements [12]. There is a need to develop local energy resources to provide reliable, clean energy to these communities, many of which have access to harvestable marine energy resources [12]. Expanding distributed generation systems may strengthen the energy resilience of communities vulnerable to extreme temperatures and climate change catastrophes. While today, it may seem as though offshore wind and hydrogen are too expensive to consider, this is not a unique challenge. Historically, all new technologies have been faced with the challenge of cost and being too expensive [14].

With these ideas in mind, this work studies how offshore wind and hydrogen can support a 100% renewable future in California. I am interested in understanding how offshore wind can be integrated with both existing and nascent technologies, specifically solid oxide electrolyzers, which have not been fully deployed nor supported by policy in California. The role of these technologies must be considered in concert with various other renewable energy resources, energy transmission and distribution, and energy storage options, such as solar, onshore wind, hydropower, pumped hydro storage, and batteries.

2 BACKGROUND

For this work, the breadth of the literature review encompasses several topics including offshore wind dynamics, seawater electrolysis, and desalination methods. Each of these topics is discussed in detail in the following subsections:

2.1 **Offshore Wind**

The ocean represents a vast majority of the area on the Earth and an immense source of renewable energy. Studies such as the "Teal Deal" proposed in Dundas et al., [2] have reframed the importance of the ocean's role in mitigating climate change and providing solutions to the climate crisis. Offshore wind is a low-carbon, nearly limitless energy resource technology that is rapidly maturing throughout the world [15]–[17]. With costs expected to decrease significantly in the next decades [1], between 35% and 41% in 2050 relative to 2014 [18], it is expected that offshore wind will attain a more significant presence globally as a formidable source of renewable energy production. In 2019 the total install capacity was 22 GW globally [19]. The potential global offshore wind generation has been estimated to be 315 PWh [20].

Europe has been leading the world in the development of offshore wind technology, with the United Kingdom having a total of 5.8 GW, the country with the highest amount of offshore wind installed [1]. The technical potential in Europe is 71,000 TWh [15]. Offshore wind is growing quickly in China, accounting for nearly half of all new global installations in 2018 [19]. Offshore wind is a nascent technology in the United States, with a total offshore wind energy resource potential up to 2000 GW [21] and an annual energy potential of 36, 819 TWh/yr [22]. The vast majority of offshore wind energy resource potential in the United States has not been explored which represents an enormous energy resource [21]. In the East Coast, offshore wind is a significant cornerstone of future clean energy portfolios in various states, where a total of 22 GW of new capacity will be installed by 2035 [19], [23]. Though offshore wind is not yet fully explored or deployed in the West Coast, it is expected to make significant contributions to energy generation in the next decades.

Historically, offshore wind farms have been deployed mainly in the North Sea and the Baltic Sea [24] which has been possible due to the convenient location of high resource potential offshore wind in shallow regions of the ocean near the shore. Fixed-bottom foundation platforms have been the main foundation technology used since they are practical and economic in depths up to 50 m [1]. Areas with the highest wind resource are generally located in depths greater than 50 m and, therefore, require floating foundation technologies [1].

In the present moment, offshore wind is an emerging technology that has not been deployed along the coast of California due to the precipitous nature of the continental shelf, which requires floating platforms for mounting turbines in the ocean. The development of floating wind turbines is essential to fully develop and deploy offshore wind in California, since 96% of the technical wind resource is located in waters deeper than 60 meters [16]. Floating turbine technology is burgeoning throughout the world; there have been successful demonstrations of floating turbines in multiple locations throughout the world [19], such as the 30 MW Hywind Pilot Park in Scotland, the world's first commercial floating offshore wind farm [15], [19], [25]. Already there are regions along the coast of California suitable for development of offshore wind especially in Northern California. (See Figure 2-1). The Central California Coast is another appealing location since it is located between two major population centers in Northern and Southern California and it is outside of National Marine Sanctuaries, and it is conveniently located next to coastal connections linked to the state's electrical grid [26].

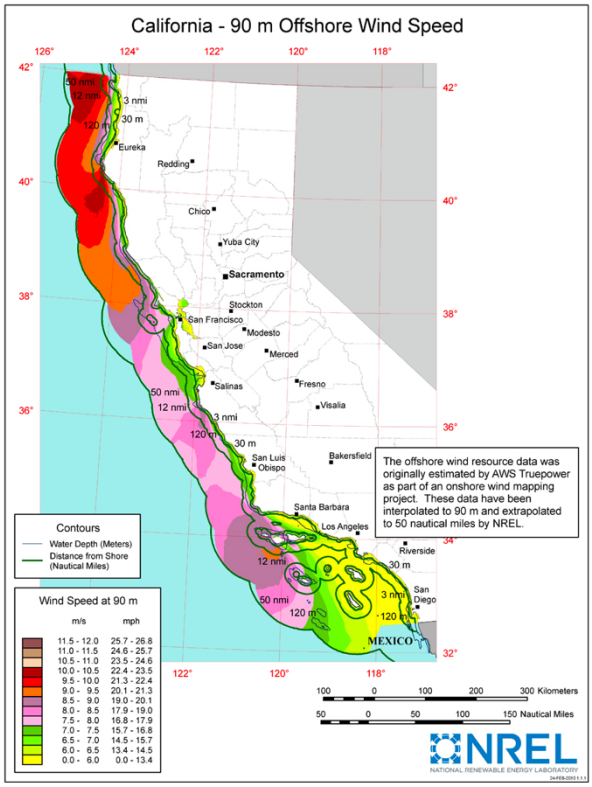

Figure 2-1: Image from [27] **shows a geospatial image of offshore wind speeds in California.**

One of the most attractive features of offshore wind is that there is a nearly limitless area on the ocean to explore and install windfarms [21]. Other advantages that have been consistently reported in the literature include: include stronger and more consistent wind velocities [26], [28], resulting in consistently higher capacity factors than solar and land-based wind; it is less likely to interfere with land-use activities [26] ; it has minimal impact on the population and sea life [21]; and it may also face less community resistance since turbines can be placed beyond the visible horizon from the shore [23]. Additionally, offshore wind is less constrained by size and noise pollution [1] and it is highly scalable [23]. It also shares important synergies with oil and gas sectors [15] which may allow future offshore wind platforms to benefit from existing infrastructure previously used for extraction, processing, and delivery of fossil fuels, which may be repurposed for the delivery and transmission of offshore wind. Subcoastal powerplants transmission infrastructure, depleted subterranean and subsea natural gas and oil reserves may be suitable for storage and delivery offshore wind via hydrogen [10]. Additionally, offshore wind may enable hydrogen to dramatically reduce emissions from sectors that are difficult to decarbonize such as iron, steel, and shipping [15]. Lastly, offshore wind turbines have the

potential to be co-located with other offshore resources such as subsea wave energy converters [28], though currently, offshore wind is the only commercially mature ocean energy technology [28].

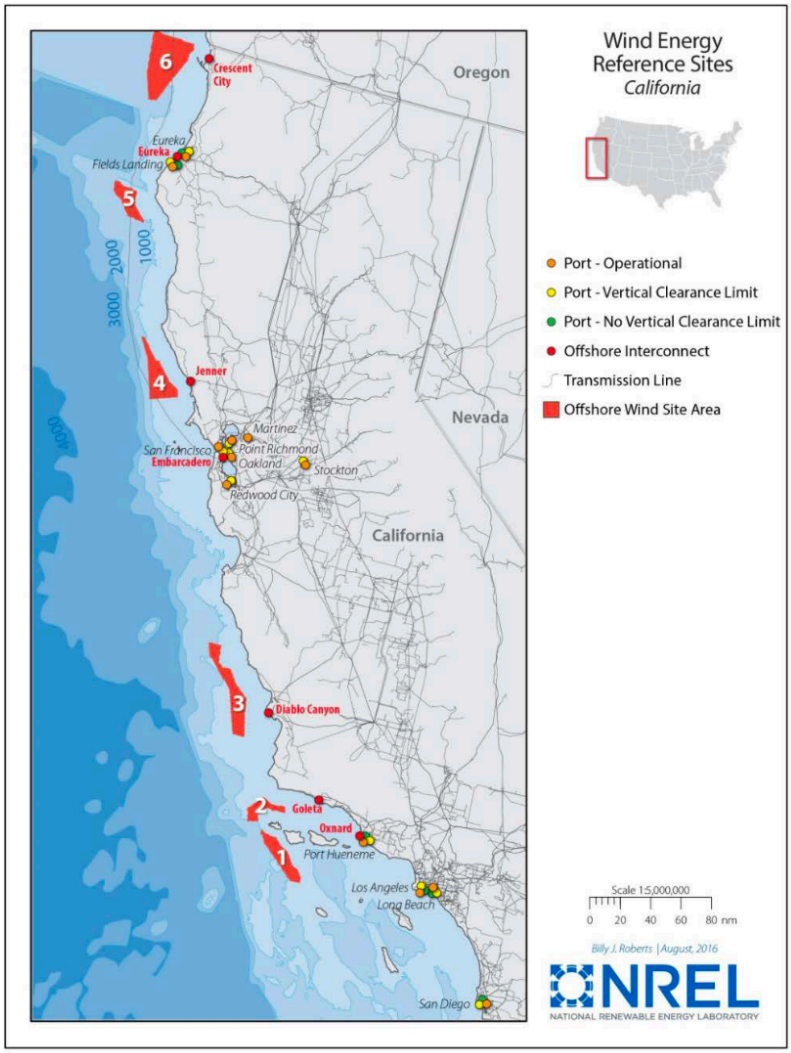

Figure 2-2: Image from [16] **shows seven potential offshore wind farm areas located near ports and offshore interconnection points.**

Offshore wind is a less explored solution to the challenge of integrating renewables with existing infrastructure and demands, reducing solar curtailment and accommodating high ramp rates. Wang et al., reported that offshore wind possesses a significant advantage for the electrical grid in the temporal alignment between peak power demand in the electrical grid and the diurnal and seasonal patterns of this resource [26]. The daily offshore wind generation peaks in the evening hours, which coincides with the timing of the daily peak demand in the evening hours [26]. This

can be seen in Figure 2-3. During the winter months, offshore wind is two to four times more valuable than solar and land-based wind when considering demand-based values [26]. In Wang et al., [26], the authors found that between solar, land-based wind, and offshore wind, offshore wind demonstrates the best temporal alignment with demand and therefore possesses the largest demand-based value when factoring in temporal correspondence between power and demand. One limitation of this study is that the authors only considered the spatiotemporal patterns of potential offshore wind production in the Central California coast. Additionally, since the authors only looked at the monthly averages, this eliminates the dynamic daily and weekly fluctuations in the profiles. While the results of this study suggest offshore wind is a promising source of renewable energy, there needs to be further investigation to determine whether the conclusions of this study can be applied to other potential wind farm sites.

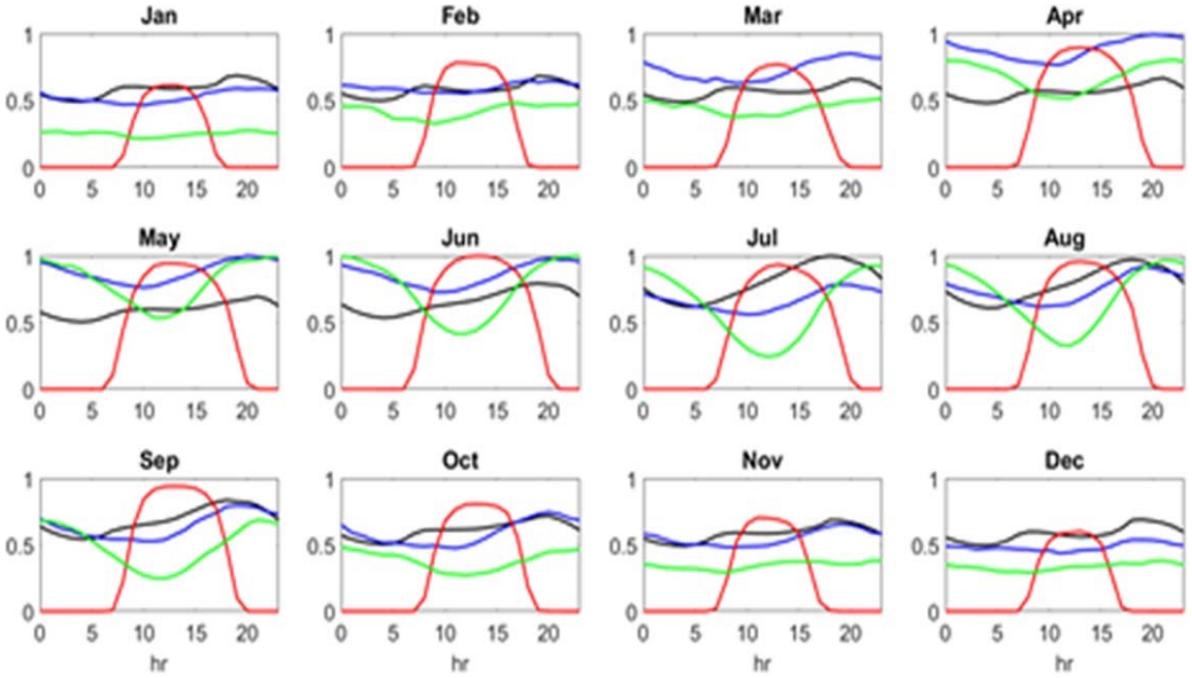

Figure 2-3: Image from [26]**. Daily normalized averages of hourly California electricity demand (black), solar production (red), onshore wind production (green), and offshore wind production (blue) in the central coast of California.**

In [23], E3 used a resource planning tool (RESOLVE) to quantify the economic value of offshore in California by estimating the potential electric system savings if offshore wind was deployed to meet the state's climate goals in 2030 and 2040. Although they predict that offshore wind will continue to have the highest capital costs in comparison to solar and onshore wind, it is

a least-cost resource option that has the potential to save ratepayers approximately $1 to $2 billion dollars [23]. E3 estimates that between 7 and 9 GW of offshore wind will be the optimal amount to meet the state's energy goals in the lowest cost manner [23]. Figure 2-4 compares the average hourly profile offshore wind, solar, onshore wind from various states, and the projected cost of electricity in 2030. This figure depicts the coincidence between offshore wind and the peak demand in the evening hours, reflected in the projected energy price.

Figure 4: Projected Average Renewable Resource Hourly Generation Profiles vs. 2030 Average Energy Prices in Model

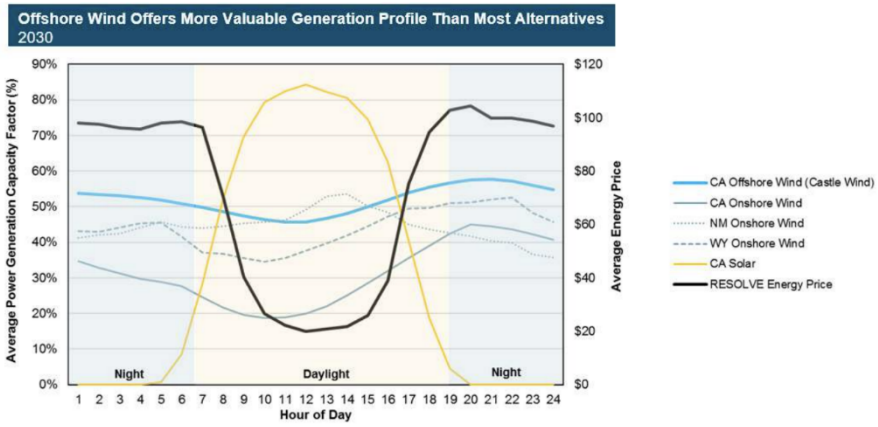

Figure 2-4: Image from [23] **that shows the value of offshore wind energy peak power during valuable and high-emission evening hours.**

In Figure 2-5, the installed capacity of offshore wind, onshore wind, solar, and battery energy storage for 2030 and 2040 are shown. The capacities are compared for scenarios with and without offshore wind. This figure illustrates why offshore wind results in electric system saving: offshore wind significantly offsets the amount of the capacities of solar and battery energy storage that are needed to achieve the state's climate goals in 2030 and 2040 [23]. In 2040, every 1 MW of offshore wind installed reduces the amount of solar and battery storage capacity by 1.7 MW and 1.09 MW, respectively.

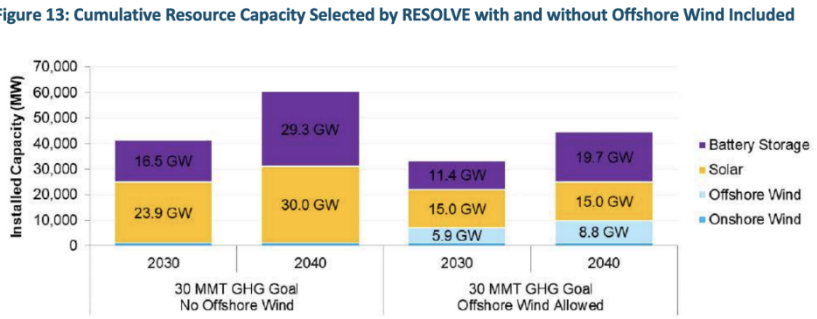

Figure 2-5: Image from Ref [23]**. The results suggest offshore wind is a low-cost resource, and it may result in $1-2 B cost savings for the electricity grid in the future.**

One important area of research related to intermittent renewables is transmission and storage of energy. Similar to solar and onshore wind, offshore wind turbines are energy conversion technologies, which transfer a form of solar energy (wind) to electricity in one step. Wind is fundamentally a form of solar energy that is caused by uneven heating of the atmosphere, irregularities of the earth's surface, and the rotation of the earth [29]. In order to convert mechanical energy to electricity, wind turbine blades are designed to capture the aerodynamic forces of the wind [29]. When wind flows across the blade of a turbine, there is a difference in air pressure across each blade which causes the blade to spin [29]. This action spins the rotor that is connected to a generator, which uses Faraday's electromagnetism principles to induce a potential difference across a coil that results in electron flow, and thus electricity [29]. Thus, since offshore wind turbines are an energy conversion technology the question of energy transmission and storage is critical.

One option for transmission is to use high voltage direct current subsea cables to deliver the offshore wind energy as electricity to the electrical grid. While this method may be the least expensive method for short transmission distances [30], the physical size of the subsea cable limits the amount of electricity can be delivered at a time [28]. Further if offshore wind energy is directly connected to the grid, it is important to understand how this resource complements the electric load. While prior studies have statistically assessed the correlation between solar and onshore wind and the electric demand [[31]–[35]], to my understanding besides the work of [26], there is no other work that quantitatively assesses the correlation and alignment of offshore wind and the electrical grid. Additionally, there is no other work that uses time series statistical

methods to assess the correlation between offshore wind and solar, onshore wind, and electrical demand. This is significant because various studies have stated that one of the advantages of offshore wind is the alignment with the electrical demand.

An alternative option for delivery of offshore wind energy is to couple it with water electrolysis in which the electricity is used to renewably produce hydrogen. When hydrogen is produced from water electrolysis reactions it does not produce any carbon emissions, making it a clean fuel. Also, hydrogen would expand the numbers sectors and end-uses that offshore wind could support, so that it is not limited to the electrical grid. Hydrogen has the advantage of being a simultaneous energy carrier and medium for energy storage and it may be the most suitable option for long-distance transmission of offshore wind power [30]. Today, several offshore-wind-to-green-hydrogen projects in Europe are underway. Current projects include the NortH2 project in the Netherlands [36], the Hornsea 2 in the United Kingdom [37], PosHYdon in the North Sea [38], and the Oyster project [39]. In Denmark, an offshore wind hydrogen project is currently under construction that will be used to power the transportation sector [40]. Although the idea of integrating offshore wind and hydrogen is not novel, there is limited work in the literature that assesses the thermodynamics of these integrated systems. There are even fewer studies that have quantitatively studied how offshore wind could be coupled with a desalination system and a solid oxide electrolyzer in an offshore platform.
Table 2-1 lists the prior work on offshore wind and hydrogen and the main findings from those studies.

Table 2-1: Summary of prior work on offshore wind conversion to hydrogen

Title and Reference	Major Conclusions
Offshore renewable energy resources and their potential in a green hydrogen supply chain through power-to-gas [28]	Conversion of offshore wind into hydrogen and subsequently methane is possible offshore with existing technology. In order to meet the spatial requirement of such a conversion infrastructure, the idea of an artificial island is presented that houses the electrolyzers, oxyfuel plant, and methanation reactors – all industrial-sized. It has also been noted that the existing CCS technique to dump carbon dioxide in continental shelves can be diverted and instead used in methanation reactors to produce synthetic natural gas. The study highlights that by

	adopting this method, the problem of transmission of electricity or energy in the form of hydrogen can be circumvented.
Bulk power transmission at sea: Life cycle cost comparison of electricity and hydrogen as energy vectors [30]	In this study, four power transmission topologies are studied: electricity, hydrogen pipeline, liquified hydrogen transported by ship, and compressed hydrogen transported by ship. Based on the levelized cost of energy, for shore distances, the best solution is power transmission through electric cables. For distances over 1000 km, the best solution is to convert the power into hydrogen and to send by ship. A significant observation in this study is that for both shallow and deep waters, transportation of liquefied hydrogen by ship is the best solution for long distances.
Sustainable Hydrogen Production from Offshore Marine Renewable Farms: Techno-Energetic Insight on Seawater Electrolysis Technologies [41]	This study conducts an energetic assessment on producing hydrogen from offshore wind using three different electrolysis technologies: direct seawater electrolysis, low-temperature electrolysis, and high-temperature electrolysis. They conclude that low-temperature electrolysis is best suited for this application because it adapts better to the power dynamics in offshore wind.
Hydrogen production with sea water electrolysis using Norwegian offshore wind energy potentials [42]	This is an analysis on the economics and feasibility of a large-scale offshore hydrogen production platform using offshore wind energy. SOECs, though they can achieve higher theoretical efficiencies than PEM, require a steam generator and a high-capacity compressor since hydrogen is produced at atmospheric pressure. It is worth considering that although offshore wind power is not highly variable within the minute or second, it is variable within the hour. An advantage of offshore wind power is that the technology for developing sophisticated platforms may already exist in the offshore oil and gas industry, since this industry builds platforms for refinery processes.

2.2 **Electrolysis Thermodynamics Fundamentals**

Electrolysis is a non-spontaneous electrochemical reaction in which electrical energy is used to dissociate an original substance into its components. Electrolysis can be used to convert electrical and thermal energy into chemical energy, and one such example of this is water electrolysis. Water can be dissociated into hydrogen and oxygen by applying electricity to an electrolysis cell:

$$H_2O \rightarrow H_2 + \frac{1}{2}0_2$$

(2-1)

In electrochemical reactions, the reaction is split into two electrochemical half reactions. The redox (reduction-oxidation) reactions are physically separated by an electrolyte so that there is a flow of ions and electrons between the electrodes.

To understand the thermodynamic principles that govern electrolysis, it is important to define some terms first:

1. Enthalpy (ΔH) is representative of the total energy required to dissociate water. It depends on temperature and pressure. When $\Delta H > 0$, the reaction is exothermic, and heat is expelled to the environment. When $\Delta H < 0$, the reaction is endothermic, and heat is required for the reaction to occur. All electrolysis reactions are endothermic.
2. Entropy (ΔS) is a property of the material, and it represents the number of microstates accessible to a system. Increasing entropy means increasing number of microstates. Entropy can increase by providing additional energy to the system. $T\Delta S$ represents the total heat required for the reaction to occur.
3. Gibbs Free Energy (ΔG) is representative of the minimum electrical energy required to dissociate water. If $\Delta G < 0$, then the reaction is spontaneous, and we can obtain work from the reaction. If $\Delta G > 0$, then the reaction is not spontaneous, and work needs to be done on the system for the reaction to occur. All electrolysis reactions are non-spontaneous. In a constant temperature and pressure process, the maximum electrical work a system can perform is the Gibbs free energy difference of the reaction. ΔG is related to the reversible voltage:

$$\boldsymbol{\Delta G = -i * U_{rev}}$$

(2-2)

4. Oxidation – refers to a reaction in which electrons are liberated.
5. Reduction – refers to a reaction in which electrons are consumed.
6. Anode – this is the electrode where oxidation reactions occur. Electrons flow out of this electrode.

7. Cathode- this is the electrode where reduction reactions occur. Electrons flow into this electrode.

At standard conditions (T=298 K and P = 1 bar), water is a liquid and hydrogen and oxygen are gaseous. Therefore, the standard entropy, enthalpy and free Gibbs energy changes for the reaction are [43]:

$$\Delta H = 284.840 \frac{kJ}{mol}; U_{tn} = 1.48\ V \quad (2\text{-}3)$$

$$\Delta S = 163.15 \frac{J}{mol\ K} \quad (2\text{-}4)$$

$$\Delta G = \Delta H - T\Delta S = 237.22 \frac{kJ}{mol}; U_{rev} = 1.23\ V \quad (2\text{-}5)$$

When water vapor is electrolyzed, the enthalpy, entropy, and free Gibbs energy are:

$$\Delta H = 241.80 \frac{kJ}{mol};\ U_{tn} = 1.25\ V \quad (2\text{-}6)$$

$$\Delta S = 44.10 \frac{J}{mol\ K} \quad (2\text{-}7)$$

$$\Delta G = \Delta H - T\Delta S = 228.66 \frac{kJ}{mol}; U_{rev} = 1.18\ V \quad (2\text{-}8)$$

Each of the energy requirements for electrolysis ($\Delta H, T\Delta S,$ and ΔG) is dependent upon the temperature and pressure. Figure 2-6 shows the temperature dependence of each of the energy demands. At low temperatures, a higher total energy is required to dissociate liquid water. Since the total energy required is mostly constant at temperatures higher than 100°C, the decrease in electrical energy required is balanced by an increase in the heat demand as the temperature

increases. Figure 2-6 shows that as the temperature increases, the requirement for electrical energy decrease and the demand for heat increases. Higher operating temperatures are thermodynamically favorable for the following reasons: (1) They require less overall electrical energy, which tends to be more valuable than heat and can be readily available as waste heat from power plants and waste industries [44]; (2) the higher operating temperatures result in a lower electrical energy required which is associated with improved electrochemical kinetics since the temperature at the reactive sites (triple phase boundaries) is high, thus reducing the activation energy for the reaction.

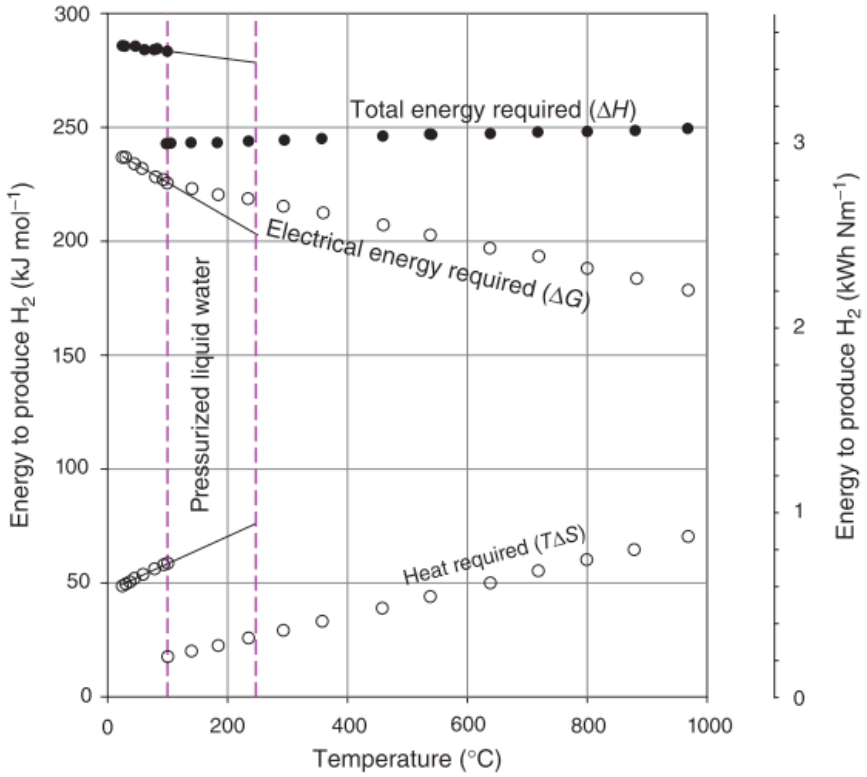

Figure 2-6: Thermodynamic fundamentals of electrolysis from [43]

Additionally, the operating voltage plays an important role in the thermal effects, allowing cells to operate in thermoneutral, exothermic, and endothermic thermal regimes. While the electrolysis reaction will always be endothermic, the heat required may be met from Joule heating. For example, in high temperature Solid Oxide Electrolysis (SOE) Systems, irreversible losses occur due to ohmic resistance and electrode overpotentials which result in heat generation [45]. In the thermoneutral mode, the heat generated through irreversible losses is equivalent to the thermal

energy required by the reaction [45], [46]. This mode implies various relations: first, the electrical energy input equals (ΔG) the total energy demand (ΔH); second, the entropy necessary for water splitting equals the heat generated by the reaction as losses; finally, the process must be isothermal and adiabatic [47]. The thermoneutral voltage is the voltage at which the reaction occurs with 100% thermal efficiency [48]. The thermoneutral voltage can be defined as:

$$U_{tn} = \frac{\Delta H}{nF} \tag{2-9}$$

In which nF, which represents the number of moles of electrons (n) times Faraday's constant (F) (the number of coulombs per mole of electrons). U_{tn} for liquid water and steam are given in equations (**2-3**) and (**2-6**). At 800°C, the U_{tn} is ~1.28V. Generally, thermal management is easier in thermo-neutral operation; the endothermicity of the reaction simplifies the temperature distribution within the stack when its operated close to thermo-neutral [47]. The theoretical electrical efficiency in this mode is 100%.

Exothermic operation occurs when the heat generated in the stack from these irreversible losses exceeds the thermal energy consumed by the endothermic electrolysis reaction [45]. In exothermic mode of operation, the temperature increases along the stack due to heat accumulation from operating at higher current densities [46]. This allows the excess heat to be recovered for processes such as heating the inlet gasses to the desired operation temperature [46]. Exothermic operation results in lower efficiencies since electricity is intentionally used to produce losses. This mode may also result in degradation due to the higher current densities (high concentration losses) from operating the voltage in excess. The electrical efficiency in this mode is $< 100\%$.

Endothermic mode of operation occurs when the thermal energy demand exceeds what is available from Joule heating [45]. In endothermic operation, the system operates at lower average current densities, which decreases hydrogen production and energy consumption [46]. In this mode, the irreversibilities are lower than the thermal energy required for the reaction resulting in less heat generation from the stack, and thus, an external heat source is required to

meet the heat demand [45], [46]. As the reaction proceeds along the stack channel, the temperature decreases [45]. Due to the low irreversibilities in this regime, the electrical efficiency in this mode is $> 100\%$.

In high temperature systems, there is a known tradeoff between using electrical energy for thermal energy generation against the additional costs for the transfer of this thermal energy from an external source [45]. Figure 2-7 shows how a solid oxide electrolysis system can behave as an endothermic sink or exothermic source depending on the operating voltage. In Figure 2-7, the system enclosure (furnace) is operated at a steady temperature of 800°C. In endothermic operation (voltages below the 1.28V), the cell acts as a thermal sink and induces cooling. When the voltage exceeds $\boldsymbol{U_{tn}}$, there is a steep temperature increase due to the exothermicity of the stack.

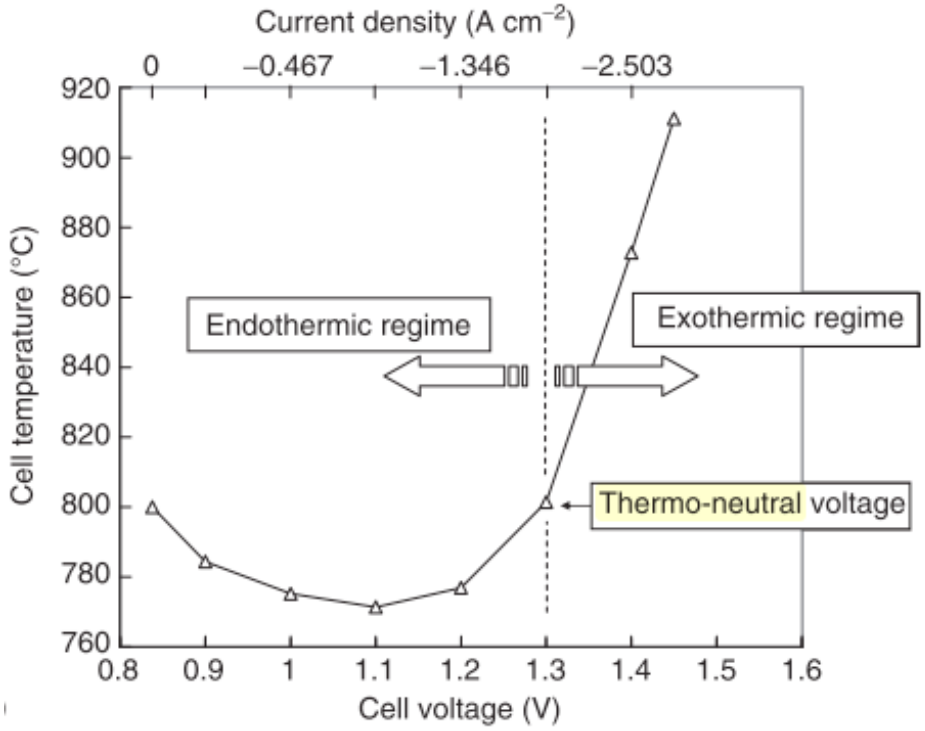

Figure 2-7: The temperature in the middle of an SOEC stack plotted against cell voltage and current density. From [43]**.**

2.2.1 **Solid Oxide Electrolysis Fundamentals**

In electrochemical reactions, the transfer of electrons takes place through an electronic conductor which allows us to separate the electron-transfer reactions and use it to do work. The electrolyte, which typically consists of yttria-stabilized zirconia (YSZ), is responsible for selectively conducting oxide ions from the cathode to the anode as shown in Figure 2-8. Note that the functional layer is made up on electronic and ionic conductors. The electrochemical reactions occur at the locations where the ions, electrons and gas species meet, called the triple phase boundary.

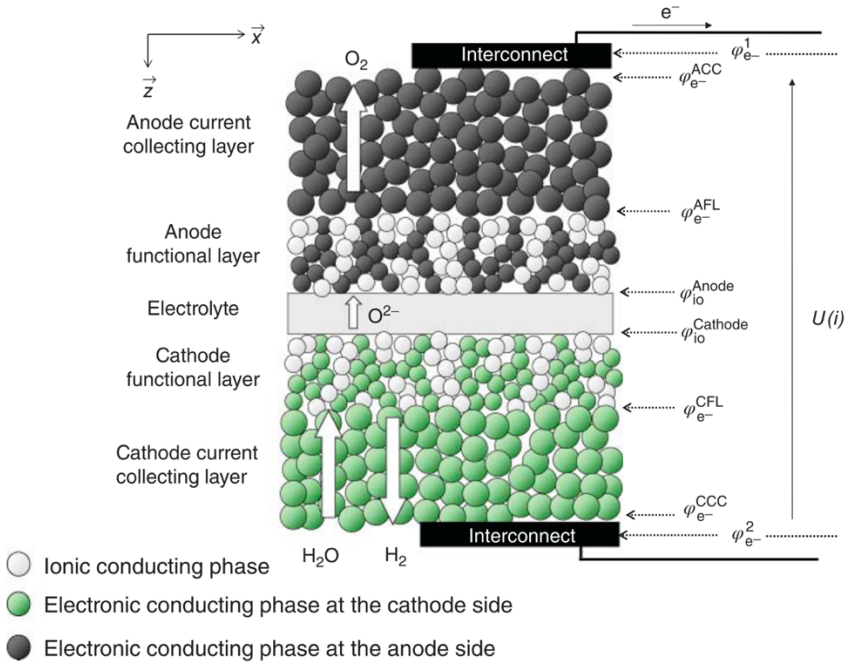

Figure 2-8: Schematic representation of an SOEC from [43]**.**

Although YSZ is known for being an excellent oxide ion conductor (1000 times more conductive than electrons), YSZ is also a semiconductor with electron conductivity at low oxygen pressures and electron hole conductivity in oxidizing environments [49]. This has important implications for the Galvani potential (ϕ) since it reflects the potential of all the charged particles in the lattice. Figure 2-9 illustrates the different types of potentials in a solid conductor. ϕ is the driving potential for the mobile oxide ions, and it is mainly driven by the lattice ions. The Fermi potential (π) is a ratio of the electrochemical potential of the electrons to Faraday's constant

[49]. The Fermi potential is the main factor that drives electrons, and since electron concentration relative to the electron concentration under standard conditions affects it strongly, the Fermi potential varies strongly across the electrolyte [49]. This is reflected in Figure 2-10.

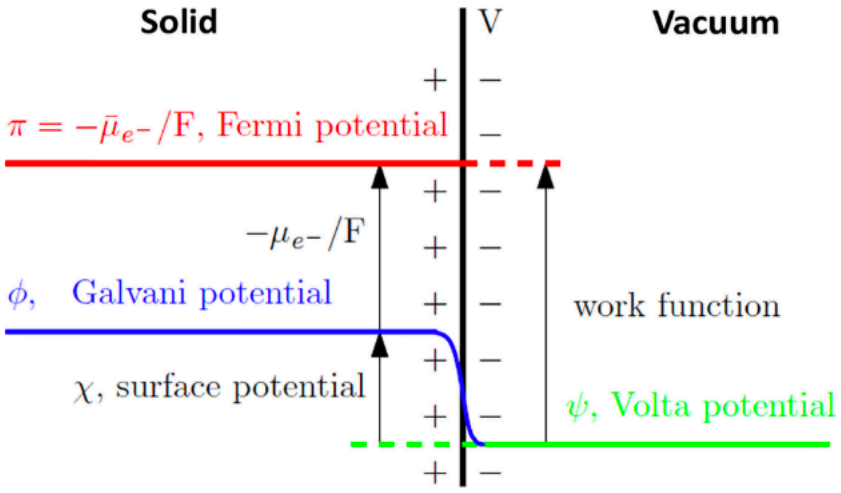

Figure 2-9: Fermi, Galvani, and Volta potential in a solid conductor relative to the outer electric potential in a vacuum. From [49]**.**

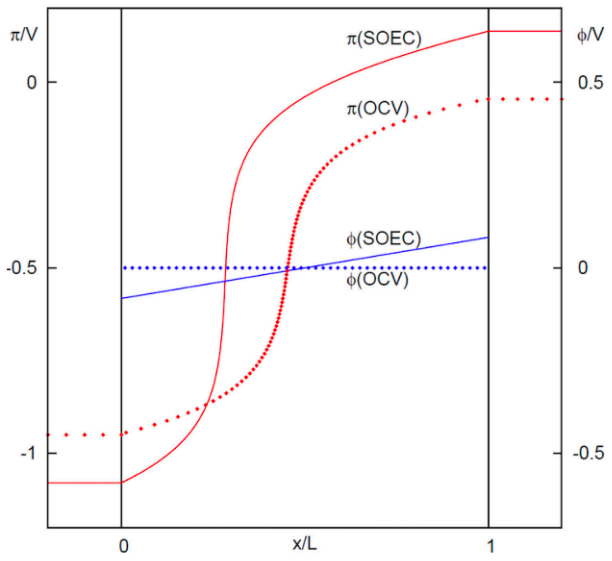

Figure 2-10: The Fermi and Galvani potentials across a YSZ electrolyte compared to open circuit conditions at 1000°C. From [49]**.**

Voltage

One of the fundamental measurements in any electrochemical analysis is the potential difference or voltage (U). Voltage is defined as the sum of the reversible voltage at equilibrium conditions plus the overpotentials (η) corresponding to entropy generation:

$$U(i) = U_{rev} + |\eta| = \varphi_{e^-}^{1} - \varphi_{e^-}^{2} \quad \textbf{(2-10)}$$

In a real cell, the voltage is a measurement of the difference in potential (φ) between two electric potentials taken at the metallic interconnects on the anode and cathode. This is defined as $\varphi_{e^-}^{1} and\ \varphi_{e^-}^{2}$ in Figure 2-8. The voltage is a representation of the amount of work per unit charge needed to move an electric charge between the electrodes or it can also be considered as the difference in energy of the electrons at the two electrodes.

Focusing first on the reversible cell voltage, it is important to consider an electrochemical system at equilibrium, in which there is no current flow and, thus, there are no net reactions at either of the electrodes. At equilibrium in each of the electrodes, the half reactions reach a dynamic equilibrium where the rates of the forward and reverse reactions are equal. The energy of each of the electrons for each of the electrodes is different and it is this difference in electron energy that drives the full reaction when the circuit is closed [50]. The equilibrium cell potential, otherwise known as the open circuit voltage, is a function of the thermodynamic state of the reactants and products. Because the hydrogen and oxygen are separated from each other at each electrode, it is possible to have an equilibrium state.

The change in Gibbs energy is a representation of the maximum work that can be done by a system for a closed reversible system at constant pressure and temperature. In electrolysis, the ΔG represents the minimum required work for the reaction to occur. The total charge transferred in a full reaction is, nF, which represents the number of moles of electrons (n) times Faraday's constant (the number of coulombs per mole of electrons). Therefore, the minimum voltage for electrolysis, U_{rev}, is given by:

$$\Delta G = -nFU_{rev}$$

(2-11)

Where ΔG is negative when the surroundings do work on the system. This fundamental equation relates the amount of work (ΔG) to the potential difference in the electron energy at the two electrodes. The cell potential, U, is defined as

$$U = \phi_{anodic\,rxn} - \phi_{cathodic\,rxn}$$

(2-12)

When the system deviates from standard conditions (25 ^{o}C, 1 atm), it is necessary to use an alternative definition of ΔG with a correction term that accounts for the activities of the gaseous species to determine the reversible cell voltage [50]. This leads to the Nernst Equation:

$$\Delta G = \Delta G^{0} + \mathrm{RT}\left(\Sigma_{ox} ln a_i^{s_i} - \Sigma_{red} ln a_i^{s_i}\right)$$

(2-13)

Where $\Delta G^{0}$is the Gibbs energy change at standard conditions, R is the gas constant, T is the temperature, and $a_i^{s_i}$ is the activity of all species, i, and s_i is the stoichiometric coefficient of species i in the reaction. For ideal gasses, the partial pressures will replace the activity. The Gibbs energy at standard conditions is tabulated as a relative value.

Therefore, using the relationship between ΔG and U at equilibrium conditions, the open circuit voltage or the reversible cell potential is:

$$U_{rev,ocv}(T, P_i) = E_{rev,ocv}^{anode}(T, P_i) - E_{rev,ocv}^{cathode}(T, P_i)$$

(2-14)

$$E_{rev,ocv}^{anode}(T, P_i) = E_{anode}^{o}(T, P) + \frac{RT}{nF}\ln\left(P_{O_2}^{\frac{1}{2}}\right)$$

(2-15)

$$E_{rev,ocv}^{cathode}(T, P_i) = E_{cathode}^{o}(T, P) + \frac{RT}{nF}\ln\left(\frac{P_{H_2O}}{P_{H_2}}\right)$$

(2-16)

$$U_{rev,ocv}(T,P_i) = U^o(T,P) + \frac{RT}{nF}\ln\left(\frac{P_{H_2}P_{O_2}^{\frac{1}{2}}}{P_{H_2O}}\right)$$

(2-17)

Where:

$U_{rev,ocv}$: Reversible, temperature dependent cell voltage (ideal OCV)

U^o: Potential of the reaction at standard conditions (equilibrium potential)

R: Gas constant (8.314 J/kmol)

F: Faraday's number 96,487 (C/equiv)

T: absolute temperature of cell (K)

$P_{reactants}, P_{products}$: partial pressures of the species involved

n: number of electrons involved (2)

The open circuit voltage (OCV) represents the theoretical maximum reversible voltage a fuel cell can draw, and the minimum voltage needed for an electrolysis reaction. The OCV of a cell, also called the Nernst potential or electromotive force, is the difference in electrochemical potentials of oxygen on the fuel and air electrodes' interfaces or triple phase boundaries [51].

When the cell is not at standard temperature conditions, we must account for the influence of temperature on the standard cell voltage (U^o). There are various expressions for correcting the standard cell voltage that are derived from the Gibbs-Helmholtz equation and thermodynamic relations. In this work, an equation from [52] is used:

$$U^0(T) = \frac{-\Delta G(T_0)}{nF}\left(\frac{T}{T_0}\right) + \frac{-\Delta H(T_0)}{nF}\left(1 - \frac{T}{T_0}\right) + \Delta a\left(T - T_0 - Tln\left(\frac{T}{T_0}\right) + \frac{(T-T_0)^2}{nF}\left(\frac{\Delta b}{2} + \frac{\Delta c}{2TT^2}\right)\right.$$

(2-18)

Where $\Delta a = 2a_{H_2O} - 2a_{H_2} - a_{O_2}$, and similarly for Δb and Δc. $\Delta G, \Delta H, a, b,$ and c are in Table 2-2.

Table 2-2: Thermodynamic data at standard conditions (298.15 K and 1 atm) [52]

	ΔG $\left(\frac{kJ}{mol}\right)$	ΔH $\left(\frac{kJ}{mol}\right)$	a_i $\left(\frac{J}{mol * K}\right)$	b_i $\left(\frac{J}{mol * K}\right)$	c_i $\left(\frac{J}{mol * K}\right)$
O_2	0.0	0.0	29.96	4.2 x 10^{-3}	-1.67 x 10^{-5}
H_2	0.0	0.0	27.28	3.3 x 10^{-3}	0.5 x 10^{-5}
$H_2O\ (g)$	-228.572	-241.818	30.54	10.3 x 10^{-3}	0.0

The Nernst voltage can also be found for a cell in which $i \neq 0$ [43]:

$$U_{rev} = U_{rev,ocv} + \Delta V_{rev}^{anode} - \Delta V_{rev}^{cathode} \quad \textbf{(2-19)}$$

$$\Delta V_{rev}^{anode} = \frac{RT}{2F} \ln\left(\frac{P_{O_2,i\neq 0}^{0.5}}{P_{O_2,i=0}^{0.5}}\right) \quad \textbf{(2-20)}$$

$$\Delta V_{rev}^{cathode} = \frac{RT}{2F} \ln\left(\frac{P_{H_2,i=0} P_{H_2O,i\neq 0}}{P_{H_2,i\neq 0} P_{H_2O,i=0}}\right) \quad \textbf{(2-21)}$$

The Nernst equation neglects any losses due to mass transfer across the electrodes which allows us to assume the partial pressure at the active electrochemical sites is equivalent to the partial pressure at the channel inlet [43]. It also neglects ohmic losses due to ionic and electronic resistivities, and kinetic effects due to multi-elementary reactions that take place at the triple phase boundary sites (see Figure 2-11) [43]. It shows us that even in the most ideal conditions, there are losses due to gas conversion process that alter the gas composition. When the cell is electrically induced, the production of oxygen increases the partial pressure of oxygen in the anode which then increases the anode potential. Similarly, the production of hydrogen and consumption of steam will decrease the cathode potential, and thus increase the cell voltage [43].

In reality, when a current is applied to the cell, that is when the cell is polarized, the actual potentials of the cell will deviate from the reversible cell voltage predicted by the Nernst

equation since current flow will result in irreversible losses due to activation, ohmic, and concentration polarizations as observed in equation (2-17). Thus, the Nernst Equation is an idealized calculation of the reversible cell voltage.

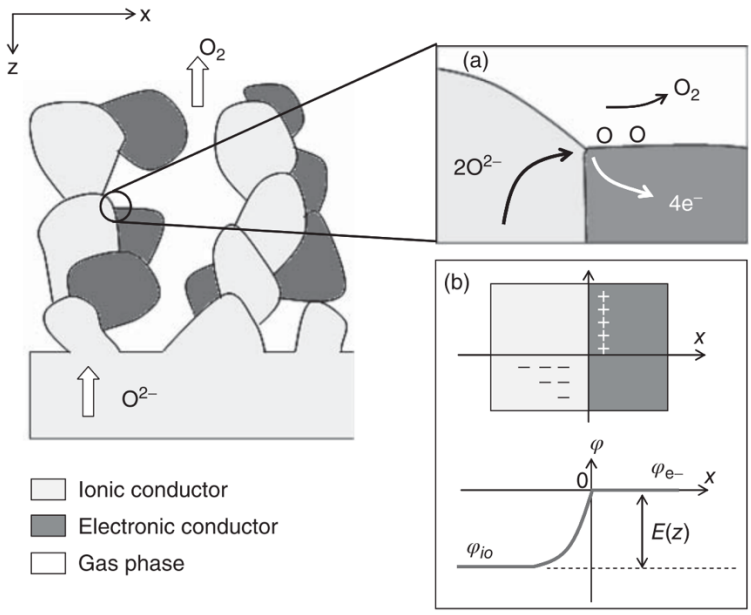

Figure 2-11: Functional layer of an SOEC anode [43]**.**

2.2.2 **Cell Resistances lead to Ohmic Losses**

The real voltage represents the increased demand for energy for the reaction when the current density increases. The losses are associated with an increase in entropy production of the system which results in heat generation in the cell and enables the SOEC cell to have various thermal regimes by which the heat generation is balanced by the endothermic electrolysis reaction. According to [43], the cell voltage can be attributed to seven contributions in Figure 2-8 related to the differences in electric potentials across the cell thickness:

$$U(i) = (\varphi_{e^-}^{1} - \varphi_{e^-}^{ACC}) + (\varphi_{e^-}^{ACC} - \varphi_{e^-}^{AFL}) + \left(\varphi_{e^-}^{AFL} - \varphi_{io}^{Anode}\right) + \left(\varphi_{io}^{Anode} - \varphi_{io}^{Cathode}\right) + \left(\varphi_{io}^{Cathode} - \varphi_{e^-}^{CFL}\right) + (\varphi_{e^-}^{CFL} - \varphi_{e^-}^{CCC}) + (\varphi_{e^-}^{CCC} - \varphi_{e^-}^{2})$$

(2-22)

- **Contact resistances (R_c) at the interfaces between the electrode and the interconnect.**

  This is due to imperfect electrical contact at the electrode/ interconnect interface, and it can be given by:

$$\varphi_{e^-}^{1} - \varphi_{e^-}^{ACC} = R_{c,anode} i \quad \textbf{(2-23)}$$

$$\varphi_{e^-}^{CCC} - \varphi_{e^-}^{2} = R_{c,cathode} i \quad \textbf{(2-24)}$$

  Where i is the current. For this contribution, $R_{c,cathode} \sim 0 \ll R_{c,anode}$

- **Ohmic losses (R^{eff}) in the current collecting layers**

  Ohmic losses across the anode and cathode current collector (CC) layers are due to electrical resistivities to flow and are represented using these terms:

$$\varphi_{e^-}^{ACC} - \varphi_{e^-}^{AFL} = R_{ACC}^{eff} i \quad \textbf{(2-25)}$$

$$\varphi_{e^-}^{CFL} - \varphi_{e^-}^{CCC} = R_{CCC}^{eff} i \quad \textbf{(2-26)}$$

  Where $R^{eff} = \frac{l}{\sigma}$ where σ is the conductivity and l is the thickness of the layer.

- **Electric potential in the Helmholtz double layer due to the potential between the electronic and ionic conductors**

  In the functional boundary layers, there is a triple phase boundary line where the reaction occurs, and charge transfer takes place. This is the point at which the gas, ions, and electrons meet. In this region, there is an electric potential between the electronic and ionic conductor due to the excess of charge on each side of the metal/ electrolyte interface. This is known as the Helmholtz double layer, and it yields a local potential E:

$$E = \varphi_{e^-} - \varphi_{io} \quad \textbf{(2-27)}$$

The electrochemical reactions locally absorb and generate charges and gas species that leads to a steep evolution of the local electrode potential on each side of the functional layer:

$$E_{anode} = \varphi_{e^-}^{AFL} - \varphi_{io}^{Anode} > 0 \quad \textbf{(2-28)}$$

$$E_{cathode} = \varphi_{e^-}^{CFL} - \varphi_{e^-}^{CCC} < 0 \quad \textbf{(2-29)}$$

During electrolysis operation, the anode potential increases while the cathode decreases, which results in a higher cell voltage.

- **Ionic Resistance in the electrolyte**

  The diffusion of oxygen ions through the electrolyte is given by:

$$\varphi_{io}^{Anode} - \varphi_{io}^{Cathode} = R_{electrolyte} * i \quad \textbf{(2-30)}$$

$$R_{electrolyte} = \frac{l_{electrolyte}}{\sigma_{io}} \quad \textbf{(2-31)}$$

Where $l_{electrolyte}$ denotes the thickness of the electrolyte membrane and φ_{io}^{Anode} and $\varphi_{io}^{Cathode}$ are the electric potentials in the ionic conducting phase at anode/ electrolyte or cathode/electrolyte interfaces. In this region the voltage drop is dependent on the ionic conductivity (σ_{io}) of the dense material using Ohm's law (above).

2.2.3 Concentration and Activation Polarizations

In addition to the Ohmic losses that are caused by ionic/ electronic charge transfer resistances described in the previous section, the cell also experiences losses at each electrode: concentration and activation polarizations. To overcome these losses, the cell potential must operate at higher overpotentials (η) than the U_{rev}.

The potential (E) at each electrode is given by:

$$E_{anode} = E_{rev}^{anode} + \eta_{anode} \quad \textbf{(2-32)}$$

$$E_{cathode} = E_{rev}^{cathode} + \eta_{cathode} \quad \textbf{(2-33)}$$

Where each polarization (η) is made up of a contribution from activation and concentration losses.

Concentration overpotentials (η_{conc}) represent the resistance to mass transfer at the triple phase boundary sites. They are mostly due to the concentration gradients that can develop when the fluxes of the reactants and products to and from, respectively, the triple phase boundary is lower than the corresponding electrical current [53]. Concentration overpotentials are most apparent at high current densities due to the high gas fluxes [43], and high steam utilization factors can also contribute to high concentration overpotentials [53]. The microstructure of the cells and partial pressure gradients can resist the transport of gaseous species from the bulk gas to the triple phase boundaries [54]. Since the production of hydrogen is balanced by the consumption of steam, the concentration overpotentials on the cathode side tend to only be due to gas diffusion. Since the anode side is not balanced by consumption and production of gaseous species, oxygen production can cause local pressure gradients at the electrode / electrolyte interface which can lead to delamination. Gas concentrations can also impact the reaction kinetics and the activation overpotentials [44]. The concentration polarization is defined from the Butler-Volmer equation as follows [43]

$$\boldsymbol{\eta_{conc}^{Cathode}(x) = \frac{RT}{2F} \ln\left(\frac{P_{H_2;i\neq0}^{canal}(x)\, P_{H_2O;i\neq0}^{TPB}(x)}{P_{H_2;i\neq0}^{TPB}(x)\, P_{H_2O;i\neq0}^{canal}(x)}\right)} \quad \textbf{(2-34)}$$

$$\boldsymbol{\eta_{conc}^{Anode}(x) = \frac{RT}{4F} \ln\left(\frac{P_{O_2;i\neq0}^{TPB}(x)}{P_{O_2;i\neq0}^{canal}(x)}\right)} \quad \textbf{(2-35)}$$

Where R is the universal gas constant, T is the absolute temperature, F is Faraday constant, $P_{species;i\neq 0}^{TPB}$ is the species' pressure at the triple phase boundary (Pa), and $P_{species;i\neq 0}^{canal}$ is the species' (either hydrogen, oxygen or steam) pressure in the corresponding gas channel. Note that the concentration potentials cause the actual potential at the triple phase boundaries to deviate from the ideal reversible potential predicted by the Nernst equation.

Activation overpotentials are due to the irreversible phenomena in the functional layer due to the kinetic rates of multi-elementary reactions [43]. The high operating temperatures of SO cells do not result in a single limiting step, and thus activation overpotentials tend to be low for SO cells. The global activation overpotentials are typically modelled by the Butler-Volmer equation which accounts for differences of gas concentrations at the triple phase boundaries and in the bulk stream [53]. The Butler-Volmer equation uses an apparent exchange current density (j_0) to characterize the electrochemical activity of a reaction. The electrode microstructure, such as the density of triple phase boundary sites, the electrochemical activity of the materials, and local temperature all contribute to the apparent exchange current density [43]. The Butler-Volmer equation relates the current density and the activation polarization and it is of the form [55]:

$$j(x)_{cathode} = j_{0,cathode}(x)\left[\exp\left(\frac{\beta n_e F \eta_{act}^{Cathode}}{RT_{PEN}}\right) - \exp\left(-\frac{(1-\beta) n_e F \eta_{act}^{Cathode}}{RT_{PEN}}\right)\right] \quad \textbf{(2-36)}$$

$$\boldsymbol{j(x)_{anode} = j_{0,anode}(x)\left[\exp\left(\frac{\beta n_e F \eta_{act}^{Anode}}{RT_{PEN}}\right) - \exp\left(-\frac{(1-\beta) n_e F \eta_{act}^{Anode}}{RT_{PEN}}\right)\right]} \quad \textbf{(2-37)}$$

Where β is called the transfer coefficient, and it is a dimensionless, positive number less than one, and it is usually 0.5 for fuel cell applications. n_e is the number of electrons transferred in the half reaction (2 for the cathode and 4 for the anode). The exchange current densities (j_0) can be found:

$$\boldsymbol{J_{0,cathode} = \frac{j_{H_2}^{*}\left(\frac{p_{H_2}}{p_{H_2}^{*}}\right)^{\frac{\beta_{H_2}}{2}}\left(\frac{p_{H_2O}}{p_0}\right)^{1-\frac{\beta_{H_2}}{2}}}{1+\left(\frac{p_{H_2}}{p_{H_2}^{*}}\right)^{\frac{1}{2}}}} \quad \textbf{(2-38)}$$

$$J_{0,anode} = \frac{j_{O_2}^{*}\left(\frac{p_{O_2}}{p_{O_2}^{*}}\right)^{\frac{\beta_{O_2}}{2}}}{1+\left(\frac{p_{O_2}}{p_{O_2}^{*}}\right)^{\frac{1}{2}}} \quad \textbf{(2-39)}$$

Where $j_{O_2}^{*}$ is the equilibrium exchange current density, $p_{species}$ is the pressure of the species in the gas streams and $p_{species}^{*}$ is the equilibrium pressure.

Lastly, all of these polarizations result in an expression for the actual cell voltage:

$$U_{cell} = U_{rev} + |\eta| = U_{OCV} + \left(\eta_{ohm} + \eta_{act,anode} + \eta_{conc,anode} - \eta_{act,cathode} - \eta_{con,cathode}\right) \quad \textbf{(2-40)}$$

Where the subscripts act and $conc$ represent the activation and concentration polarizations, respectively. It is important to note that each of these terms depends upon the operating current and the location on the cell. The ohmic losses can be summarized as the combination of ionic and electronic resistances [43]:

$$\eta_{ohm} = \left(R_{electrolyte} + R_{ACC}^{eff} + R_{CCC}^{eff} + R_{c,anode} + R_{c,cathode}\right) * i \quad \textbf{(2-41)}$$

In which the ionic resistances contribute significantly to the overall resistance in $R_{electrolyte}$. Cathode supported cells lower the overall ohmic losses since they have a lower electrolyte thickness.

2.3 **Seawater Electrolysis**

Electrolyzers are electrochemical devices that separate a chemical compound into two or more elemental species [41]. Electricity is stored in the form of chemical bonds in electrolysis reactions [56]. Since hydrogen generation, consumption and regeneration have the potential to be emissions-free if powered renewably from clean technologies [56], hydrogen has been proposed as a sustainable fuel that can achieve a carbon-free future. As mentioned previously, one potential end use of offshore wind is to convert the electricity to hydrogen through seawater

electrolysis. Indirect seawater electrolysis can be achieved in multiple stages using existing commercial electrolyzers, such as solid oxide (SO), proton exchange membrane (PEM), and alkaline electrolyzers, by coupling these electrolyzers with desalination systems and offshore wind farms. Unlike indirect seawater electrolysis which requires desalination and ultra-purification equipment to remove contaminants present in the seawater, direct electrolysis of seawater is a popular area of research because it directly uses seawater in the electrolysis reactions. This results in a system with fewer ancillary components (e.g. desalination equipment and water purification systems) thus reducing material investment and maintenance costs [56]. Figure 2-12 shows the different types of electrolytes that can be used in direct and in indirect seawater electrolysis, which includes alkaline, proton exchange membrane (PEM), and solid oxide (SO) electrolytes.

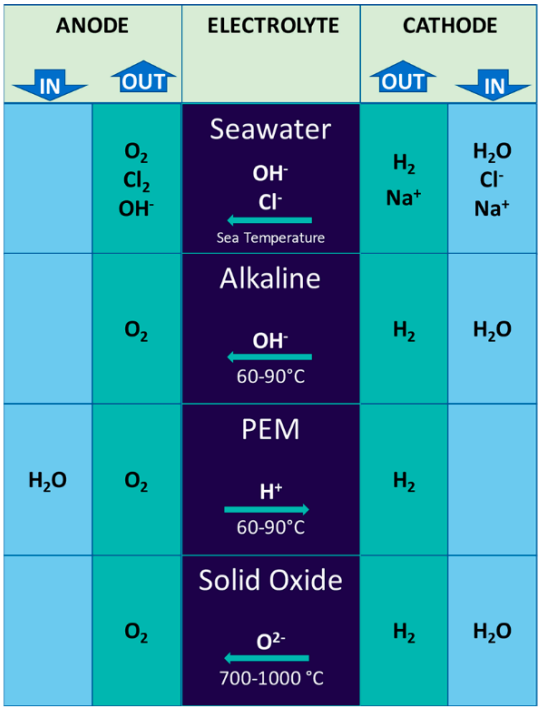

Figure 2-12: Different types of electrolytes used in seawater electrolysis. From [41].

2.3.1 **Direct Seawater Electrolysis**

Contaminants in seawater present significant obstacles for direct electrolysis that prevent it from being commercially available today. This includes dramatic pH fluctuations that may cause catalyst degradation, the presence of bacteria/ microbes, non-innocent ions, and small particles which may poison electrodes and catalysts, and may disrupt their stability [56]. A key challenge

accompanying direct seawater electrolysis is undesired chemical processes associated primarily with chloride electro-oxidation chemistry that compete with the desired oxygen evolution reaction in the anode [56], [57]. In the chlorine chemical industry, these chemical reactions are well-understood, and hydrogen is considered a byproduct of the reaction in the cathode which produces OH^- [41]. The competing reactions are represented in the Pourbaix diagram (Figure 2-13) for the oxygen evolution reaction in an aqueous 0.5 NaCl electrolyte. It shows the potential areas where the oxygen evolution reactions and the chloride oxidation reactions are thermodynamically possible. It also shows the two main reactions that compete with the OER: the chlorine evolution reaction at low pH and the hypochlorite formation in high pH.
The green line indicates the thermodynamic equilibrium between water and oxygen. When the electrode potentials are more positive than the green line, the OER is possible. At the two pH extremes, the following chloride oxidation reactions are possible:

Chloride Evolution Reaction [56]: (pH < 3)

$$2Cl^- \rightarrow Cl_2 + 2e^- \quad \textbf{(2-42)}$$

Hypochlorite Formation [56]:

$$Cl^- + 2OH^- \rightarrow ClO^- + H_2O + 2e^- \; Cl^- + 2OH^- \rightarrow ClO^- + H_2O + 2e^- \quad \textbf{(2-43)}$$

OER in an alkaline environment is [56]:

$$4OH^- \rightarrow 2H_2O + O_2 + 4e^- \quad \textbf{(2-44)}$$

In the cathode, gaseous hydrogen is produced as a byproduct [41]:

$$2H_2O + 2e^- \rightarrow H_2 + 2OH^- \quad \textbf{(2-45)}$$

Between 3 and 7.5 pH, hypochlorous acid formation is the major reaction. The difference between the standard electrode potentials increases until it reaches 0.480 V at 7.5 pH where the hypochlorite formation begins. Under alkaline conditions, the difference stays at 0.480 V which indicates the OER can achieve up to 0.480 V in kinetic overpotential [56].

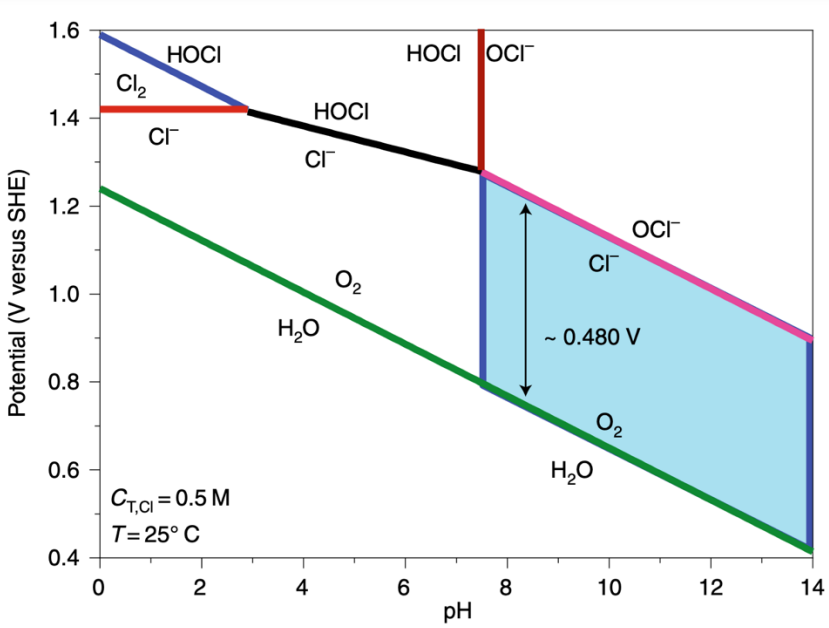

Figure 2-13: Pourbaix diagram from Reference [57]**.**

Even though direct seawater electrolysis would simplify the design of an offshore wind-to-hydrogen production platform, this process is unsustainable and impractical due to the following reasons listed in [41]: (1) the production of Cl_2 can be detrimental to the environment if allowed to leak; (2) there is low ionic conductivity in seawater increases ohmic losses; (3) the presence of contaminants such as magnesium and calcium leads to scaling, which requires more maintenance and cleaning; (4) expensive materials are needed to prevent corrosion; (5) the rejected brine can result in strong alkalization of the ocean which is harmful;(6) lastly, this is an inefficient process due to the high operating voltages (4 V). Furthermore, direct seawater electrolysis would require 160% more energy than low-temp electrolysis and it has a high environmental impact.

2.3.2 **Indirect Solid Oxide Seawater electrolysis**

While PEM electrolysis has been reported as the preferred method for indirect seawater electrolysis (e.g., see [41] and [28]), the high temperatures (700 – 1000 ^{o}C) in which SO electrolysis cells (SOEC) operate results in improved thermodynamics and kinetics [58]. Therefore, less electrical energy is required per unit hydrogen produced in comparison to low temperature electrolysis such as PEM [58]. SO electrolysis is a promising area of research for

offshore wind-to-hydrogen because of the possibility of integrating thermal steam generation with desalination and its ability to operate at high efficiencies.

In SO electrolysis, superheated water vapor (steam) is introduced into the cathode where the water reduction reaction occurs that produces hydrogen and releases oxide ions in the process [56]. Then, the hydrogen produced is purified to separate it from the remaining water in the cathodic stream [59]. The additional purification required of hydrogen at the exit of the cathode is one drawback of SOECs, which requires an additional step to remove the water content in the cathodic stream [59]. The SO electrolyte selectively passes O^{2-} ions from the cathode to the anode to produce O_2 and electrons via the OER [56], [59]. The oxygen ions recombine to form oxygen molecules as they release electrons in the process [45]. Typically, yttria-stabilized Zirconia is used in the electrolyte in SOECs, due to its ability to conduct ions [45]. SOECs are assembled in stacks in which several repeating cells are stacked to produce a sufficient rate of hydrogen [45].

Water Reduction Reaction:

$$\boldsymbol{H_2O + 2e^- \rightarrow H_2 + O^{2-}} \quad \textbf{(2-46)}$$

The oxygen evolution reaction:

$$\boldsymbol{O^{2-} \rightarrow \frac{1}{2}O_2 + 2e^-} \quad \textbf{(2-47)}$$

The overall reaction:

$$\boldsymbol{H_2O \rightarrow H_2 + \frac{1}{2}O_2} \quad \textbf{(2-48)}$$

SOECs possess a possible unique configuration in which the steam is generated from the seawater before it reaches the catalyst and membrane [56]. For example, to use seawater in SO electrolysis, reference [58] propose spray injecting seawater into a heated chamber to achieve the required minimum moisture content. However, this presents the possibility of poisoning the nickel in the fuel electrode and blocking off triple phase boundaries which would reduce the catalytic activity [58].

There are few studies that investigate the thermodynamics and kinetics of SO electrolysis of seawater. To my knowledge, there are only two studies that experimentally assess SO electrolysis of seawater. Kuan et al., [58] use an SOEC button cell to investigate the effects of using steam produced from simulated seawater on the electrochemical performance and degradation of the cell. They check for impurities in the steam produced from seawater and seawater contamination in the Ni-YSZ fuel electrode. They find that steam produced from the simulated seawater is free of contaminants, the electrochemical performance is not impacted by the steam from seawater (polarization curves and the impedance spectra is the same), and that the degradation rate is not impacted by using seawater. The results from this paper suggest a promising finding; that the electrolysis of steam produced from seawater may not negatively impact the performance or degradation of SOECs [58].

Additionally, in [60] an experiment is conducted using pure seawater and a flat tube SOEC to investigate the efficiency and stability of SO electrolysis from seawater. They observe no major effects on the cell after 420 hours of operation and they achieve energy conversion efficiencies of up to 72.47% [60]. While this study uses real seawater, they find that after 420 hours of operation the inlet fuel pipe is “completely blocked” by sea salt (see Figure 2-14). The red circles in the figure represent the areas where the flow was blocked by accumulated sea salt. Notice that it occurs on the outlet of the elbows. This important challenge suggests that an alternative method to boiling may be needed to successfully achieve continuous operation of offshore SOE systems. This also suggests that there is a need for longer testing and a more thorough analysis of the effects of marine environments on the balance of plant components. Lastly, this suggest there is a need in the literature for studies that investigate how to sustainably and safely management brine in offshore SOEC systems. Other papers that look at SO electrolysis of seawater have only

completed high level analyses exploring the energetic and environmental aspects without going into the details of the dynamics and thermodynamic integration.

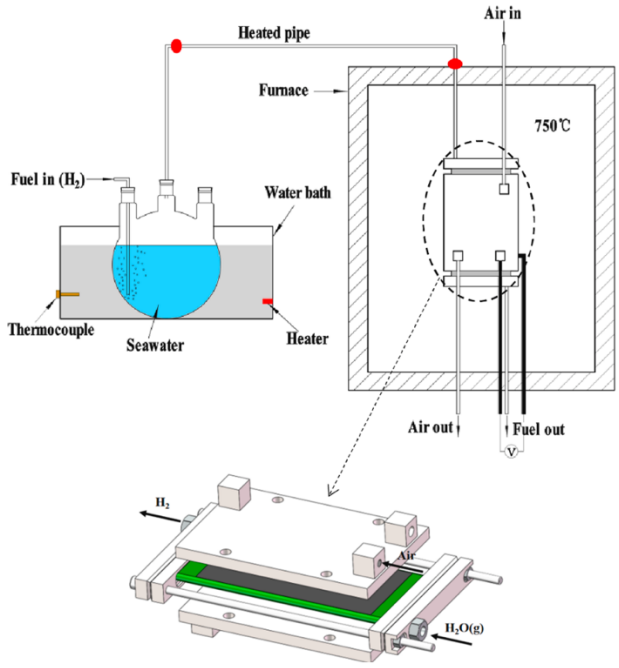

Figure 2-14: Image from [60] **that shows the experimental SOEC system.**

One interesting challenge that is uniquely related to high temperature electrolysis is that a heat input is required to produce the superheated water vapor that feeds into the cathode. In the ocean, there are no natural sources of heat. A similar challenge that occurs with indirect seawater electrolysis is the desalination stage, which requires an energy input. In the analysis of SO seawater electrolysis in [41], the authors select ohmic heating as the preferred method to produce heat for the production of steam. However, in the configuration they designed (shown below in Figure 2-15), they find that there is a 1.21% concentration of steam mixed with the hydrogen and they attribute this to the high temperature (80ºC) of hydrogen exiting the cathode. They also find that the balance of plant consumes more energy in this arrangement due the additional compression needs driven by the excess water vapor in the cathodic stream. Lastly, they conclude by stating that no additional ohmic heating is needed to boil seawater since it can be accomplished with just cogeneration [41]. The authors conclude there is less heat delivered to the marine environment in high temperature electrolysis than in low-temperature electrolysis [41], which has important implications for the impact on the local marine environment. Since low temperature electrolysis has the ability to operate with quick dynamics, the authors assert that

PEME is best suited for indirect seawater electrolysis due to rapid changes in offshore wind power.

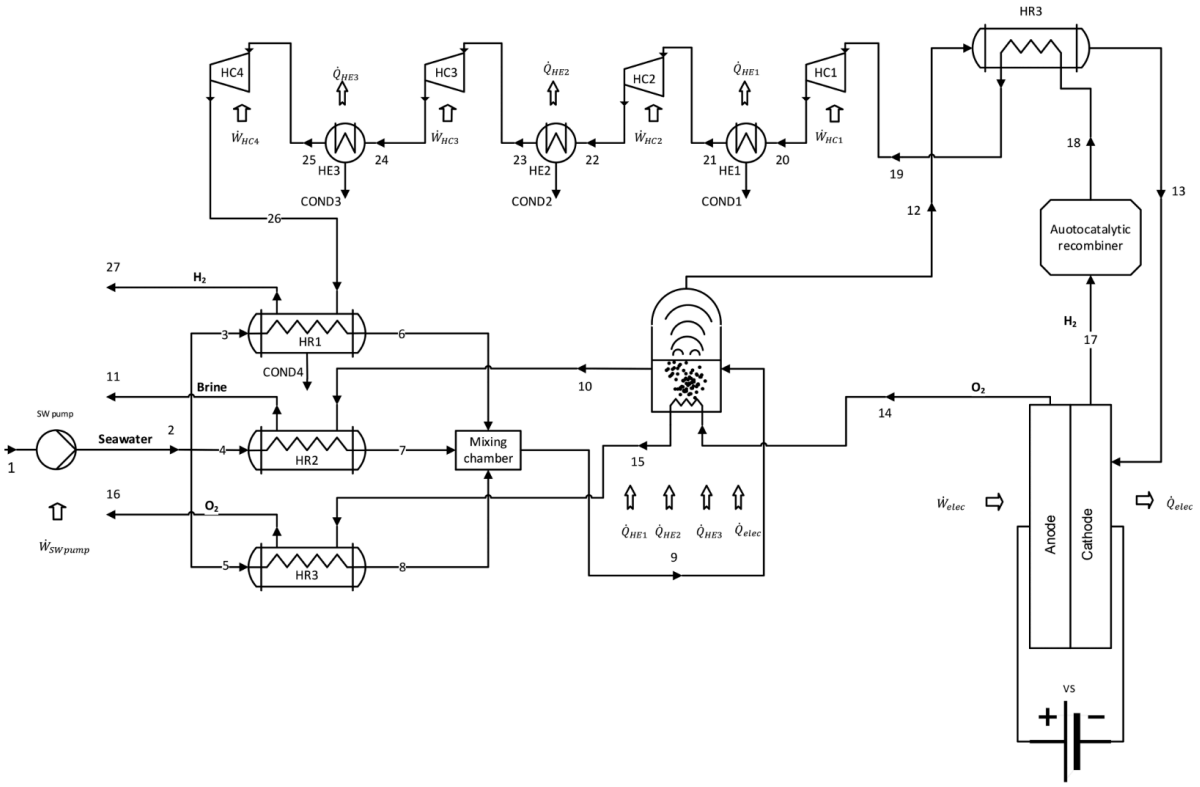

Figure 2-15: This is the SOEC schematic proposed in [41] **for indirect seawater electrolysis.**

Although there are limited studies on SO electrolysis of seawater, there are various papers that assess SO seawater electrolysis for coastal regions in which the electrolyzer is coupled with desalination systems and solar photovoltaics [61], [62], or dish-sterling collectors [63].

In [61], the authors propose a system that is comprised of a parabolic trough collector, thermal storage tanks, a PEME, an Organic Rankine Cycle, and a humidification dehumidification-based (HDH) desalination unit. The system incorporates a heat exchanger which uses the waste heat from the ORC as the heat source of the HDH desalination system. In this system the total mass flow the desalinated water is greater than the mass flow required for the PEME. They assume that the salinity of the water is 35 g/kg, the dehumidifier and humidifier effectiveness is 0.85, the

mass flow rate ratio of the desalination is 1.8. The desalination bottom and top temperature are 298 k and 333 k.

In Kumari et. al., [62] a solar photovoltaic system is coupled with a PEME which uses seawater-humidified air at 80% relative humidity to produce hydrogen. A significant finding from this study is that they experimentally prove the feasibility of a novel solar-driven seawater vapor electrolysis system. They also show that vapor fed PEM electrolysis is possible. They find the effects of fluctuations in the humidity are minimal and tolerable to the entire system. The assert that the relative humidity near the surface of the ocean is fairly consistent between 75-85%.

In [63] Rokni et al., present an innovative thermodynamic model design of a reversible SOC system integrated with Dish-Stirling collectors, a parabolic trough solar collector, and a direct contact membrane distillation (DCMD) system. When the system is operating in fuel producing mode (SOEC), the steam is generated using the parabolic trough solar collector. The DCMD uses waste heat from the SOEC for seawater distillation. This is a poly-generation plant that is self-sustaining. Also, they assume the seawater has a temperature of 15 deg C and salt concentration of 35 g/kg. To learn more about DCMD, check out reference 40 (modelling) and reference 44 (experimental data).

Additionally, the design of a seawater SO electrolysis system for use with offshore wind must consider dynamic operation due to the intermittency of this renewable resource. Dynamic operation of SOECs is a growing area of research (e.g., see [48], [64]) because delicate components in SOECs can experience fractures due to significant temperature fluctuations [45]. In SOECs, the stack temperature distribution is heavily dependent on the average current density, which requires strict temperature control for dynamic operation [45]. This is reflected in Figure 2-16, which shows the temperature versus axial position for an SOEC stack operated at 7000 and 5000 A/m^2 with an inlet temperature of 1023 K.

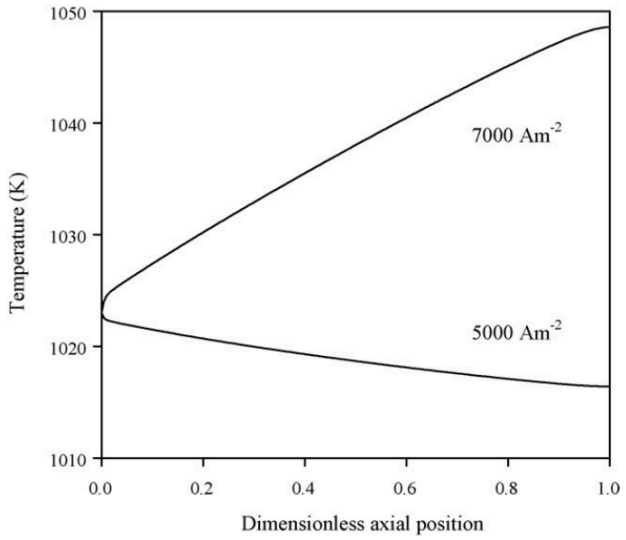

Figure 2-16: From [45]**, which shows the temperature distribution along the SOEC stack.**

Therefore, cell temperature control strategies are of utmost importance in the design and modelling of an SOEC stack to prevent damage to the sensitive components in the stack. Previous studies in the literature have studied the feasibility and control strategies of dynamic operation of SOEC systems. Saeedmanesh et al. [48] developed a model of a quasi 3D SOEC system to investigate the behavior of the system when it is integrated with a dynamic photovoltaic system [48]. The system layout is shown in Figure 2-17. The system has been designed to stand-alone so only inputs are the water stream, the ambient air stream, and electrical energy [48]. It is comprised of a temporally and spatially resolved SOE stack model and various sub-models for balance of plant components, such as heat exchangers, compressors, electric heaters, valves, and an air blower [48].

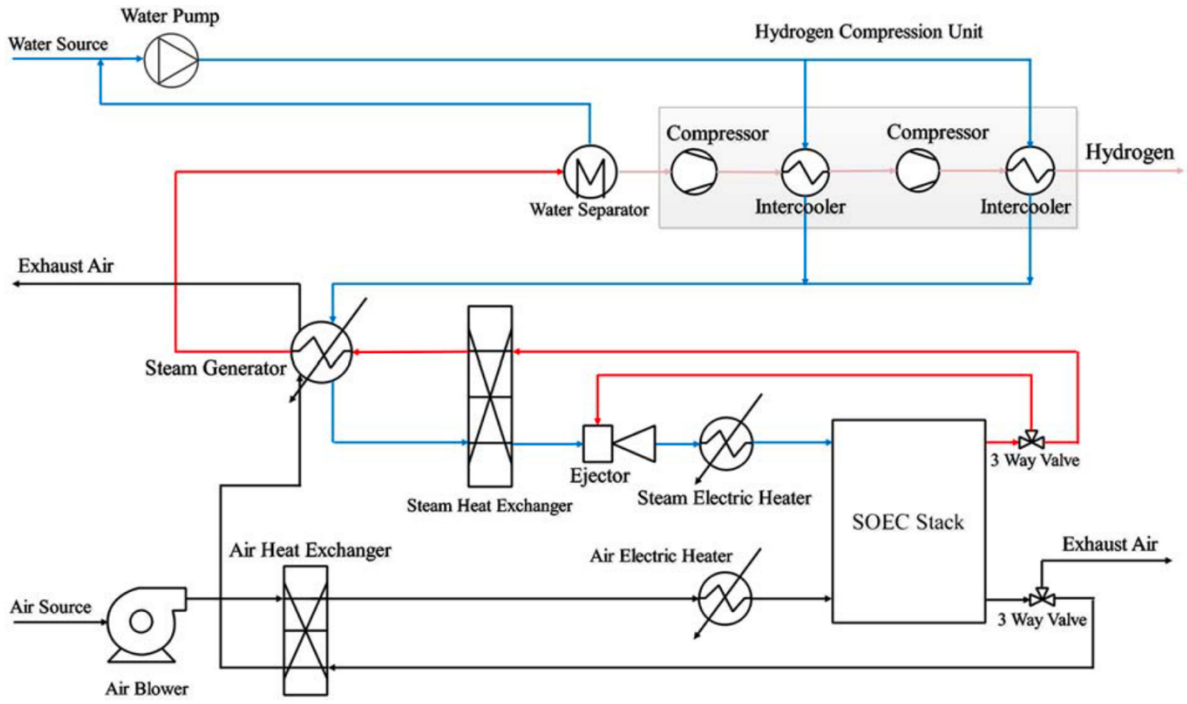

Figure 2-17: SOEC System layout from [48]**.**

In this configuration, the water is preheated in two-stage intercoolers in the hydrogen compression unit. After it is preheated, it enters the steam generator which recovers heat from the stack cathode and anode outlets. An electric heater is implemented following the steam generator and a heat exchanger to raise the temperature of the steam to the desired stack temperature of 1023 K. Since 10% molar fraction of hydrogen is needed at the cathode inlet to prevent oxidation of stack materials, a three-way-valve is inserted at the outlet of the SOEC stack so that a portion of the hydrogen can be recirculated to the cathode inlet. The hydrogen is then compressed in a hydrogen compression unit comprised of two stages to achieve a desired pressure of 3 MPa. Additionally, an electric heater and a heat exchanger are used to raise the inlet air temperature to 1023 K. Dynamic operation of this system was simulated for a representative sunny day and a representative cloudy day. The system, stack, and voltage efficiencies are shown in Figure 2-18. It can be observed that the voltage and stack efficiencies are above 100%. This occurs when the cell operating voltage is lower than the thermoneutral voltage [48]. When the system is operated dynamically, it cycles between endothermic, thermoneutral, and exothermic operation. When the stack efficiency exceeds 100%, a portion of

the energy input is provided by the electric heaters for the endothermic reaction. When the system is simulated on a highly dynamic cloudy day, it operate endothermically for a considerable amount of time [48]. Thus, the thermal inertia is low and the SOEC relies on integrated heat sources [48].

One novel aspect about this configuration is the actuator which controls the blower power to control the temperature of the stack [48]. In this design the air inlet temperature and the volumetric flow rate are kept constant for a wide range of operating temperatures and the average cell temperature is allowed to vary between minimum and maximum set points [48]. This study demonstrates success dynamic operation of a SOEC system.

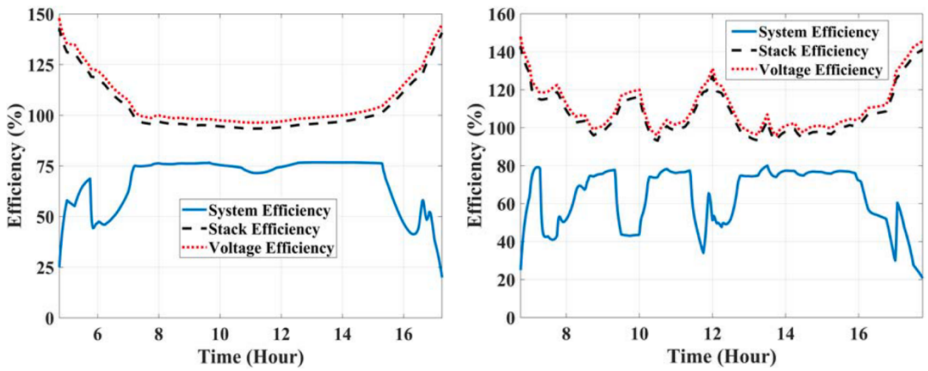

Figure 2-18: Image from [48]**. This figure shows the SOE system, stack, and voltage efficiencies for load-following solar power on a sunny and cloudy day.**

2.4 Desalination

Seawater is comprised of various compounds such as microorganisms, particles, dissolved solids and chloride, sodium, sulfate, magnesium, calcium, and potassium ions. For indirect seawater electrolysis, desalination is a critical stage in the hydrogen production process because these ions can negatively impact the electrolyte and electrodes by inhibiting catalyst activity and can result in the competing chloride electro-oxidation reactions which inhibit the oxygen evolution reaction. There are two main types of desalination processes: thermal and membrane [65]. In thermal-based desalination processes, thermal energy is supplied to seawater to evaporate the water vapor, which is then condensed [65]. Some examples of thermal-based processes include multi-stage flash distillation, multi-effect distillation, and vapor compression distillation [65]. Humidification dehumidification desalination is another type of thermal desalination, which uses

a low-temperature source [66]. Multi-effect distillation and multi-stage flash distillation are the two most common thermal desalination systems. Multi-effect distillation is considered to have a higher thermodynamic efficiency than multistage flash distillation since it operates in equilibrium [67]. Membrane-based technologies require lower specific energy consumption, have a smaller environmental footprint, and have more flexible capacity [65]. Electricity is the main input for membrane based technologies [67]. Some examples of membrane-based desalination processes include ultrafiltration, electrodialysis, and reverse osmosis [65]. For indirect seawater electrolysis, [42] recommends using multistage flash distillation or multi-effect distillation for desalination since it can produce high quality freshwater and requires less post-treatment than reverse osmosis, which is the most common method for desalination. There are two main steps in multi-effect distillation: evaporation and condensation [67]. Seawater is fed into the evaporation compartment where it is heated until it boils [67]. The evaporated water then enters the condensation unit where it is cooled down by dissipating heat until it condenses. Minimal mechanical work is needed to maintain the vacuum of the distillation due to the compressibility of the liquids [67]. This process is shown in Figure 2-19. When there are multiple stages combined, each stage operates at a different pressure; this pressure is typically below 1 atm [67]. Figure 2-20 shows a three stage multi-effect distillation system. In each stage, the heat that is released in the condensation step is used as the heat input of the evaporation stage of the following unit [67].

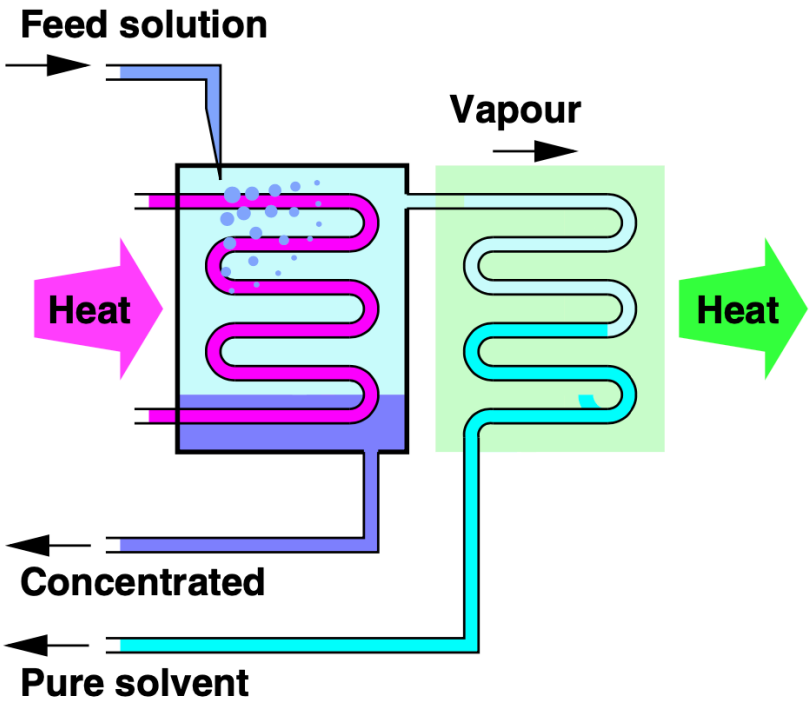

Figure 2-19: Schematic of a single effect distiller from [67].

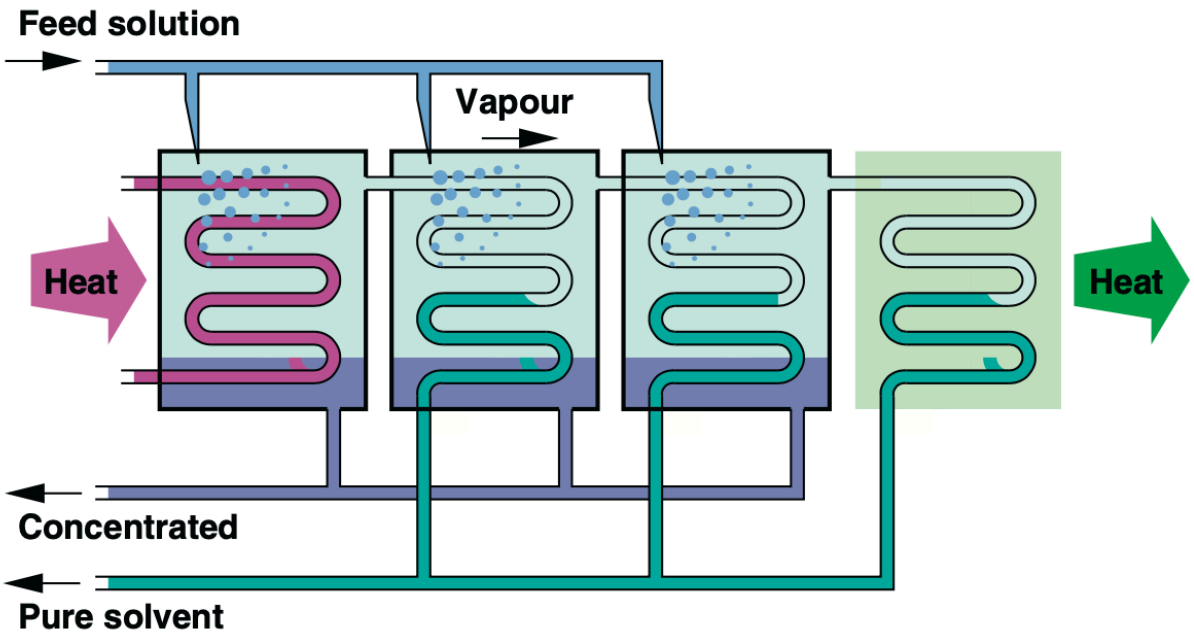

Figure 2-20: Multiple effect desalination system from [67].

2.5 **Brine Management Strategies**

One important environmental concern of indirect seawater electrolysis is associated with the brine that is generated from desalination. Depending upon salt and other constituent concentrations, brine can harm the local aquatic species and pollute the water if it is expelled into the sea. It has a higher density that seawater and it often contains chemical residues from treatment to minimize algal growth, reduce corrosion, and inhibit scaling [68]. Fortunately, the brine contains industrially useful compounds, such as sodium, calcium, magnesium, and lithium [69], rare earth metals, precious metals, radioactive metals and more [70]; and has many potential uses including energy storage and extraction of lithium and other rare metals. Therefore, it is important to view the brine as an output of the process that has valuable uses rather than purely waste product [69]. Figure 2-21 shows three main methods used to treat brine: direct disposal, brine minimization, and direct reuse. The two main approaches for brine management are volume reduction and zero liquid discharge/ crystallization [68]. Brine treatment can be coupled with CO_2 capture to produce useful products for industrial applications [69], [71]. The Solvay process, widely used for carbon capture, reacts saturated sodium chloride (brine) with ammonia and CO_2 to produce sodium bicarbonate, $NaHCO_3$ in the precipate form [69], [72]. Unfortunately, the reaction rate decreases with increasing salinity [69], and it has a low percentage conversion of sodium [71]. Combining brine with CO_2 capture presents an opportunity for reducing the salinity of the brine to make it more treatable.

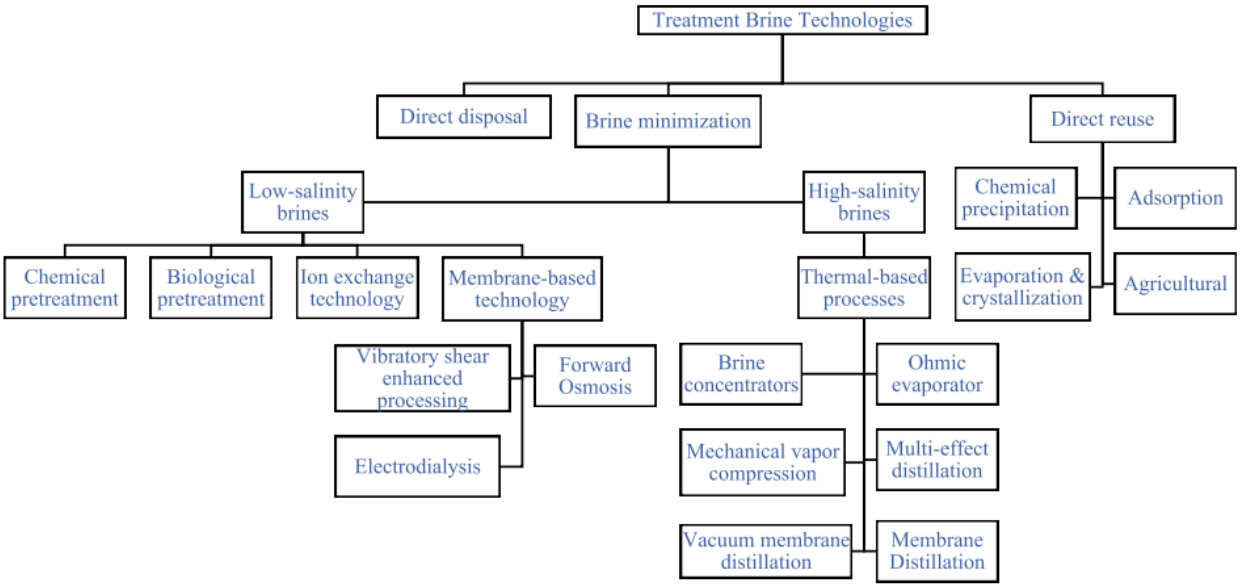

Figure 2-21: A summary of brine disposal and management methods. From [69].

Regarding energy storage, one study proposed that brine could be used for energy storage using salinity differences because energy in the form of chemical potential is available in solutions of differing concentration [73]. The difference in concentration of salt can be converted to electrical energy using reverse electrodialysis, pressure-retarded osmosis, and capacitive cells [73]. Though, currently, none of these methods are at a technology readiness level in which they may be immediately deployed.

Thermal energy storage systems store energy in the form of internal energy of a storage medium [74]. If the medium goes through a phase change, then more energy is available as a storage medium due to the latent heat from the phase change resulting in a higher heat capacity [75]. For example, in concentrating solar plants, where thermal energy storage is essential for dispatchability and load shifting, the storage medium is molten salt mixtures (KNO_3 and $NaNO_3$) due to their low vapor pressure, high specific heat, and chemical stability [74]. In [74], [76]–[78], the authors propose using reverse osmosis concentrate (the reject of the reverse osmosis water treatment process) for thermal energy storage. The concentration of total dissolved solids in a typical reverse osmosis concentrate is 70,000 mgL^{-1} [68]. Reverse osmosis concentrate (brine) is typically a mixture of salts dissolved in water (NaCl, KCl, MgC_{l2}, $MgSO_4$, etc.) [74], although it depends on the feed source. In order to use the reverse osmosis concentrate for thermal energy storage, the water content in the brine needs to be removed for the remaining salt content to be

processed as a thermal energy storage medium [74]. The remaining salt is grinded into a powder where it is packed inside a containment to form a thermal energy storage module. The total amount of thermal energy storage available will depend on the heat capacity of the salt mixture, thermo-physical properties of the medium, and the containment material [74]. Prior experiments found that salt changes phase from a liquid to solid between 550^{o}C and 647^{o}C [77]. In [77], Lee et al. found that the dominant component of the thermal energy medium was sodium and chlorine, so they used the properties of chloride salt to model melting [77]. In this study, I will use a similar approach to use the brine generated from the steam generation as a thermal energy storage medium in the offshore system.

3 GOAL & OBJECTIVES

The goal of this Ph.D. is to investigate the ways in which offshore wind and hydrogen can be used in a 100% renewable future. Offshore wind energy has the potential to be used immediately as electricity or to be converted into renewable hydrogen to be stored or delivered for various end uses, such as shipping. In this dissertation, I will focus on two potential pathways: electrical end-use and hydrogen conversion. Understanding the electrical pathway, will require using time series statistical methods to quantitatively analyze the seasonality and periods in the offshore wind data. To investigate the offshore wind-to-hydrogen pathway, I will need to design and simulate the thermodynamics of an offshore platform that uses offshore wind to produce hydrogen. Additionally, the offshore wind to hydrogen pathway will also require a experimental analysis to understand the potential impacts of seawter on the performance of a solid oxide electrolysis cell.

To complete this goal, the following objectives (1 - 4) have been developed:

Objective 1: Conduct a thorough and continuous literature review on renewable energy and solid oxide electrolysis systems and dynamics,

Objective 2: Understand and analyze the dynamics of offshore wind relative to the demand, solar and onshore wind dynamics,

Objective 3: Conduct an experiment to understand how impurities in the desalinated water (or seawater) can impact the performance and degradation of SOECs, and

Objective 4: Design a system for hydrogen production from seawater that includes the desalination and brine/salt management system.

4 APPROACH

In this section I will discuss the tasks necessary to complete each objective.

Objective 1: Conduct a thorough and continuous literature review on renewable energy and solid oxide electrolysis systems and dynamics.

Complete a literature review and maintain an organized record with a summary and significance of each article that focuses on time-series analysis of renewable energy data, dynamic operation of SOECs, integration of SOECs with desalination methods, and techno-economic analyses. This task is pivotal to this dissertation and to the rest of the objectives listed below. Equally important to reading is the task of keeping a record of the literature reviewed and reflecting and summarizing. My goal is for this summary to generate new ideas and inspire creative thinking.

Objective 2: Understand and analyze the dynamics of offshore wind relative to the demand, solar and onshore wind dynamics.

The following tasks have been planned meet this objective:

a. Use time-series statistical methods to analyze offshore wind data and how it is related to the demand and solar and onshore wind.
b. Use the fast Fourier transform method to understand the seasonality in the offshore wind data.
c. Develop generation duration curves to study the probability distribution of offshore wind.
d. Assess the value of offshore wind using a demand-based metric.

Objective 3: Conduct an experiment to understand how impurities in the desalinated water (or seawater) can impact the performance and degradation of SOECs.

The goal of this objective is to build on the prior work of Lim et al., [58] who used an SOEC button cell to investigate the effects of using steam produced from seawater on the electrochemical performance and degradation of the cell. This objective requires the design and engineering of a test rig that can be continuously operated for hundreds of hours to test the SOE cell. I will use the following methods to study the performance of the cell:

a. Electrochemical Impedance Spectroscopy

b. Polarization Curves
c. Post-mortem imaging and analysis through Scanning Electron Microscopy (SEM) and Energy Dispersive X-ray Spectroscopy (EDS)

Objective 4: Design a system for hydrogen production from seawater that includes the desalination and brine/salt management system.

The following tasks have been planned to meet this objective:

a. Develop an SOEC model to evaluate the thermodynamics of an offshore SOEC platform coupled with offshore wind.
b. Assess the excess heat that is available in the SOEC model under exothermic conditions to inform the design and integration of a desalination system and steam generation component in the model.
c. Investigate thermal and brine management and control strategies for the integrated SOEC hydrogen production platform.
d. Perform a sensitivity analysis on the models to determine the most important design and performance parameters and impacts.
e. Accomplish techno-economic analyses for the platform to estimate the future cost of hydrogen and electricity if produced from offshore wind in a 100% renewable energy scenario in the state of California. For this objective, I will refer to prior work by [30] to inform my approach to this objective.

5 CASE STUDY OF OFFSHORE WIND BENEFITS AND CHALLENGES IN CALIFORNIA

5.1 Introduction

The global emergency to swiftly transition to more sustainable ways to generate and deliver energy in our society is driving us to consider alternative and creative energy conversion and storage systems. The ocean represents a vast majority of the area on the Earth and an immense source of mostly untapped renewable energy. Studies such as the "Teal Deal" proposed in [2] have reframed the importance of the ocean's role in mitigating climate change and providing solutions to the climate crisis. While deployment of solar and onshore wind has grown substantially in the last decade, due to technological innovations, cost reduction and policies that support the adoption of both technologies, the role of offshore wind is burgeoning in the renewable energy sector. Offshore wind is a low-carbon, abundant and widely available energy resource technology that is rapidly maturing around the world [15], [16]. With costs expected to decrease significantly in the next decades [1], [17], from between 35% and 41% by 2050 relative to 2014 [17], offshore wind is expected to attain a more significant presence globally as a formidable source of renewable energy production. The International Renewable Energy Agency (IRENA) predicts over 2000 GW of offshore wind will be installed by 2050 in its 1.5 ^{o}C scenario [79]. In 2020, the global offshore wind industry grew by over 5.5 gigawatts (GW) achieving a cumulative installed capacity of 35 GW globally [80], [81]. Although China and Europe accounted for most new installations in 2020, it is expected that Asia will emerge as the prominent continent for offshore wind [80], [82]: Japan and the Republic of Korea have the goal to deploy 45 GW by 2040 and 12 GW by 2030, respectively [79]. In the United States, two operational projects (the Block Island Wind Farm and the Coastal Virginial Offshore Wind projects) accounted for a total offshore wind capacity of 35 MW in 2020 [81]. The global offshore wind capacity potential is 126 terawatts (TW) with a potential global generation of 315 petawatt hours (PWh) per year [20] (1 PWh = 10^{15} Wh = 10^{6} GWh).

Some of the advantages of offshore wind that have been consistently reported in the literature include (1) stronger and more consistent wind velocities [11], resulting in consistently higher capacity factors than solar and land-based wind; (2) less likely to interfere with land-use activities [11]; (3) minimal impact on the population and sea life [12]; and (4) it may potentially

face less community resistance since turbines can be placed beyond the visible horizon from the shore [13]. Additionally, offshore wind is less constrained by size and noise pollution [4], it is highly scalable [13], it shares important synergies with oil and gas sectors [2], and it has the potential to be coupled with high voltage direct current for efficient electric transmission for sites far from the shore (more than 50 km) [14], [15]. Existing offshore infrastructure, previously used for extraction, processing, and delivery of fossil fuels, could be repurposed for the delivery and transmission of offshore wind energy. Subcoastal powerplant transmission infrastructure, and depleted subterranean and subsea natural gas and oil reserves may be suitable for storage and delivery of offshore wind via hydrogen produced from wind power [16]. Additionally, offshore wind may enable hydrogen to dramatically reduce emissions from sectors that are difficult to decarbonize such as iron, steel, and shipping [2]. Lastly, offshore wind turbines have the potential to be co-located with other offshore resources such as ocean current energy converters [17], although currently, offshore wind is the only commercially mature ocean energy technology [17].

Historically, offshore wind farms have been deployed mainly in the North Sea and the Baltic Sea [24] which has been possible due to the convenient location of high resource potential offshore wind in shallow regions of the ocean near the shore. However, advancements in floating platform technology have opened the opportunity for installation of this resource in deep waters. Today, various countries including Germany, the United Kingdom, Denmark, Belgium, India, China, Chile, and others are seriously considering offshore wind an essential element of a viable renewable energy mix to achieve a 100% renewable future. Europe and China have been leading the world in the development of offshore wind technology. Currently, over 70% of the installed capacity is either in the North Sea or the Atlantic Ocean [79]. The United Kingdom and China account for 28.9 % and 28.3% of total installations, respectively [80]. In 2020, China accounted for 50% of new installations, making China the country with highest amount of new offshore wind installations. The improved technological efficiencies, reduced transmission constraints, and successful offshore wind farm sites in Europe have made offshore wind more attractive in North American and economically competitive [1], [84]. Offshore wind is a nascent technology in the United States, with a total gross offshore wind energy resource potential up to 10.8 TW [22] and a gross annual energy potential of 44,378 TWh/yr [22]. The vast majority of offshore

wind energy resource potential in the United States has not been explored which represents an enormous energy resource [21]. In the East Coast, offshore wind is a significant cornerstone of future clean energy portfolios in various states, where a total of 22 GW of new capacity will be installed by 2035 [19], [23]. Recently the Biden-Harris administration set a goal to install 30 MW of offshore wind by 2030 as part of their plan to achieve 100% renewable electricity by 2035 in the United States [85]. This includes 4.6 GW of offshore wind energy in the California Coast, where the potential for offshore wind energy is immense.

NREL has identified six potential offshore wind farm sites in California based on proximity to infrastructure, wind resource quality, known existing site use, and physical site conditions [16]. One challenge for deploying offshore wind in California is the near-shore precipitous drop of the continental shelf along the Pacific Coast which requires floating platforms; however, as noted above, this technology is rapidly advancing and has already been successfully demonstrated in the North Sea (see [86]). If offshore wind is deployed in California and connected to the electrical grid, it is important to understand the extent of its temporal variability and its complementarity with solar and onshore wind. Furthermore, offshore wind is still susceptible to the intermittency, volatility, and seasonal characteristics of renewable resources [87]. The extent of complementarity and supplementarity has important consequences for energy storage and back-up capacity as well as the operational requirements of a highly renewable electrical grid [32]. This is especially important as more renewable generation resources are installed [88].

While prior studies have investigated the relationship between onshore wind and solar (e.g., [32]–[34], [89]), limited studies have considered offshore wind. Even fewer studies have completed statistical analyses of the complementarity and extent of correlation of offshore wind with the demand and other renewable resources. Wang et al., reported that offshore wind possesses a significant advantage in the temporal alignment between peak power demand in the electrical grid and the diurnal and seasonal patterns of offshore wind [26]. The daily offshore wind generation peaks in the evening hours, which coincides with the timing of the daily peak demand in the evening hours [26]. During the winter months, offshore wind is two to four times more valuable than solar and land-based wind when considering demand-based values [26]. The authors of the study found that between solar, land-based wind, and offshore wind, offshore wind

demonstrates the best temporal alignment with demand and possesses the largest demand-based value when factoring in temporal correspondence between power and demand [26]. One limitation of this study is that the authors only considered the spatiotemporal patterns of potential offshore wind production in the Central California coast. Additionally, since the authors only analyzed the value of the monthly averages, this eliminates the dynamic daily and weekly fluctuations in the profiles and does not allow determination of long-duration and seasonal storage requirements. While the results of Wang et al. [26] suggest offshore wind is a promising source of renewable energy, there needs to be further analysis to determine whether the conclusions of this study can be expanded to other potential offshore wind farm sites.

In [23], E3 used a resource planning tool (RESOLVE) to quantify the economic value of offshore wind in California by estimating the potential electric system savings if offshore wind was deployed to meet the state's climate goals in 2030 and 2040. Although they predict that offshore wind will continue to have the highest capital costs in comparison to solar and onshore wind, it is one of the least-cost resource options that has the potential to save ratepayers approximately $1 to $2 billion dollars [23]. E3 estimates that between 7 and 9 GW of offshore wind will be the optimal amount to meet the state's energy goals in the lowest cost manner [23].

The literature has reported that offshore wind possesses various inherent advantages over land-based wind and solar energy. This warrants further investigation and consideration for deployment and development of offshore wind in California. Motivated by recent policies in California, we present a case study on offshore wind: We assess the advantages and challenges by examining the dynamics of different offshore wind farm sites and evaluating the performance of different combinations of resources (solar, onshore wind, and offshore wind). To achieve this goal, we use the Pearson Correlation, generation duration curves, a demand-based metric, and the Fast Fourier Transform to analyze hourly dynamics of the capacity factor over a five-year period. First, we present a statistical and quantitative analysis of the dynamics of offshore wind in relation to solar, onshore wind, and demand to investigate whether the advantages reported in the literature are consistently true for potential offshore wind sites. Then, we use the Fast Fourier Transform algorithm to investigate the periodicity and dynamics of offshore wind in relation to solar and onshore wind. Understanding the coincidence, variability, alignment, and predictability

of offshore wind power production with electricity demand and onshore renewable resources has important implications for the grid system flexibility, energy storage, backup capacity, and power system reliability.

5.2 Methods

5.2.1 Data Collection

Offshore winds can vary interannually, seasonally, synoptically, daily, and spatially which requires careful consideration of the spatiotemporal variability when estimating power production from offshore wind [26]. For each of the six potential offshore wind farm sites identified in [16], we estimated the hourly and spatially resolved offshore wind capacity factors using simulated hourly and spatially resolved wind speeds at an altitude of 100 meters from NRELs WIND Toolkit [90]–[92] for the years 2007 – 2012 (see Table 5-1 and Figure 5-1). The goal was to capture spatial variation in wind energy availability in each potential site. To calculate the wind power at each site, we assumed a representative turbine with a maximum capacity of 15 MW, with turbine specifications from Siemens Gamesa [93]. To estimate the wind power curve, we used the following expression [94]:

$$P_{wind,k} = c_p \frac{1}{2} \rho a v_k^3 \quad \textbf{(5-1)}$$

where P_{wind} is the power output at time k (W), c_p is the power coefficient, ρ is the air density (kg/ m^3), a is the swept area of the turbine (m^2), and v_k is the wind speed (m/s) at time k. A value of 0.35 was selected for the power coefficient, which is consistent with real-world power coefficient values [15]. Consistent with prior studies [95], the cut-in speed was 3 m/s, and the cut-out speed was 25 m/s.

We adjusted the wind data for an altitude of 149 m, which corresponds to the hub-height of a 15 MW turbine previously reported in the literature [95] using the following relation:

$$v_k = \tilde{v}_k \left(\frac{h}{h_{meas}} \right)^{\beta} \quad \textbf{(5-2)}$$

Where $\tilde{v}_k$ is the measured-wind speed at a time k, h is the height of the wind turbine (149 m), h_{meas} is the height of initial wind speed measurement (100 m), and β is a friction coefficient (0.11 for offshore wind [96]).

The onshore wind and solar capacity factors used in this study represent the capacity factors in the Western Interconnection region, excluding Mexico and Canada, and we acquired them from Dowling et al., [11]. We used the same range of data that we used for the offshore wind speeds with a time step of one hour: July 2, 2007 – July 1, 2012. Additionally, the hourly electricity demand is representative of the total California electricity demand for a five-year period. The demand was acquired from a publicly available dataset record that spans from July 2, 2015 to July 1, 2020 (ref [97]). Ruggles et al. developed a data cleaning technique to predict erroneous data, such as outliers and missing data, in the EIA's public electricity demand records. We used the entirety of the demand data with data from the renewable resources between July 2, 2007 – July 1, 2012. Figure 5-2, which shows the box plots of the capacity factors for each resource (average offshore wind, solar, and onshore wind) and the normalized demand, reveals the monthly trends for the capacity factor of different resources (onshore wind, onshore wind, and solar) and the normalized demand. The boxes show the quartiles of the dataset, with the bottom of the box showing the 25th percentile and the top of the box showing the 75th percentile. The black horizontal line represents the mean. The whiskers of the boxplots represent the 5th and 95th percentiles, while any points outside the whiskers are considered extreme values that lie outside of the 5th and 95th percentiles. The hourly dynamics for selected offshore wind farm sites can be seen in Figure 5-14- Figure 5-16. For the remainder of the paper, the capacity factors and normalized demand data were used with a time step of one hour in each of the subsequent analyses.

Table 5-1: Mean and median capacity factor of offshore wind farm sites, solar and onshore wind

Site Name	**Site Number**	**(Latitude, Longitude) from** [16]	**Mean Water Depth (m) from** [16]	**Mean Hourly Capacity Factor between 2007-2012**	**Median Hourly Capacity Factor between 2007-2012**	**Variance**	**Standard Deviation**

Channel Islands South	1	(33.72,-120.21)	746	0.48	0.4	0.16	0.4
Channel Islands North	2	(34.16, -120.59)	575	0.53	0.49	0.16	0.4
Morro Bay	3	(35.32,-121.45)	713	0.41	0.27	0.15	0.38
Bodega Bay	4	(38.41,-123.59)	446	0.52	0.47	0.18	0.42
Humboldt	5	(40.13,-124.72)	870	0.59	0.69	0.17	0.41
Crescent City	6	(41.66,-124.80)	805	0.56	0.61	0.18	0.42
Solar	-	-	-	0.28	0.03	0.11	0.32
Onshore Wind	-	-	-	0.37	0.36	0.03	0.18

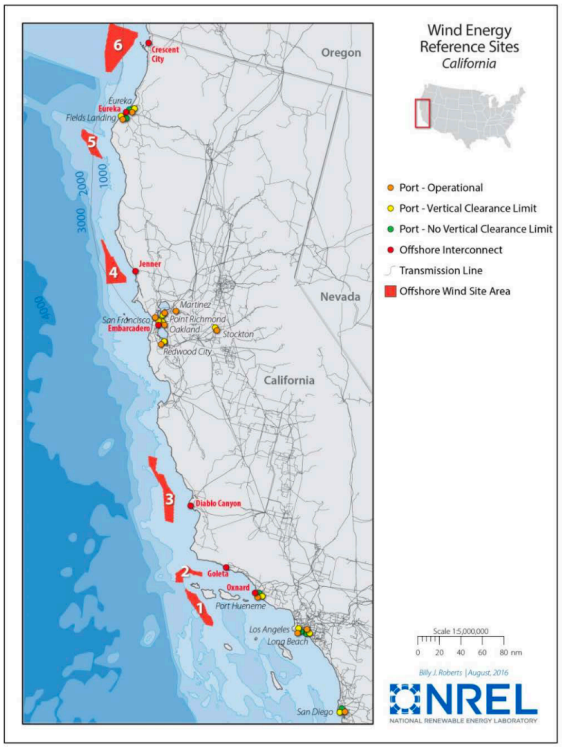

Figure 5-1: Image from [16] **shows six potential offshore wind farm areas located near ports and offshore interconnection points.**

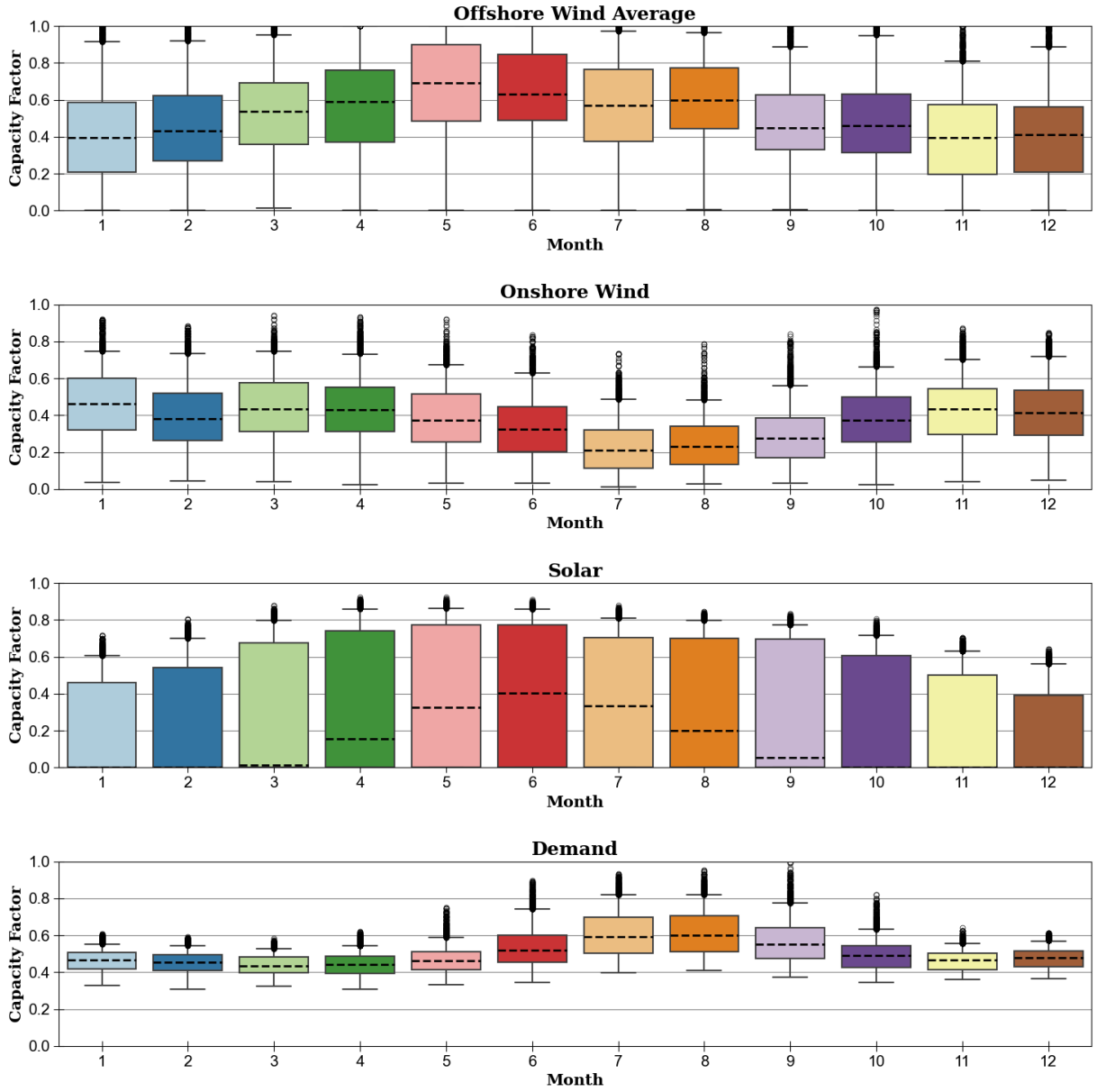

Figure 5-2: The boxplots reveal the general monthly patterns in the renewables data.

5.2.2 Generation Duration Curves

We used generation duration curves to compare the probability distribution of offshore wind with solar and onshore wind. The curves reflect the percentage of time each resource can operate at a particular output. We also used a metric for reliability, firm capacity, from [89] to assess the reliability of power production. Firm capacity is defined as the capacity factor that can be expected at least 87.5% of the time [89]. Instead of using capacity factors for the generation duration curves, we assumed relative capacities for each resource to scale each resource by its

potential capacity to have more practical results. We analyzed a total of four configurations based on current offshore wind targets and solar and onshore wind capacities in California (see Table 5-2). The capacity of offshore wind is based on the Biden-Harris administration's goal to deploy 4.6 GW of offshore wind in California with a focus on Morro Bay and Humboldt [85]. Additionally, we assumed 13 GW of solar [98] and 6 GW of onshore wind [88] for each configuration.

Table 5-2: Configurations for the generation duration curves.

Configuration	Solar (GW)	Onshore Wind (GW)	Offshore Wind (GW)
1	13	6	0.767 at each site (4.6 total)
2	13	6	2.6 at Morro Bay 2 at Humboldt
3	13	6	2 at Morro Bay 2.6 at Humboldt
4	13	6	2.3 at Morro 2.3 at Humboldt

In the generation duration curves (shown in Figure 5-3 - Figure 5-6) the hours were rearranged based on decreasing capacity factor value; this was plotted as a decreasing curve [99]. Then, the capacity factors of each resource were multiplied by the resource's power capacity from Table 5-2. In the generation duration curves, the y-axis represents the potential generation (GW), and the x-axis represents the percentage of hours in which that potential generation is available [89]. The firm capacity threshold (87.5%) is specified by the vertical solid black line in Figure 5-3 - Figure 5-6.

5.2.3 Correlation Analysis

The Pearson correlation is used to assess the degree of complementarity between the renewable energy resources and their alignment with the electricity demand. The Pearson Correlation Coefficient measures the linear dependence between two variables [100]. Prior studies have used the Pearson correlation to analyze the complementarity between different resources [89], [100], [101]. This methodology was applied between each of the renewable energy resources (onshore wind, solar, and offshore wind), between renewable energy resources and the demand, and between various offshore wind sites. The Pearson Correlation coefficient varies between -1 and 1; resources with values close to 1 are highly correlated in time, and

resources with values close to -1 are anticorrelated in time and are complementary. A value near 0 suggests no positive or negative correlation. Results are shown in Figure 5-7.

5.2.4 **Demand-Based Metric**

Various studies in the literature have reported that one of the attributes of offshore wind is temporal alignment with peak electrical demand. In California, the peak demand occurs from 16:00 to 22:00 PST [102]. To investigate the value of offshore wind during peak demand hours, we calculated a demand-based metric for each hour of energy production. This analysis was based on the demand-based value metric developed by Wang et al., [26]. In [26], the authors use this metric to illustrate the relative value of power produced at each hour for solar, onshore wind, and offshore wind. We use a variation of the metric used by Wang et al. [26] :

$$Metric = CF * Normalized\ Demand$$

Where CF is the capacity factor at each hour. This metric represents the demand-based value of the energy generated during peak hours. The higher the metric, the more valuable the resource is during peak demand. The statistics for the value of this metric for peak hours in the summer and winter months are presented in Figure 5-8 and Figure 5-9.

5.2.5 **Fast Fourier Transform Analysis**

To understand the seasonal components, predictability, and time series patterns in the data, we used the Fast Fourier Transform (FFT) algorithm in the SciPy library in Python to perform a discrete Fourier transform (FT) on the hourly capacity factors of the solar, onshore wind and each of the six offshore wind sites. The model to perform the FFT on the datasets is adapted from the model in [103]. The goals of the FFT analysis were to (1) identify the fundamental seasonality of offshore wind and to understand how it compares with the seasonality of solar, and onshore wind and (2) to understand the level of predictability of offshore wind energy. Previously, the FFT has been used to detect the seasonal periods of discrete time series [104], however one challenge is that the FFT method is only suitable for stationary data, that is, time-series data with static properties [105]. Time series data are nonlinear and non-stationary, which may require decomposition of the original data [106]. While we cannot completely eliminate the

non-stationary nature of our time series data, we divided the data into groups of meteorological seasons so that we can more appropriately assume the data are stationary. After the time-series data were transformed to the frequency domain, we used the frequencies and amplitudes to replicate the data using a series of Fourier terms and periodic functions (sines and cosines). The resulting terms were then used as inputs in a linear regression model from the Scikit-learn Python package [107]. To assess the predictability of the data, we calculated the R-squared value of the original data with the modelled data. This is shown in Figure 5-13.

5.3 Results and Discussion

5.3.1 Generation Duration Curves

In this section, we present the generation duration curves for each of the configurations listed in Table 5-2. The firm capacity is used as a metric to assess the reliability of different configurations of the resources. A summary of the firm capacities for each configuration is shown in Table 5-3. Since the capacities of solar and onshore wind do not change for any of the scenarios, the firm capacities of solar and onshore wind are constant values: 0 GW and 0.901 GW, respectively. Furthermore, firm capacity values of 0.426 GW and 2.15 GW can be expected 50% of the time for solar and onshore wind, respectively.

In the generation duration curves (Figure 5-3 - Figure 5-6), the black line represents the capacity factor available at least 87.5% of the time. The x-axis represents the percent of total hours in the 5-year dataset that corresponds to a minimum potential capacity available. The generation duration curve for configuration one (13 GW solar, 6 GW onshore wind, 4.6 GW of offshore wind (0.767 GW of offshore wind deployed at each site)), shown in Figure 5-3, shows that the firm capacity of offshore wind alone is 1.51 GW. This means that 87.5% of the time, 0% of the installed solar, 15% of the onshore wind, and 17% of the offshore wind capacity should be expected. Additionally, 2.71 GW can be expected 50% for offshore wind, which is 59% of the installed capacity. Figure 5-3 also shows that, while the firm capacity for these resources is moderate, when the resources are paired the firm capacity increases: 1.94 GW for the solar and offshore wind pairing, 1.92 GW for the solar and onshore wind, and 3.21 GW for the onshore wind and offshore wind. The most resilient case is when offshore wind, solar, and onshore wind are deployed at the same time, which results in a firm capacity of 4.32 GW, or 18% of the total renewable capacity. If only solar and onshore wind are deployed, 4.08 GW can be expected 50%

of the time. In contrast, if solar, onshore wind and offshore wind are all deployed under configuration one, 7.08 GW can be expected 50% of the time.

Figure 5-4 displays the results for configuration two (13 GW solar, 6 GW onshore wind, 2.6 GW in Morro Bay, 2.0 GW in Humboldt). The firm capacity of offshore wind in this configuration is 1.51 GW. This is 33% of the total offshore wind capacity installed. The most resilient combination of resources is when onshore wind, solar and offshore wind are combined, which results in a firm capacity of 4.36 GW. This represents 18.4% of the installed capacity.

The remaining results for configurations three and four are shown in Figure 5-5 and Figure 5-6, and they show similar findings to configuration one and two. The combinations of resources with solar offer the largest potential capacity until approximately 40% of the time. This is due to the large installed capacity of solar (13 GW) and its diurnal generation pattern. The combination of all resources provides the largest firm capacity, and the combination of offshore and onshore wind provides the second largest firm capacity. This emphasizes that interconnecting resources is advantageous for not only increasing the maximum potential capacity but also for improving the reliability of highly renewable energy systems.

The results of a prior studies [99] about the advantages of interconnecting multiple onshore wind farm sites are reflected in the results of this study with offshore wind farms: Interconnecting multiple wind farms results in an increase in the firm capacity. Deliberately interconnecting multiple offshore wind farm sites results in higher firm capacities such as in configuration one. Of the four configurations studied, the one with the highest firm capacity was configuration one with 0.767 GW of offshore wind deployed across six sites and connected to 13 GW solar and 6 GW onshore wind.

Pairing existing solar and onshore wind resources with offshore wind will result in higher firm capacity values than when only solar and onshore wind resources are paired. This can be observed across each of the four configurations: For each configuration, the combination of offshore wind, solar and onshore wind resulted in the highest firm capacities.

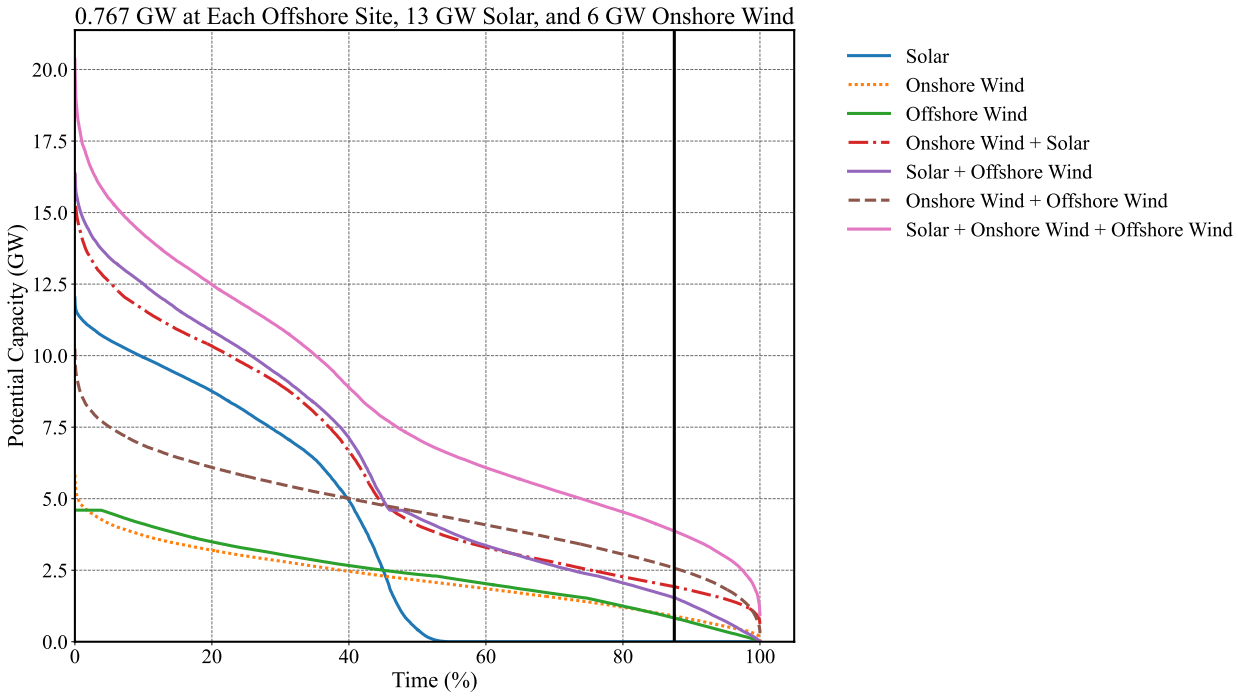

Figure 5-3: Generation Duration Curves for configuration one.

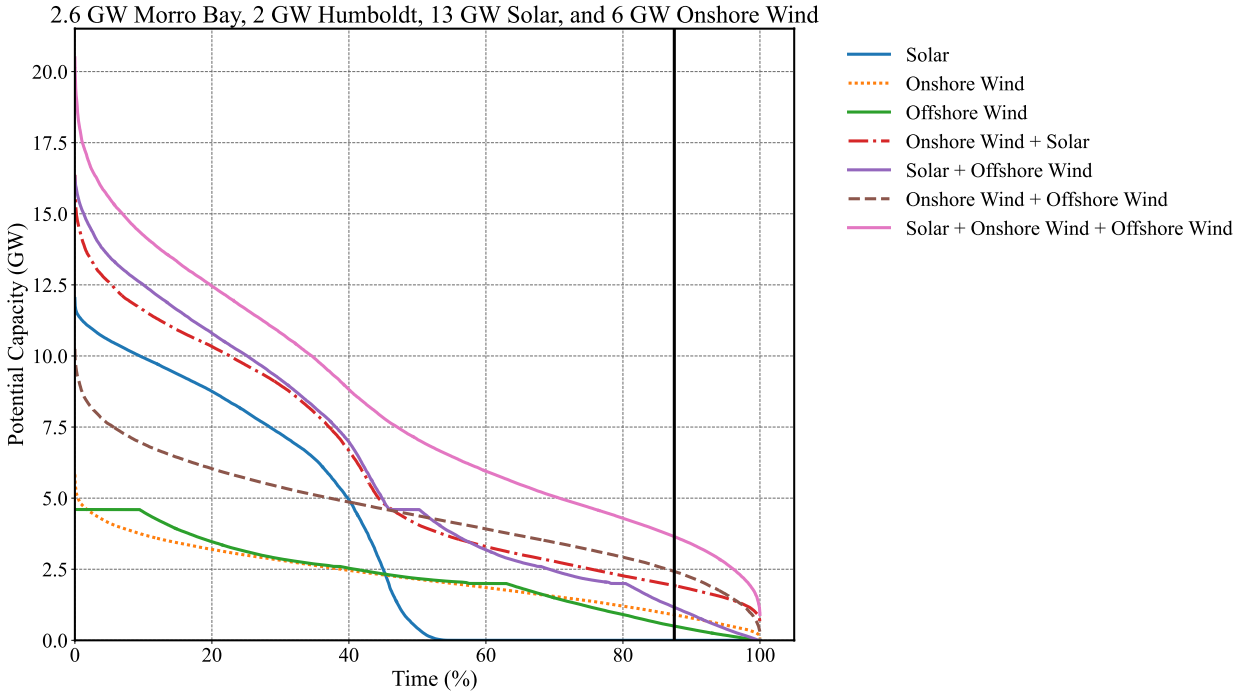

Figure 5-4: Generation duration curve for configuration two.

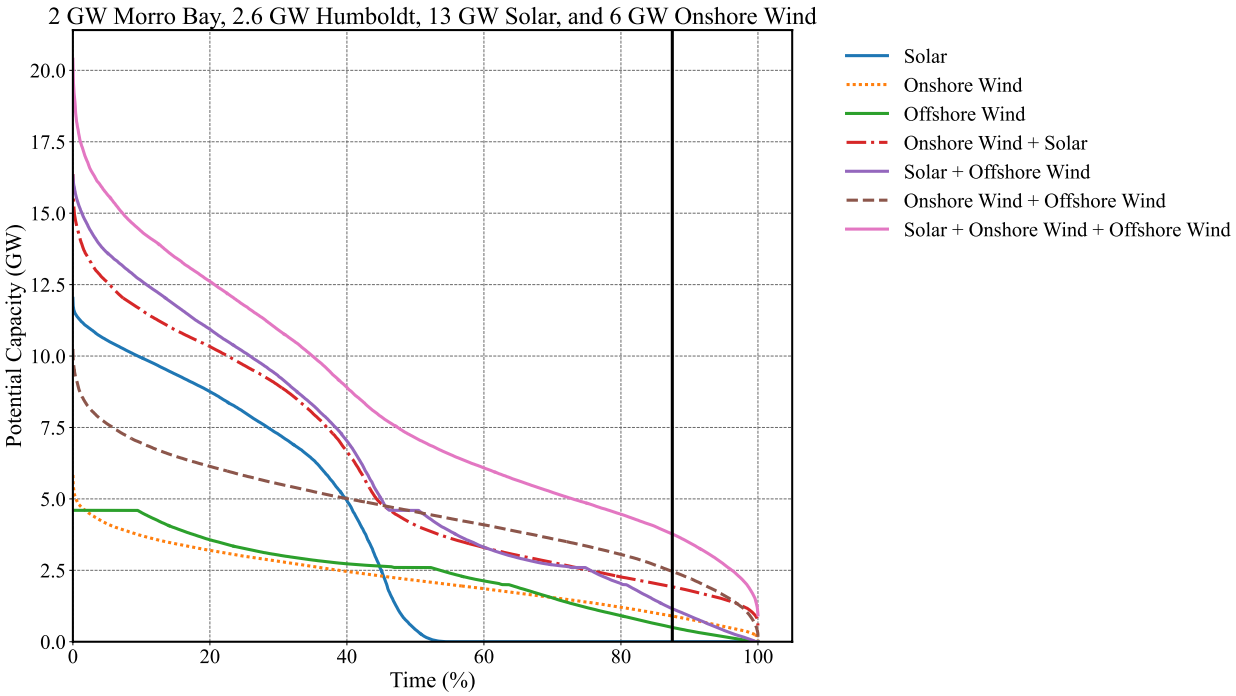

Figure 5-5: Generation duration curve for configuration three.

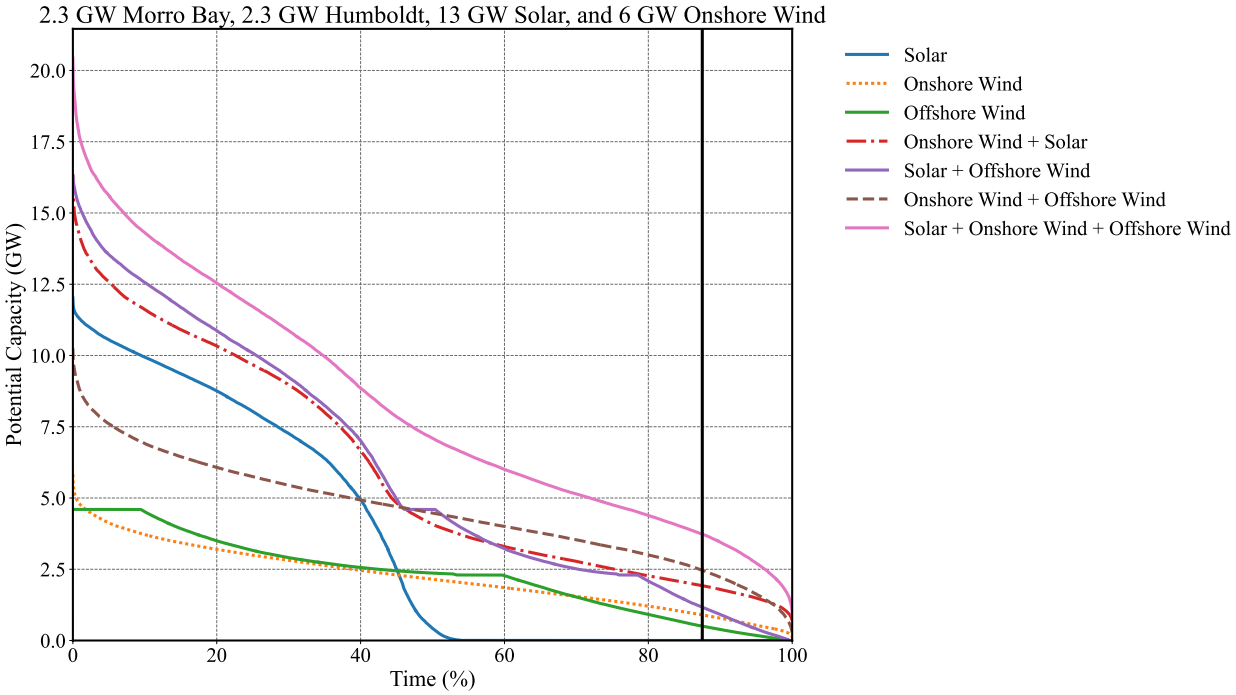

Figure 5-6: Generation duration curve for configuration four: 13 GW solar, 6 GW onshore wind, 2.3 GW in Morro Bay and 2.3 GW in Humboldt.

Table 5-3: Firm capacities for different configurations (GW)

	Configuration 1: 0.767 GW All OSW	Configuration 2: 2.6 GW Morro Bay, 2 GW Humboldt	Configuration 3: 2 GW Morro Bay, 2.6 GW Humboldt	Configuration 4: 2.3 GW Morro Bay, 2.3 GW Humboldt
Solar	0	0	0	0
Onshore Wind	0.901	0.901	0.901	0.901
Offshore Wind	0.829	0.503	0.501	0.497
Solar + Offshore Wind	1.538	1.172	1.158	1.158
Onshore Wind + Offshore Wind	2.573	2.464	2.462	2.421
Solar + Onshore Wind	1.924	1.924	1.924	1.924
Onshore Wind + Offshore Wind + Solar	3.872	3.732	3.771	3.65

5.3.2 **Correlation Analysis**

The Pearson Correlation analysis suggests that the strongest complementary pair are onshore wind and solar over the 5-year period (Figure 5-7), since these resources have a Pearson correlation coefficient value of -0.39. This has been well-reported in the literature previously (e.g., [89]). The demand is most strongly correlated with solar (0.19) and most strongly anticorrelated with onshore wind (-0.26). The near zero value of the Pearson correlation coefficient between the offshore wind farm sites and the demand and solar suggests there is no observable correlation. There is a weak positive correlation between onshore wind and Channel Islands North (0.17), Channel Islands South (0.14), and Morro Bay (0.12). Additionally, the analysis shows that the offshore wind sites are not consistently coincident with each other. Crescent City and Humboldt, which are in close proximity with each other, have a significant level of correlation, demonstrated with the correlation coefficient of 0.7. Bodega Bay has a medium positive correlation with Humboldt (0.54) and Morro Bay (0.43), and a weak correlation with Channel Islands North (0.22) and Channel Islands South (0.29). Morro Bay has a strong correlation with Channel Islands North and South with coefficient values of 0.68 and 0.75, respectively. The two Channel Islands locations are strongly correlated with each other (0.88). The correlation between offshore wind farm sites is heavily dependent upon location; the closer the sites are the higher the correlation, as expected. Further, these results demonstrate that the offshore wind sites are not ubiquitously correlated or complementary with each other. Unlike

solar and onshore wind, the seasonal patterns of offshore wind are far more variable and dependent upon the location. The strong seasonal patterns in Figure 5-2 are not apparent in the Pearson Correlation results.

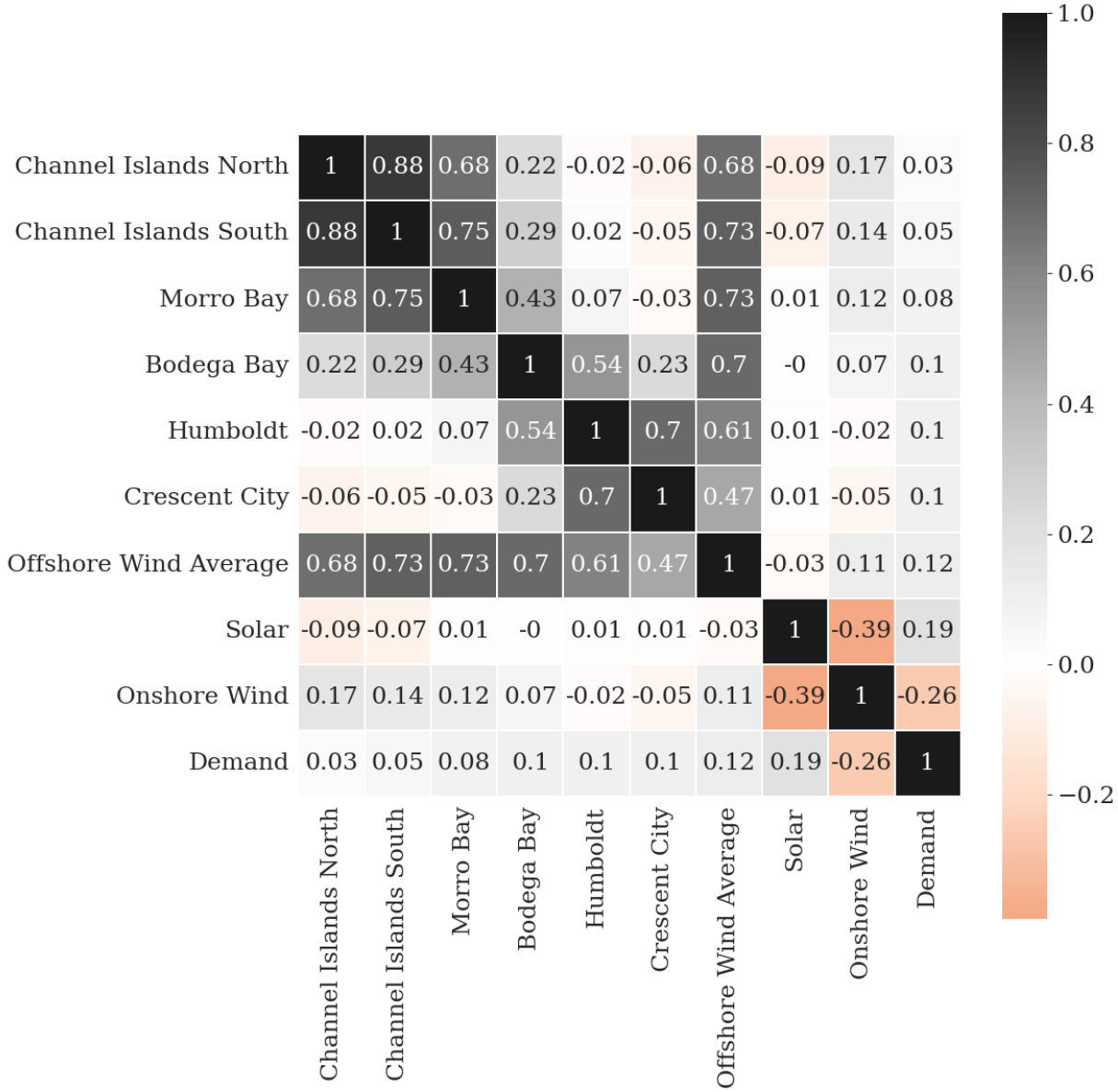

Figure 5-7: Pearson correlation values for the six offshore wind sites identified by NREL with solar, onshore wind and the demand.

5.3.3 **Meteorological Seasonal variation in demand-based metric**

In the present analysis, we summarize the demand-based value metric results during peak demand hours (4 - 9 PM) in the summer (Figure 5-8) and winter (Figure 5-9) for each renewable energy resource and for each of the six representative offshore wind sites. The boxes show the quartiles of the dataset, with the bottom of the box showing the 25th percentile and the top of the box showing the 75th percentile. The black horizontal line represents the mean. The whiskers of the boxplots represent the 5th and 95th percentiles, while any points outside the whiskers are considered extreme values that lie outside of the 5th and 95th percentiles. The metric captures how well power generation from these sites aligns with the demand during peak hours. When the metric value is 1, the alignment is perfect, and when the metric value is 0, the alignment is poor.

In the summer (Figure 5-8), the median values are significantly higher for the offshore wind sites than for solar and onshore wind. This is also true for the average value of the offshore wind metric. There are multiple instances where the metric for offshore wind reaches values that are above 0.8. In the summer, the most valuable offshore wind sites are located Bodega Bay, Humboldt, and Crescent City. During peak demand hours in the summer, offshore wind is highly valuable and a desirable resource for the electric grid.

In the winter (Figure 5-9), the median value for solar is zero, and the majority of the metric values range between 0 and 0.1. The metric for offshore wind is more variable in the winter than in the summer and the median values are lower. Additionally, the median value for the combined offshore wind metric (0.23) is nearly equivalent to the onshore wind median (0.22). For the Channel Islands North, Channel Islands South, Morro Bay, and Bodega Bay sites, the median metric tends to fall between 0.11 and 0.20. Of the offshore wind sites, Morro Bay represents the site with the lowest median metric, and it has significant variability. This suggests that Morro Bay may have the least complementary dynamics with the electrical demand. The two most valuable sites are Humboldt and Crescent City, which have a median metric value between 0.25 and 0.28 in the winter. These results further illustrate that the value of offshore wind is highly dependent upon both temporal and spatial factors. The value of offshore wind depends upon the location of the offshore wind site (e.g., Morro Bay vs Crescent City) and the time of year studied (e.g., summer vs winter). Interestingly, in both the summer and winter, the demand-based value metric for onshore wind experiences the least amount of variability. This is because the onshore

wind data is the aggregate value of wind speeds over the Western Interconnection region in the United States.

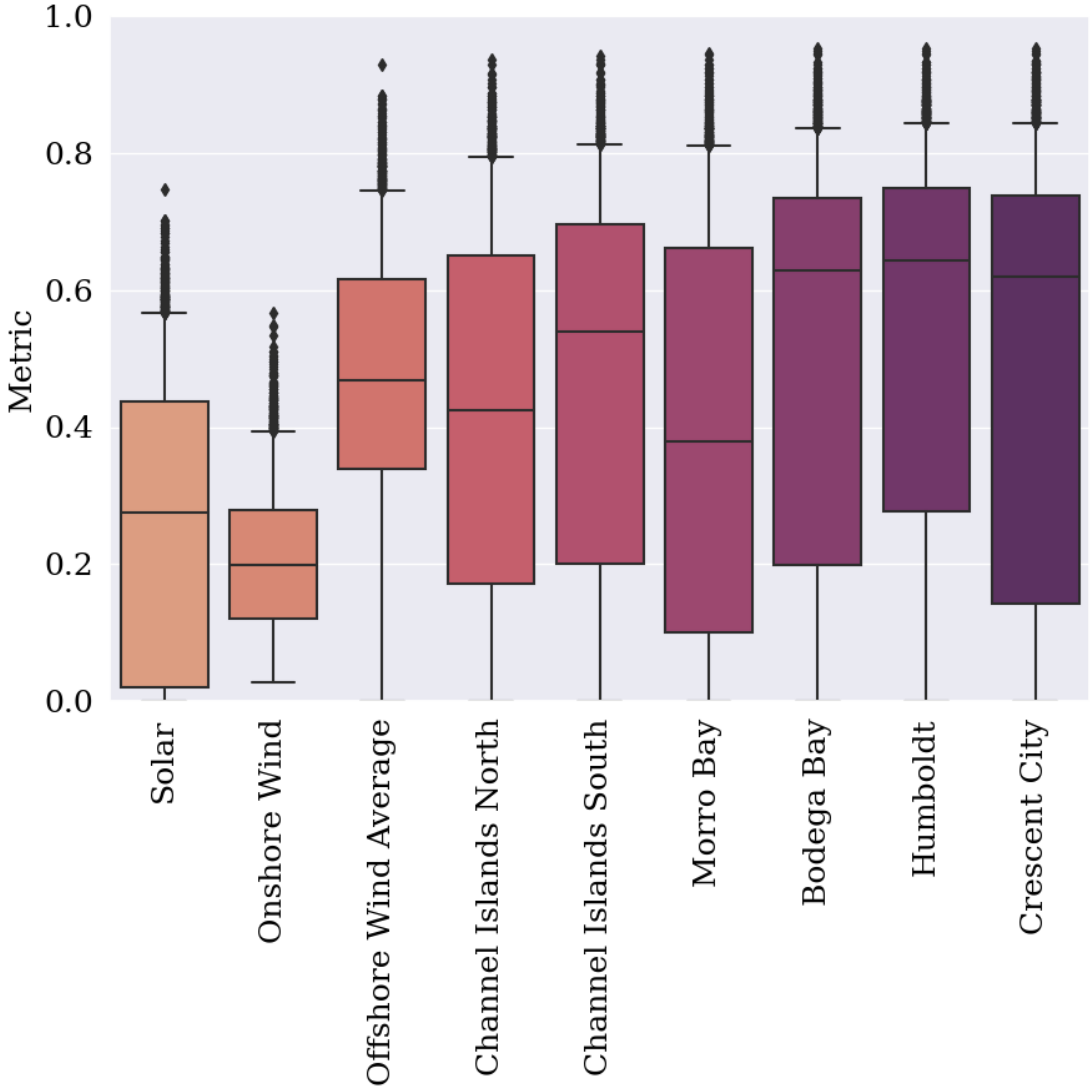

Figure 5-8: Demand-based value metric for solar and onshore wind resources and each offshore wind farm site during the peak hours of the summer season (June, July, August).

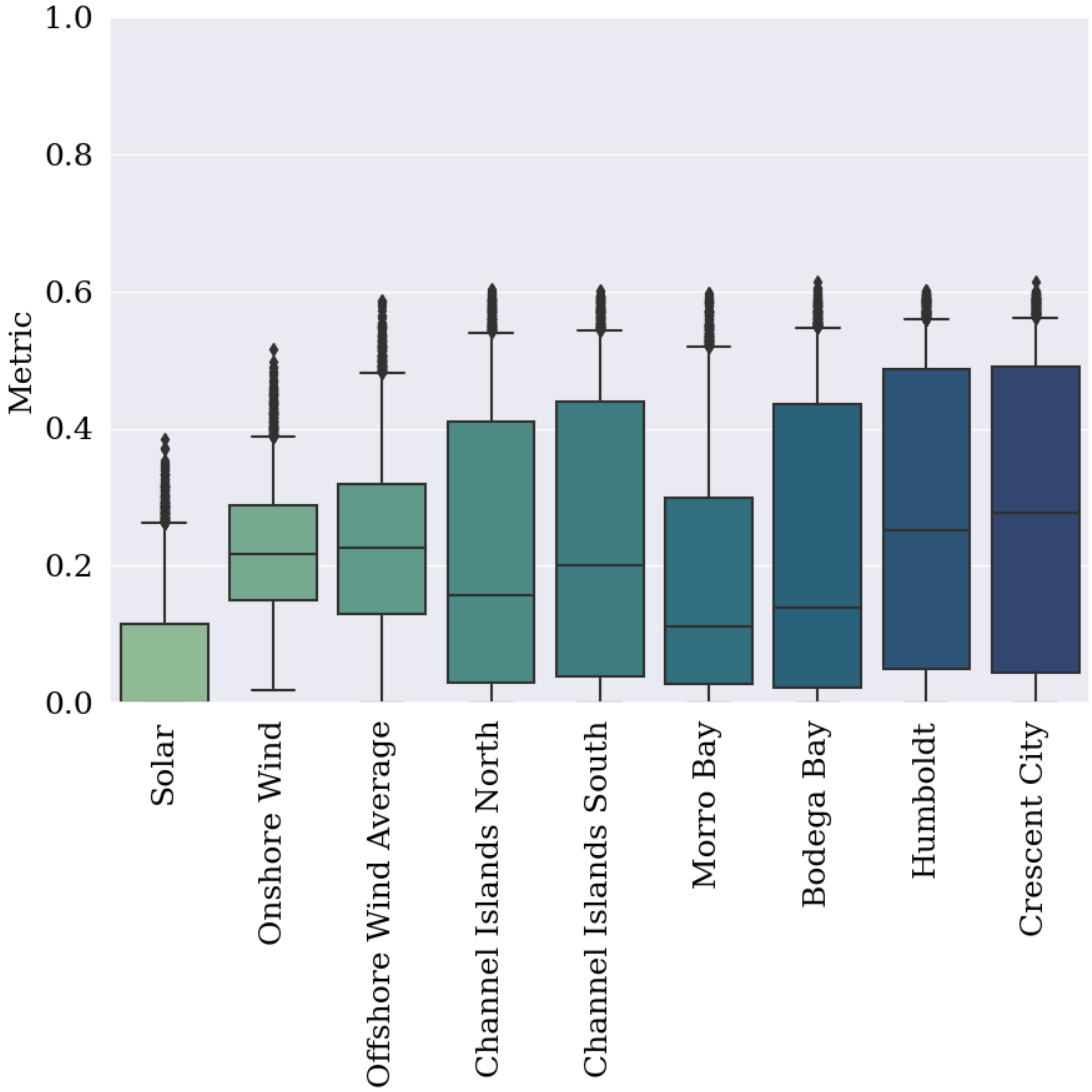

Figure 5-9: Demand-based value metric for solar and onshore wind resources and for each offshore wind farm site during the peak hours of the winter season (December, January, and February).

5.3.4 Fast Fourier Series Analyses

To further assess the seasonality of the renewable resources, we used the FFT to identify the most important frequencies. For the offshore wind analysis, we selected three representative sites to study (Channel Islands South, Morro Bay, and Humboldt). The results of these analyses are

shown in Figure 5-10 - Figure 5-16. In each of these figures, the original capacity factor dataset is plotted in dotted black lines, and the model results are plotted as solid colors. When the data is highly predictable, such as it is with solar power (

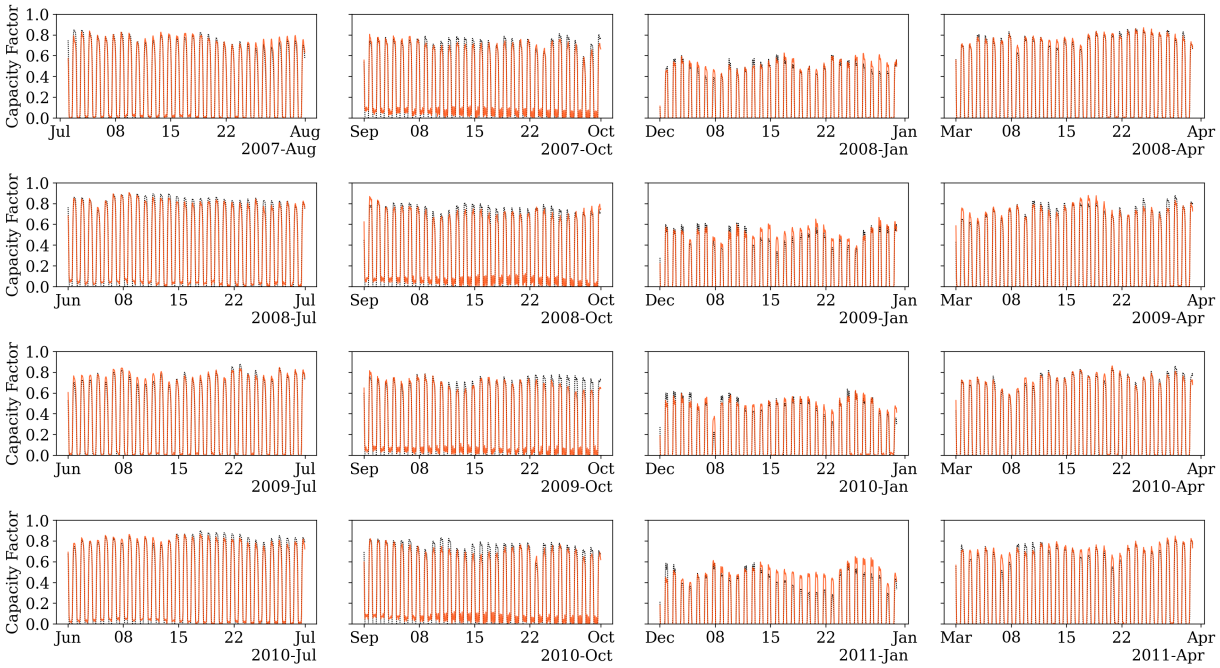

Figure 5-12: Comparing model (solid orange) to original data (dashed black) for solar. Note that this shows solar is highly predictable.

), the real data can be modelled and replicated quite precisely using the model that uses the FFT produced frequencies and magnitudes. The FFT produced frequencies with the highest magnitudes in the model reveal the underlying trends and most important periodic components of the data. The most significant periodic trends are provided in the appendix. The results for the average offshore wind, onshore wind and solar capacity factors are presented in Figure 5-10, Figure 5-11, and Figure 5-12 respectively.

The most significant period in the onshore wind data is 1-day. For onshore wind, the R-squared value for comparison of the model to the original data varies between 0.52 and 0.87 for the seasons studied. The FFT performs very well for the solar data, shown in Figure 5-12, and it reveals that the top three periods with the highest signal for solar are 1 day, 0.5 day, and 0.25 day. This was consistent across all the seasons studied. The high R-squared values for solar, which are consistently greater than 0.9, indicate that solar is highly predictable and consistent across the seasons and locations studied. In contrast to onshore wind and offshore wind, the FFT

model is able to capture the periods and trends of the solar data very well, and thus, the model well matches the original data.

Figure 5-13 presents a summary of the average R-squared values obtained for the comparison of FFT models to the original data for solar, onshore wind, and the average offshore wind capacity factors. Note that in all the seasons analyzed in this four-year period, solar power is the most predictable with R-squared values equal to or above 0.95, while onshore wind ranges between 0.52 and 0.87, and offshore wind ranges between 0.45 and 0.73. The R-squared values for offshore wind may be lower than onshore wind because the onshore wind dataset is representative of the Western Interconnection region, whereas the offshore wind is the average of six sites. Additionally, to analyze the dynamics of individual offshore farm sites, the FFT results are also presented for Channel Islands South in Figure 5-14, Morro Bay in Figure 5-15, and for Humboldt in Figure 5-16. This analysis suggests that offshore wind significantly varies temporally and spatially so that a general generation profile of offshore may not be representative of all sites. It may be that offshore wind is more susceptible to several factors such as localized wind currents, local temperature gradients, local turbulence, and interactions with waves. The current analysis also questions the temporal advantage of offshore wind that has been reported in prior studies. While there are many benefits of deploying offshore wind due to the value of having variety and diversity in renewable energy resources, the temporal value of offshore wind may not be universally complementary to other renewable energy resources. While it could be true that some offshore wind sites tend to peak in the evening, the current analysis shows that this is not revealed with the FFT and suggests that offshore wind is highly variable.

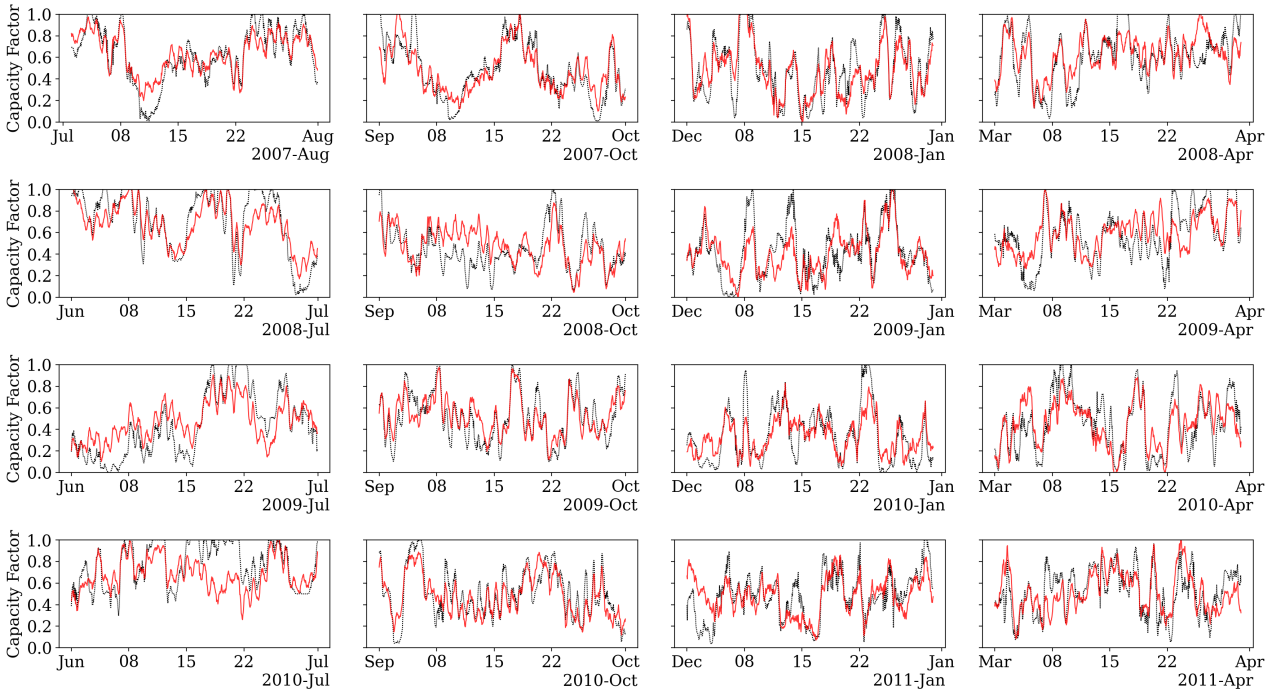

Figure 5-10: Comparing model (solid red) to original data (dashed black) for average offshore wind.

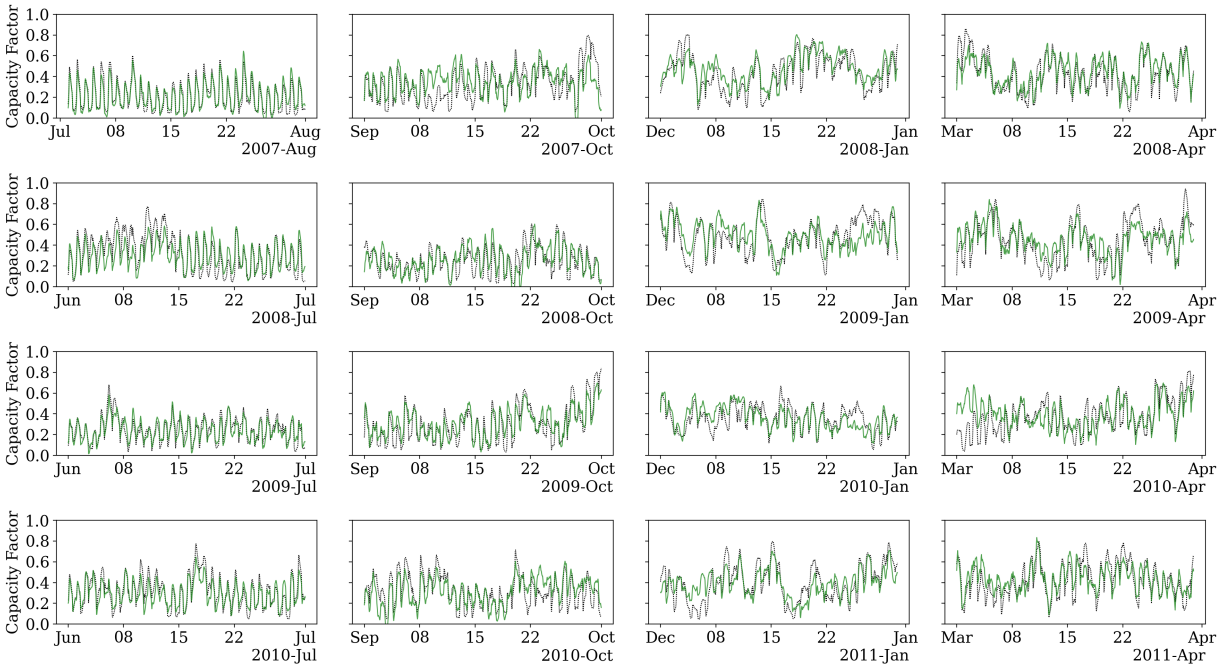

Figure 5-11: Comparing model (solid green) to original data (dashed black) for offshore wind.

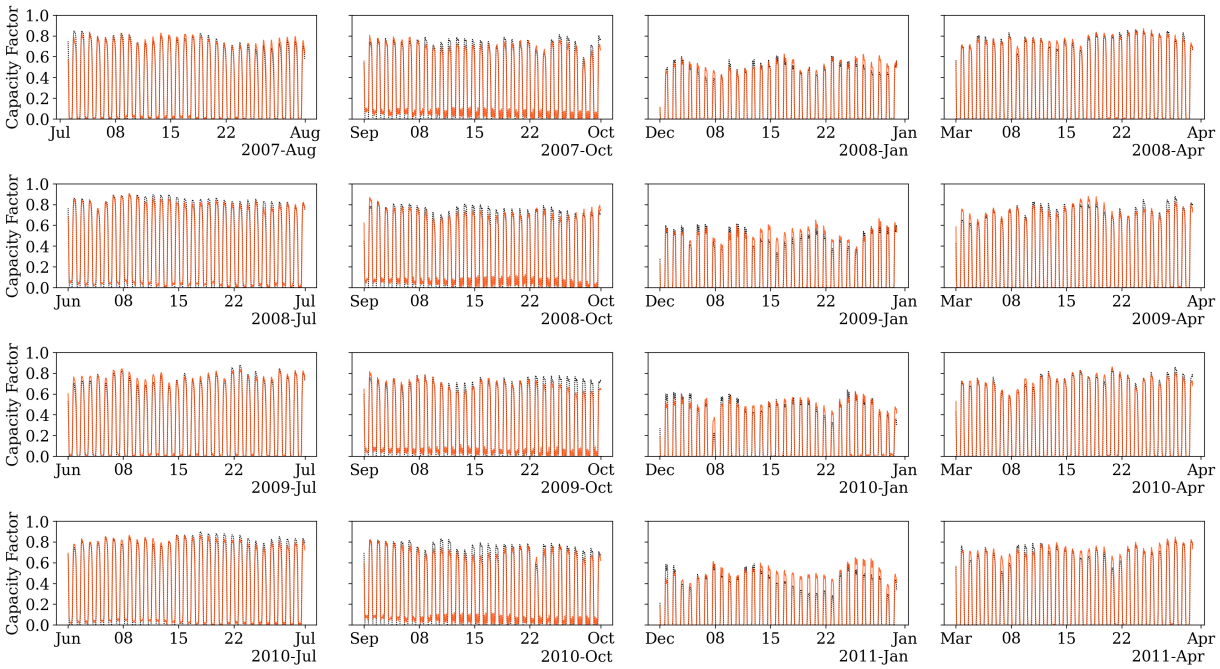

Figure 5-12: Comparing model (solid orange) to original data (dashed black) for solar. Note that this shows solar is highly predictable.

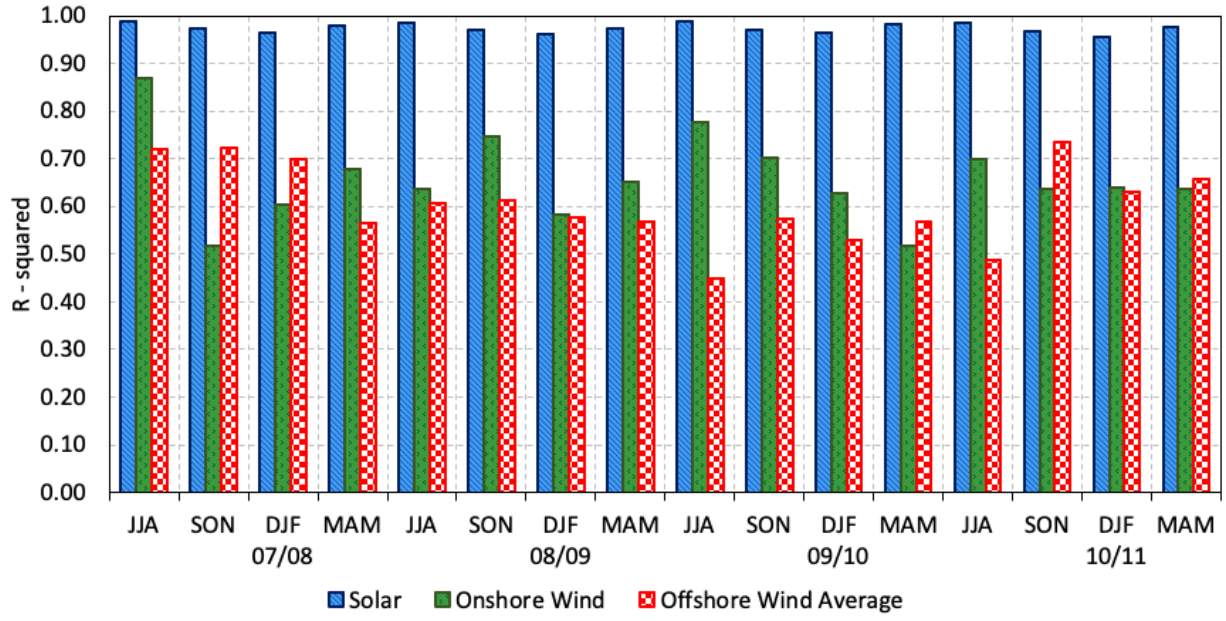

Figure 5-13: R-squared values for the FFT model results. JJA = June, July, August; SON = September, October, November; DJF = December, January, February; MAM = March, April, May

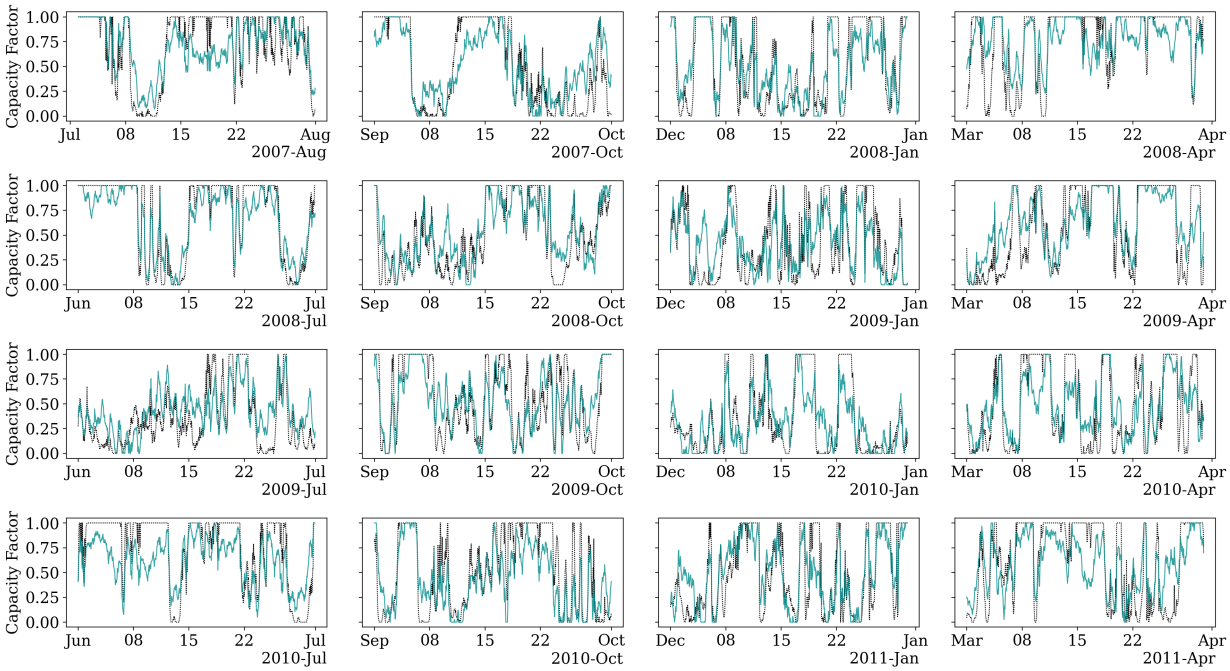

Figure 5-14: Comparing model (solid blue) to original data (dashed black) for Channel Islands South offshore wind site.

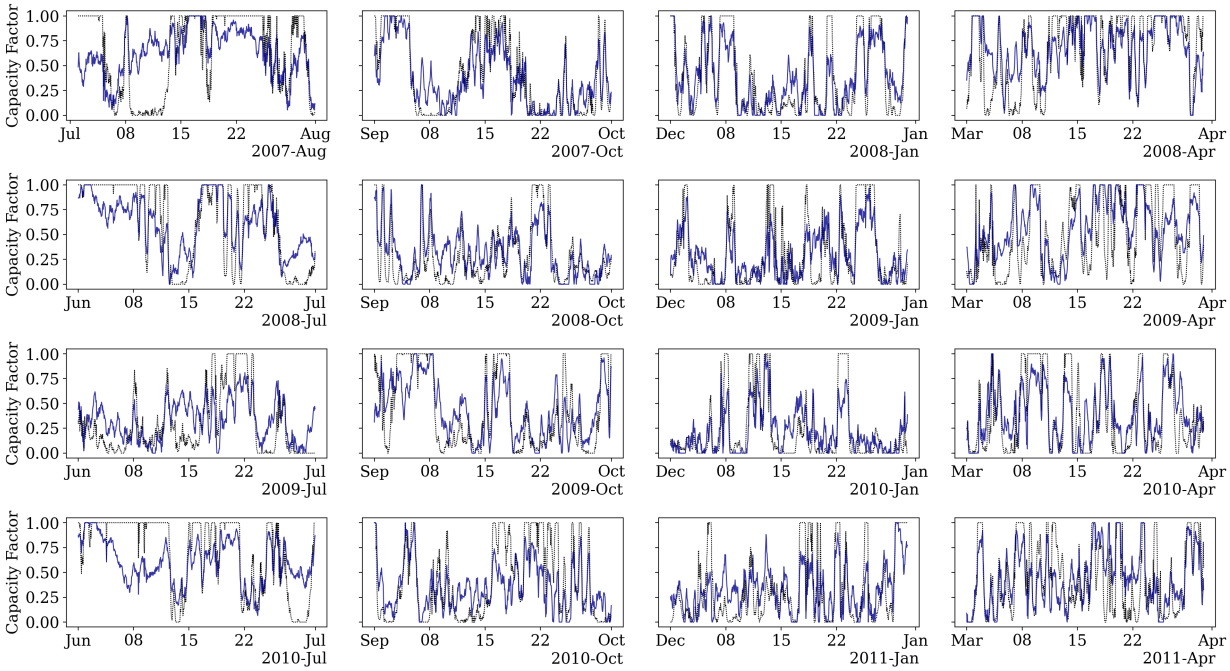

Figure 5-15: Comparing model (solid purple) to original data (dashed black) for the Morro Bay offshore wind site.

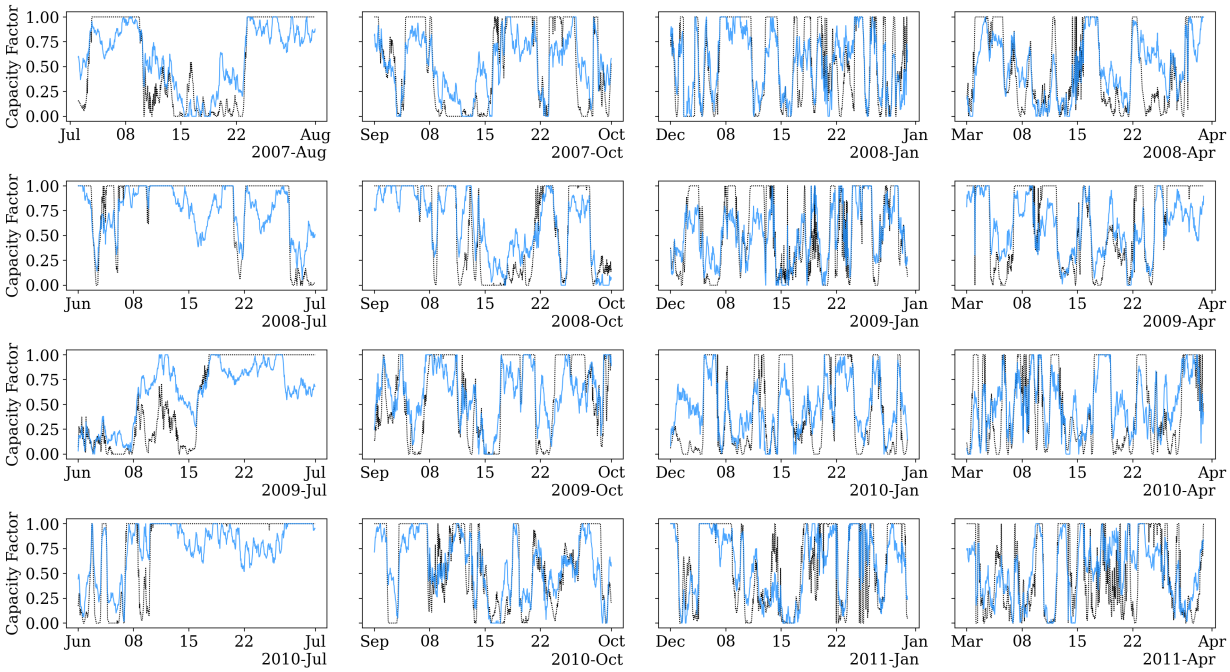

Figure 5-16: Comparing model (solid blue) to original data (dashed black) for the Humboldt offshore wind site.

5.4 Summary and Conclusions

In this study, we use statistical methods to evaluate the coincidence, variability, alignment, and predictability of offshore wind with demand and onshore renewable resources. The goal of this study is to investigate the benefits and challenges of deploying offshore wind and to evaluate the dynamics of offshore wind to verify if the advantages of offshore wind previously reported in the literature are true amongst the variety of possible offshore wind resources available in California. The major findings of this study are:

- Across different configurations, the most resilient combination of resources occurs when offshore wind is paired with solar and onshore wind. This is reflected in the firm capacity.
- Onshore wind and solar are the most complementary renewable power generation resources.
- There is no consistent correlation (positive or negative) between the offshore wind sites and the demand, or with solar, or with onshore wind.

- There are some offshore wind sites with a strong positive correlation with each other, but this is not ubiquitous across all the offshore wind sites. This suggests that unlike solar, offshore wind is not a resource with high predictability and that this resource has a high degree of spatial variability.
- When using a demand-based metric to analyze the value of the different renewable energy resources and the six potential offshore wind sites investigated, we found that offshore wind is the most valuable resource during peak demand hours in the summer and winter in California.
- The value of offshore wind varies spatially and temporally since not all wind sites have uniform patterns.

6 SEAWATER SOLID OXIDE ELECTROLYSIS THERMODYNAMIC MODEL

This section presents a steady-state model of an offshore wind platform that is coupled with a high temperature solid oxide electrolysis system. The system includes the balance of plant components for hydrogen production such as compression. The system uses air to sweep the oxygen from the anode. The electrolyzer is assessed under exothermic, endothermic and thermoneutral operation. This section explores the feasibility of operating the stack exothermically so that the net heat generated is enough to meet the thermal demands of the reaction and the balance of plant such as steam generation and the superheating the inlet streams. Motivated by the enhanced thermodynamics that result in higher efficiencies and the ability to operate in galvanic and electrolytic modes, this study considers the benefits and challenges of an offshore solid oxide electrolysis platform and compares its potential performance with low temperature and high temperature PEM electrolysis. It also assesses how an offshore solid oxide platform could be coupled with offshore wind to provide clean reliable energy.

6.1 Methods: Electrochemical Model

The electrochemical model is a steady-state 0-dimensional model of a stack comprised of 7000 planar cells, each with an area of 100 cm^2. As previously discussed in 2.2 Electrolysis Thermodynamics Fundamentals, electrochemical cells experience three main types of polarization losses which cause the actual voltage to deviate from ideal conditions. The ohmic (η_{ohm}), activation (η_{act}), and concentration polarization (η_{conc}) are considered in the calculation of the voltage of each cell (U_{cell}):

$$U_{cell} = U_{rev} + |\eta| = U_{OCV} + (\eta_{ohm} + \eta_{act} + \eta_{conc}) \quad \textbf{(6-1)}$$

Where the open circuit voltage (U_{OCV}) is calculated using the Nernst equation (2-17). To model the ohmic losses (η_{ohm}) in the cells, ohm's law was used:

$$\eta_{ohm} = \left(R_{electrolyte} + R_{anode} + R_{cathode} + R_{contact}\right) * i \quad \textbf{(6-2)}$$

Where $R_{electrolyte}, R_{anode}, R_{cathode}, R_{contact}$ are the resistances of the electrolyte, anode, cathode, and contacts; and, i is the current. The Ohmic losses occur due to resistance to ionic conduction in the electrolyte, and electronic conduction in the electrodes, interconnects, and contacts between cell components. The contact resistance is adjusted to fit the experimental results from [108] to validate the model. It is important to note here that while single cell test results are often used to represent potential stack performance, real SOC stacks will experience higher contact resistances, that will lead to reduced performance [55].

The activation polarization (η_{act}) is typically represented by a modified version of the Butler-Volmer equation that uses a transfer coefficient of 0.5. It is typically expressed as [55], [109]:

$$\eta_{act} = \frac{RT}{nF}\arcsin\left(\frac{J}{2J_{0,Anode}}\right) + \frac{RT}{nF}\arcsin\left(\frac{J}{2J_{0,Cathode}}\right) \quad \textbf{(6-3)}$$

Where R is the universal gas constant, T is temperature (K), n is the number of electrons that participate in the reaction, F is the Faraday constant, J is the operating current density, and J_0 is the exchange current density and is found from [110], [111] for the cathode and anode:

$$J_{0,cathode} = \frac{j^*_{H_2}\left(\frac{p_{H_2}}{p^*_{H_2}}\right)^{\frac{\beta_{H_2}}{2}}\left(\frac{p_{H_2O}}{p_0}\right)^{1-\frac{\beta_{H_2}}{2}}}{1+\left(\frac{p_{H_2}}{p^*_{H_2}}\right)^{\frac{1}{2}}} \quad \textbf{(6-4)}$$

$$J_{0,anode} = \frac{j^*_{O_2}\left(\frac{p_{O_2}}{p^*_{O_2}}\right)^{\frac{\beta_{O_2}}{2}}}{1+\left(\frac{p_{O_2}}{p^*_{O_2}}\right)^{\frac{1}{2}}} \quad \textbf{(6-5)}$$

Where $p_{species}$ is the species' (either hydrogen, oxygen or steam) pressure in the corresponding gas channel, and $P^*_{species}$ is the pressure at equilibrium. β is the transfer coefficient which is equal to 0.5. The exchange current density is the current density at equilibrium in which the reverse and forward reaction are occurring at the same rate and the net reaction rate is zero. The equilibrium pressures ($p^*_{O_2}\ and\ p^*_{H_2}$) can be found using the following expressions from [110]:

$$p^*_{O_2} = 4.9 * 10^8 \exp\left(-\frac{200*10^3}{RT}\right)\{atm\}\exp\left(-\frac{200*10^3}{RT}\right)\{atm\} \quad \textbf{(6-6)}$$

$$p_{H_2}^{*} = 2.1362 * 10^5 \exp\left(-\frac{9.6*10^4}{RT}\right) \{atm\} \exp\left(-\frac{9.6*10^4}{RT}\right) \{atm\} \quad \textbf{(6-7)}$$

The equilibrium exchange current densities can be found using the Arrhenius expressions from [110]:

$$j_{O_2}^{*} = \gamma_{O_2} \exp\left(-\frac{E_{act}^{O_2}}{RT}\right) \quad \textbf{(6-8)}$$

$$j_{H_2}^{*} = \gamma_{H_2} \exp\left(-\frac{E_{act}^{H_2}}{RT}\right) \quad \textbf{(6-9)}$$

Where $\gamma_{species}$ is the pre-exponential factor of each species, and $E_{act}^{species}$ is the activation energy for each half reaction.

Finally, the concentration polarization is necessary to represent mass transfer losses. It is especially influential to the overall voltage at high current densities and low steam utilizations. Concentration losses occur when concentration gradients develop in the cells that cause the movement of the reactants and products to and from the reaction sites to be slower than the rate at which current is discharged. The concentration polarization (η_{conc}) is given by:

$$\eta_{con,cath} = \frac{RT}{nF} \ln\left(\frac{1+\frac{jRT\delta_c}{2FD_{H_2O}^{eff} p_{H_2}^0}}{1-\frac{jRT\delta_c}{2FD_{H_2O}^{eff} p_{H_2O}^0}}\right) \quad \textbf{(6-10)}$$

Where j is the current density, R is the gas constant, T is the temperature, F is the Faraday constant, δ_c is the cathode thickness, $D_{H_2O}^{eff}$ is the average effective diffusivity coefficient of the cathode, P_{H_2} is the partial pressure of hydrogen in the cathode, and P_{H_2O} is the partial pressure of steam in the cathode.

$$\eta_{con,ano} = \frac{\mathrm{RT}}{nF} \ln\left(\left(1 + \frac{jRT\delta_a}{4FD_{O_2}^{eff} p_{O_2}^0}\right)^{\frac{1}{2}}\right) \quad \textbf{(6-11)}$$

Similarly, $D_{O_2}^{eff}$ is the average effective diffusivity coefficient of the anode, and P_{O_2} is the partial pressure of oxygen in the anode.

Table 6-1 lists the model input values used in each of the equations listed above.

Table 6-1: Properties and parameters used in the electrochemical model.

Properties	Value	Reference
δ_c Fuel Electrode thickness (m)	310 x 10^{-6}	[110]
O_2 Electrode thickness (m)	10 x 10^{-6}	[110]
Electrolyte Electrode thickness (m)	10 x 10^{-6}	[110]
Fuel electrode conductivity $\left(\frac{1}{\Omega\,\mathrm{m}}\right)$	$\frac{10^7}{T}\exp\left(\frac{1150}{T}\right)$	[110]
O_2 electrode conductivity $\left(\frac{1}{\Omega\,\mathrm{m}}\right)$	$\frac{4.6*10^6}{T}\exp\left(\frac{1100}{T}\right)$	[110]
Electrolyte ionic conductivity $\left(\frac{1}{\Omega\,\mathrm{m}}\right)$	$\frac{3.6*10^7}{T}\exp\left(\frac{-8*10^4}{RT}\right)$	[110]
$E_{act}^{O_2}$	87400	[110]
$E_{act}^{H_2}$	88750	[110]
γ_{H_2}	3.504 x 10^8	[110]
γ_{O_2}	1.698 x 10^8	[110]
β_{H_2}	0.5	[110]
β_{O_2}	0.5	[110]
$D_{H_2O}^{eff}$ and $D_{H_2}^{eff}$	2 x 10^{-5}	[109]
$D_{O_2}^{eff}$	5.11 x 10^{-5}	[109]
Cell Area (cm^2)	100	[48], [112]
Cathode Channel Height (m)	0.001	[53]
Anode Channel Height (m)	0.001	[53]
Interconnect Height (m)	500 x 10^{-6}	[53]
Endplates thickness (m)	0.01	[113]
Insulation thickness (m)	0.3	[114]

The model was validated using data from Jensen et al., [108] which was previously used for validation in [110], [115]. A polarization curve at 850°C is used as the reference case for validation and calibration of the model. The numerical data from the model aligns well with the validation data, as shown in Figure 6-1. The ohmic, activation, and concentration polarizations

are plotted in Figure 6-2.

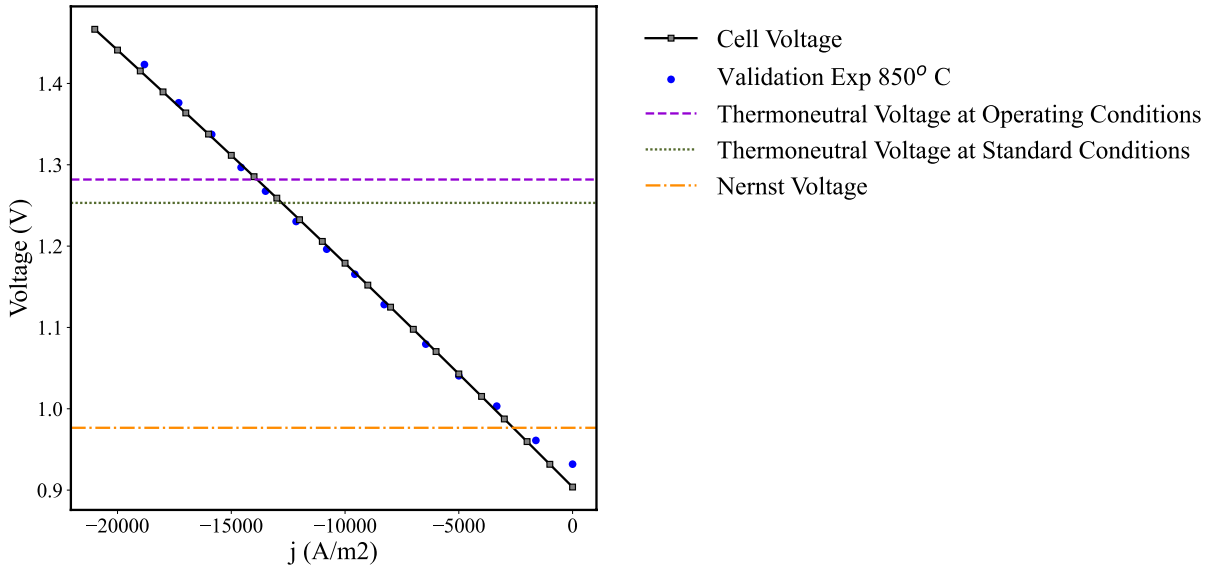

Figure 6-1: Model validation using experimental data from [108]

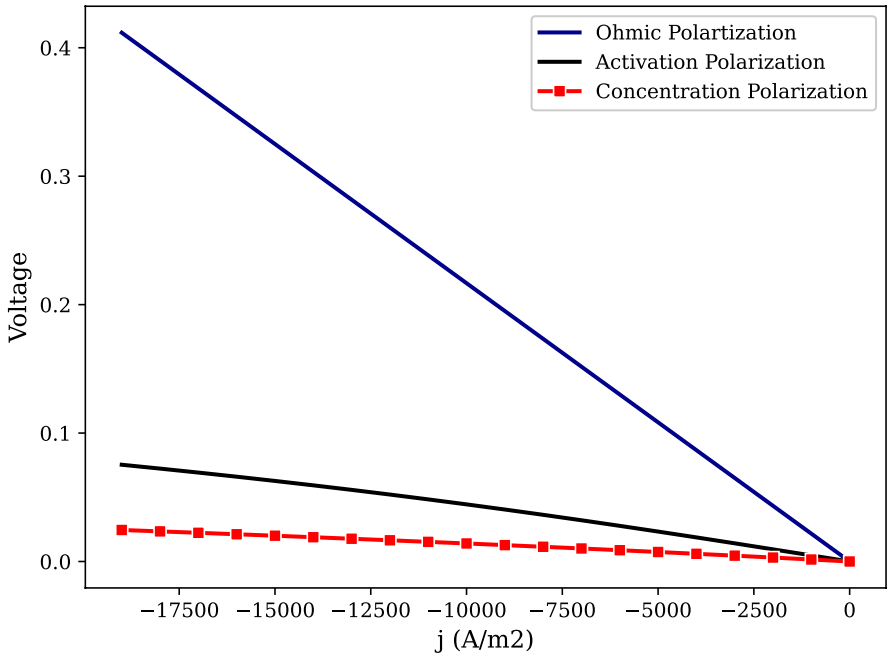

Figure 6-2: Ohmic, activation, and concentration losses at 850ºC.

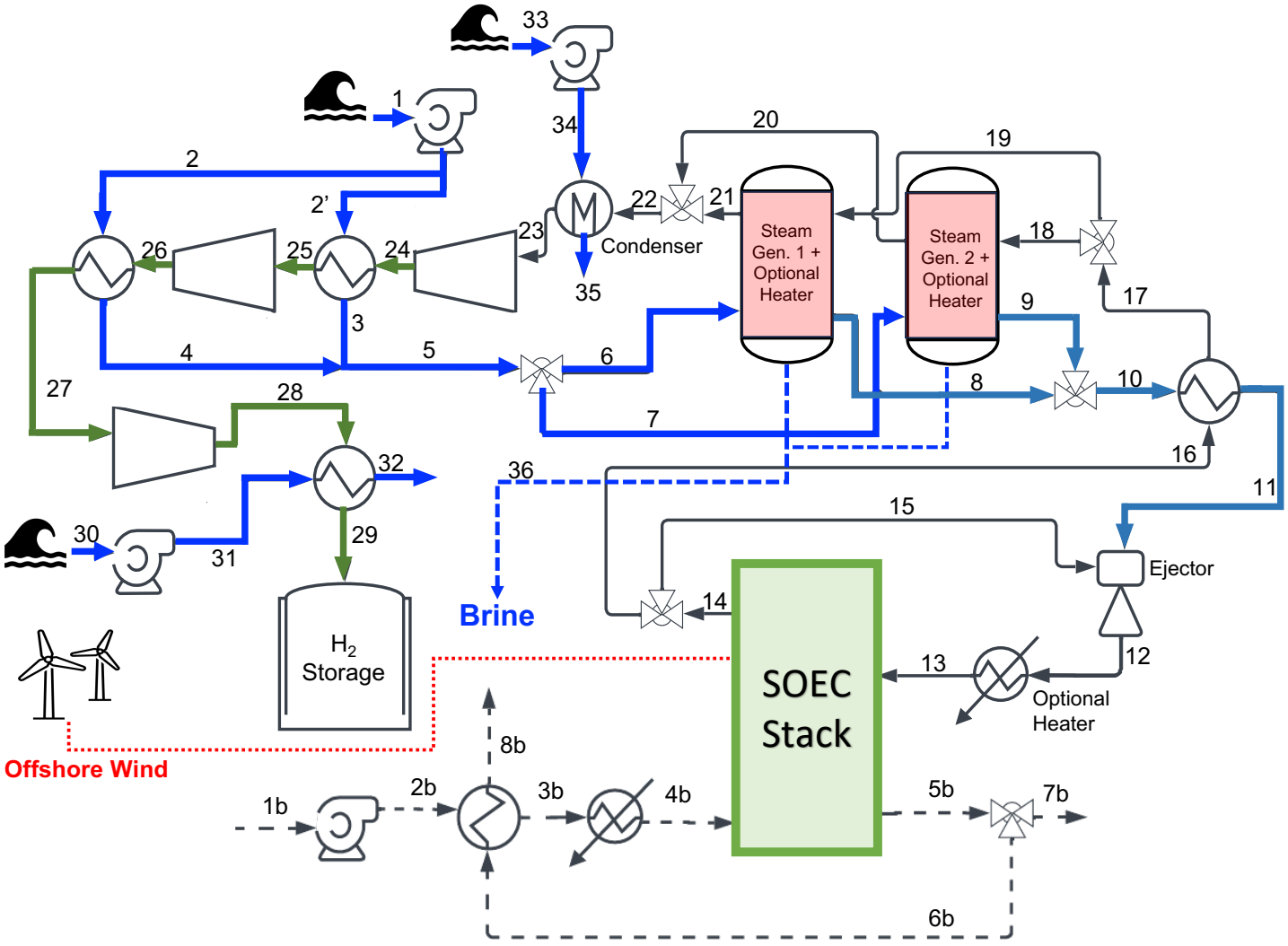

LEGEND				
Seawater	Steam	Steam – H_2 Mixture	H_2	Air

Figure 6-3: Schematic of the offshore wind H_2 platform

6.2 Methods: System Design and Balance of Plant

The seawater solid oxide model is comprised of a series of pumps, heat exchangers, steam generators, a condenser, and the electrolyzer (see Figure 6-3). First, seawater is pumped to the intercoolers (states 1, 2, and 2'), where the hydrogen preheats the seawater while the seawater simultaneously cools the hydrogen between compression stages. At state 1, a simple pump pumps the seawater that will be used in the electrolyzer; the seawater is split into two flows with equal flow rates, where each seawater stream enters an intercooler (states 2 and 2'). In the third intercooler, (state 1') enough seawater is flowed into the intercooler so that temperature difference of the seawater inlet and outlet is 10^{o} Celsius to prevent thermal pollution. The seawater in the first two intercoolers is a gas-vapor mixture, and it exits the intercoolers at a temperature of approximately 100^{o}C. The inlet streams recombine at state 5. In the steam generator, the thermal energy from the hydrogen- water mixture (states 18 and 19) heats the seawater so that the steam that exits the steam generators at states 8 and 9 is entirely in the vapor phase. The steam generator is equipped with an additional heater to ensure the outlet is in the saturated vapor phase. The steam then gets further heated in the heat exchanger (state 10 and 11) with the hot hydrogen- steam mixture so that the steam is superheated. It is advantageous to operate the system in this way because the outlet mixture of H_2 and H_2O is cooling as it is preheating the inlet steam, which is beneficial for H_2 compression at states 23-29.

Furthermore, after the inlet steam passes through the heat exchanger it enters the ejector (state 11) where it mixes with a mixture of high temperature hydrogen and steam (state 15) from the outlet of the stack. The ejector is used to accomplish the desired stack inlet blend of 10% hydrogen with 90% steam (by volume). The system is equipped with an optional heater at state 12-13 in case the thermal heat from the exit streams was insufficient for superheating the steam. Lastly, after passing through the heat exchanger and the steam generator, the outlet hydrogen-steam mixture passes through a condenser where seawater is used to cool and condense the steam so that only the hydrogen remains in state 23, the compression unit inlet. The compressed hydrogen is then stored at a pressure of 350 bar (state 29).

Lastly, the system also uses an air sweep in the anode electrodes to avoid potential harmful material issues [55]. The air is compressed using a blower in state 1b and 2b. The air is preheated

using a portion of the oxidant outlet stream in state 2b to 3b. The preheated air goes through an optional heater that turns if the air temperature is below the stack inlet temperature in state 3b to 4b. Air enters the stack and oxygen-enriched air exits the stack in 5b. Depending on the thermal requirements of the air stream, a portion of the air is recirculated to preheat the inlet air. It is assumed that the air flows at a rate that is 1.5 times the generation rate of oxygen.

Notably, as shown in Figure 6-3, the system uses a 3-way valve between states 5,6, and 7; states 8,9, and 10; and states 17,18, and 19 to control the two steam generators. The model contains two separate steam generators for brine management; each steam generator can be periodically flushed without interruption to the overall operation of the system. The following section will discuss the governing equations for each of the components and the related assumptions. Table 6-2 lists the efficiencies of each component.

Table 6-2: Efficiencies of Components

Component	Efficiency (%)
Compressors	75
Intercoolers	85
Condenser	95
Steam Generator	90
Electric Heaters	95
Fuel Heat Exchanger	98
Air Heat Exchanger	85

6.2.1 Solid Oxide System Governing Equations

Seawater Pump

Starting with state 1, the seawater pump is modelling using the following equation:

$$\dot{W}_{pump} = \dot{n}_{H_2O} * mw_{H_2O} * g * s \quad \textbf{(6-12)}$$

Where $\dot{n}_{H_2O}$ is the flowrate of the seawater, mw_{H_2O} is the molecular weight of water, g is gravity and s is the height to which the seawater needs to be pumped. The height of 10 m is from [41], which assumes the seawater plant is 10 m above the seawater.

Heat Exchangers

The heat exchangers in the system are modelled in a counter flow configuration using the heat exchanger effectiveness (ε) – NTU (number of transfer units) method derived from the long mean temperature difference method described in [116]. When the outlet temperatures are not known, the $\varepsilon - NTU$ method provides an equivalent, but alternative to the LMTD approach.

The theoretical maximum amount of heat transfer ($\dot{q}_{max}$) in a counterflow heat exchanger of infinite length is limited by the maximum possible temperature different at the hot inlet ($T_{h,i}$) and cold inlet ($T_{c,i}$):

$$\dot{q}_{max} = C_{min}(T_{h,i} - T_{c,i}) \quad \textbf{(6-13)}$$

Where C_{min} is the minimum fluid heat capacity rate, either equal to C_c or C_h, whichever is smaller. The heat capacity rates are given by:

$$C_C = \dot{n_c} * Cp_c \quad \textbf{(6-14)}$$

$$C_H = \dot{n_h} * Cp_h \quad \textbf{(6-15)}$$

Where the subscripts c and h represent the cold and hot streams respectively, and $\dot{n}$ and Cp are the molar flow rate and specific heat capacity.

The heat exchanger effectiveness (ε) measures the performance of a heat exchanger. It is defined as the ratio of the actual heat transfer rate to the maximum heat transfer rate:

$$\varepsilon = \frac{\dot{q}_{max}}{\dot{q}} \quad \textbf{(6-16)}$$

Where ε must be $0 \leq \varepsilon \leq 1$.

ε is a function of the heat capacity rates, and the number of transfer units (NTU), which is a dimensionless parameter defined as:

$$NTU = \frac{UA}{C_{min}} \quad \textbf{(6-17)}$$

Where U is the overall heat transfer coefficient and A is the total surface area over which heat is exchanged.

C_r is the ratio of the minimum heat capacity rate to the maximum heat capacity rate:

$$C_r = \frac{C_{min}}{C_{max}} \quad \textbf{(6-18)}$$

For a counterflow heat exchanger, ε and NTU are related by the following equations:
If $C_r < 1$,

$$\varepsilon = \frac{1-\exp\left[-NTU(1-C_r)\right]}{1-C_r*\exp\left[-NTU(1-C_r)\right]} \quad \textbf{(6-19)}$$

If $C_r = 1$,

$$\varepsilon = \frac{NTU}{1+NTU} \quad \textbf{(6-20)}$$

Therefore to model the heat exchangers, the Reynolds number (Re) was first calcuated to identify the flow regime of the cold and hot stream. For turbulent flow in a pipe with diameter, D, the following relation can be used to find the Nusselt number:

$$Nu = \left(0.027 * Re_D^{\frac{4}{5}}\right) \mathrm{Pr}^{0.4} \quad \textbf{(6-21)}$$

Where Pr is the Pradlt number listed in [117]. The heat transfer coefficient (h) is calculated using the Nusselt number in the following equation:

$$h = \frac{Nu*K}{D} \quad \textbf{(6-22)}$$

Where K is the thermal conductivity.

From the h of each stream, the overall heat transfer coefficient is calculated:

$$U = \frac{1}{\frac{1}{h}+\frac{1}{h}} \quad \textbf{(6-23)}$$

It is assumed that each heat exchanger is comprised of 0.025 m diameter pipes with a total length of 5m.

Lastly, using the overall heat transfer coefficient, the area of the heat exchanger, and the heat capacity flowrates, the model calculates the NTU and effectiveness of the heat exchanger. The effectiveness is then used to determine the heat exchanged in the heat exchanger and the temperature of the outlet flows.

Applying the first law of thermodynamics to the cold and hot streams, the unknown outlet temperatures were found using:

$$\dot{q} = \dot{n} Cp (\Delta T) \quad \textbf{(6-24)}$$

Where $\dot{q}$ is the thermal energy power, $\dot{n}$ is the molar flowrate, Cp is the heat capacity of the fluid, and ΔT is the temperature difference between the inlet and the outlet of the stream. The heat exchanger on the air side of the stack uses half of the moles coming out of the anode to preheat the inlet air stream (states 2b, 3b, 6b and 7b).

Intercoolers:

The hydrogen is cooled using intercoolers between compression stages. The intercoolers are treated as heat exchangers with a certain effectiveness (see Table 6-2). For the intercooler at states 2-5, 24-27, and 28-31, $T_{h,i}$ is the temperature out of the compressor and $T_{ci} = 10^o C$, which is about the average temperature of seawater near Humboldt, CA [118]. The design point of the compression unit, which is the ultimate hydrogen pressure at state 29, is 350 bar. The thermal energy available in the intercoolers (q_{ic}) is found using equation **(6-24)**.

To calculate the energy exchanged in the intercooler, the amount of energy required to heat up the seawater to the steam generator temperature (sensible energy) and for phase change (latent energy) is first calculated:

$$\dot{q}_{H_2O} = \dot{n}_{H_2O,liq} \left(h_{lat_{H_2O}} (100^o C) + C_{p_{liq\ H_2O}} (T_{out} - T_{in}) \right) \quad \textbf{(6-25)}$$

Where $\dot{q}_{H_2O}$ is the sum of the thermal energy required for preheating the liquid seawater, phase change of the seawater, and steam generation; $\dot{n}_{H_2O,liq}$ is the flowrate of the seawater; $h_{lat_{H_2O}}$ is

the latent heat of water at 100°C; $C_{p_{liq,H_2O}}$ is the heat capacity of the liquid water, and T_{out}=100°C and T_{in}= 10°C.

Then, the total available thermal energy for the water stream in the intercooler ($\dot{q}_{ic}$) is calculated using equation **(6-24)**, where $T_{h,i}$ is the inlet temperature of the hydrogen into the intercooler. Depending on the energy available, the model determines the quality and temperature of the water at the outlet of the intercooler.

If $\dot{q}_{ic} > \dot{q}_{H_2O}$, then the amount of heat available in the intercooler exceeds the heat required to preheat the seawater to its saturation temperature and phase change, which means that all of the seawater is converted to the vapor phase ($\dot{n}_{sw,vap} = \dot{n}_{H_2O,liq,in} = \dot{n}_{H_2O}$) and that excess heat is available to increase the temperature of the gaseous H_2O vapor. In this case, the excess heat available is found by:

$$\dot{q}_{ic} - \dot{q}_{H_2O} = \dot{n}_{H_2O} C_{p_{vap\ H_2O}} (T_2 - T_1) \qquad \textbf{(6-26)}$$

Where T_1=100°C and T_2 represents the outlet temperature of the steam in the intercooler (the unknown variable in the equation).

If $\dot{q}_{ic} < \dot{q}_{H_2O}$, then the amount of heat available in the intercooler is insufficient to the heat liquid water to 100°C and to change phase. Since it was assumed that the water will first be heated to 100°C before it begins to change phase, the model calculates if $\dot{q}_{ic}$ is sufficient to heat the liquid water to 100°C first. If it is not, the model will determine that the intercooler has only preheated the liquid water. If $\dot{q}_{ic}$ exceeds what is required for preheating the water, then the model determines the remaining energy that is available for phase change:

$$\dot{q}_{avail} = \dot{q}_{ic} - C_{p_{liq\ H_2O}} (T_{out} - T_{in})(T_{out} - T_{in}) \qquad \textbf{(6-27)}$$

The flowrate of steam from the intercooler is then calculated using $\dot{q}_{avail}$ and the latent heat of water.

Lastly, the third intercooler uses a separate pump for the seawater and is not involved in preheating seawater for electrolysis. The maximum outlet temperature of the seawater (T31) in

this intercooler is 20°C to reduce thermal pollution on the ocean. Therefore, the total amount of water that flows in the third intercooler is given by:

$$\dot{n}_{sw,ic_3} = \frac{q_{ic,3}}{C_{p_{liq\,H_2O}(20-10)}} \frac{q_{ic,3}}{C_{p_{liq\,H_2O}(20-10)}} \quad \textbf{(6-28)}$$

Compressor model:

Compressors are used to pressurize hydrogen up to 350 bar from 1.01325 bar. This is consistent with the literature [41]. The total number of intercooling and compression stages is 3. This is determined from [41], which states that additional stages (N) are needed when the pressure ratio (r_p) exceeds seven in the following equation:

$$r_p = \left(\frac{P_{out}}{P_{in}}\right)^{1/N} \left(\frac{P_{out}}{P_{in}}\right)^{\frac{1}{N}} \quad \textbf{(6-29)}$$

Where P_{out} is the pressure at the outlet of the compressor and P_{in} is the pressure at the entrance of the compressor.

The work ($\dot{w}_{compressor}$) of the compressor is determined using:

$$\dot{w}_{compressor} = \dot{n}\frac{kR(T_{out}-T_{in})}{k-1} = \dot{n}\frac{kRT_{in}}{k-1}\left(\left(\frac{p_{out}}{p_{in}}\right)^{\frac{k-1}{k}} - 1\right) \quad \textbf{(6-30)}$$

Where $\dot{n}$ is the flowrate of the fluid entering the compressor; $k = 1.405$ for H_2; R is the gas constant, and T is the temperature at the inlet (in) and outlet (out).

Based on the partial pressure of water at state 16, the model can estimate the desired temperature at the outlet of the condenser (state 23) from the saturation temperature that corresponds to the partial pressure of water at state 23. For a current of 90 Amps, with 70% steam utilization, $x_{H_2O} = 0.27$ at state 19, the partial pressure at state 23 will be 27 kPa, which corresponds to a saturation temperature of approximately 70°C.

Thus, equation $\boldsymbol{wcompressor} = \dot{n}\frac{kR(T_{out}-T_{in})}{k-1} = \dot{n}\frac{kRT_{in}}{k-1}\left(\left(\frac{p_{out}}{p_{in}}\right)^{\frac{k-1}{k}} - 1\right)$ **(6-30)**

can be rearranged to determine T_{out}:

$$T_{out} = T_{in} + T_{in}\left(\left(\frac{p_{out}}{p_{in}}\right)^{\frac{n-1}{n}} - 1\right)$$

Where the actual work of the compressor is found using the following equation:

$$\dot{w}_{compressor,actual} = \frac{\dot{w}_{compressor}}{\eta_{comp}} \quad \textbf{(6-31)}$$

Steam generator

The energy required for the steam generator is the energy required to raise the temperature of the water to the steam generator temperature plus the energy for the phase change (latent heat), which is given in (6-25).

An alternative form to find the energy required to preheat the seawater ($\dot{q}_{H_2O,1}$) can be found using enthalpies instead of heat capacities. The sensible energy that is necessary to raise the temperature of seawater to the steam generator temperature is given by:

$$\dot{q}_{H_2O,1} = \dot{n}_{H_2O} * \left(h_{H_2O}(T_{SG}) - h_{H_2O}\left(T_{intercooler,cold\ out}\right)\right)\left(h_{H_2O}(T_{SG}) - h_{H_2O}\left(T_{intercooler,cold\ out}\right)\right)$$

(6-32)

The energy required for changing the phase of the seawater, $\dot{q}_{H_2O,2}$, (Latent heat of energy) is found using:

$$\dot{q}_{H_2O,2} = \dot{n}_{H_2O} * \left(h_{lat_{H_2O}}(steam\ gen)\right) \quad \textbf{(6-33)}$$

where $h_{lat_{H_2O}}$ is the latent heat of water at 100°C.

Combining sensible and latent heat energies:

$$\dot{q}_{steamgen} = \dot{n}_{H_2O}\left(\left(h_{H_2O}(T(SG) - h_{H_2O}\left(T_{intercooler,cold\ out}\right)\right) + \left(h_{lat_{H_2O}}(T_{SG})\right)\right)$$

$$= \dot{n}_{H_2O}\left(\left(C_{p_{H_2O,liq}}\left(T_{SG} - T_{intercooler,cold\ out}\right)\right) + h_{lat_{H_2O}}(T_{SG})\right)$$

(6-34)

The steam generator is modeled as a heat exchanger where its cold input is the stream at the outlet of the intercoolers. The outlet of the steam generator (state 10) is also the cold inlet of the heat exchanger that supplies the hot inlet to the steam generator. For this reason, an iteration is required to determine a steam generator outlet temperature that allows both sets of equations to converge.

The steam generator is modelled similarly to the intercooler, where the latent heat, quality of the inlets, and an effectiveness are considered. When the thermal energy available from the stack outlet is insufficient to provide enough energy for the steam generator, an additional heater in the steam generator turns on which provides the necessary sufficient heating. It is assumed that this heater provides the additional heating necessary for complete phase change of the water.

Stack

The governing thermal balance equation of the stack is given by:

$$\dot{Q} + \dot{W}_{stack} = \sum \dot{n_p} * h_p - \sum \dot{n_r} * h_r = \frac{i}{2F} * n_{cell} * h_{rxn}(T)$$

(6-35)

Where $\dot{Q}$ is the heat consumed or rejected, depending on the operating conditions and the stack; $\dot{W}_{stack}$ is the stack power; $\dot{n_p} * h_p$ is the moles of each product multiplied by the corresponding enthalpy; $\dot{n_r} * h_r$ is the moles of the reactants multiplied by the corresponding enthalpy; i is the operating current; F is the Faraday constant; n_{cell} is the number of cells (1000); and $h_{rxn}(T)$ is the enthalpy of the reaction.

The stack power can be found using:

$$\dot{W}_{stack} = V * i * n_{cell} \quad \textbf{(6-36)}$$

Where V is the operating voltage of the cells.

Since the system can operate under thermoneutral conditions, the thermoneutral voltage (V_{tn}) is:

$$V_{tn} = \frac{h_{rxn}}{2F} \quad \textbf{(6-37)}$$

Where the heat of the reaction, h_{rxn}, which is a function of temperature, is given by:

$$h_{rxn}(T) = \left(h_{H_2,T} - h_{H_2,298}\right) + \frac{1}{2}\left(h_{O_2,T} - h_{O_2,298}\right) - \left(h^o_{f,H_2O} - \left(h_{H_2O,T} - h_{H_2O,298}\right) - h_{fg}\right) \quad \textbf{(6-38)}$$

Where $h_{H_2,T}$ and $h_{O_2,T}$ are the enthalpy of the hydrogen and oxygen, respectively, at the operating temperatures; $h_{H_2,298}$ and $h_{O_2,298}$ are the enthalpy of the hydrogen and oxygen, respectively, at standard conditions; h^o_{f,H_2O} is the enthalpy of formation of the steam; and $h_{fg}$is the latent heat of steam.

Therefore, combining these equations, the total heat rejected or consumed by the stack $\left(\dot{Q}_{stack}\right)$ will be found by the difference in the thermoneutral voltage and the operating voltage:

$$\dot{Q}_{stack} = \frac{i}{2F} * n_{cell} * h_{rxn}(T) - V * i * n_{cell} = i * n_{cell} * \left(\frac{h_{rxn}(T)}{2F} - V\right) = i * n_{cell} * (V_{tn} - V) \quad \textbf{(6-39)}$$

If $V > V_{tn}$, then $\dot{Q} < 0$, and the stack will operate under exothermic conditions. Conversely, if $V < V_{tn}$, then $\dot{Q} > 0$, and the stack will operate under endothermic conditions.

The stack outlet temperatures (T_{14}) have various implications for the degradation of the stack and the model. First, a large temperature gradient between the inlet (T_{13}) and the outlet of the stack will result in deleterious material challenges. Additionally, the temperatures also play a significant role in determining the excess stack heat that is available in the heat exchangers for the balance of plant and will depend largely on the thermal mode of the stack. The model used

conservation of energy principles for a steady state system to assess endothermic, thermoneutral and exothermic cases:

$$\dot{Q}_{net} + \dot{W}_{net} = \sum \dot{n_p} * h_p - \sum \dot{n_r} * h_r \quad \textbf{(6-40)}$$

$$\sum \dot{n_p} * h_p\,(T) = \sum \dot{n_r} * h_r(T) + \dot{W}_{Stack} - \frac{i}{2F} n_{cell} h_{rxn}(T) - \dot{Q}_{Loss} \quad \textbf{(6-41)}$$

Where $\dot{Q}_{Loss}$ is the heat lost due to heat transfer from the hotbox to the surroundings. The energy of the products and the reactants is found using the following equations:

$$\sum \dot{n}_p * h_p = \dot{n}_{H_2} h_{H_2}(T_{14}) + \dot{n}_{H_2O} h_{H_2O}(T_{14}) + \dot{n}_{O_2} h_{O_2}(T_{14}) + \dot{n}_{Air} h_{Air}(T_{14}) \quad \textbf{(6-42)}$$

$$\sum \dot{n}_r * h_r = \dot{n}_{H_2} h_{H_2}(T_{13}) + \dot{n}_{H_2O} h_{H_2O}(T_{13}) + \dot{n}_{Air} h_{Air}(T_{13}) \quad \textbf{(6-43)}$$

For the endothermic and thermoneutral cases, the outlet temperature is equal to the stack setpoint temperature. In the endothermic scenario, the assumption is that the optional heater in the hot box of the electrolyzer provides the thermal energy required for the endothermic reactions. In the thermoneutral case, the heater is not necessary since the reactions provide the necessary thermal energy for the entirety of the length of the cells.

The exothermic scenarios required careful consideration due to elevated temperatures. Two approaches were considered for the exothermic analysis: (1) the first approach represented an ideal scenario in which the material limitations due to temperature gradients were ignored; (2) the second approach considered a constrained temperature difference between the inlet and the outlet temperature that was limited by a maximum allowable current to account for the potential deleterious impacts of high temperature gradients on the materials.

The model uses an equation solver (using Scipi's *fsolve*) to calculate the temperature of the outlet streams of the stack to solve the energy balance of the stack. In the second approach, the

maximum temperature gradient between the inlet streams and the outlet streams is set to 100 K. This limits the operating current range of the system in exothermic operation.

Electric Heater:

$$\dot{w}_{heater} = \frac{\dot{m}_{12}(h_{out} - h_{in})}{\eta_{heater}} \quad \textbf{(6-44)}$$

Where the work of the heater is $\dot{w}_{heater}$, the mass flow rate of the

Three-way valve (only one inlet and outlet at a time)

$$\dot{m}_{in} h_{in} = \dot{m}_{out} h_{out} \quad \textbf{(6-45)}$$

$$\dot{m}_{in} = \dot{m}_{out} \quad \textbf{(6-46)}$$

$$h_{in} = h_{out} \quad \textbf{(6-47)}$$

Mixing Valve/ Ejector

The ejector and the mixing valve in states 11, 12, and 16 and 3,4 and 5, respectively, are modelled similarly, assuming the principles of an ideal gas in which the enthalpy change of an isothermal expansion process is zero. The ejector provides a mixture of steam and hydrogen so that the inlet of the cathode is composed of a mixture of 10% hydrogen and 90% steam. The enthalpy of the mixture of the two species can be found using the following:

$$\dot{n}_{in,1} h_{in,1} + \dot{n}_{in,2} h_{in,2} = \dot{n}_{out} h_{out} \quad \textbf{(6-48)}$$

Where $\dot{n}_{in,1}$ is the inlet molar flowrate of Stream 1 of the ejector/ mixer; $\dot{n}_{in,2}$ is the inlet molar flowrate of Stream 2 of the ejector/ mixture; $h_{in,1}$ is the enthalpy of Stream 1; $h_{in,2}$ is the enthalpy of stream 2; $\dot{n}_{out}$ is the molar flowrate out of the ejector; and h_{out} is the flowrate of the stream existing the ejector.

The molar flowrates of the ejector are key to determining the required inlet seawater flowrates. The molar flowrates are found using a set of molar balance expressions:

$$\dot{n}_{H_2O,12} = \frac{i}{2Fu_f} n_{cell} \quad \textbf{(6-49)}$$

$$\dot{n}_{H_2O,13} = \dot{n}_{H_2O,12} \quad \textbf{(6-50)}$$

$$\dot{n}_{H_2O,14} = \dot{n}_{H_2O,13} - \frac{i}{2F} n_{cell} \quad \textbf{(6-51)}$$

$$x_{H_2,13} = 0.10 \quad \textbf{(6-52)}$$

$$x_{H_2O,13} = 0.90 \quad \textbf{(6-53)}$$

$$\dot{n}_{13} = \frac{\dot{n}_{H_2O,12}}{x_{H_2O,12}} \quad \textbf{(6-54)}$$

$$\dot{n}_{12} = \dot{n}_{13} \quad \textbf{(6-55)}$$

$$\dot{n}_{H_2,13} = x_{H_2,13}\dot{n}_{13} \quad \textbf{(6-56)}$$

$$\dot{n}_{H_2,14} = \dot{n}_{H_2,13} + \frac{i}{2F} n_{cell} \quad \textbf{(6-57)}$$

$$\dot{n}_{H_2,15} = \dot{n}_{H_2,12} \quad \textbf{(6-58)}$$

Where n_{cell} is the number of cells in the stack; $u_f$is the utilization factor (0.75); i is the operating current; $\dot{n}_{H_2O,12}$ is the flowrate of steam that enters the optional preheater from the ejector; $\dot{n}_{H_2O,13}$ is the molar flowrate of the steam that enters the stack; $\dot{n}_{H_2O,13}$ is the steam flowrate the exits the stack; $\dot{n}_{13}$ represents the stack inlet stream mixture that is comprised of 10% hydrogen ($x_{H_2,11}$) with 90% steam ($x_{H_2O,11}$) by volume; $\dot{n}_{15}$ represents the mixture of steam and hydrogen is recycled at the stack outlet, which enters the ejector.

Condenser

The hydrogen-water liquid separator (points 22 and 23) is modelled as a heat exchanger, where the cooling is provided from the ocean water. The separation occurs at the saturation pressure of steam at its partial pressure in the mixture. For a system with 70% steam utilization, the partial pressure of H_2O is 27 kPa, which has a corresponding saturation temperature of approximately 70°C. The thermal energy (q_{cond}) available between the hot stream and the cold stream is determine using:

$$q_{cond} = \epsilon \dot{n} Cp(T_{high} - 10^o C) \quad \textbf{(6-59)}$$

Where T_{high} is the temperature of the steam generator hot outlet stream; ϵ is the effectiveness of the condenser; $\dot{n}$ is the molar flowrate; and Cp is the heat capacity. The number of cooling stages is determined by:

$$n_{cond} = \frac{q_{cooling}}{q_{cond}}$$

(6-60)

Where $q_{cooling}$ is the cooling required to cool the hydrogen and water to 70ºC and to change the phase of water from vapor to liquid.

Brine Management

The molar flowrate of seawater ($\dot{n}_{seawater}$) needed is given by:

$$\dot{n}_{seawater} = \frac{i}{2Fu_f} * n_{cell}$$

(6-61)

Where u_f is the utilization factor and F is Faraday's constant (96,845).

The mass flowrate of brine ($\dot{m}_{brine}$) generated is given by:

$$\dot{m}_{brine} = \dot{m}_{seawater} * \frac{tds_{sw}}{tds_{br}}$$

(6-62)

Where $\dot{m}_{seawater}$ is the mass flowrate of seawater and tds represents the parameter for total dissolved solids in the seawater (sw) and brine (br). The values of tds_{sw} and tds_{br} are 35.165 g/kg and 120g/kg [41].

6.2.2 **Heat Transfer Analysis**

The heat transfer analysis in this model is based on the work conducted in reference [113]. First, the analysis begins by developing a schematic of a hot box (see Figure 6-5), which is the thermally insulated box that encloses the stack, heating elements, and other supporting components [119]. The hot box schematic is used to develop an equivalent thermal circuit of

each of the major resistances. Starting with Region I, an equation for the total thermal resistance (R_{total}) for heat transfer is defined as:

$$R_{total} = \frac{1}{(h_{air} + h_{rad})A_I} + \frac{\Delta x_{insulation}}{K_{insul,mean}(T)A_{III}} + \frac{1}{(h_{air} + h_{rad})A_{III}} + \frac{\Delta x_{cabinet}}{K_{steel}(T)A_{IV}} + \frac{1}{(h_{wind} + h_{wind,rad})A_V} \quad \textbf{(6-63)}$$

Where each of the terms is described next:

- h_{air} is the heat transfer coefficient of air due to natural convection.
- h_{rad} is the radiation coefficient of air.
- A_I is the surface area of Region I.
- $\Delta x_{insulation}$ is the thickness of the insulation.
- $K_{insul,mean}$ is the thermal conductivity coefficient of the insulation.
- A_{III} is the surface area of Region II.
- $\Delta x_{cabinet}$ is the thickness of the cabinet.
- $K_{steel}(T)$ is the thermal conductivity coefficient of steel.
- A_{IV} is the surface area of Region IV.
- h_{wind} is the forced convection heat transfer coefficient of wind.
- $h_{wind,rad}$ is the radiation heat transfer coefficient of wind.
- A_V is the surface area of Region V.

The total thermal resistance is then used to find the total heat transfer from the stack to the environment ($\dot{Q}_{heat\ loss}$):

$$\dot{Q}_{heat\ loss} = \frac{T_{Surr} - T_{stack}}{R_{total}} \quad \textbf{(6-64)}$$

Where T_{Surr} and T_{stack} refers to the surrounding temperature and the stack temperature, respectively.

The analysis relies on the following assumptions:

- The temperature of the surrounding air (T_{Surr}) ranges from 4 to 20 °C. This is based on data from NREL for Humboldt (see Figure 6-6).
- The stack is isothermal and therefore any temperature gradients are neglected.
- Quiescent air fills the space between the components, which refers to region II and IV.
- The total distance between the layers in region II and IV is one centimeter.
- The analysis assumes the stack has an emissivity value equivalent to aluminum foil (0.1), since the emissivity needs to be as low as possibility to limit the heat lost through radiation [113] .
- According to [113], high performance insulation has a microporous structure in which the heat flux through the material involves radiation and convection in the pores and conduction through the solid material. Since conduction is the dominant mode of heat transfer at low temperatures and radiation is the dominant mode at high temperatures, the heat transfer through the insulation can be approximated as [113]:

$$\dot{Q}_{insulation} = -\frac{K_{mean}(T)A\left(T_{insul,2}-T_{insul,1}\right)}{\Delta x} \quad \textbf{(6-65)}$$

Where K_{mean} is [113]:

$$K_{mean}(T) = K_{conduction} + K_{radiation}T_{mean}^{3} \quad \textbf{(6-66)}$$

In order to calculate the average convection heat transfer coefficient in region VI of the schematic, the following equations and definitions were used:

$$\bar{h}_{wind} = \frac{\overline{Nu}*K}{x} \quad \textbf{(6-67)}$$

Where the average Nusselt number can be found from the follow relation for turbulent flow with a Prandtl number greater than 0.6 and less than 60 [117]:

$$\overline{Nu} = \left(0.037 * Re_{L}^{\frac{4}{5}}\right)\mathrm{Pr}^{\frac{1}{3}} \quad \textbf{(6-68)}$$

Figure 6-4 shows the dependence of the heat transfer coefficient on wind speed.

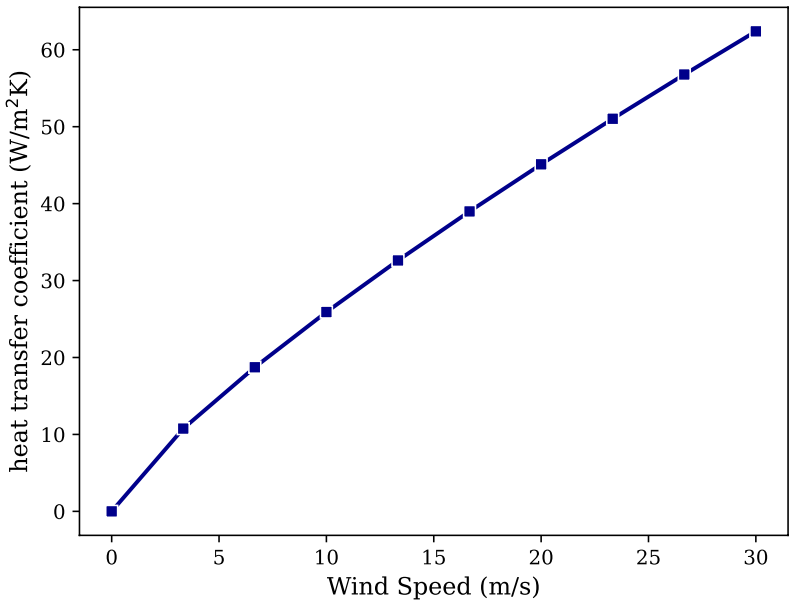

Figure 6-4: Convective heat transfer coefficient as a function of wind speed

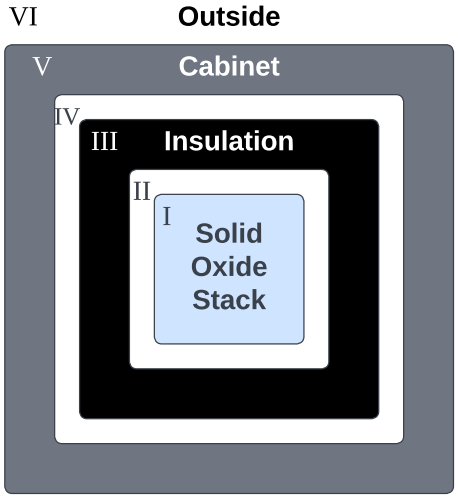

Region	Process	Temperature
I	Conduction and Convection	T_{Stack}
II	Free Convection & Radiation	T_{Stack} and $T_{Insul,1}$
III	Conduction and Radiation (Convection is negligible)	$T_{Insul,1}$ and $T_{Insul,2}$
IV	Free Convection & Radiation	$T_{Insul,2}$ and $T_{Cab,1}$
V	Conduction	$T_{Cab,1}$ and $T_{Cab,2}$
VI	Free Convection & Radiation	$T_{Cab,2}$ and T_{Surr}

Figure 6-5: Schematic of the hot box and the corresponding heat transfer processes

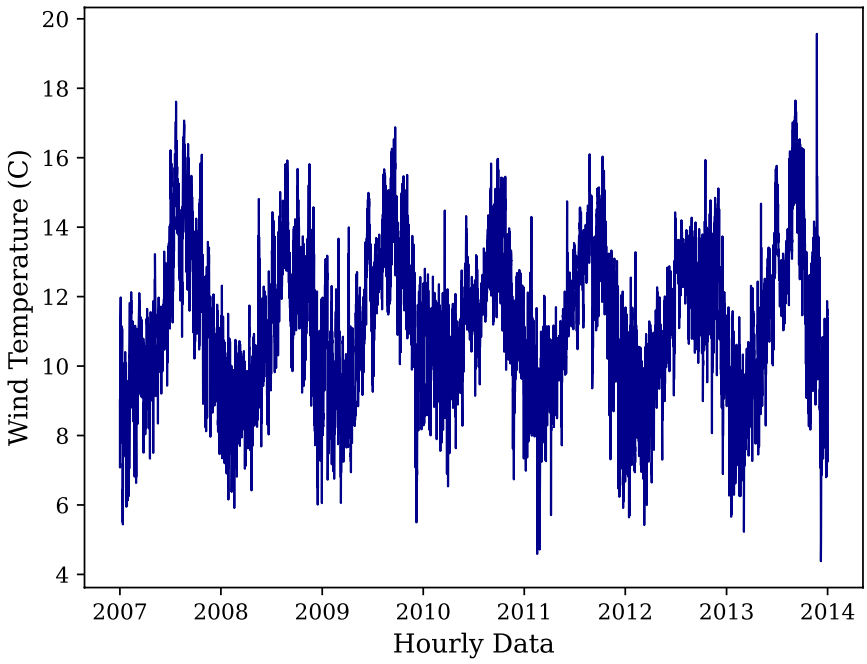

Figure 6-6: Hourly wind temperature in the offshore site near Humboldt. Data from [90]–[92]

Table 6-3: Material properties for the heat transfer analysis

Property	Value	Ref
Emissivity of stack (ε)	0.1	[113]
Stefan-Boltzmann constant ($Wm^{-2}K^{-4}$)	$5.67 * 10^{-8}$	n/a
$K_{insulation}$ ($Wm^{-1}K^{-1}$)	0.18	[114]
$K_{radiation,\ insulation}$ ($Wm^{-1}K^{-4}$)	$7*10^{-12}$	[113]
K_{steel} ($Wm^{-1}K^{-1}$)	20	[113]
K_{air} ($Wm^{-1}K^{-1}$)	0.0263	[117]
$h_{free\ air}$ ($Wm^{-2}K^{-1}$)	10	[113]
$h_{rad,\ air}$ ($Wm^{-2}K^{-1}$)	3	[113]
h_{wind} ($Wm^{-2}K^{-1}$)	0-65	* for wind speeds from 0-30 m/s

$\mathbf{Pr_{air}}$	0.707	[117]
$\boldsymbol{\mu_{Air}}$ **(N s m^{-2})**	184.6 * 10^{-7}	[117]
$\boldsymbol{\rho_{air}}$ **(Kg m^{-3})**	1.1614	[117]
$\boldsymbol{c_{p_{air}}}$ **(Kg m^{-3})**	1.007	[117]
$\boldsymbol{\Delta x_{insulation}}$ **(m)**	0.3	[114]
$\boldsymbol{\Delta x_{cabinet}}$ **(m)**	0.05	[113]
$\boldsymbol{\Delta x_{II}}$ **(m)**	0.01	n/a
$\boldsymbol{\Delta x_{IV}}$ **(m)**	0.01	n/a

The total heat generated and consumed in the stack is:

$$Q_{total} = Q_{ohmic} + Q_{activation} + Q_{concentration} + Q_{reaction} + Q_{environment}$$
$$= Q_{polarization} + Q_{reaction} + Q_{environment} \quad \textbf{(6-69)}$$

Where $Q_{ohmic} + Q_{activation} + Q_{concentration}$ refers to the sum of irreversible heat losses ($Q_{polarization}$) due to ohmic, activation, and concentration polarizations in the stack. $Q_{reaction}$ refers to the heat consumed during the reaction, and $Q_{environment}$ refers to the heat lost to the environment through heat transfer. If the total amount of irreversible heat losses (Q_{loss}) exceeds $Q_{reaction}$, then the system is operating in exothermic mode, and there is a net generation of heat. The excess heat can be used for further preheating of the inlet streams to the stack and for steam generation.

Since the total heat lost to the environment is a function of the surrounding air temperature and the wind speed, a sensitivity analysis was conducted to understand that impact of these factors. The sensitivity analysis in Figure 6-7 - Figure 6-9 reveals that the total heat loss is strongly dependent on the wind temperature, wind speed, and insulation thickness. Figure 6-7, analyzes the total stack heat loss according to wind speed and wind temperature. Figure 6-8 shows the impact of the stack temperature on the overall heat loss. The heat loss is minimized at lower stack temperatures and high wind temperatures, and it is maximized at high stack temperatures

and low wind temperatures. Under the assumptions in this section, the overall heat loss is low, and it reaches a maximum value of approximately 1.25 kW at the highest stack temperature (1000 ^{o}C) and at the intersection of the highest wind speed (25 m/s) and lowest temperature (0^{o}C). This heat loss estimate is consistent with what has been previously reported in the literature. In [114], the authors report that a popular design parameter for commercial scale systems is to set the temperature of the outer surface of the insulation to 353 K. When this design parameter is employed in the current system a similar heat loss is calculated: 1.10 kW. For the remainder of this study, the model will assume an average wind temperature of 11.3^{o}C for the wind, which is the mean temperature in Figure 6-6.

Furthermore, in Figure 6-4, the heat transfer coefficient is presented as a function of wind speed. At the maximum wind speed in the dataset (approximately 30m/s), the heat transfer coefficient reaches a value of 65 W/m^{2}K. Additionally, the Figure 6-9 shows the that the heat loss is strongly dependent on the insulation thickness. Whereas the insulation thickness used in this study (0.3m) results in minimal heat losses, without insulation the system would be losing over 16kW of heat.

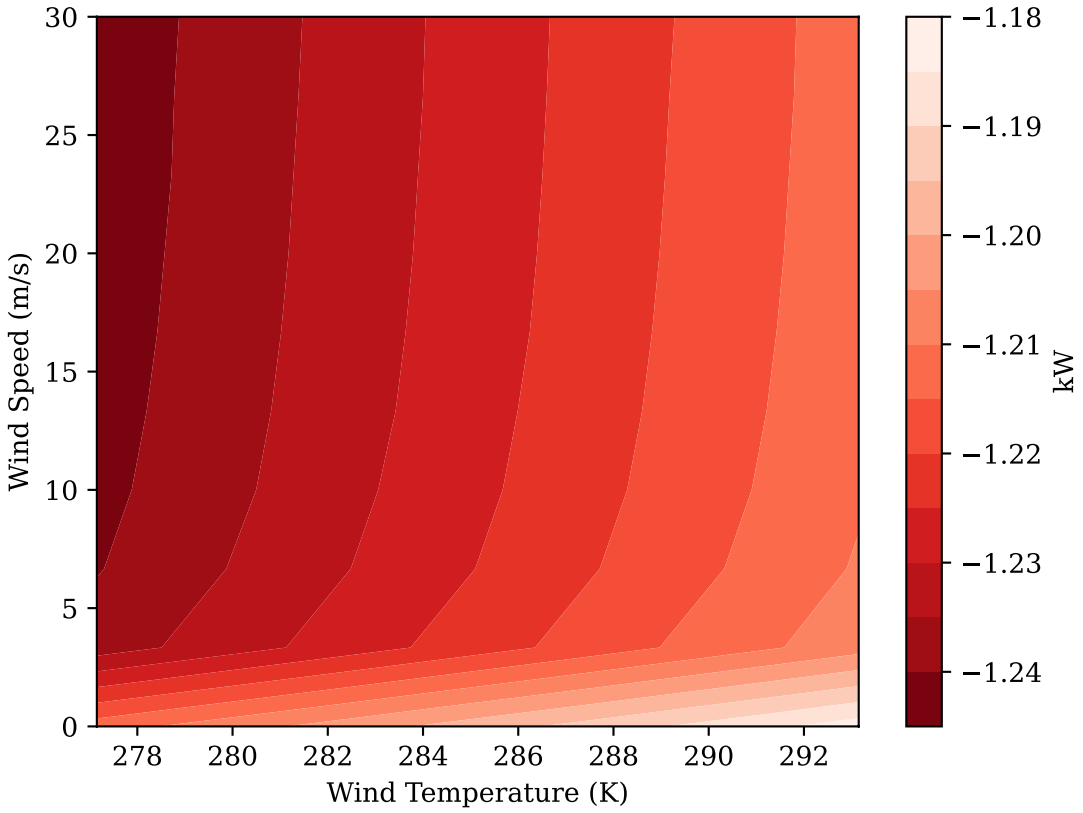

Figure 6-7: Sensitivity analysis on the total heat loss from the stack for a stack temperature of 850°C

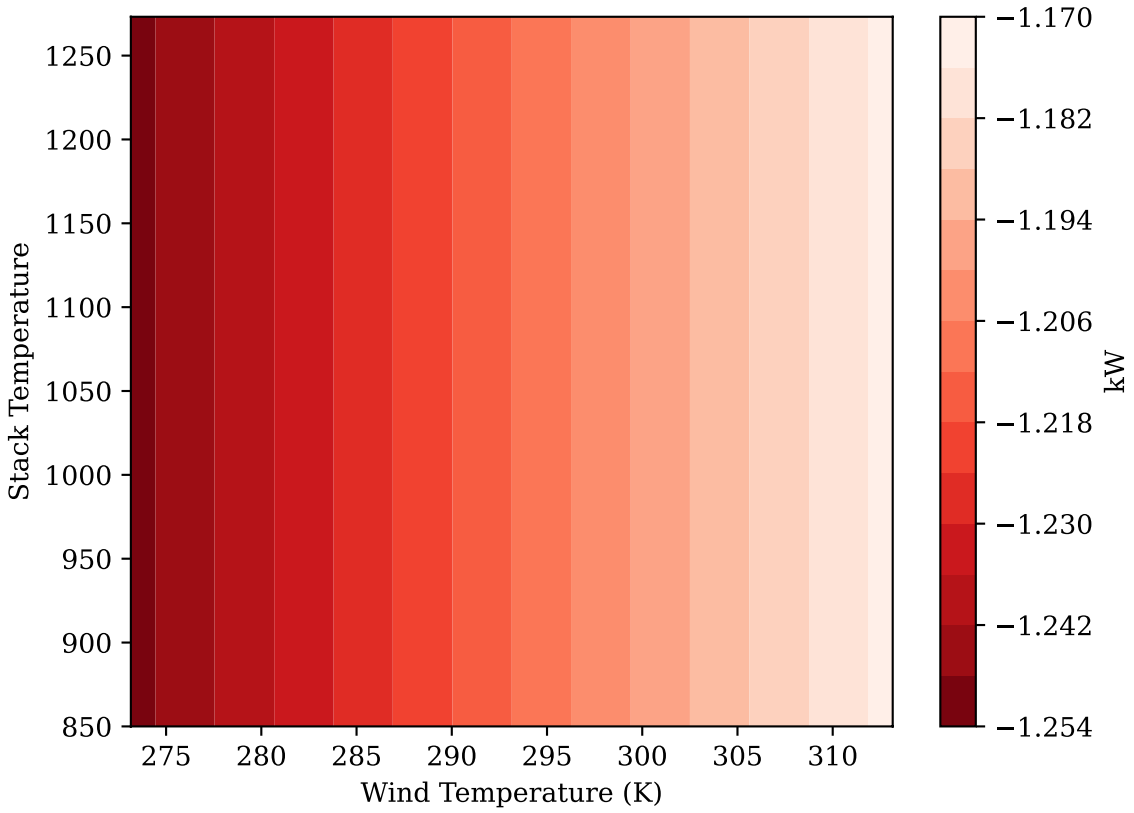

Figure 6-8: Sensitivity analysis of the stack temperature and wind temperature on the total heat loss

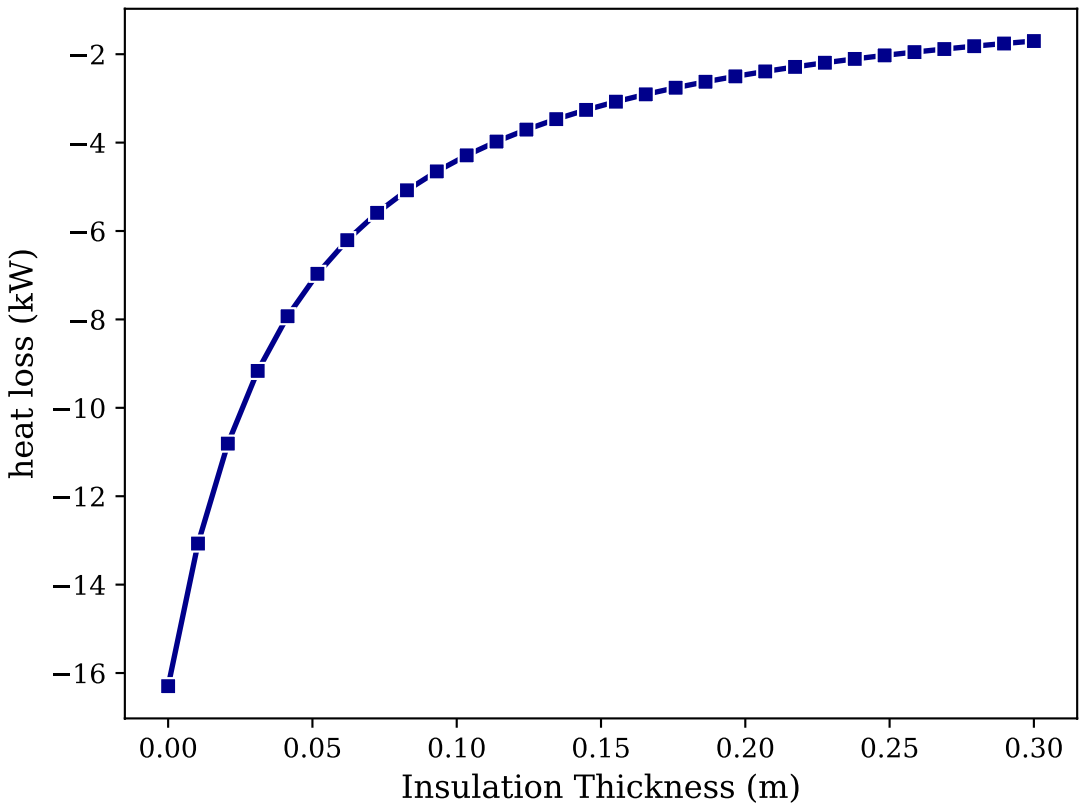

Figure 6-9: Heat loss as a function of insulation thickness

6.2.3 Hot Standby Mode

In order to prepare for periods where there may be an interruption in the electricity supplied to the stack, like periods when the wind speed is too low or too high for the turbines to operate, the system design includes a hot standby mode of operation to avoid thermal cycling of the stack. This type of standby mode of operation is a common control strategy used in SOECs (e.g. [112], [120], [121]), in which the SOEC is operated reversibly in fuel cell mode to maintain the stack at the operating temperature. This is an important mode to prevent degradation from thermal cycling, and to allow the stack to resume electrolysis as soon as electricity is available. In reversible SOC cells, heat is generated when the cells are operated in galvanostatic mode (fuel cell mode). Therefore, to maintain the stack temperature and to prevent shutdown, the stack will produce 0.5 kW in idle mode [112]. Interpolating the polarization curve in electrolysis mode revealed that the corresponding current and voltage is 0.08 amps and 0.9761 volts to generate 0.546 kW of power. In this mode, the stack consumes 1.19×10^{-6} and 4.74×10^{-6} g/sec of

hydrogen and oxygen respectively, with. Utilization ratios of 70%. Therefore, the system will use the air compressor to supply the oxygen required during standby operation. This amount of hydrogen is 8.826 x 10^{-6} % of the total hydrogen produced at the design point. In order to prepare for periods where there may be an interruption in the electricity supplied to the stack, like periods when the wind speed is too low or too high for the turbines to operate, the system design includes a standby mode of operation to avoid shutting down the stack. Standby mode of operation is a common control strategy used in SOECs (e.g. [112], [120], [121]), in which the SOEC is operated reversibly in fuel cell mode to at the operating temperature. This is an important mode to prevent degradation from thermal cycling, and to allow the stack to resume electrolysis as soon as electricity is available. In reversible SOC cells, heat is generated when the cells are operated in galvanostatic mode (fuel cell mode). Therefore, to maintain the stack temperature and to prevent shutdown, the stack will produce 0.5 kW in idle mode [112]. Interpolating the polarization curve in electrolysis mode revealed that the corresponding current and voltage is 0.08 amps and 0.9761 volts to generate 0.546 kW of power. In this mode, the stack consumes 1.19 x 10^{-6} and 4.74 x 10^{-6} g/sec of hydrogen and oxygen respectively, with. Utilization ratios of 70%. Therefore, the system will use the air compressor to supply the oxygen required during standby operation. This amount of hydrogen is 8.826 x 10^{-6} % of the total hydrogen produced at the design point.

6.3 **Model results**

6.3.1 **SOE Stack Results**

The model is used to explore the system performance, thermodynamics, and the potential offshore wind dynamics of the system. First, the model examines the impact of temperature and current on the overall operating conditions of the system. Because of the unique thermodynamics such as the ability of the system to operate in endothermic and exothermic mode, the system has can meet its thermal demand in various ways: (1) the system can use the stacks surplus thermal energy from its electrochemical losses; (2) the system can use secondary subsystems such as heaters to generate the steam and to provide enough heating for superheating the steam to the furnace temperature. The amount of excess heat available from the stack will depend on its operating temperature and current density. While the stack's thermoneutral voltage is only a function of temperature (see Figure 6-10), the stack's operating voltage will increase with current

and decrease with temperature. Figure 6-11 maps these relationships onto a contour plot. The stack voltage is the highest at the location where the current is the highest and the temperature is the lowest (bottom right corner). This is because high currents and low temperatures result in higher losses: higher currents increase the concentration losses from the cell and higher temperatures increase the ohmic losses from the cell. The increase in stack voltage is directly correlated to the efficiency of the stack, which will also increase with current if temperature is held constant (see Figure 6-11). This has important implications for the platform. While operating the stack at a voltage greater than the thermoneutral voltage will result in a lower stack efficiency, it also means that the system overall will have a lower or near zero thermal load.

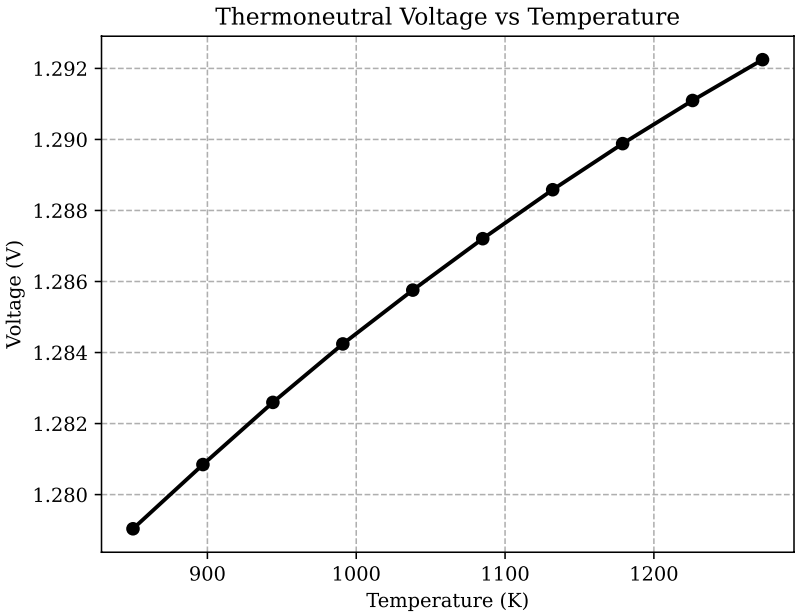

Figure 6-10: Stack thermoneutral voltage increases nearly linearly with stack temperature

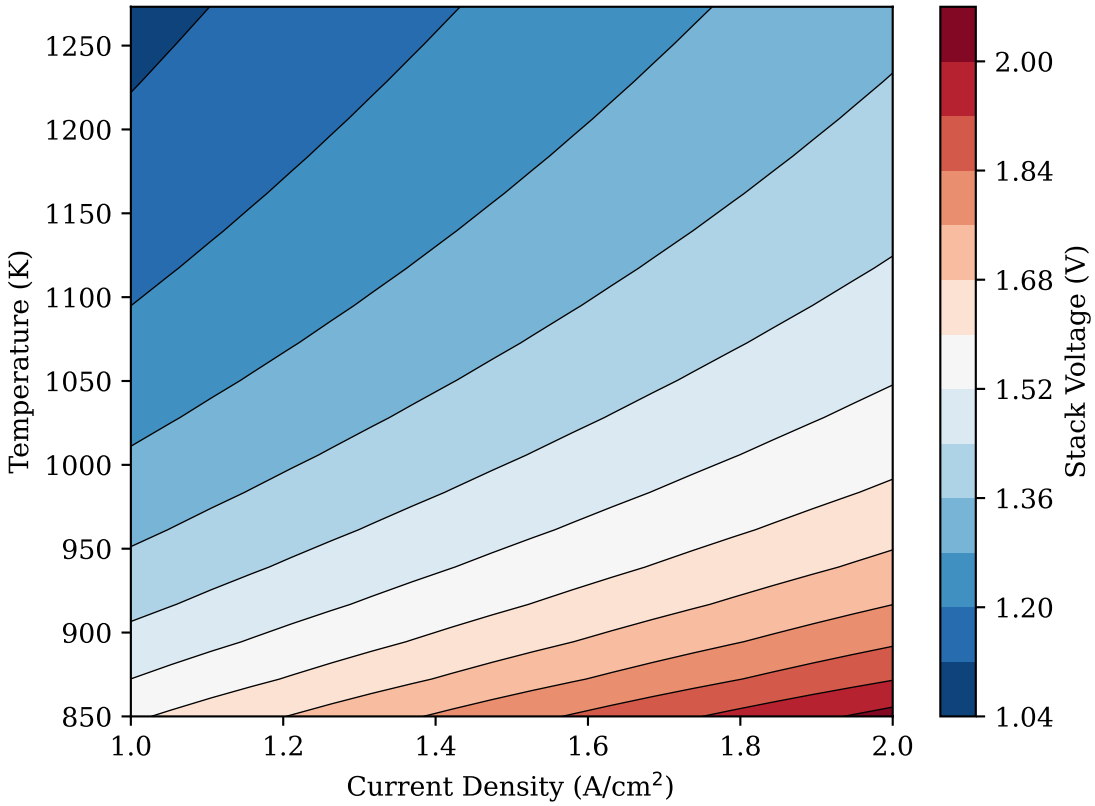

Figure 6-11: Stack voltage as a function of temperature and current density

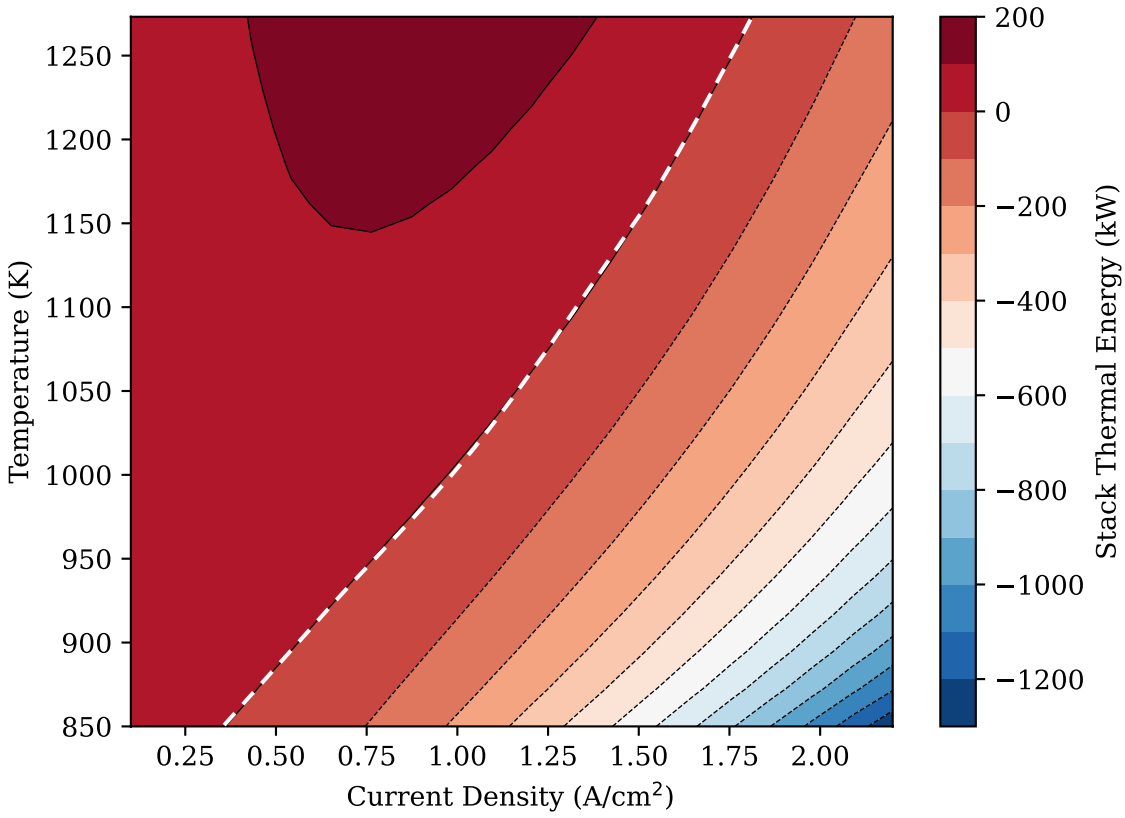

Figure 6-12: Thermal operating conditions of the stack

Figure 6-12 maps the thermal operating conditions of the stack as a function of current and temperature. Negative values indicate the stack is operating exothermically, while positive values indicate it is operating endothermically. The white dashed line indicates thermoneutral conditions, where the stack thermal regime is equivalent to $Q_{SOEC} = 0$ kW, and the voltage is the thermoneutral voltage. The stack thermoneutral voltage is only a function of temperature, as shown in Figure 6-10. An increase in temperature signifies an increase in the thermoneutral voltage, which is met with an increase in the endothermicity of the stack. In other words, for a constant operating current, an increase in stack temperature decreases the losses, and thus Q_{SOEC} becomes more positive and endothermic, which means there is less excess net heat available for the system. These interesting features of the SOEC system suggest there is an optimal operating condition (voltage and current) for each operating temperature that supplies enough excess energy to meet the thermal demands of the system. Operating in the endothermic regime will

require additional auxiliary equipment to maintain the stack temperature and for generating the steam and preheating the inlet streams to the stack. Conversely, operating in the exothermic regime will reduce the overall external thermal load of the system, but will result in higher electrochemical losses, and thus a lower stack efficiency. Additionally, Figure 6-12 also illustrates that polarization increases with increasing current. This is consistent with the polarization curves of electrochemical systems that show concentration polarization becomes exponentially more significant with increasing current.

At each of the possible operating conditions illustrated in Figure 6-12, there is a specific thermal demand for steam generation. As the current density increases, the energy required to preheat the inlet seawater, convert it to the gaseous phase, and superheat it to the stack operating temperature will proportionally increase, resulting in a higher thermal energy demand. Additionally, with an increase in the stack operating temperature, more thermal energy will be needed to superheat the steam to the stack's operating temperature. Figure 6-13 shows the balance of plant gross thermal

demand. It clearly demonstrates the proportional increase in demand as the stack current and temperature rise.

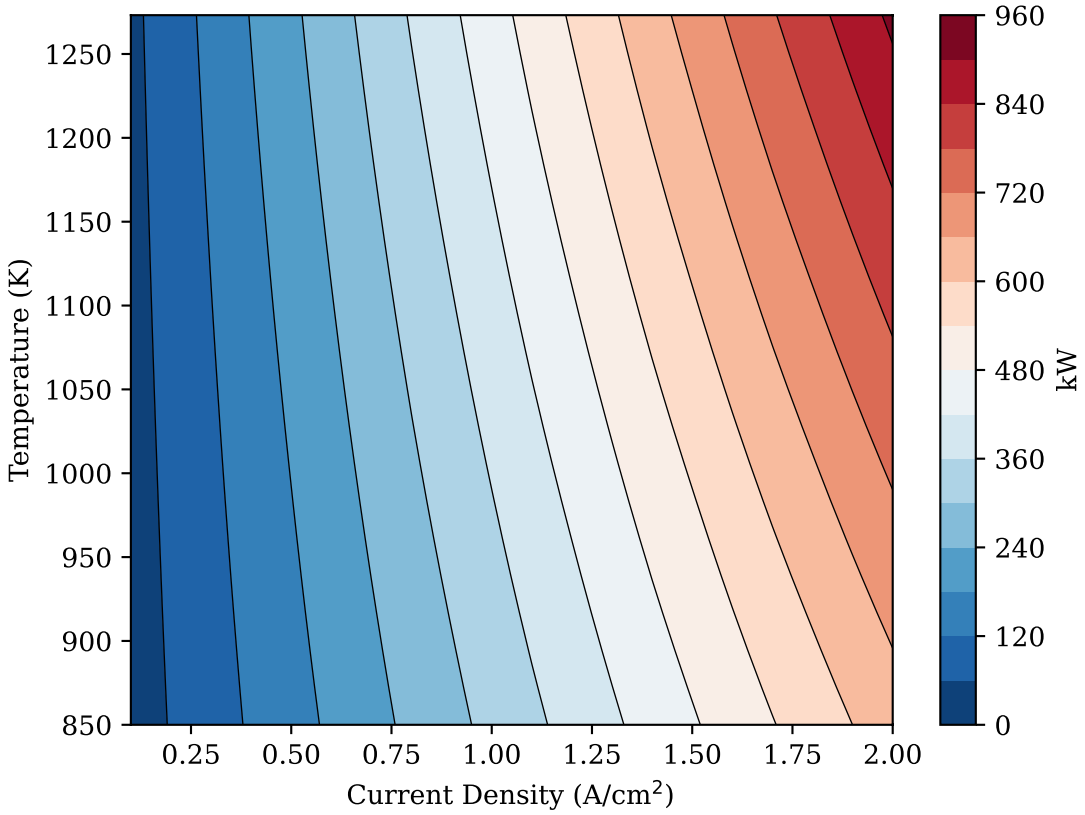

Figure 6-13: Balance of Plant gross thermal demand in kW.

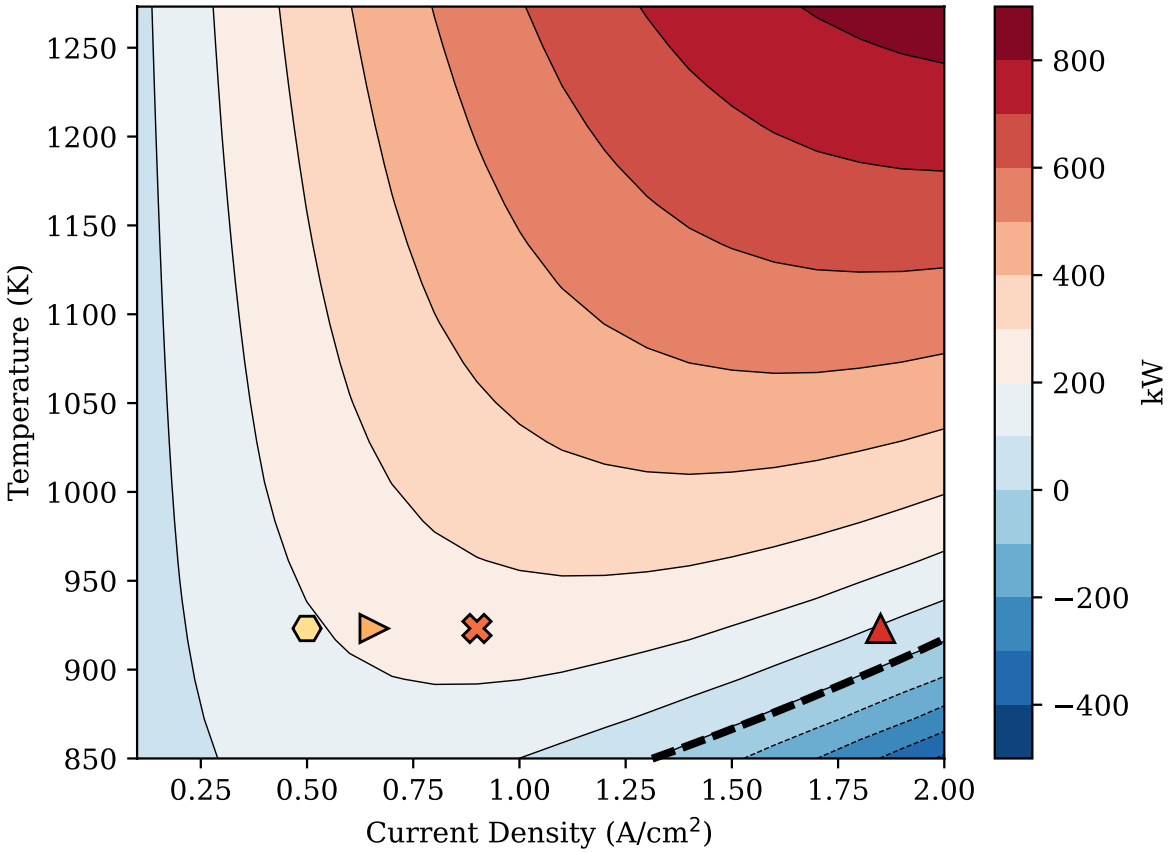

Figure 6-14: Net system thermal energy after accounting for the energy required for steam generation, superheating the steam, preheating the inlet air stream, and heat loss

The endothermicity of a system is directly related to the system's energy demand. In Figure 6-14, the net system thermal energy is plotted with respect to the stack operating temperature and the current density. The dashed black line in Figure 6-14 is the line of system thermoneutrality: these are the states at which the entire system is operating thermoneutral conditions. The system operates with thermoneutrality when the stack's excess heat can be used to meet all of the thermal demand of the balance of plant.

There is an interesting trend associated with the system's endothermicity. Although the stack tends to operate in increasingly endothermic conditions with increasing temperatures and current

densities, the stack deviates from these conditions in the region of low current density. For example, consider how the system's net thermal energy varies if the temperature is held at a constant value of 900 K. At this temperature and at current density values of 0.10, 0.5, and 1.70 A/cm^2, the corresponding net thermal demand is approximately 49, 170 and 34 kW, respectively. The system requires more thermal energy when it operates at 0.5 A/cm2 than when it operates at 0.10 and 1.70 A/cm^2. Even when the air is neglected from the calculation, the trend is the same. At very low current densities, the stack must rely on its electric heaters to meet the thermal energy demand for electrolysis. Additionally, when the stack operates at these low current densities, the thermal energy required for steam generation and to superheat the steam is low enough such that the heat that can be recovered from the outlet streams of the stack is more than sufficient to meet the thermal energy demands of the system. The balance of plant results in Figure 6-13 can further explain by illustrating the low thermal energy demand at low current densities, which is in direct contrast to the high thermal energy demand in the region of high current density and high temperature.

Interestingly, Figure 6-14 shows that the system is net thermoneutral at very high current densities (>1.3 A/cm^2). In the present system, there is no thermodynamic value in operating the stack in conditions that fall below the black line because any surplus heat generated will be wasted and more energy will be required to cool the hydrogen-steam mixture at the outlet of the stack. Additionally, Figure 6-14 reveals that the range of temperatures that allows the system to operate without any additional heating are quite limited in range of operating current densities presented (1-2 A cm^{-2}). This means that at the typical operating temperatures of SOECs (650 – 850^{o}C), the stack would need to operate at an extremely high current density (> 2 A cm^{-2}) in order to achieve net system thermoneutrality. While prior studies have successfully shown that bimodal nanocomposite electrodes can support high current densities at (>3 at 750^{o}C and >4 A/cm at 800^{o}C), this has only been shown in the lab; typical state of the art SOEC demonstrations operate at maximum current densities of 1 A cm^{-2} [122]. Therefore, considering the current state of existing SO technology, a feasible operating current is 100A, which falls above the black line in Figure 6-14, and thus will require additional external heating. Since the system's thermal demand for superheating the steam increases with operating temperature (see Table 6-4), operating the stack at higher temperatures results in thermal loads that cannot be met

through the stack's excess thermal energy from exothermic operation. In other words, the stack becomes more endothermic (and efficient) as the operating temperature increases, which decrease the potential thermal energy that can be used to meet the system's thermal load. Figure 6-14 also shows the operating conditions of each of the four cases evaluated in the following section. Note, that all of the cases fall in the endothermic region of the figure.

Table 6-4: Energy for heating, phase change, and superheating of the water to steam at various operating temperatures for an operating current density of 0.90 A/cm^2 (inlet water temperature is 283K [118]**)**

Operating Temperature (K)	Liquid Water Heating (kW)	Boiling (kW)	Steam Superheating (kW)
850	30.6	181	83.7
897	30.6	181	93.3
944	30.6	181	103
991	30.6	181	113
1038	30.6	181	123
1085	30.6	181	134
1132	30.6	181	144
1179	30.6	181	155
1226	30.6	181	167
1273	30.6	181	178

6.3.2 **System Results**

Considering the thermal analysis in the previous section and that most SOECs operate between 650-850^{o}C [123], this section analyzes the operation of the stack in four different scenarios. The first scenario (case 1) presents the most optimistic scenario in which the stack operates with a high current density that falls near the black line of net system thermoneutrality in Figure 6-14. The second scenario represents a more feasible exothermic operating condition, in which additional heating is still needed to meet the system's thermal demand. The second case takes into consideration the upper threshold for temperature gradients that cells handle. The third and fourth scenarios represent the stack thermoneutral and endothermic operation, respectively. The four proposed operating cases are shown in Figure 6-15 along the polarization curve and in Figure 6-14 with the same icons. In each of the scenarios, the stack operates at a temperature of

650°C with a steam utilization of 70%. Table 6-5 lists the stack parameters that are constant for each case, and Table 6-6 lists the operating conditions for each case.

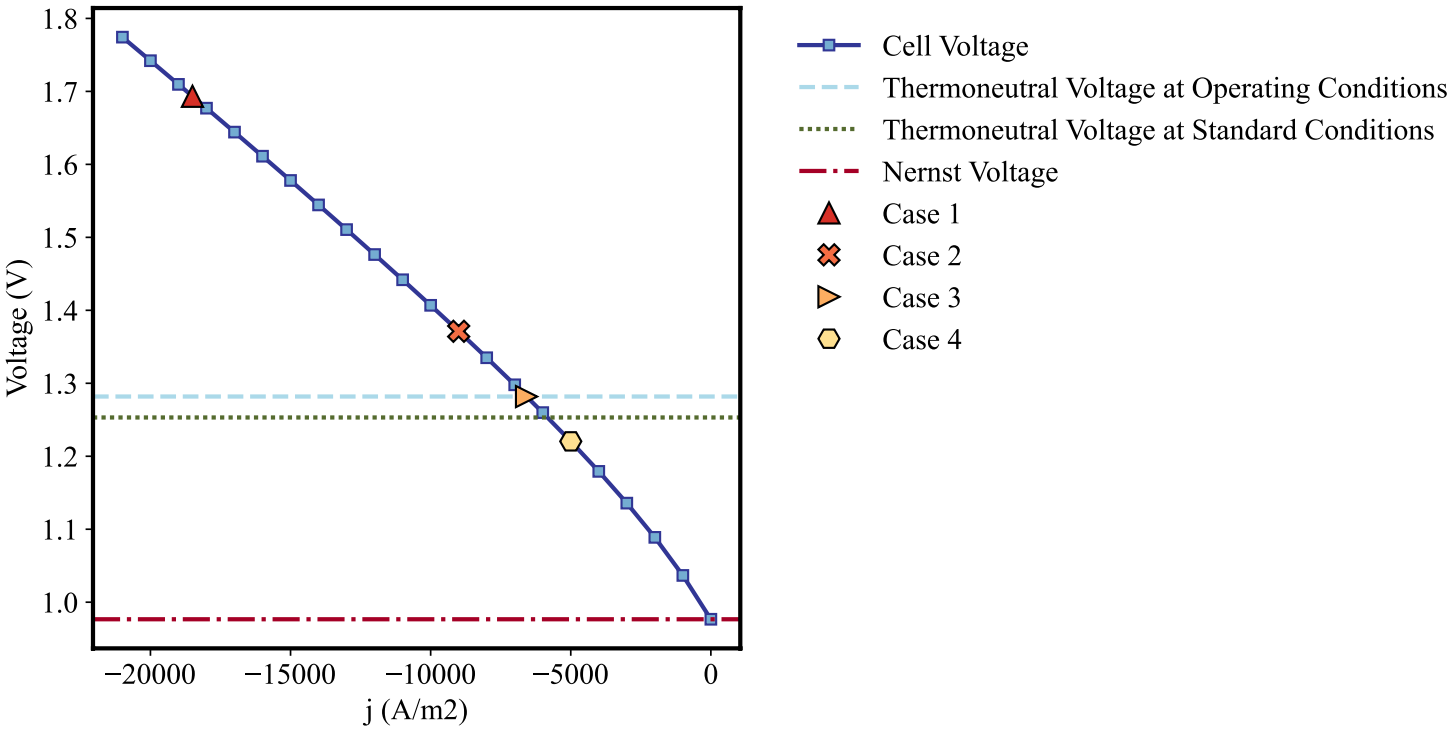

Figure 6-15: Stack Polarization curve at the operating temperature and case operating points

Table 6-5: Stack parameters held constant for each case

Parameter (units)	Value
H_2O Utilization (%)	70%
Number of cells in the stack (--)	1000
Cathode Inlet Composition (x_{H2}, x_{H2O}) (%)	10%, 90%
Stack Operating Temperature (K)	923

Table 6-6: Case Parameters

	Case 1	Case 2	Case 3	Case 4

Current (A)/ Current density (A/cm2)	185/ 1.85	90/ 0.90	65.8/ 0.658	50/ 0.50
Voltage (V)	1.69	1.37	1.28	1.22
Power Density (W/cm2)	3.14	1.24	0.0877	0.610
Stack Power (kW)	2190	863	590	578
Stack Outlet Temperature (K)	1590	1020	923	923
H_2O Consumed at State 1 (kg/day)	14,300	6960	5089	3860
H_2 Produced (kg/day)	1170	567	416	315
Brine produced (kg/day)	4190	2040	1490	1130
Stack Efficiency (%)	74.0%	91.3%	97.9%	102%
System Efficiency (%)	67.3%	75.1%	76.0%	75.6%

6.3.2.1 Case 1: Exothermic Operation I

In the first case, the stack operates at 650°C at a current of 185 amps and voltage of 1.69 volts. At this operating point, almost all of the system's thermal needs for the steam will be met by the excess heat from the electrolyzer. If the stack operates continuously at this design point, the stack will produce over 1 ton of H_2 per day. The power density of this case is 3.14 W/cm^2, which is an ambitious power density since the US Department of Energy's technical targets for SOEC cells are 1.54 W/cm^2 by 2026 and ultimately, 2.56 W/cm^2 at 1.28 V/cell [124]. Table 6-7 shows lists the temperatures at each state in the process flow diagram. Under this operating condition, the

system is not operating net thermoneutrally, as the system will need to use the optional heater located between State 12 and 13 to preheat the inlet hydrogen-steam mixture from 883 K to 923 K. The system produces 3.57 grams of brine per gram of hydrogen, which is 4,190 kg brine per day. This is a significant amount of brine and will require proper disposal. Due to the high exothermicity of this operation point, the stack's electricity demand and the energy required for compression accounts for 45% of the energy demand of the system. However, while this results in a very high overall system efficiency, the outlet temperatures of the stack reveal that this design point is likely not feasible. Operating with such a high current density would result in significant thermal gradients within the cells that would lead to deleterious material issues. Therefore, operating the stack under conditions that allow the entire system to be net thermoneutral are likely not feasible. In this scenario, the system consumes 178 kJ of electrical energy per gram of hydrogen produced.

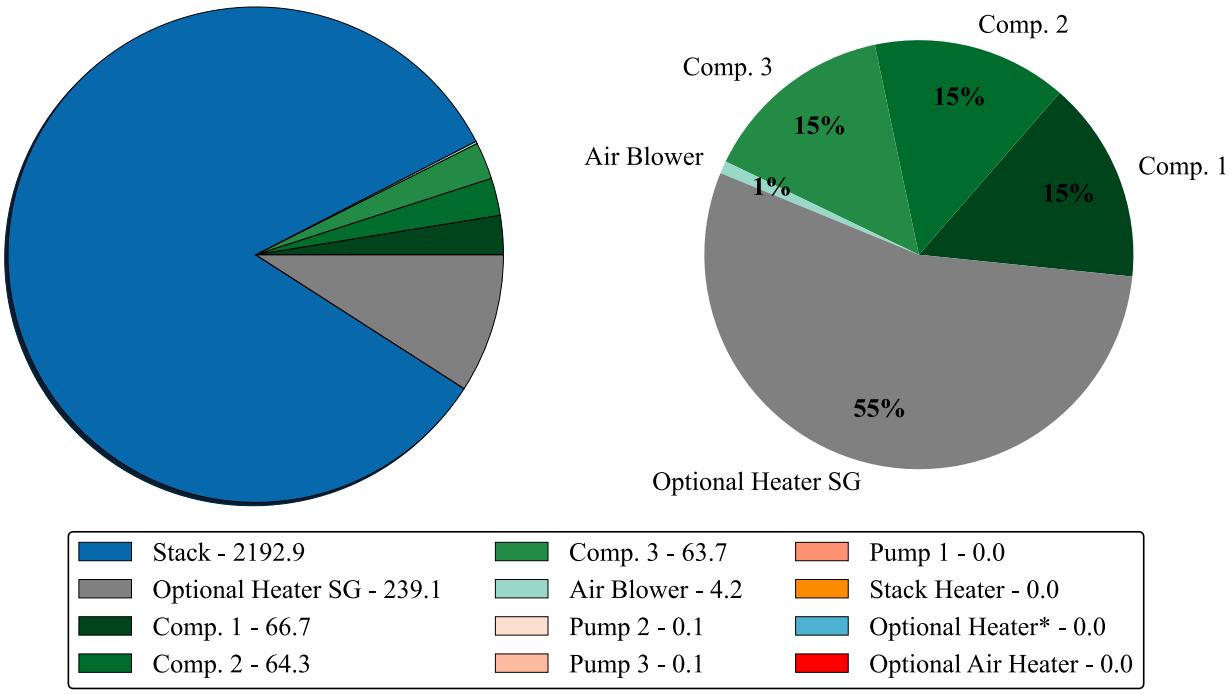

Figure 6-16: (left) Electric loads of all components in Case 1 (kW) (right) Electric loads of balance in Case 1 (kW) with the demand listed in the legend.

Table 6-7: Temperatures at each state in the process flow diagram for case 1

State number in schematic	Temperature (K)	State number in schematic	Temperature (K)
1	288	**19**	477
2	288	**20**	384
3	373	**21**	384
4	373	**22**	384
5	373	**23**	343
6	373	**24**	602
7	373	**25**	335
8	373	**26**	588
9	373	**27**	333
10	373	**28**	584
11	595	**29**	333
12	883	**30**	283
13	923	**31**	283
14	1588	**32**	293
15	1588	**33**	283
16	1588	**34**	283
17	477	**35**	293
18	477	**36**	373

6.3.2.2 Case 2: Exothermic Operation II

Case 2 represents the maximum current that the stack can operate at without exceeding a temperature gradient of 100 K across the cells from the inlet to the outlet. The literature reports that an allowable temperature gradient ranges from 5 to 8 ^{o}C/cm. Therefore, a temperature gradient of 100 K is adequately close to the temperature variation (50-80^{o}C) that is tolerated by manufacturers [125]. To meet the thermal energy requirements for steam generation, Case 2 requires approximately 66 kWe and 24 kWe to operate the heater in the steam generator and the

optional heater in state 12 and 13, respectively. In comparison to Case 1, Case 2 will consume less electrical energy than Case 1: Case 2 consumes 160 kJ of energy per gram of hydrogen produced. This scenario consumes less energy per gram of hydrogen produced because the stack and system efficiency are significantly higher. The electrolyzer makes up approximately 82% of the total electrical consumption (see Figure 6-17). Although in Case 2 the balance of plant consumes a larger proportion of the total electricity, it also operates with an electrolyzer and system efficiency that is much higher (91% and 75%, respectively) than Case 1. This result suggests that there is an optimal point of exothermic operation: if the stack operates with high exothermicity, then the lower efficiency will compromise the benefits of co-generation of heat and hydrogen due to the lower stack and system efficiencies. Lastly, the temperatures of each state are listed in Table 6-8.

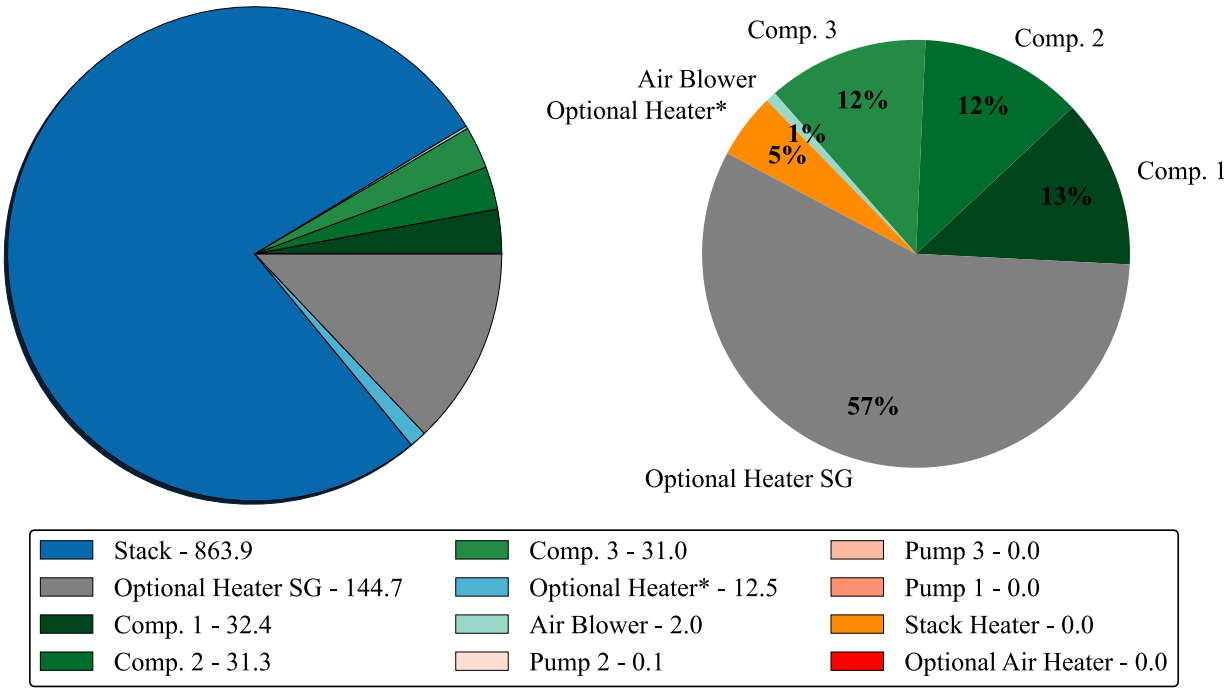

Figure 6-17: Electric loads of (left) all components and (right) balance of plant in Case 2 (kW) with the demand listed in the legend.

Table 6-8: Steady-State temperatures at each state point in the process flow diagram for Case 2

State number in schematic	Temperature (K)	State number in schematic	Temperature (K)
1	283	**19**	520
2	283	**20**	387
3	373	**21**	387
4	373	**22**	387
5	373	**23**	343
6	373	**24**	602
7	373	**25**	335
8	373	**26**	588
9	373	**27**	333
10	373	**28**	584
11	862	**29**	333
12	864	**30**	283
13	923	**31**	283
14	1022	**32**	293
15	1022	**33**	283
16	1022	**34**	283
17	520	**35**	293
18	520	**36**	373

6.3.2.3 Case 3: Stack Thermoneutral Operation

In the third case, the system operates at the stack's thermoneutral voltage (1.281 V) and current (65.8 A). Table 6-9 lists the temperatures of each state. Because the present system uses sweep air in the oxygen electrode, the heat released from the reactions is insufficient to meet the thermal load of the stack: there is a need for additional heating in the stack to maintain a constant temperature of the air stream in the anode. In this case, the net amount electricity consumed per unit of hydrogen is lower than Case 1 and 2: 157 kJ of electricity is consumed per gram of hydrogen produced. Energy for the electrolysis reactions makes up 78% of the total electricity consumed (see Figure 6-18). Of the four cases assessed, the system efficiency is highest in this

scenario: 76%. This is partly due to the high stack efficiency, which is 97.9%. Although the system operates very efficiently in Case 3, the stack thermoneutral condition does not represent the system's most efficient operating point. An iterative solution revealed that the lowest electricity consumed per unit of hydrogen occurs slightly above the stack's thermoneutral point, at a current of approximately 66.9 amps. At this optimal current condition, the system operates in the stack's exothermic regime and the total system efficiency is 76.4%.

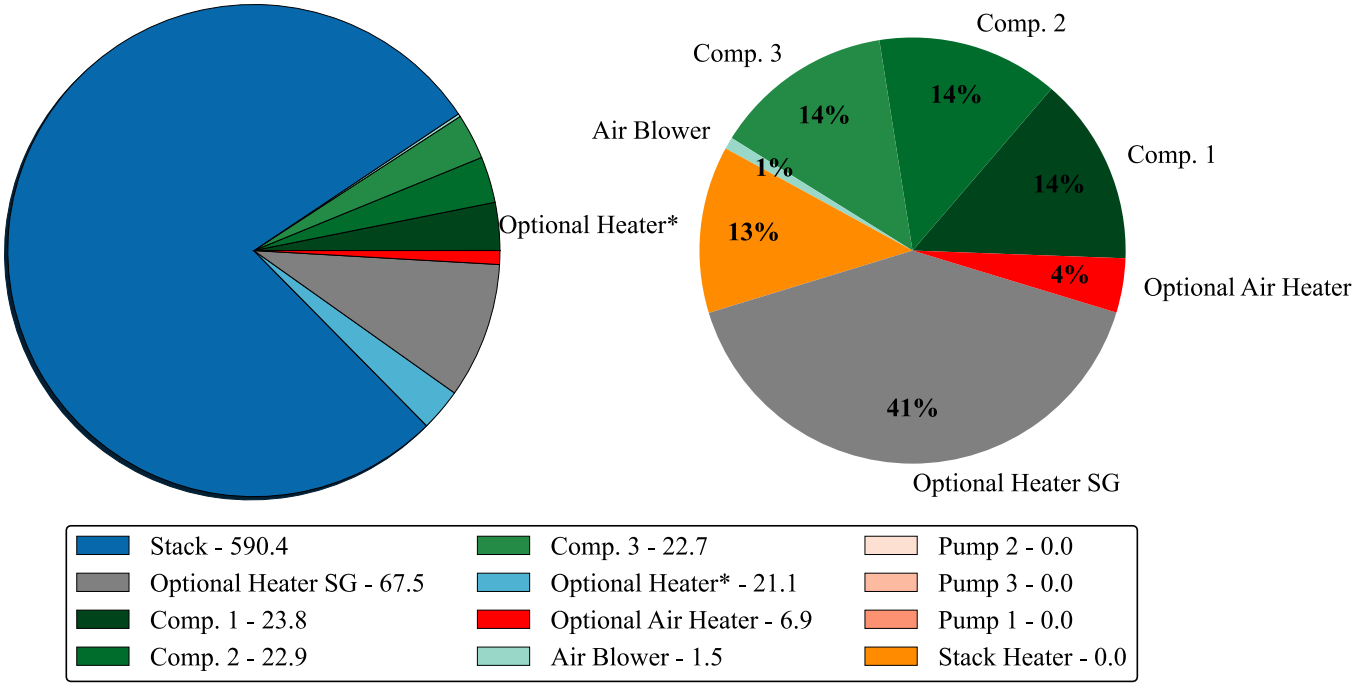

Figure 6-18: Power demand of various components in the thermoneutral condition (Case 3)

Table 6-9: Steady-State temperatures at each state point in the process flow diagram for Cases 3 and 4

State number in schematic	Temperature (K)	State number in schematic	Temperature (K)
1	288	**19**	384
2	288	**20**	374
3	373	**21**	374
4	373	**22**	374

5	373	**23**	343
6	373	**24**	602
7	373	**25**	335
8	373	**26**	588
9	373	**27**	333
10	373	**28**	584
11	373	**29**	333
12	797	**30**	283
13	923	**31**	283
14	923	**32**	293
15	923	**33**	283
16	923	**34**	283
17	384	**35**	293
18	384	**36**	373

6.3.2.4 Case 4: Endothermic Operation

In the fourth case, the stack's voltage falls below the stack's thermoneutral voltage and thus, the stack is in the endothermic regime. In this case, the system must use all of its optional heaters to provide sufficient heat for the system. The system consumes 159 kJ of electricity per gram of hydrogen produced, which is only slightly higher than Case 3 and equivalent to Case 2. The stack and system efficiencies are approximately 102% and 75.6%, respectively. Although this operating point falls in the stack's endothermic regime, the system's electricity consumption per

gram of hydrogen produced is relatively low though. This is because, as shown in

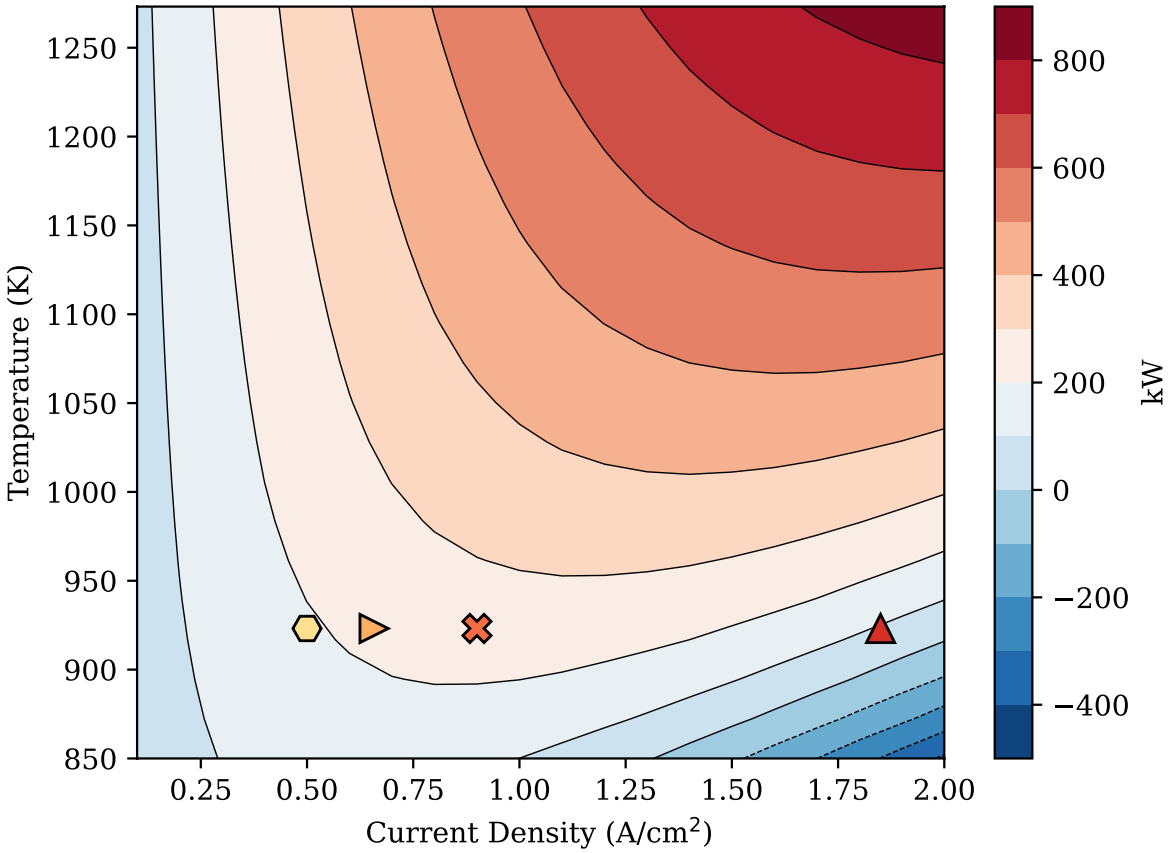

Figure 6-14, Case 4 has a lower net thermal energy demand than Case 3 and 2. This explains why the system's electricity demand per kg of hydrogen does not increase despite the endothermicity of the stack. Case 4 represents a scenario in which a substantial portion of the electricity available is used for the balance of plant components. Whereas in Cases 1-3, the electrolyzer makes up between 78 - 90.9% of the total electricity demand, in the current scenario the electrolyzer consumes 74% of the system's total electricity demand. The temperatures of the system components for this case are the same as those in Table 6-9 for the thermoneutral Case 3.

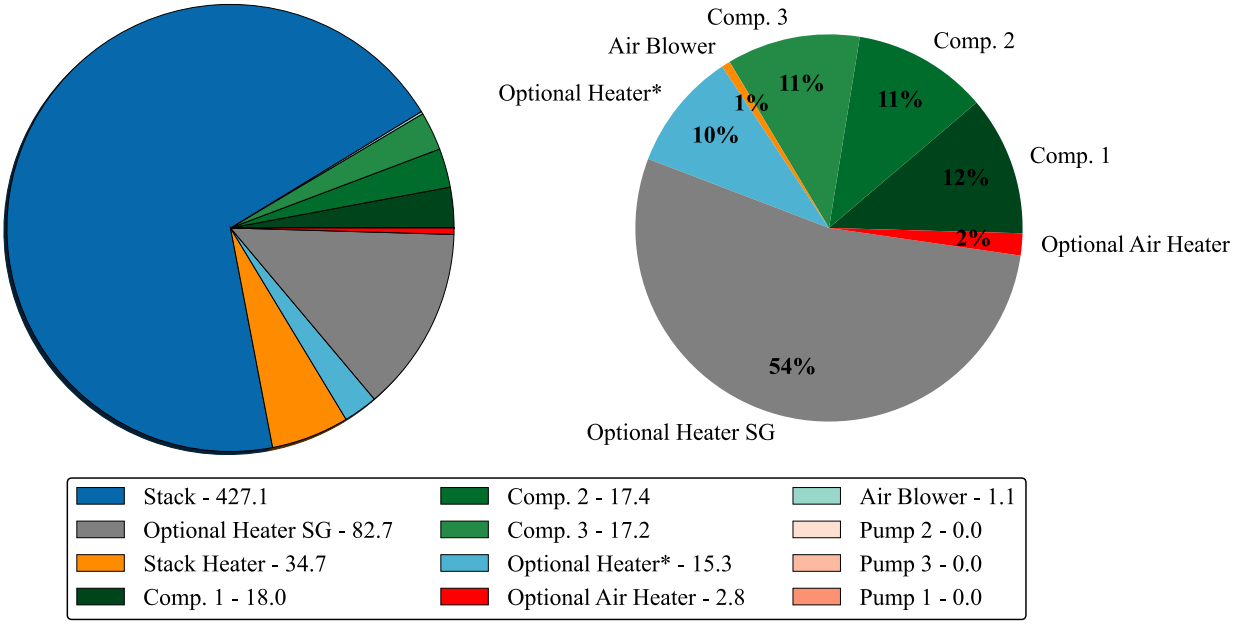

Figure 6-19: Power demand of components in the endothermic scenario (Case 4)

6.4 Discussion

6.4.1 Brine

One important component of the offshore platform is the brine that is generated from the steam generation process. In Figure 6-20, the brine generation is presented as a function of steam utilization and current density. The amount of brine generated is highest when the stack's steam utilization is low, and the operating current density is high. Prior work by [41] assumed the concentration of salt in the seawater and brine is 35.165 g/kg and 120g/kg, respectively. The following section will expire the concentration of brine and the amount of brine generation for a dynamic scenario.

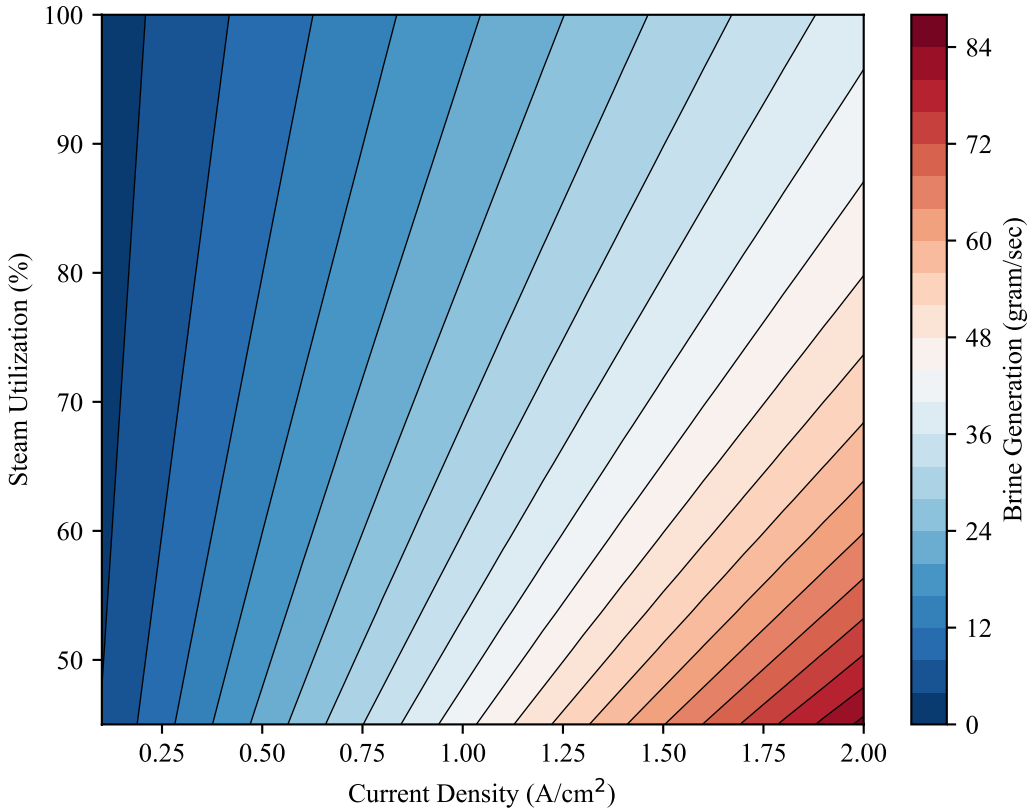

Figure 6-20: Brine generation heat plot as a function of steam utilization and current density

6.4.2 **Dynamic Operation Assessment**

Dynamic operation is essential to successfully couple SO systems with offshore wind. Intermittent and unstable renewable power is challenging for SO stacks because it may result in temperature gradients that can lead to thermal stresses and degradation in the cell. Prior work by Skafte showed dynamic operation of an SOE stack is possible by rapidly pulsing between the endothermic region in electrolysis and fuel cell mode to prevent significant temperature gradients [125]. As long as the system operates most of the time in electrolysis mode, the system will produce hydrogen.

This section first analyzes the extent to which an SO system would have to operate dynamically if it were to be directly connected to an offshore wind platform. As a thermal management

strategy, the stack is designed to operate in a hot standby mode in periods where renewable power is not available. In the hot standby mode, the system operates in fuel cell mode to produce enough heat to stay warm. This section proposes a 3.5 MW offshore wind platform in Humboldt, California that is coupled with a 1730 kW SO electrolyzer. It is assumed that there are two stacks in series that can operate up to 90 amps in electrolysis. The polarization curve developed in the previous section is used to interpolate the operating current and voltage of the stack based on the available wind power. Additionally, the electrolyzer in the platform is comprised of two of the stacks from Case 2. A winter and summer month in 2008 are used as representative dynamic data.

Figure 6-21 illustrates the profiles for each month studied. The offshore wind profile is very dynamic in the winter month, particular between January 21, 2008 and January 25, 2008. In comparison, in June, the offshore wind profile is mostly steady and there are long periods over which the output power is constant, and the stacks operate at their rated output power. Although the month of January is very dynamic, prior work by Konrad suggests that offshore wind variations occur on an hourly basis not a minute or second basis. This suggests that the dynamics of offshore wind may be suitable for solid oxide electrolysis [42].

Figure 6-22 shows the rate of hydrogen production and consumption. In January and June, the system produces a net total of 20,681 and 261,128 kg of hydrogen, respectively. In the standby mode, which is especially relevant for the month of January, the system consumes 4332 and 481 kg of hydrogen in January and June, respectively. The month of June is an extremely productive month for hydrogen production, which is due to the continuous power available from the offshore wind. One of the benefits of operating a stack with approximately 50% capacity of the offshore wind is that the stack is not susceptible to the dynamics that occur at higher wind powers.

Based on these results, if a high temperature SO stack is deployed to an offshore wind platform, it may be more feasible to have planned periods of operation to prevent significant degradation from dynamic wind patterns. One option is to plan for continuous operation of the platform in the summer, when the wind speeds are high and consistent, and to have the system operate in

fuel cell mode in the winter to supplement the variable energy from offshore wind for the grid. If the system is not connected to the grid, then it may be worth shutting down the system in the winter months when the wind is most dynamic and hydrogen generation is low. Economics and technical feasibility will play an important role in determining how and when to operate the offshore SO system. Further work should explore these possibilities.

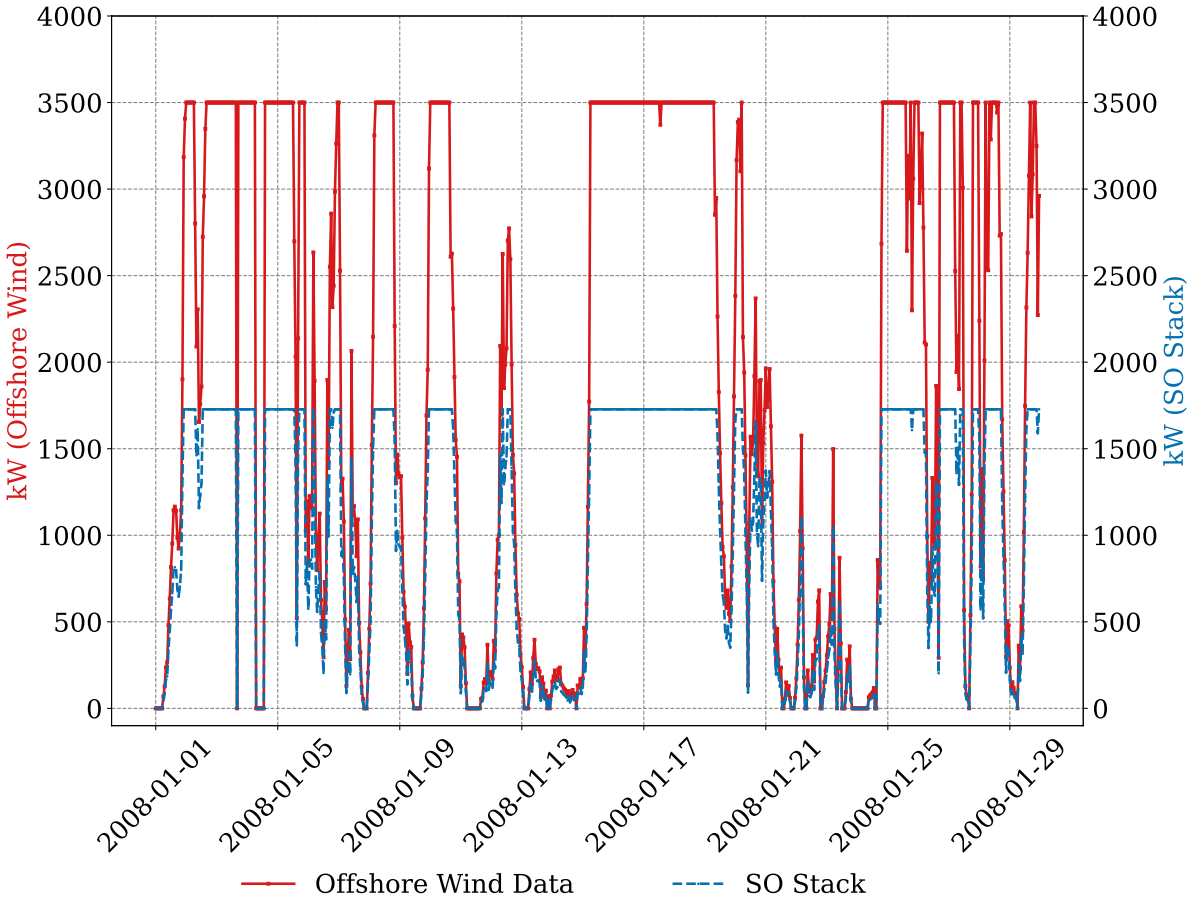

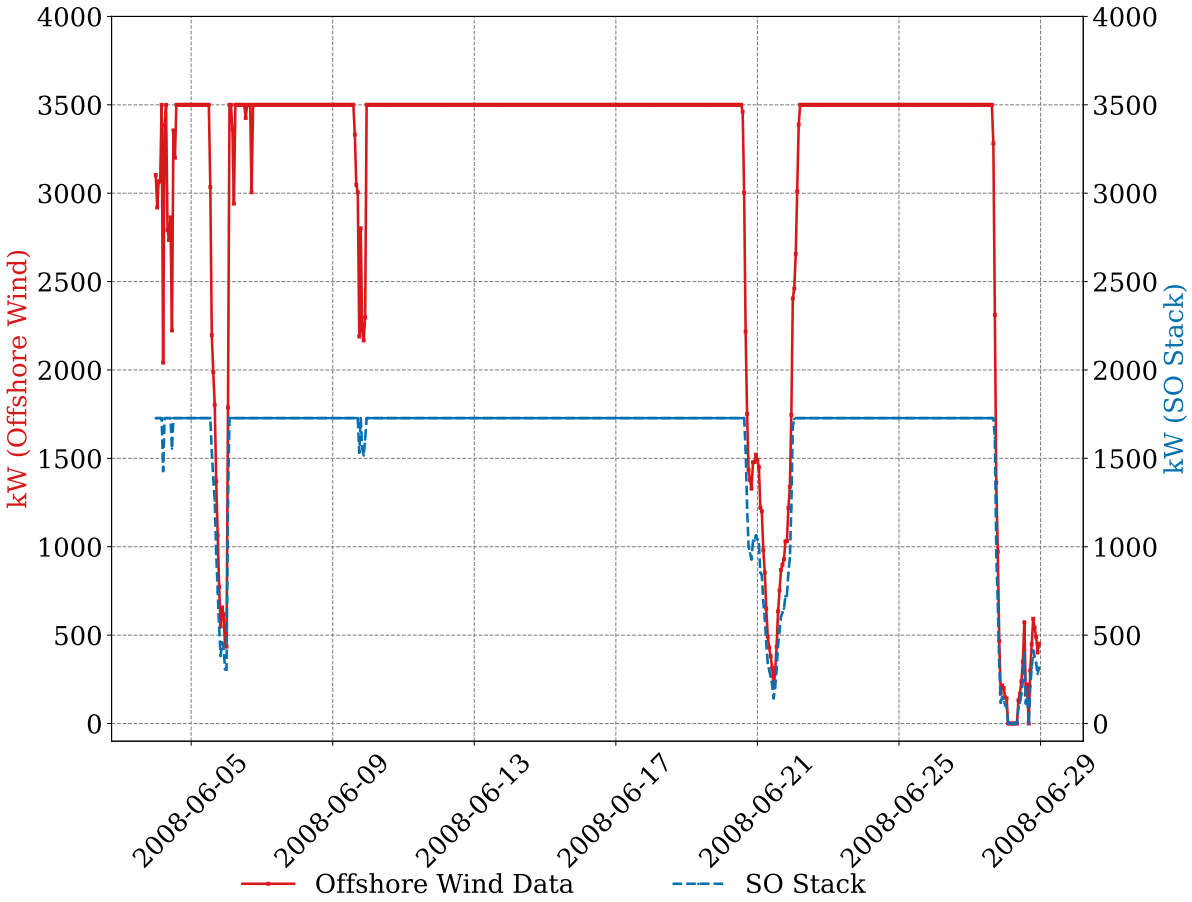

Figure 6-21: Offshore wind and SO stack power in January (top) and June (bottom)

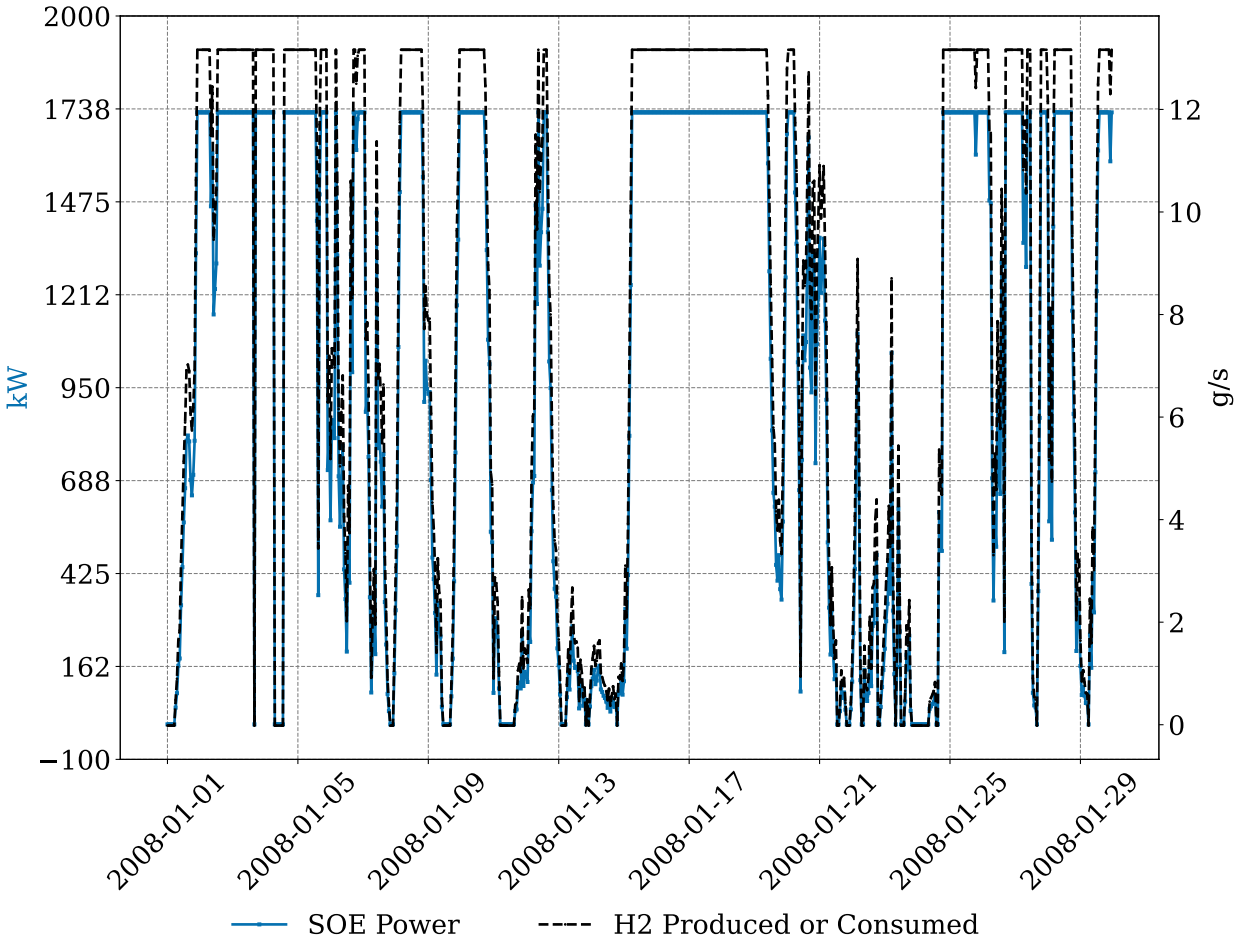
2000
1738
1475
1212
950
688
425
162
−100
kW
12
10
8
6
4
2
0
g/s
2008-01-01
2008-01-05
2008-01-09
2008-01-13
2008-01-17
2008-01-21
2008-01-25
2008-01-29
SOE Power
H2 Produced or Consumed

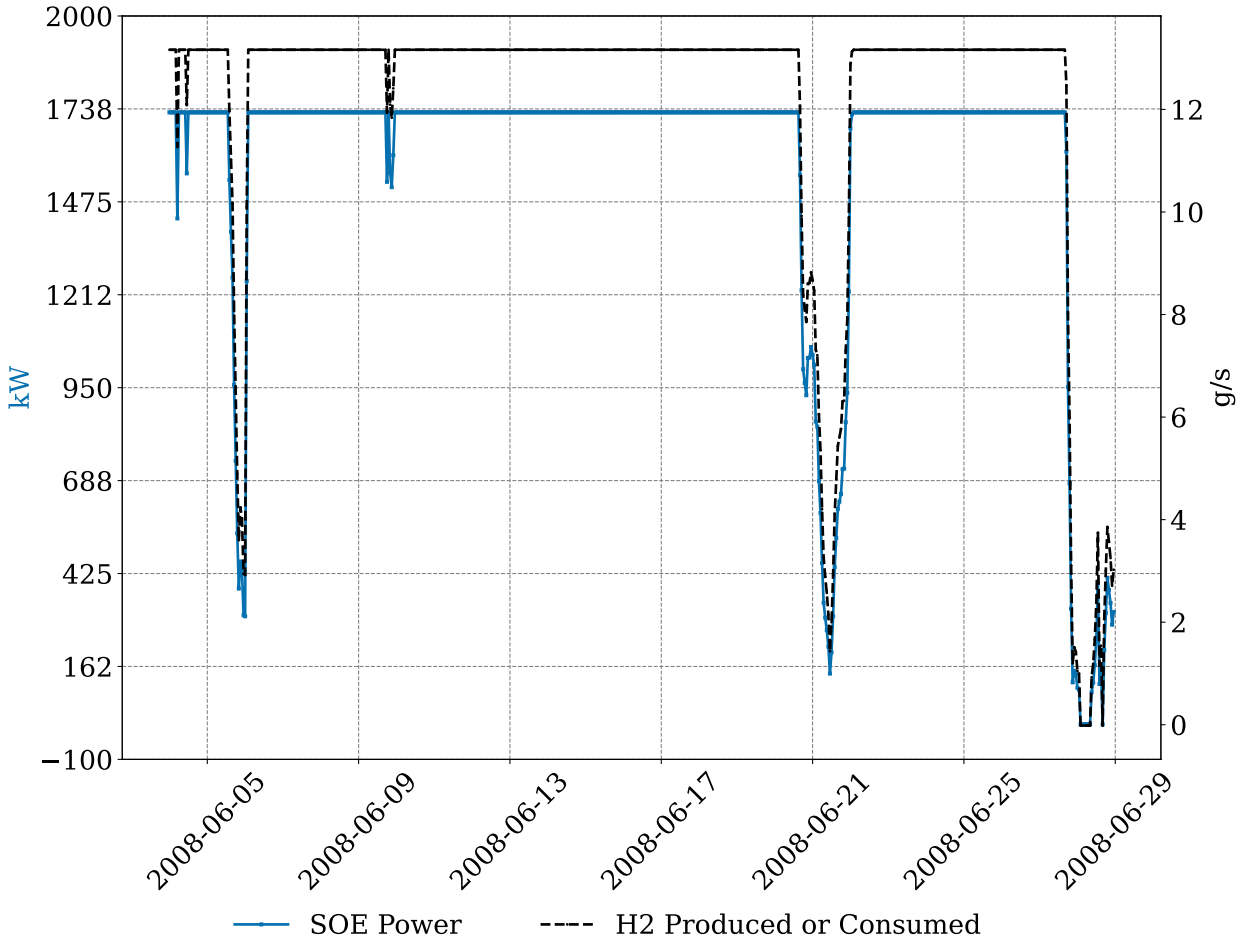

Figure 6-22: SO stack power and hydrogen produced in January (top) and June (bottom).

Additionally, this section also presents the dynamic profiles of the balance of plant. First, the water consumption and brine generation are compared for the two months in Figure 6-23. The amount of brine generated in January is 8000 metric tons, and in June 10,000 metric tons. This is a significant amount of brine that needs to be properly managed to prevent environmental pollution. Additionally, Figure 6-24 illustrates the stack outlet temperature and stack heater power. The stack heater consumes much more energy in the January scenario since the profile is so much more dynamic, which causes the temperature to vary from 920 to 1020 K. It is assumed that the heater ensures the stack temperature remains at 920 K even in the periods where the stack operates endothermically, It is also assumed that the stack operates in fuel cell mode to sustain its thermal load when the wind energy is low.

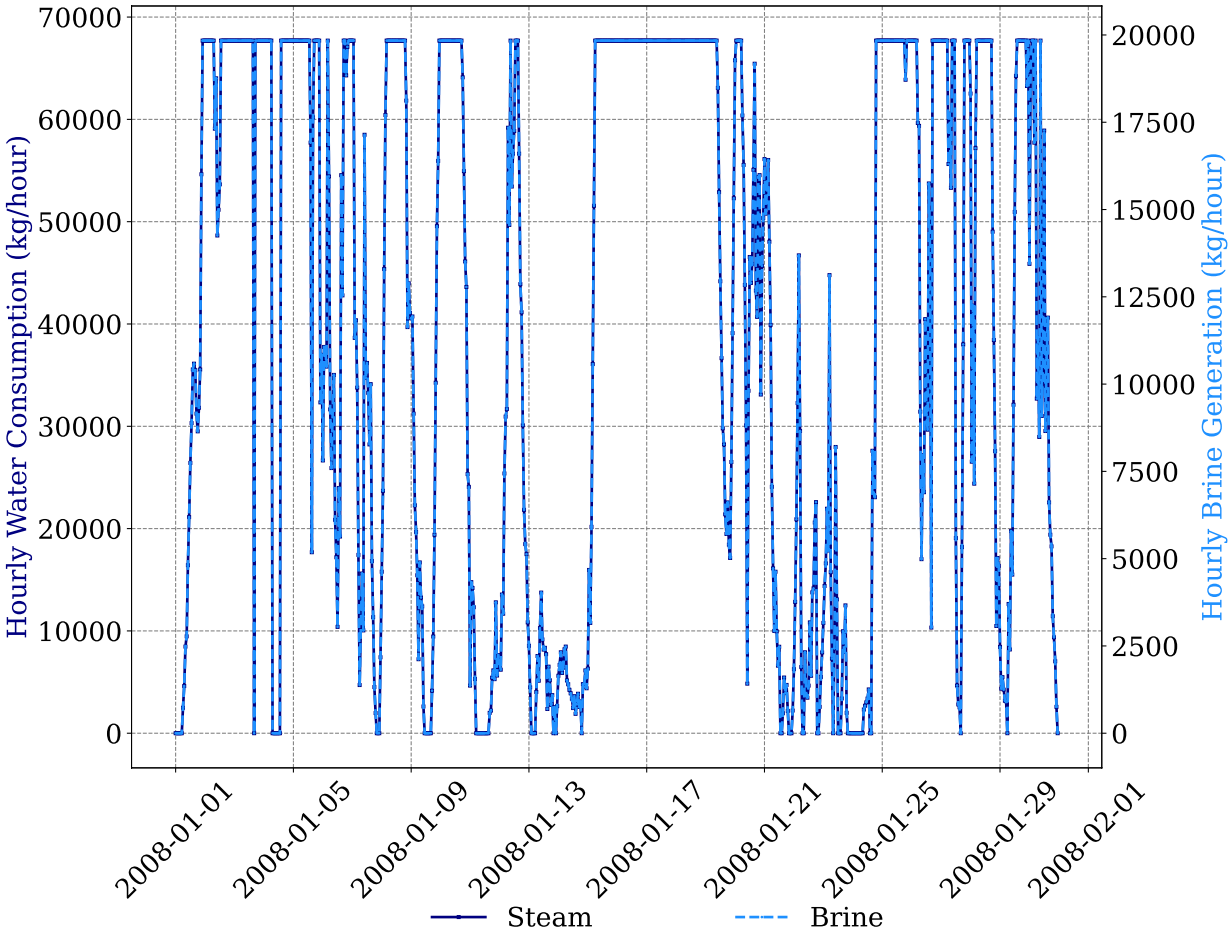
Hourly Water Consumption (kg/hour)
Hourly Brine Generation (kg/hour)
70000
60000
50000
40000
30000
20000
10000
0
20000
17500
15000
12500
10000
7500
5000
2500
0
2008-01-01
2008-01-05
2008-01-09
2008-01-13
2008-01-17
2008-01-21
2008-01-25
2008-01-29
2008-02-01
Steam
Brine

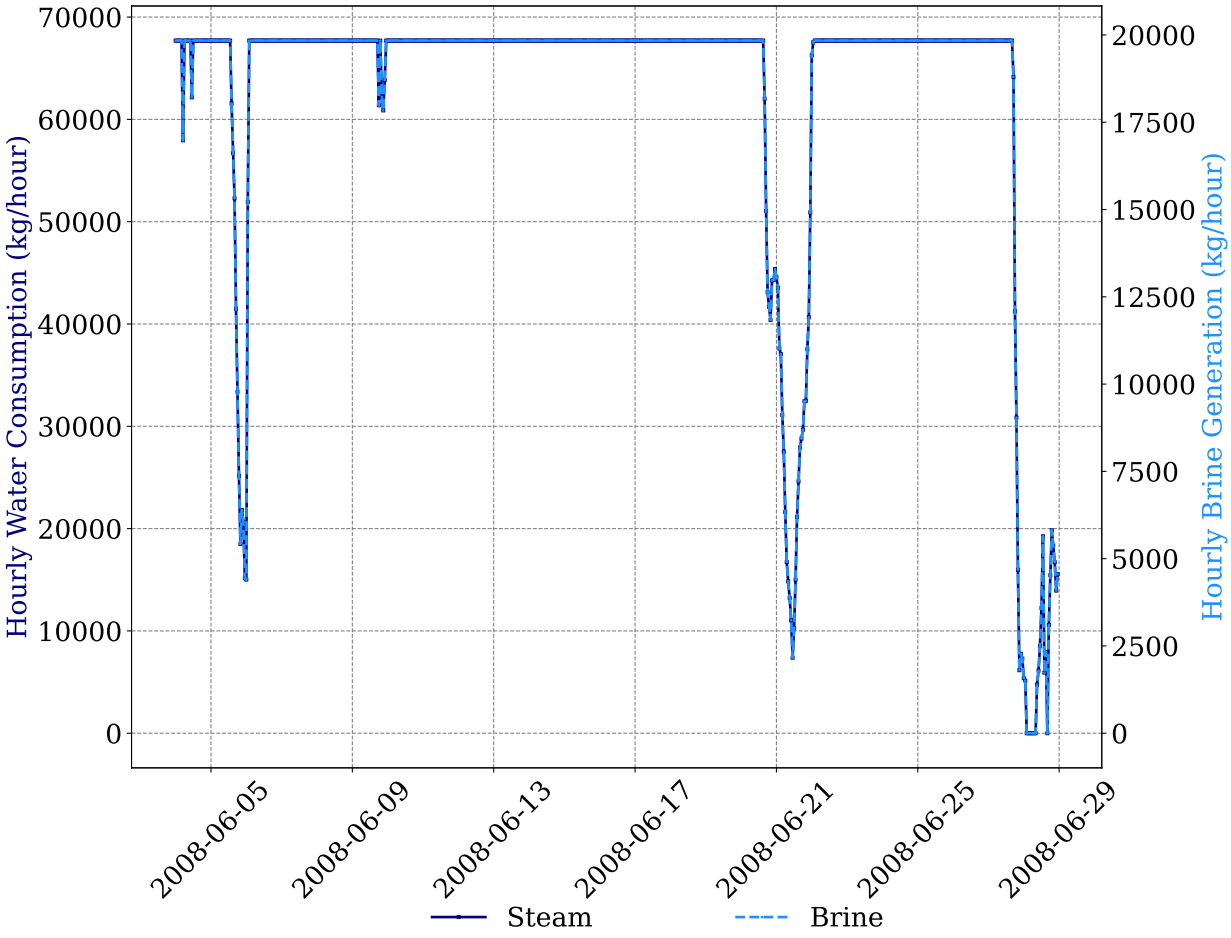

Figure 6-23: Hourly water consumption and brine generation in January (top) and June (bottom).

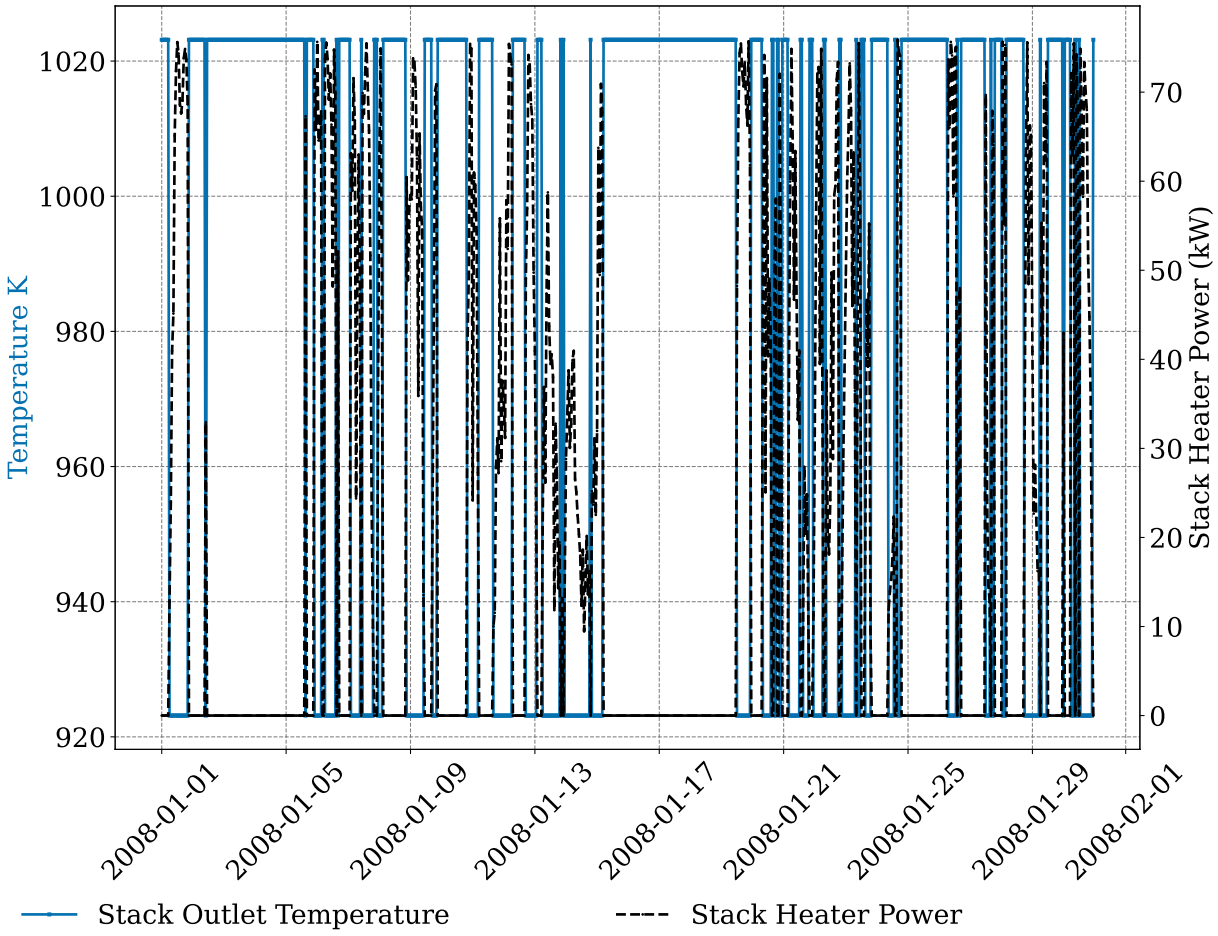
Temperature K
1020
1000
980
960
940
920
Stack Heater Power (kW)
70
60
50
40
30
20
10
0
2008-01-01
2008-01-05
2008-01-09
2008-01-13
2008-01-17
2008-01-21
2008-01-25
2008-01-29
2008-02-01
Stack Outlet Temperature
Stack Heater Power

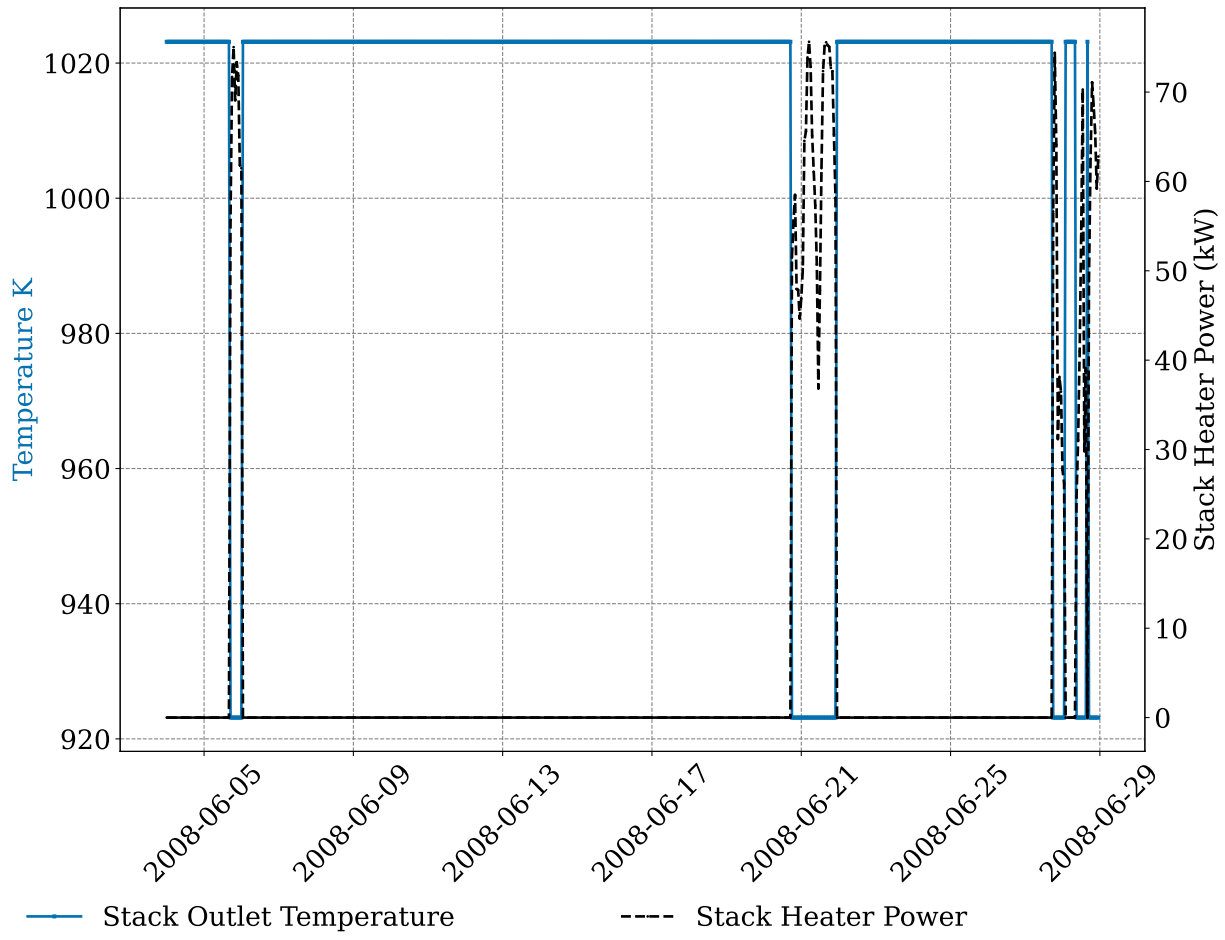

Figure 6-24: Stack outlet temperature and stack heater power in January (top) and June (bottom).

6.4.3 Comparison to LT-PEM and HT-PEM

The results from this study suggest that integrating offshore wind with SO electrolysis has one significant benefit: the high operating temperatures and the exothermicity of the stack allow the system to co-produce heat and hydrogen. Even though the system may require additional heating for steam generation, the total thermal demand of the system is less than what it would require for typical desalination equipment. One potential drawback of SO electrolysis is the operational challenge of dynamic and variable power that can lead to fluctuations in the temperature of the stack and degradation of the cells. This can be addressed by operating in standby mode during periods of low to zero wind energy.

In comparison to SOE systems, low temperature PEM (LT-PEM) electrolysers will require heavy duty reverse osmosis. Since the typical operating temperatures of low temperature PEM electrolyzers is typically around 50-80 ^{o}C [126], indirect PEM seawater electrolysis systems are unable to use high quality heat for desalination, and thus will require additional electricity consumption for desalination. Although reverse osmosis is the most common desalination technology used in the USA, Europe and Australia, it is an energy intensive process that can consume anywhere between 28.5 - 79.9 kwh/ kg H_2O of electrical energy [127]. Other potential options of desalination include multi-effect distillation, multi-stage flag distillation, and vapor compression. In [41], d'Amore-Domenech use distillation with vapor recompression for water purification in their PEM seawater electrolysis model, which they find consumes 0.47 MJ/kg H_2.

To compare the performance of SOE systems with LT-PEM and HT-PEM, the potential performance the analysis in scenario 2 is used as the basis for comparison. A LT-PEM system with the same parameters as the SOE system studied (same utilization factor (70%) and the same hydrogen and water flow rates (3.26 mole/s and 4.47 mole/s respectively)) will also consume approximately 6957 kg of water daily. The additional energy to desalinate the water for a LT-PEM system via reverse osmosis would be between 6957 – 555,915 kWh per day. While PEM electrolysis may result in slightly lower energy for compression due to the lower temperatures of hydrogen at the compression stages, the amount of energy for desalination may exceed the daily amount of energy required for high temperature electrolysis. This initial analysis suggest that PEM electrolysis may consume more energy if deployed offshore than a SO electrolysis system. Figure 6-25 shows the total energy demand (in kW) for LT-PEM that uses reserve osmosis and compares this with the net energy demand for water treatment in HT-PEM and SO.

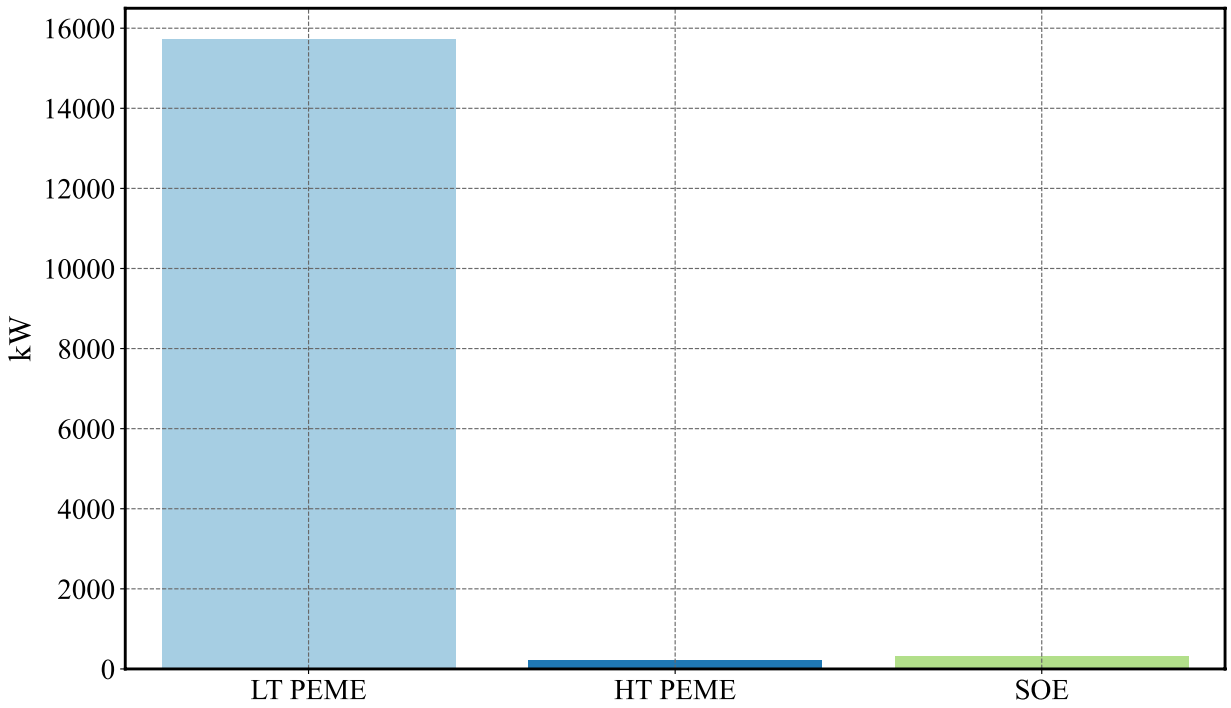

Figure 6-25: Net energy demand for seawater treatment and desalination.

Similar to SOECs, high temperature PEM (HT-PEM) electrolysis has features that allow it to use the surplus heat for secondary applications [128]. In comparison to LT-PEM electrolysis, HT-PEM electrolysis cells typically operate at temperatures above 100°C which results in improved reaction kinetics and ionic conductivity, reduced polarization and electrocatalyst loading [129], as well as higher electrical efficiencies [130]. Prior studies have demonstrated that HT-PEM systems can use either steam or pressurized liquid water for electrolysis. HT-PEM systems that use liquid water will also need heavy duty desalination for water purification. Considering a HT-PEM system that operates with steam at 120°C [128], its thermoneutral voltage is 1.48 V [130]. Figure 6-26 shows a comparison of the relative heating demands for high temperature PEM electrolysis and SO electrolysis. The initial results show that a HT-PEM electrolysis system would have a lower overall thermal demand than the SO electrolysis system because the energy required to superheat the steam to the stack operating temperature is significantly lower. The intermediate operating temperatures of HT-PEM electrolysis may also be more favorable for operating the system dynamically. In addition, the HT-PEM system may be less susceptible to the aggravated degradation that occurs due to high temperatures. Unfortunately, HT-PEM

electrolysis is still in its infancy, and like its low temperate counterpart, it relies on noble metals that are expensive limit scalability [130].

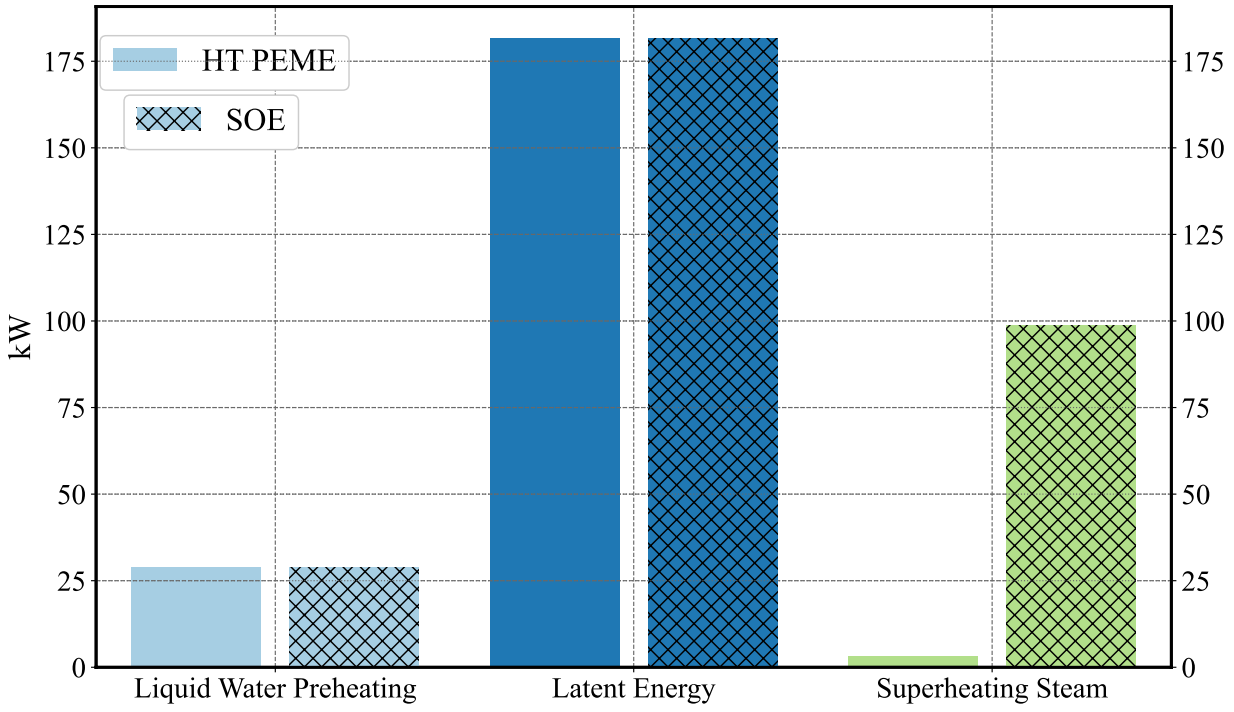

Figure 6-26: Thermal energy demand for High Temperature PEM electrolysis and SO Electrolysis

6.5 Summary and Conclusions

This chapter addresses Objective 4: Design a system for hydrogen production from seawater that includes the desalination and brine/salt management system. It presents a steady state model of an offshore solid oxide electrolysis plant coupled with offshore wind. The results include an analysis of various cases; brine management; dynamic performance analysis; and a comparison to LT and HT PEM electrolysis. The conclusions of this chapter are the following:

- The system must use additional equipment to meet its thermal loads even when the stack operates in exothermic mode.
- In both exothermic and endothermic operation, the steam generator represents the largest source of electricity consumption of the balance of plant.

- The amount of brine generated in the steam generator is enormous and will require proper management to prevent pollution.
- With proper controls, offshore wind may have one of the most suitable renewable energy profiles for high temperature SO electrolysis.
- The ability to couple steam generation and desalination with high temperature electrolysis significantly reduces the net energy demand for offshore hydrogen production.

7 EXPERIMENTAL ANALYSIS OF SEAWATER SOLID OXIDE ELECTROLYSIS

There are many challenges that pertain to using steam from seawater in SOECs: (1) impurities in the seawater may be soluble in the steam that can harm components in the system, such as salt deposits which can lead to blocked pipes [60]; (2) impurities may affect the long-term durability of the cell; (3) the cathode electrode may be poisoned by the contaminants. While prior studies have examined hydrogen generation from seawater via proton-exchange membrane electrolysis [61], [62], and there are prior theoretical analyses on seawater electrolysis with existing technologies [41], [42], [63], [131], there are limited experimental studies on SO electrolysis of seawater. In this chapter, I present a study on the long-term performance and degradation of a solid oxide electrolysis cell operated with simulated seawater for over 400 hours. The electrochemical performance of the cell is studied via polarization curves and electrochemical impedance spectra. Additionally, we presently upon a theoretical framework for the degradation mechanisms that occur from seawater contamination in solid oxide cells. Lastly, we examine sustainable ways to manage the brine that is left in the steam generator.

7.1 Data Analysis Methods Background

7.1.1 Polarization Curves

One of the first steps to characterize the performance of electrochemical systems is through current-voltage measurements to develop polarization curves that provide information about the quality of the cell and performance. The polarization curve represents the major losses of the cell: activation, ohmic and concentration polarization.

7.1.2 **Electrochemical Impedance Spectroscopy**

Electrochemical impedance spectroscopy (EIS) is one of the most powerful tools for understanding the processes in electrochemical systems. EIS is an electrochemical technique that is a special case of a transfer function: it relies on the relationship between electrical input and electrical output, as shown in Figure 7-1. In EIS, a small AC perturbation is applied and the responding impedance vs frequency is recorded based on the voltage response [132]. Because the cell experiences dynamic processes, the impedance response will vary depending on the frequency applied. The impedance consists of the ohmic resistance (R_e) and the charge transfer reaction impedances of the cathode and the anode (R_t) [132].

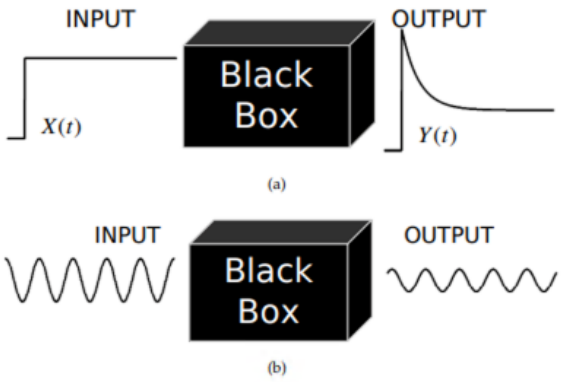

Figure 7-1: Representation of a transfer function with a step change and sinusoidal input. From [133]**.**

The Nyquist plot is a valuable tool for representing impedance spectrum results. Each of the points of the Nyquist plot is a representation of the imaginary impedance, real impedance, and the associated frequency. An example is shown in Figure 7-2. The graph needs to be plotted with a 1:1 ratio with a few labels that indicate the frequencies. It is essentially a 2D representation of a 3D figure. The ohmic resistances are represented with the intersection with the real axis at the high frequency end [134]. The ohmic resistance is due to ionic transport resistance in the electrolyte and it is considered to be independent of AC frequencies, which is why it does not possess any capacitive behavior and only has a real component. It is often represented as a resistor in equivalent circuit. The low frequency intersection with the real axis (x-axis) is the sum of R_e and R_t. The characteristic frequency is the frequency at which the maximum value of the

negative imaginary impedance occurs. The Nyquist plot reveals information about the time constants and capacitance of the electrochemical cell. When multiple semi circles appear, each circle is due to reactions and processes that occur at different time scales with resistive and capacitive behaviors [135]. The capacitive behavior is often due to the double-layer capacitance that is a result of the charge accumulation of the interface [136] . It may also be due to channel flow and channel diffusion that cause a capacitive behavior [137]. The resistances of each semi-circle can be lotted against the temperature in an Arrhenius plot to determine the activation energy [135].

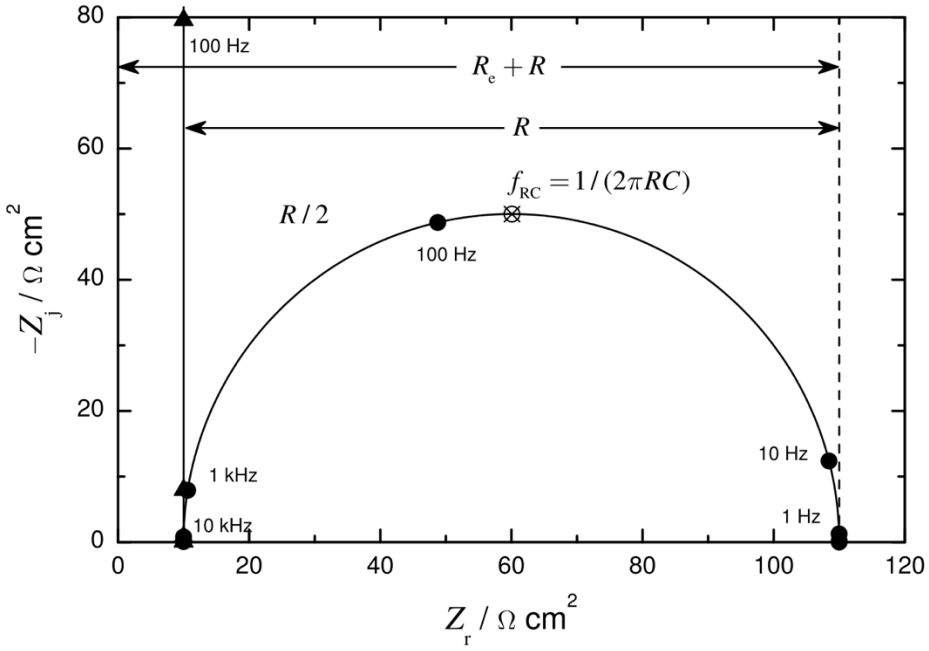

Figure 7-2: Nyquist plot of impedance data. From[133]

Generally, analysis of the impedance spectra from EIS requires an evaluation of the error structure and interpretation of the physics and chemistry of the system. Errors in impedance measurements can be expressed as the difference between an observed value and a model value [133]:

$$\boldsymbol{z_{ob}(\omega) - z_{mod}(\omega) = \varepsilon_{res}(\omega) = \varepsilon_{fit}(\omega) + \varepsilon_{stoch}(\omega) + \varepsilon_{bias}(\omega)} \quad \textbf{(7-1)}$$

Where $\varepsilon_{res}(\omega)$ is the residual error, $\varepsilon_{fit}(\omega)$ is the systematic error due to inadequacies of the model and refers to the lack of fit of the model, $\varepsilon_{stoch}(\omega)$ is the stochastic error, and $\varepsilon_{bias}(\omega)$ is the systematic experimental bias error. Stochastic errors (and the variance of stochastic errors) are a strong function of frequency and are randomly distributed about a mean of zero; they result from integrating time-domain signals with noise from the cell and instrumentation [133].

In order to determine the quality of the EIS data, I used a tool developed by researchers at the University of Florida: Measurement Model. This tool distinguishes between bias and stochastic errors and is based on a generalized model as a filter for non-repeatability of impedance data [133]. The Measurement Model program identifies the stochastic error structure of the measurements used to weigh further regressions. It uses the Kramers-Kronig relations to check for causality, linearity and time invariance (stability) [49], [133]. The Kramers-Kronig relations make it possible to use the real portion to reconstruct the imaginary portion of the spectra and vice versa [138]. Bias errors can result in the measurement to be inconsistent with the Kramers-Kronig relations. Kramers-Kronig relations can identify whether or not the assumption of stationarity (stability) during an impedance test is valid. While no system is perfectly stationary, EIS tests assume the system does not change during the duration of the impedance measurement; and the Kramers-Kronig relations can be used to assess the validity of this assumption [133]. Selecting a proper input sine wave perturbation amplitude that is small enough is necessary to ensure the pseudo linear conditions [139]. If the system is indeed linear, then the measured amplitude data will not change regardless of the input amplitude size applied [139]. This strategy can be used to assess the linearity criterion of the Kramers-Kronig relations. For example, in [139], the authors showed that the Bode plot and the DRT spectra at did not change regardless of the input amplitude perturbation (see Figure 7-3). Additionally, the Kramers-Kronig relations will also easily identify the influence of drift, that is, changes in the system with time [140]. This can be seen by transforming the real to imaginary and the imaginary to real on a Bode plot and comparing the results.

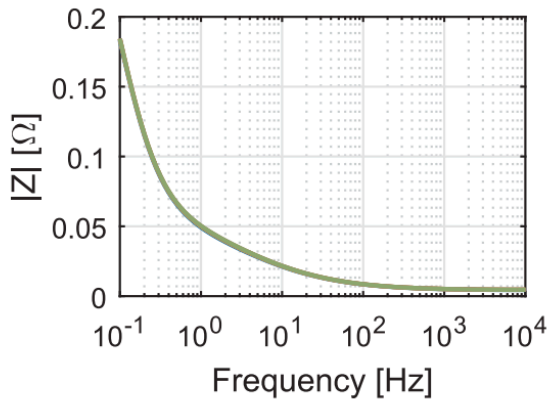

(a) Bode plot for varied amplitudes at OCV

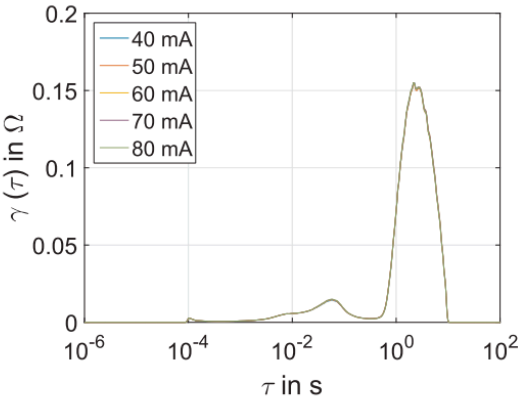

(b) DRT spectra at OCV

Figure 7-3: Figure from [139]**, shows that the linearity criterion is satisfied: the spectra do not change with varying perturbation amplitude.**

The Measurement Model represents the impedance spectra using Voigt elements in series with a resistor as a generalized measurement model. Super positioned line-shapes make up the measurement model, which has been shown to be a general measurement model for a variety of electrochemical systems [133]. The Kramers-Kronig relations require that all the resistances be positive [140]. Since the Voight model is consistent with Kramers-Kronig relations, the ability to fit the model to the data shows the data satisfies the Kramers-Kronig transform. The noise (stochastic errors) limit the number of Voight elements that can be obtained from the measurements [133]. The greater errors in a dataset, the smaller the number of necessary Voigt elements [140]. The residual errors can be fitted with weighting to fit the order of the stochastic noise [133]. The measurement model takes advantage of the noise present to limit the number of parameters that can be resolved. The inability to fit an impedance spectrum to the measurement model is an indication of the failure of the data to satisfy the Kramers-Kronig relations [133]. In other words, if the original and the transformed data look very different on the Nyquist plot, it means the original data does not comply with the Kramer-Kronig relations and that it cannot be used [140]. It is important be mindful of data outliers in the data which can often occur near the line frequency (60 and 120 Hz in the US) and at the beginning of a measurement due to transient conditions. The Measurement Model program can also be used for preliminary characterization of impedance data; it can estimate the capacitance and ohmic resistance to identify the

characteristic frequency above which the geometry of the electrode may cause frequency dispersions.

The Kramers-Kronig transform has been previously used in multiple solid oxide cell studies. For example, the authors used the KK transform to examine the performance and degradation of solid oxide cells in a stack in [134]. Figure 7-4 shows a typical KK typical test residuals plot for impedance data. The authors used a frequency range from 0.1 Hz to 10 kHz, with an AC current of 1 A and a DC offset of +/- 5 A [134]. They also calculated an average area specific resistance from the difference between the average Nernst voltage and the measured voltage at a given density [134].

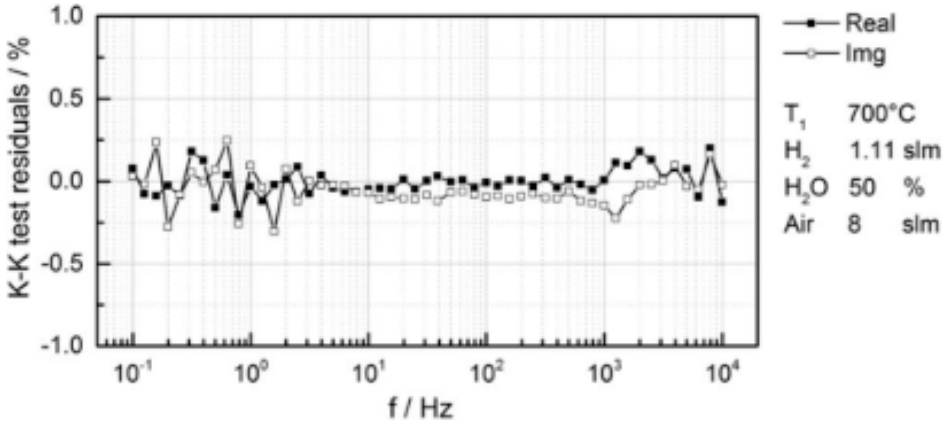

Figure 7-4: Typical KK test residuals of an impedance spectrum that shows the errors of the real and imaginary data were within +/- 0.3%. From [134]**.**

7.1.3 **Distribution of Relaxation Times (DRT)**

Distribution of relaxation times (DRT) is an electrochemical technique that can be used to aid the in the analysis of impedance spectra. It represents the impedance by using an infinite number of differential RC-elements and solves each process by its intrinsic time constant [141]. If DRT is applied on a measured impedance spectrum, the distribution function (g_k) can be discretized on a limited amount of time constants [141]:

$$Z(\omega) = R_0 + R_{pol} \sum_{k=1}^{N} \frac{g_k}{1+j\omega\tau_k} \quad \textbf{(7-2)}$$

Where R_0 is the ohmic resistance, R_{pol} is the overall polarization resistance of the fuel cell, and τ_k is the time constant of a single RC element. The term, $\sum_{k=1}^{N} \frac{g_k}{1+j\omega\tau_k}$, corresponds to R_{pol}, and it is indicative of the relaxation times of the various processes. g_k represents the relative contribution of each time constant on R_{pol}. Because equation **(7-2)** cannot be solved numerically, a regularization must be used that accounts for the smoothness of the solution. Regularization values that are too high will hide features and values that are too low will cause erroneous oscillations [141].

DRT requires comprehensive tests under different conditions including temperature and gas composition to understand the results [134]. It is used to identify kinetics, transport mechanisms, anode and cathode processes and cell degradation. It has been used previously in various studies of solid oxide cells, mostly in fuel cell mode. There is a need for more research that uses DRT on SO cells operated exclusively in electrolysis mode. Next is a summary of a few key papers in the literature that use DRT for SO cells:

- In [139], the authors used EIS to assess the degradation effects due to carbon deposition in an anode supported SOFC. They measured the impedance at OCV and under load in a frequency range between 10kHz and 100 MHz, with a current amplitude of 60 mA. They used DRTOOLS from [142] to use the Gaussian discretization method with 40 points per decade and with a regularization parameter of 10^{-4} [139].
- The authors from [134] used DRT to analyze their impedance spectrum data. The authors used the real part of the spectra to calculate the distribution functions. They identified three major processes, which are shown in Figure 7-6. Their results suggest a few interesting findings: first, the impedance responses are similar in SOFC and SOEC modes; second, most of the degradation was caused by increasing ohmic resistance; finally, the impedance at the air electrode is higher than the fuel electrode [134].
- The authors from [141] used DRT after validating their data with the Kramers Kronig relations and demonstrated the residuals were below 0.5% for the whole frequency range. They carefully identified that a regularization parameter of $1 * 10^{-5}$ was suitable for their DRT analysis.

- In [124], Jeanmonod et al., evaluate the poisoning effects of HCL on a solid oxide cell operated in co-electrolysis. They exposed the cell to 5 – 10 ppm of HCL, and they observed an increase in the resistance of the cell due to the charge transfer processes. Figure 7-5 presents six significant DRT peaks suggested by Jeanmonod et al.
- In [143] Subotic et al. presented a thorough summary and general guidelines for performing DRT analyses on SOFCs and SOECs. Figure 7-7 shows a summary of their literature review on the relevant frequencies for SO cells.
- Subotic et al. also studied the viability of DRT to analyze SOC single cells and stacks in fuel cell and electrolysis modes of operation in [144]. They found that for most of the electrolysis cases the electrode processes could be determined by two DRT peaks in the range of approximately 20 – 200/300 Hz [144]. They also found that increasing the steam, and decreasing the hydrogen quantity, shifts the processes towards lower time constants and decreases the resistance [144]. They state that processes at frequencies higher than 200 Hz are likely related to overlapped process in the fuel electrode.
- In Ref [145], Liu et al use Ciuccci's DRTtools program with a regularization factor of $1*10^{-3}$ to assess the performance of reversible operation of an SO cell operated with seawater. They were able to successfully operation the cell for 31 cycles with over 1000 hours.

Attribution of the DRT peaks to processes according to Caliandro et al. [30], reprinted from [10].

Name	Frequency	Attribution
P1	< 1 Hz	Conversion and diffusion at the O_2-electrode Transport in reforming mixture (H_2-electrode)
P2	1 to 10 Hz	Gas conversion (H_2-electrode)
P3	10 to 100 Hz	H_2-electrode diffusion O_2-electrode reaction and solid state diffusion
P4	100 to 500 Hz	Secondary peaks (H_2-electrode and O_2-electrode transport)
P5	0.5 to 1 kHz	H_2-electrode charge transfer
P6	5 to 200 kHz	Not attributed[a]

[a] *Possibly: solid–solid O_2-electrode transfer processes or electronic current losses between the O_2-electrode and the current collector*

Figure 7-5: Major processes identified in [124].

Table II. Processes identified in stack F1002-165 by DRT analysis.

Process	Frequency range	Physical process
I	1–10 Hz	Gas diffusion in substrate (fuel electrode) Overlapped with gas conversion impedance
II	10–300 Hz	Chemical surface exchange of O_2 and O^{2-} bulk diffusion in air electrode
III	200–10 kHz	Overlapped processes, including gas diffusion, coupled with charge transfer reactions and ionic transport in YSZ (the functional layer of the fuel electrode)

Figure 7-6: The major processes identified in [134]**.**

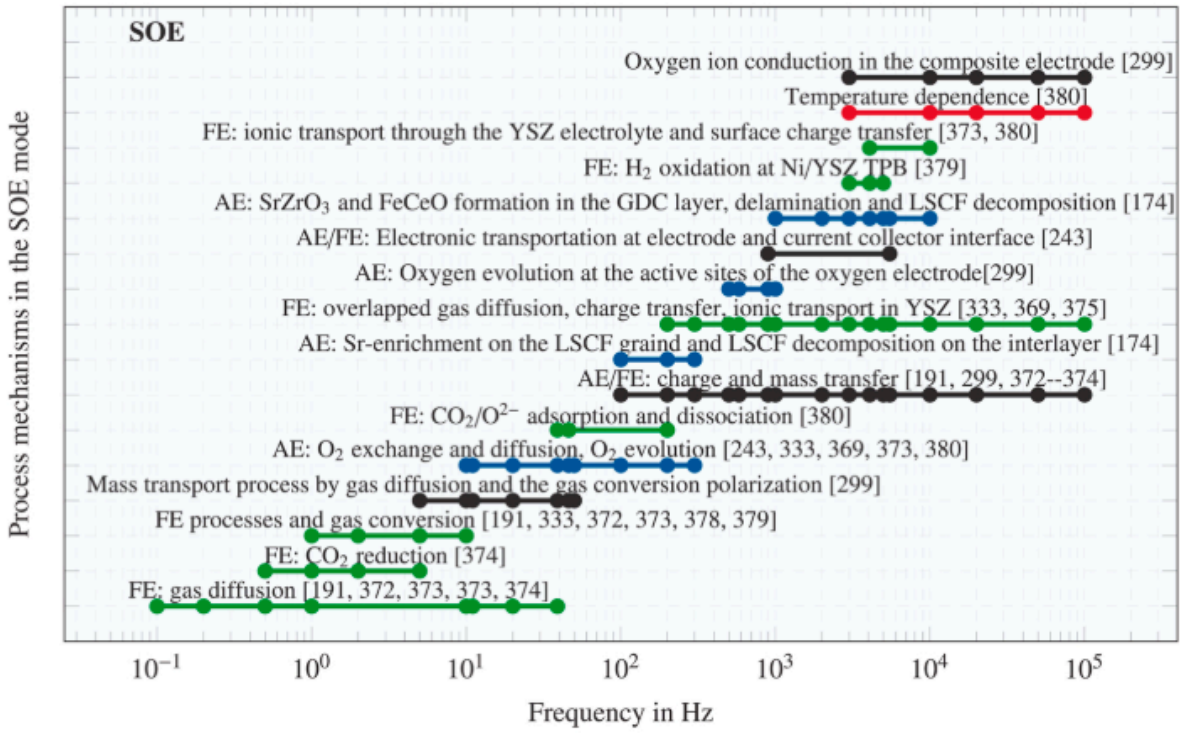

Figure 7-7: From Ref [143] **: a summary of the literature on relevant frequencies for SO cells operated in electrolysis mode.**

7.2 Methodology

7.2.1 Preparation of the cell

We used a 25 cm^2 cathode supported solid oxide cell from Fuel Cell Materials. The cell's active area is 16 cm^2; it has a 50 µm Ni- YSZ cathode, YSZ electrolyte, and 50 µm LSC anode. We prepared the cell for testing by following the instructions in [146]. Silver and nickel current collector meshes were used in the anode and cathode, respectively. To ensure proper contact between the copper current collection wires and the manifold pipes, we used silver paste. We used a platinum wire for the voltage measurements. In the final step of the cell preparation, we applied a glass sealant to the manifold and outer edges of the cell. After the assembled manifold was placed

in the furnace, we placed a seven-pound weight on the manifold to apply sufficient compression to the cell. During the furnace warm-up phase, N_2 and air flowed at 0.150 SLPM in the cathode and anode, respectively. The furnace was set to increase the temperature to 750°C over a period of 14 hours. Once the furnace reached 750°C, the reduction of NiO to Ni followed by introducing H_2 in increments of 0.025 SLPM to the cathode and simultaneously decreasing the flow rate of N_2 until the flow rates were 0.25 and 0 SLPM for H_2 and N_2, respectively. During the reduction phase, the air flow rate slowly increased to 0.750 SLPM. The next phase of the start-up was the conditioning of the cell. In this phase, N_2 was reintroduced at 0.25 SLPM to the cathode while the H_2 and air flowrates remained constant. The voltage and current of the cell were measured at open circuit conditions (OCV), 1 V, 0.8 V, and OCV for an hour at each voltage. Table 7-2 shows the test parameters for the experiments in this study.

7.2.2 **Test Stand Set-up and Instrumentation**

Figure 7-8 shows the schematic of the electrolysis system. A 2250 cm^3 stainless steel tank, adhesive heater, thermocouples, pressure gauges, pressure relief valve, and insulation comprises the system. In order to provide sufficient steam for the electrolysis reactions, we designed a steam generator that uses H_2 and N_2 as the carrier gas for the steam generator, shown in Figure 7-9, which was inspired by the design of John Stansberry. The electric adhesive heater is glued to the outside of the tank, which is insulated. During seawater operation, the tank is filled with the desired water type. Once the tank is heated to the desired temperature based on the desired humidity ratio, dry H_2 and N_2 enter the steam generator at the desired flow rate to transport the steam to the anode electrode of the cell. The piping that connects the steam generator to the furnace is heated to 150°C using an electric line heater and insulated to prevent condensation.

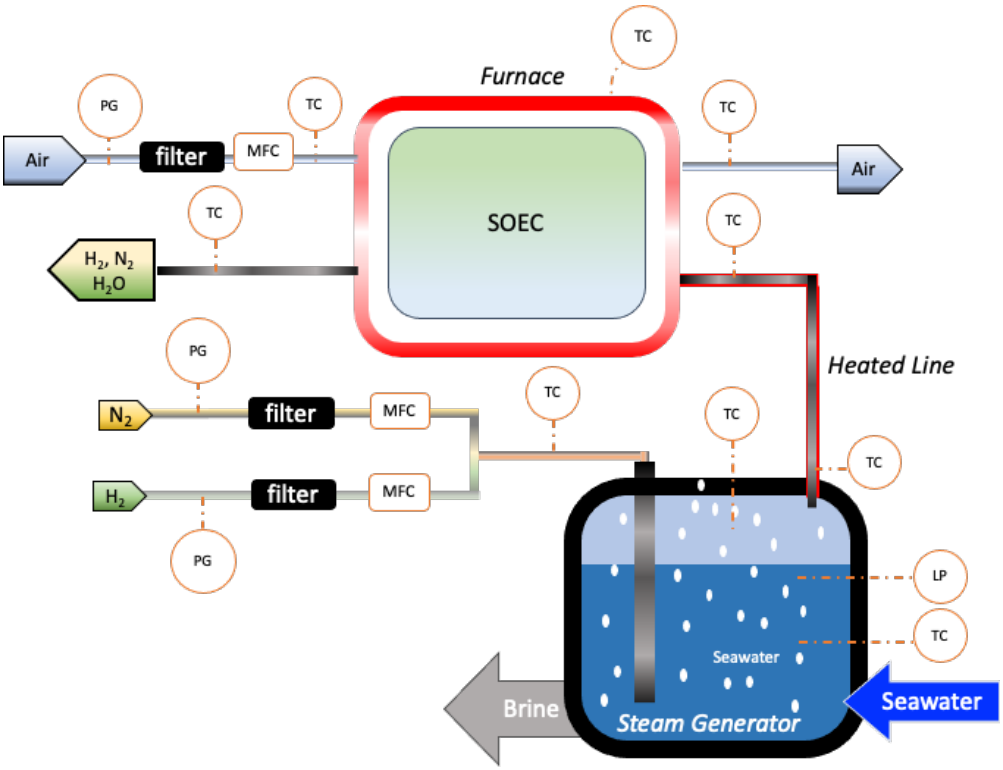

Figure 7-8: Experimental Setup Schematic

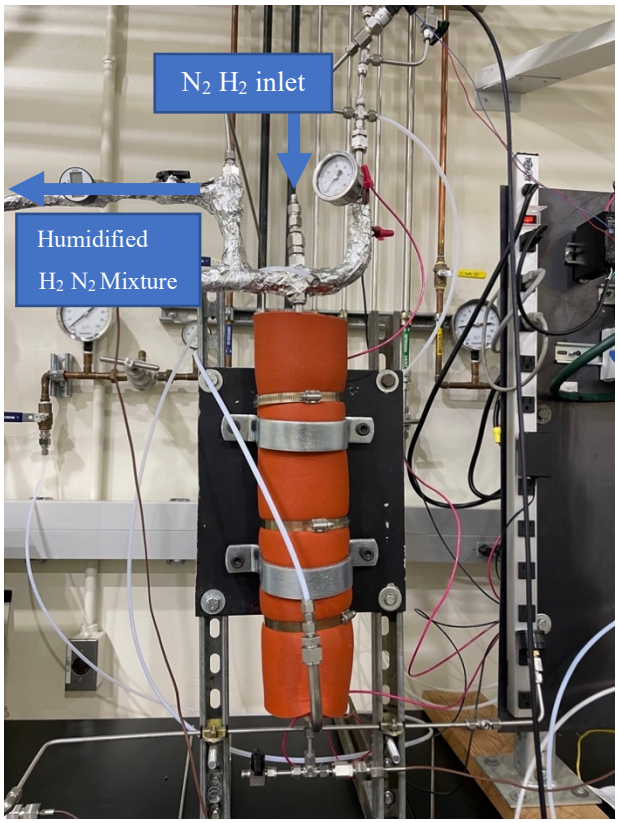

Figure 7-9: Steam generator system

Prior to the electrolysis tests, we calculated the moisture content, which is shown in below, using the humidity ratio and Dalton's law. To calculate the saturation vapor pressure of water, we used a formula derived from the Clausius-Clapeyron equation from [147]:

$$P_s = \frac{\exp\left(34.494 - \frac{4924.99}{t+273.1}\right)}{(t+105)^{1.57}} \qquad t > 0°C \qquad \textbf{(7-3)}$$

where Ps is the saturation pressure of water in kilopascals and t is temperature in Celsius. This equation is valid for temperatures greater than 0° Celsius.

Similar to prior work [[58], [60]], the moisture content is controlled by changing the temperature of the tank. This is relationship is expressed in the following equation:

$$\dot{n}_{H_2O} = x_{H_2O} * \dot{n}_{total} = x_{H_2O} * \dot{n}_{total} = x_{H_2O} * \frac{\dot{n}_{H_2} + \dot{n}_{N_2}}{1 - x_{H_2O}} \qquad \textbf{(7-4)}$$

Where $x_{H_2O} = \frac{P_s}{P}$ and P_s is the saturation pressure of water in kilopascals.

7.2.3 **Water Preparation**

In order to prepare the system for seawater electrolysis, we tested the system with four water types: deionized (DI) water, tap water, simulated seawater, and real seawater from Newport Beach, California. We prepared the simulated seawater by mixing sea salt with DI water to achieve an average concentration between 33-37 g/L, which is the average salinity in seawater [148]. Since conductivity can be used to assess the purity of water, we measured the conductivity of the condensate of the four different water types. We also measured the conductivity of each water type before evaporation, the condensate we collected after evaporating the water, the water in the steam generator tank. These results are summarized in Table 7-6.

One important observation about this experimental setup and similar setups with seawater is that the concentration of salt increases with time, as more of the water evaporates leaving the steam

generator with a higher concentration of salt each time. The seawater with a higher concentration of salt has a higher probability of contaminating the cell and ancillary parts of the experimental set-up. In order to account for the potential contamination effects of salt at different solubilities, we used a conductivity sensor to periodically measure the levels of salinity in the tank throughout the experiment. We also measured the purity of the condensate of water at various different levels of salinity (low, medium, high).

7.2.4 **Electrochemical Performance Characterization**

We used polarization curves and electrochemical impedance spectroscopy (EIS) to characterize the performance of the cell with the different water types. The polarization curves and electrochemical impedance spectra were obtained using Princeton Applied Research Versastat 3 potentiostat with a booster for potentiostatic measurements (applied voltage). Following the statistical analysis presented in [149], the polarization curve measurements were analyzed with a t-student distribution with 3 degrees of freedom to assess the statistical significance of the data:

$$\bar{x} - t_{95\%,3}SE \leq \mu \leq \bar{x} + t_{95\%,3}SE \quad \textbf{(7-5)}$$

Where $\bar{x}$ is the sample mean, $t_{95\%,3}$ is the cutoff value of the t-distribution based on the confidence interval and the degrees of freedom, SE is the sample error, and μ is the 95% confidence interval. The sample error is given by:

$$SE = \frac{s}{\sqrt{n}} \quad \textbf{(7-6)}$$

Where s is the standard deviation and n is the sample size.

The EIS measurements were performed with a signal amplitude of 10 mV between a frequency range of 0.1-100,000 Hz. The impedance data was checked for consistency with the Kramer's Kronig relations using the Measurement Model Python program ([150]). Representative residuals of the Kramer's Kronig relations are shown in Figure 7-10 for two of the EIS results. To assess the impedance spectra data, we used Ciucci's DRTtools software on Python from [142] to perform a Tikhonov regularization, which was previously used to study solid oxide fuel cells [139]. A Gaussian discretization method with a first order regularization derivative, a regularization

parameter of 0.001, 2000 samples, and a coefficient of 0.5 for the full width half maximum of the radial basis function. Table 7-1 shows the test plan for EIS tests.

Table 7-1: Test plan for Electrochemical Impedance Tests

EIS Experiment	Voltage (V)	# of tests
1	OCV (0.88)	4
2	1.08	4
3	1.38	4

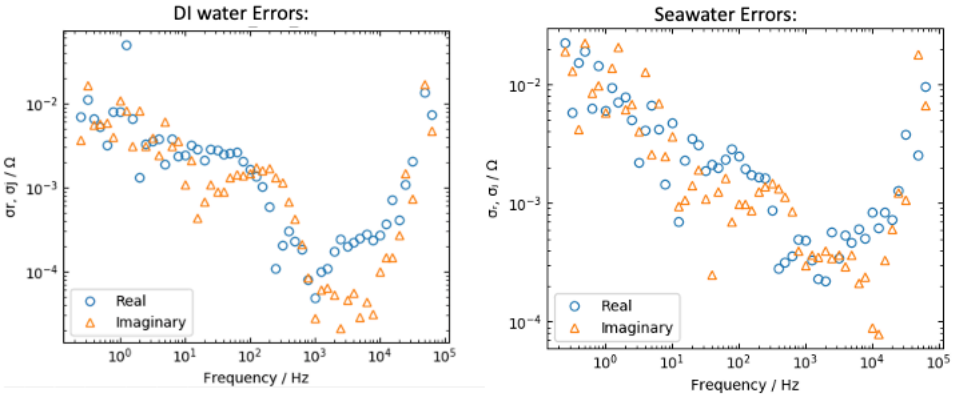

Figure 7-10: Sample residuals of the Kramers-Kronig residuals as a function of frequency for the DI and seawater results with 0.5 SLPM H_2 at 1.38 V.

7.3 Experimental Results and Discussion

7.3.1 Initial Electrochemical Characterization

The cell was operated for over 1000 hours with DI water, tap water, and simulated seawater. The polarization curves and electrochemical impedance spectra were performed for various experimental parameters, which are shown in Table 7-2. For these operating conditions, the theoretical open circuit voltage from the Nernst equation is **0.871 V.** For convenience and clarity, the Nernst equation I used to calculate the open circuit voltage is pasted below:

$$U_{rev,ocv}(T, P_i) = U^o(T, P) + \frac{RT}{nF} \ln\left(\frac{p_{H_2} p_{O_2}^{\frac{1}{2}}}{p_{H_2O}}\right) \quad (7\text{-}7)$$

The units for the pressures should be in bar.

Table 7-2: Experimental Parameters

Fuel Flow (SLPM)	N_2 Flow (SLPM)	Air Flow (SLPM)	H_2O Flow (SLPM)	H_2 (%vol)	N_2 (%vol)	H_2O (%vol)	Furnace Temp (°C)	Steam Generator Temp (°C)
0.5	0.5	1	1.105	21	21	57	750	85
0.25	0.25	1	0.497	21	21	57	750	85
0.125	0.125	1	0.276	21	21	57	750	85

Figure 7-11 shows the polarization curves for the initial DI water tests at these various operating conditions. The three flowrates tested represent different steam utilizations, which should lead to differences in the polarization curves. In theory, lower steam utilization, which is associated with a higher nitrogen and hydrogen flowrate, should result in lower concentration losses since the concentration of steam at the reaction sites will increase. The lower concentration losses should result in lower voltages. Figure 7-11 clearly shows that the DI water test with the 0.5 SLPM flow deviates significantly from the cases with 0.125 SLPM and 0.25 SLPM. The results suggest the cell performed best initially in the scenarios with the 0.5 SLPM flowrate than in the 0.125 and 0.25 SLPM scenarios. There are a few possible reasons for this deviation: (1) the 0.5 SLPM flowrate scenario shows improved performance due to the lower concentration losses associated with the higher flowrates and steam utilization; (2) since the 0.5 SLPM test occurred at approximately hour 400, and the 0.25 and 0.125 SLPM tests occurred approximately at hours 530 and 550, respectively, it may be that the test at 0.5 SLPM occurred during the break-in period of the cell, before it endured morphological changes that degraded its performance due to a significant amount of chronopotentiometry and EIS testing; (3) it may also be that the higher flowrates at 0.5 SLPM resulted in a higher convection coefficient in the flow channels of the cell that increased the temperature of the reaction sites in the cell, although this is unlikely.

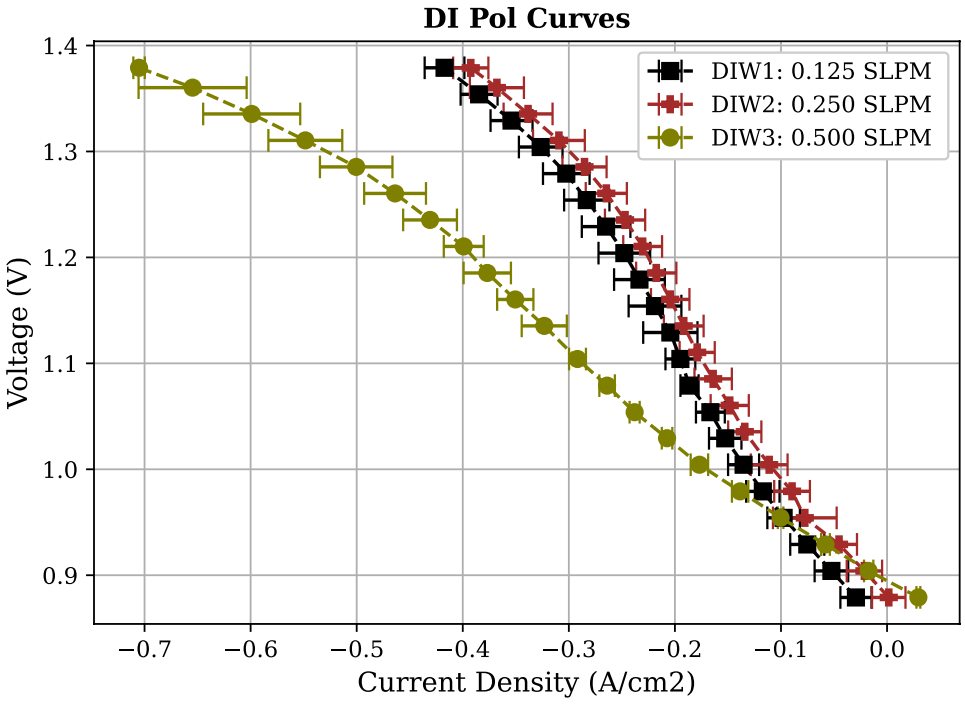

Figure 7-11: Initial polarization curve for the DI water scenario.

The fact that there is no difference between the 0.125 and the 0.250 SLPM tests is a surprising result because in theory, the different flowrates should affect the polarization curve results and the 0.250 SLPM test should reflect better performance than the 0.125 SLPM results. One possible explanation for these results is that at the range of current densities tested, the concentration losses are miniscule in comparison to the ohmic losses. If this is true, then any improvements in the concentration losses will not be noticed in the polarization curves.

It is also important to point out the shape of the polarization curve in the initial DI water tests which shows a deviation from expected results in the region of higher current density. Typical polarization curves for SOEC tests experience mostly ohmic losses with negligible evidence of activation polarization in the low current density region and little to negligible concentration polarizations in the high current density region. The result shows an unexpected nonlinear and non-exponential behavior in the region of higher current densities, which would suggest concentration losses and resistances that are lower than expected and seen in most SOEC experiments. A possible explanation for this is that the cell undergoes a significant break-in

period in the first 500 hours of operation, making it more susceptible to changes in flowrates and utilization factors. Since the concentration polarization is a function of the microstructure (tortuosity), diffusion, adsorption/ desorption effects, partial pressures and current density [54], it may be that the cell experienced microstructural changes that affected both the gas diffusion and increased the resistance of the cell in the period between the 0.500 SLPM test and 0.125 and 0.25 SLPM tests. It is unlikely that these differences at high polarization are due to temperature since the concentration polarization is a weak function of temperature according to Singhal and Kendall in Ref [54]. To assess these possible explanations, the Nyquist plots and Bode plots are analyzed and presented in the following section. Because the 0.500 SLPM test deviates so significantly from the other tests, the 0.500 SLPM result will not be considered in subsequent analyses.

The results for the tap water tests are more consistent with each other. First, the polarization curves of each of the three scenarios are mostly in agreement with each other. All of the tests occurred within 72 hours of each other with the 0.250, 0.125, and 0.5 SLPM tests occurring approximately at hours 600, 648, and 672, respectively. Interestingly, the 0.500 SLPM scenario shows a small but noticeable deviation from the other two scenarios. Although, the deviation is not as significant as in Figure 7-11 the trend resembles the DI water results: 0.500 SLPM shows improved behavior in comparison to the 0.125 and 0.25 SLPM scenarios, which may be due to reduced concentration losses at the higher flowrates that enable lower steam utilization. These results also show a mostly linear behavior between current and density, suggesting that the ohmic losses dominate in the cell. There is a slight nonlinear behavior observed for the 0.125 and 0.25 SLPM cases in the moderate to high current density region (-0.25 – 0.4 A/cm2).

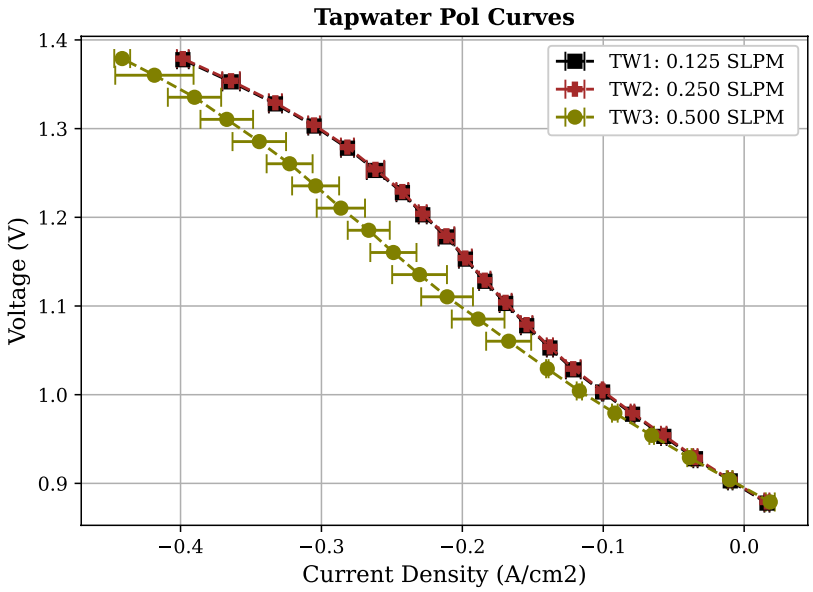

Figure 7-12: Polarization Curve results for the tap water scenarios.

When comparing the DI water results to the tap water results in Figure 7-12, it can be clearly seen that all of the polarization curves of the tap water results are in good agreement with the polarization curves of the DI water scenarios 0.125 and 0.25 SLPM. This means that the cell did not experience any noticeable degradation between hours 550 and 672, which is the period between the end of the DI water tests and the beginning of the tap water tests. There is a noticeable difference in the 0.500 SLPM results with DI water (see Figure 7-13), which highlights the transient effects of changes in the morphology of the cell in the first 550 hours of operation. This can be further verified by comparing the EIS spectra of the DI water and tap water results.

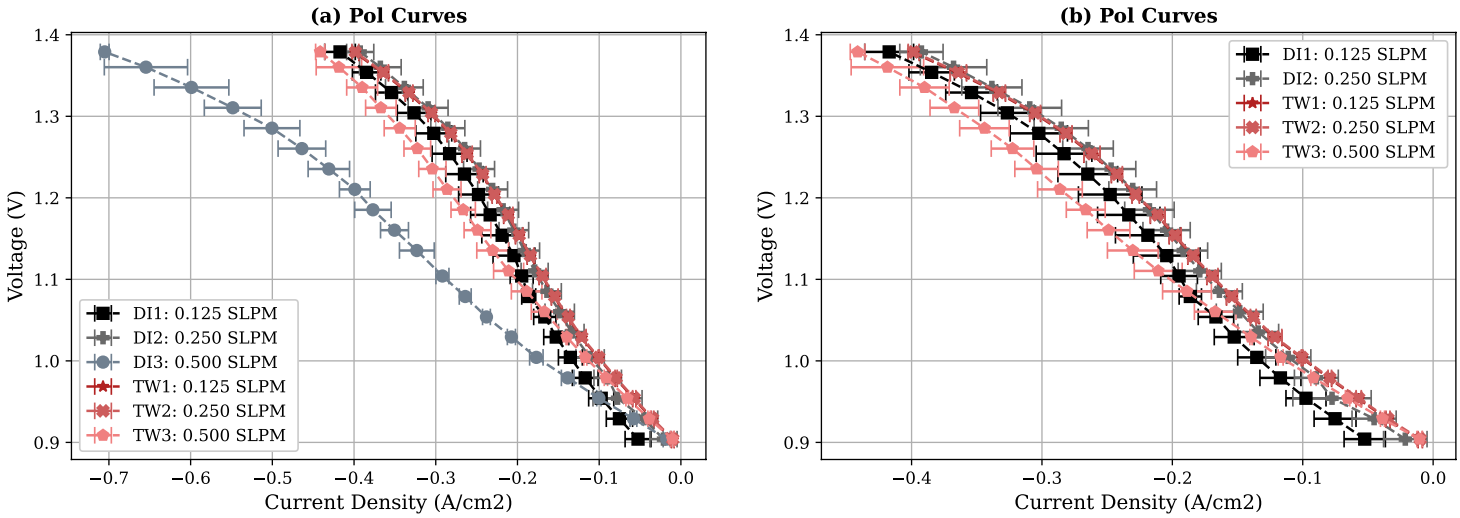

Figure 7-13: Comparison of the polarization curves for tap water and DI water.

The results for the seawater tests are shown in Figure 7-14. The polarization curves for the three scenarios in the seawater tests are entirely linear and show good agreement with each other. The entirely linear behavior suggests ohmic losses are the dominant polarization, which will be confirmed via EIS. The results for the 0.125, 0.250, and 0.500 SLPM scenarios occurred at hours 792, 768, and 720, respectively. Furthermore, an additional polarization curve test occurred at hour 840 in which each point along the curve was held for 900 seconds instead of 240 sec. These results are show in Figure 7-14. Figure 7-14 demonstrates that the error bars increase significantly with increasing magnitude of current density. Although the mean results for the long hold test suggests that there is a mostly linear current-voltage relationship, it may be that as the effects of concentration polarization become more prevalent in the cell, the cell's performance is more unstable due to the impact of gas diffusion, which may have transient effects on the cell. These results also illustrate that each polarization curve represents a snapshot in time of the cell and that its performance may be highly transient and dynamic, which may have important implications for the EIS results.

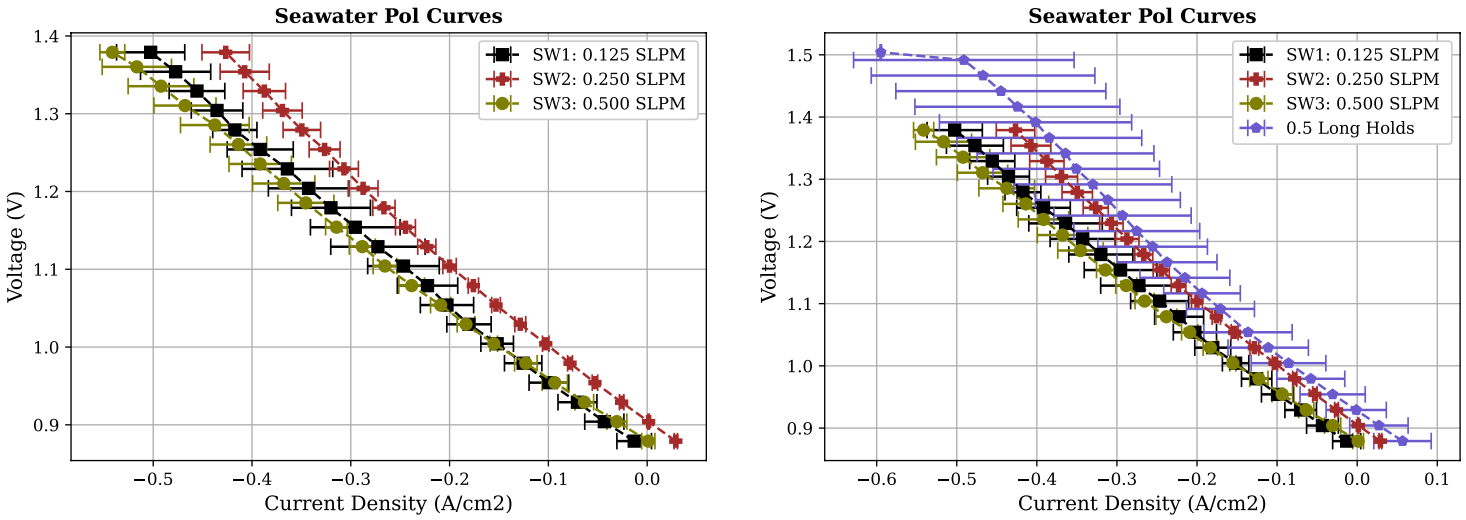

Figure 7-14: Seawater polarization curves. The right figure shows the results with long holds.

Furthermore, compares the performance of the cell under the various water types and operating conditions. Note, that the DI water test at 0.500 SLPM is omitted since it is likely due to initial changes in the morphology of the cell during the "break-in" period. The results in - Figure 7-16 are not what one would expect from a comparison of seawater to DI water. First, the results for 0.125 and 0.500 SLPM seawater cases (SW1 and SW3), show lower voltages for the same current density than for all of the other cases. This means that for the same hydrogen produced (linearly related to current density), a lower voltage, and thus power), was required in the SW case. The expectation is that there would be reduced performance in the seawater case due to the possibility of contaminants in the steam and the typical cell degradation that occurs over time. It is important to note that the results for the seawater case with 0.250 SLPM are in alignment with the tap water and DI water results. This suggests that there could have been some morphological changes during testing that reduced the resistance and improved the performance of the cell. Passivation will be further analyzed in the EIS section that follows. The cell successfully operated with non-traditional water types for over 400 hours, after operating with DI water for approximately 550 hours. The results do seem to suggest that solid oxide electrolysis cells may be able to successfully operate without the ultrapure water that is typically used in existing systems. This can have significant implications for the balance of plant, environmental footprint,

and deployment of these systems. Ultimately, the impurities in the water did not cause the cell to fail. The cell failed due to an interruption in the fuel electrode gas flow when LabView crashed.

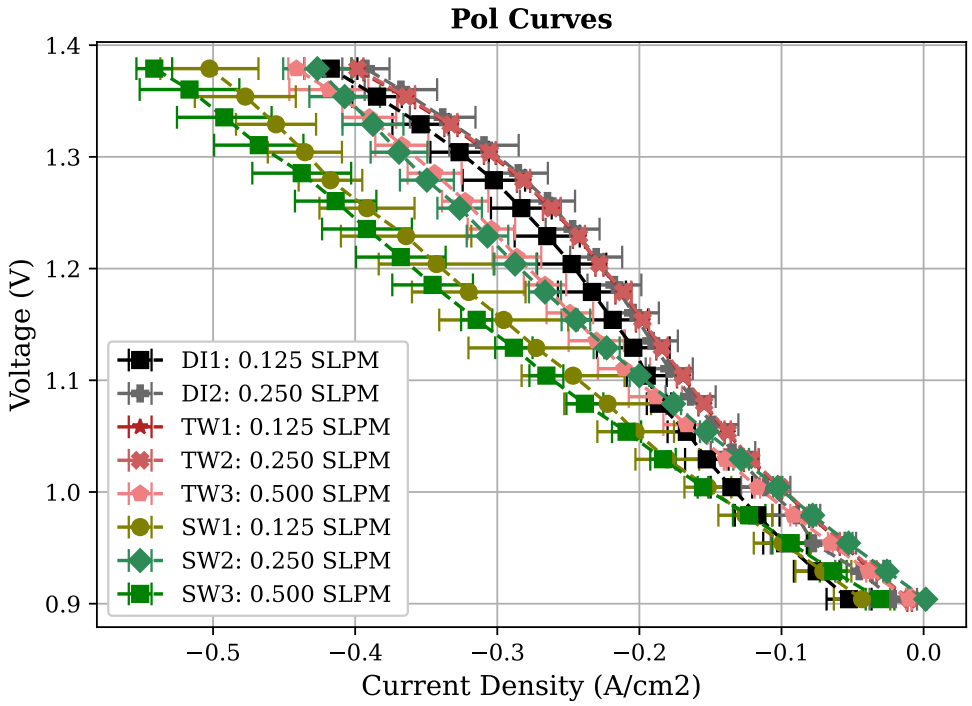

Figure 7-15

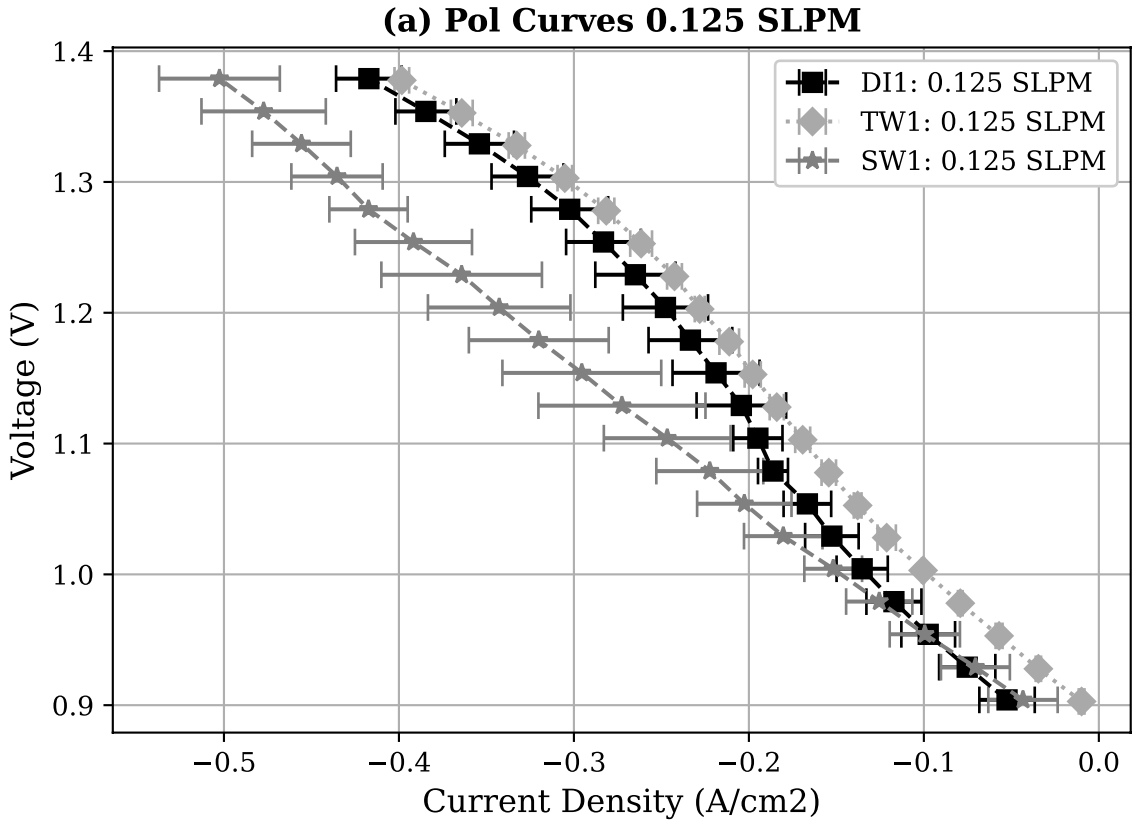
(a) Pol Curves 0.125 SLPM
DI1: 0.125 SLPM
TW1: 0.125 SLPM
SW1: 0.125 SLPM
Voltage (V)
Current Density (A/cm2)
1.4
1.3
1.2
1.1
1.0
0.9
−0.5
−0.4
−0.3
−0.2
−0.1
0.0

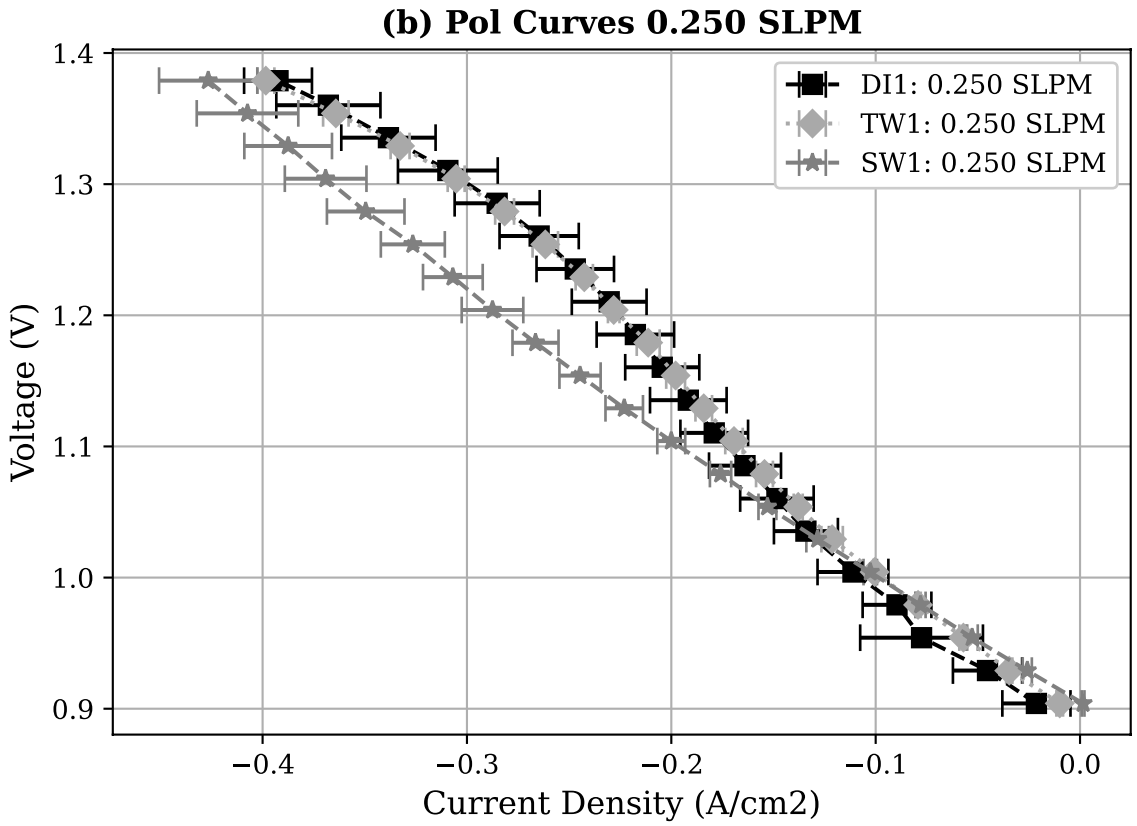
(b) Pol Curves 0.250 SLPM
DI1: 0.250 SLPM
TW1: 0.250 SLPM
SW1: 0.250 SLPM
Voltage (V)
Current Density (A/cm2)
1.4
1.3
1.2
1.1
1.0
0.9
−0.4
−0.3
−0.2
−0.1
0.0

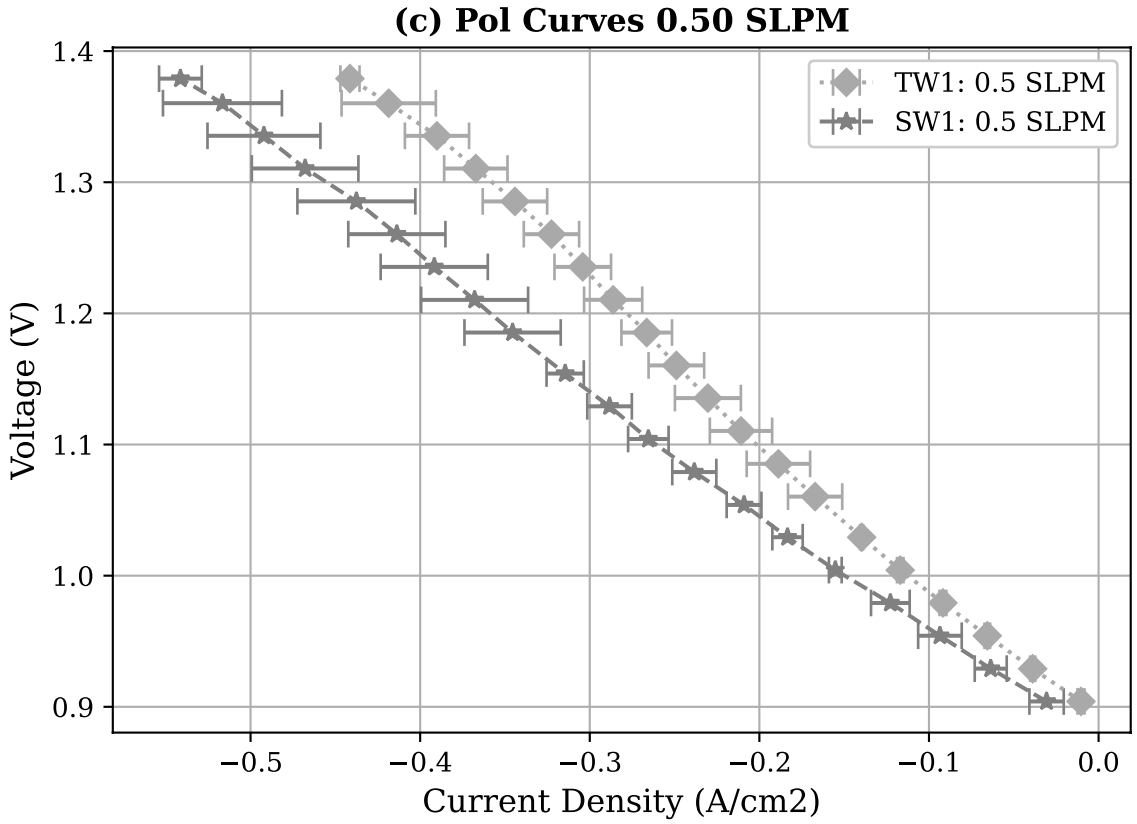

Figure 7-16: Comparison of the polarization curves of each water type for (a) 0.125 SLPM; (b) 0.250 SLPM; and (c) 0.500 SLPM.

7.3.2 **Electrochemical Impedance Spectroscopy**

The literature states that only validated impedance spectra data should be analyzed and used for modelling, and that the data must be repeatable and stationary [140]. This should be checked in the Nyquist plots and Bode plots. To begin the EIS analysis of the DI water data, the Nyquist and bode plots at various voltages are shown below in Figure 7-17 and Figure 7-18 using the raw data. Recall that each test was repeated four times under a potentiostatic perturbation (an AC voltage was applied, and an AC current measured) at various different operating voltages with an amplitude of 10 mV. First, note that the Nyquist plots of the 0.125 and 0.25 SLPM scenarios are in agreement with each other for all of the cases. This is consistently true for all of the voltages tested and it can be confirmed in the Bode plots, which suggest these results are suitable for modeling and analysis. For the OCV scenario, there is significant variability and noise in the

region of low frequency. This is observed across all of the voltages tested, and it is confirmed in the Bode results that show the data tends to be noisiest in the region of low frequency. The ohmic polarization tends to be approximately 0.48 Ohms cm^2 for each of the voltages tested with 0.125 and 0.25 SLPM.

Secondly, notice that the 0.500 SLPM scenario deviates from the results for the 0.125 and 0.25 SLPM scenarios; its ohmic and polarization resistance are significantly smaller for each of the voltages. This result is in agreement with the polarization curves which confirms that the 0.5 SLPM scenario for DI water performed better than the scenarios with lower flowrates. A lower resistance will result in improved performance. The difference in performance between the 0.500 SLPM scenario and the lower flow rate scenarios could be attributed to transient effects in the microstructure of the cell that led to significant degradation in the oxygen-electrode electrolyte interface that has been reported as the major type of degradation in SOECs [151].

An additional observation here is that although we would expect to see the overall polarization resistance to increase with voltage, the impedance at 1.38 V is significantly smaller than the impedances at the 1.08 V, 1.18V, and 1.28V. In the 0.125 and 0.25 SLPM scenarios, the polarization resistance increases from approximately 0.82 to 1.45 Ohms cm^2 between OCV and 1.28V. In the final voltage, 1.38V, the polarization resistance decreases to about 1.28 Ohms cm^2. A similar trend can also be observed for the 0.500 SLPM scenario. This finding also may suggest an interesting result about the initial state of the cell that is related to the unexpected nonlinear curvature of the polarization curves in the area of high current density/ high voltage: in the first 550 hours of the cell operation with DI water the cell experienced reduced concentration polarization in the region of high current density. An investigation of the morphology of the cell may reveal the reasons for this finding. Additionally, the appendix includes the Bode plots with the imaginary and real impedance on the y-axis for each set of tests. The plots for each test are plotted together in the appendix for an easier comparison of the voltages. Due to the low drift and high replicability, the results chosen for further analysis and modeling are the 0.125 and 0.250 SLPM DI water scenarios at the following voltages: OCV, 1.08V, and 1.38V.

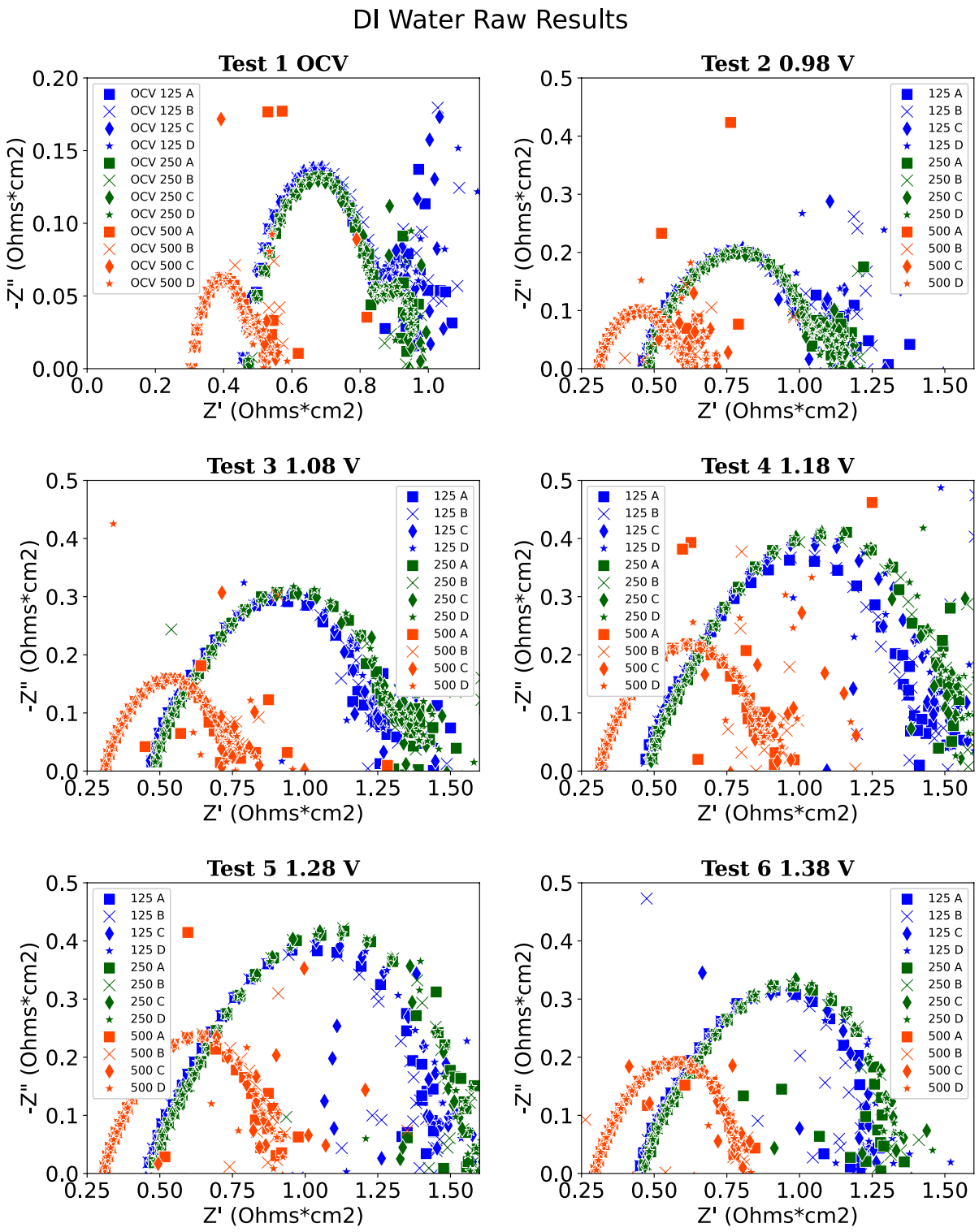

Figure 7-17: DI water EIS results using raw data.

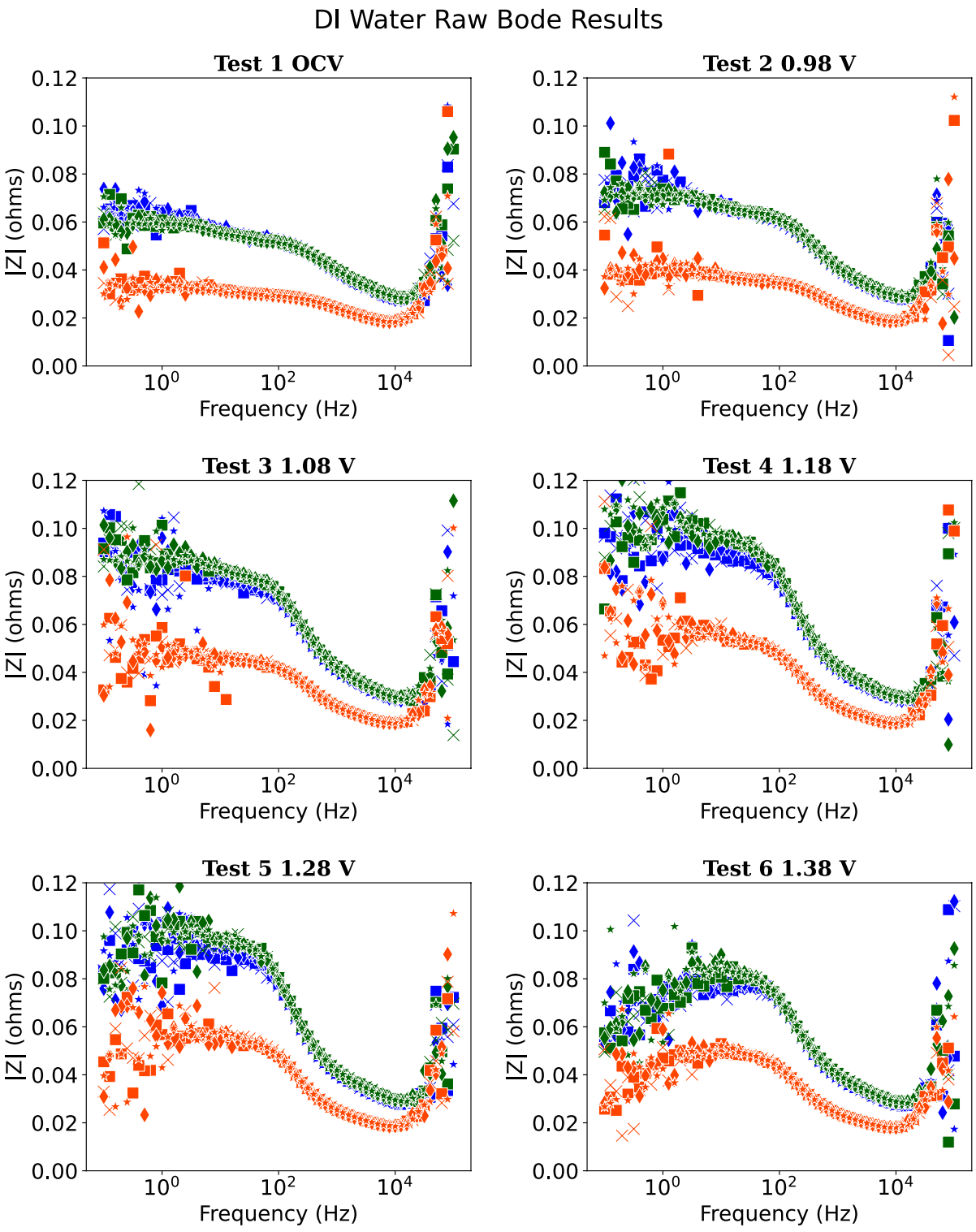

Figure 7-18: DI water bode results with the raw data.

Next, the results for the tap water EIS tests will be presented and discussed in Figure 7-19 and Figure 7-20. Unfortunately, due to a problem with the software (Versastudio), the EIS results for the 0.125 SLPM case with tap water could not be recovered. Therefore, only the results for the 0.25 and 0.500 SLPM cases can be shown and analyzed. The results at OCV and 0.98 V are nearly identical in the Nyquist plot and the Bode plots for both flowrates. The results in the Bode plots are in excellent alignment across all of the voltages examined. The ohmic resistances are consistently approximately 0.45 Ohms cm^2 in all of the voltages, which means that the ohmic resistance did not change. There is a noticeable increase in the overall polarization resistance in both flowrate scenarios for voltages of 1.08, 1.18,1.28 and 1.38V (test 3 – 6) that is due to the higher contribution of charge transfer reaction impedances in the electrodes and concentration polarizations. The Nyquist plots show that the polarization resistance stays at relatively constant value of approximately 1.0 Ohms cm^2 in the 1.08 and 1.18 V tests; and for the 1.28 and 1.38 V tests, the polarization resistance is approximately 1.2 Ohms cm^2. The results suggest that the 0.25 SLPM results have a slightly higher polarization resistance in comparison to the 0.5 SLPM case that is more noticeable with increasing voltage. This is consistent with the polarization curves which showed that the 0.5 SLPM scenario had better performance at higher current densities. Additionally, the results seem to suggest the polarization resistance increases with voltage except for the final voltage tested, 1.38V. Similar to the DI water results, it appears are though the cell experiences a reduction in the resistance at high current densities. This is an unexpected finding that is correlated to the results observed in Figure 7-17 for the DI water scenario.

In comparison to the DI water results, the tap water results are much more consistent with each other. Additionally, the ohmic resistances are similar to those in the DI water results with flowrates of 0.125 and 0.25 SLPM. The tap water results show a lower overall polarization resistance for the tests at 0.98 - 1.38 V. The comparison of EIS results is mostly consistent with the polarization curves that show very similar behavior between the 0.125 and 0.25 SLPM cases with the DI water and all of the tap water flowrates.

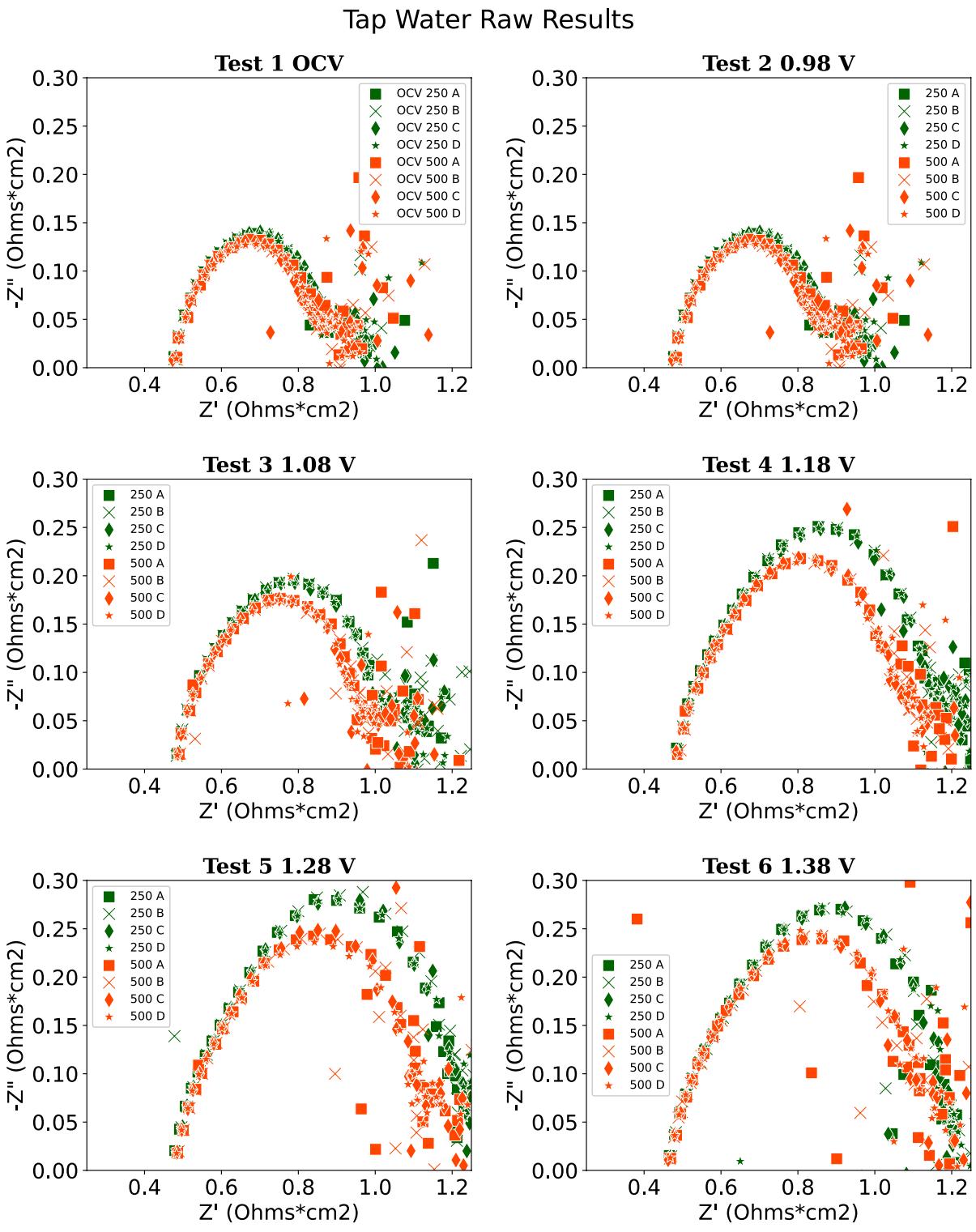

Figure 7-19: Tap water EIS results with raw data.

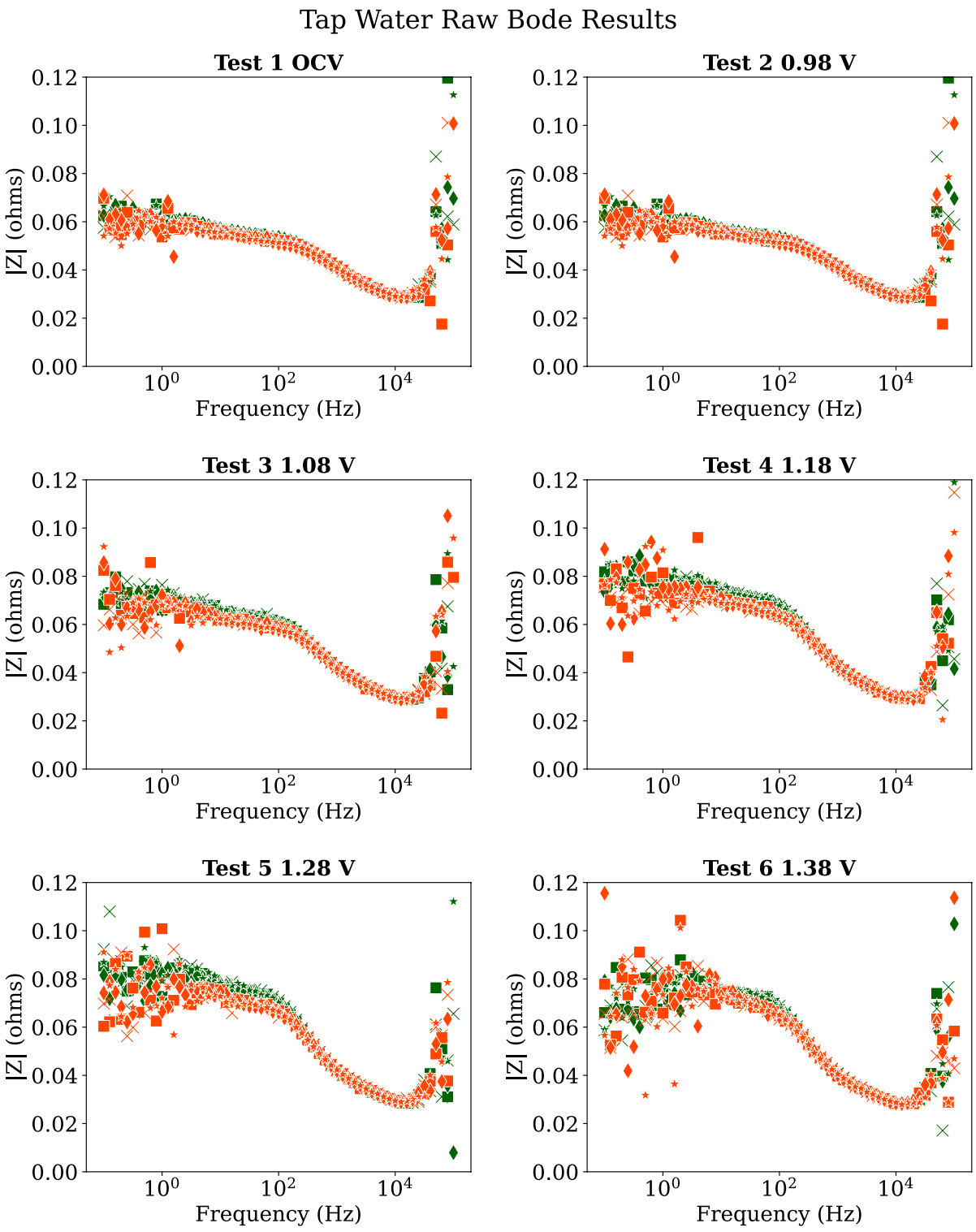

Figure 7-20: Tap water bode results with raw data

Lastly, the initial characterization of the impedance will be discussed for the seawater scenarios in Figure 7-21 and Figure 7-22. At a first glance, the seawater results suggest that the 0.25 and the 0.500 SLPM cases have high replicability and low drift. The Bode figures and the Nyquist plots show there is a high resemblance between these two cases. This result matches the polarization plot which showed similar performance between the 0.25 and the 0.500 SLPM flowrates. Additionally, the figures show that the data is quite noisy in the low frequency region, which is consistent with the tap water and DI water results. The data becomes significantly noisier as the voltage increases. For all of the voltages and flowrate scenarios studied, the ohmic resistance (approximately 0.49 Ohm cm^2 for all the cases) appears to match the ohmic resistance observed in the tap water and DI water cases. In the OCV results, the 0.125 SLPM Nyquist plot is shifted to the right slightly. It has a slightly higher overall polarization resistance. The drift becomes less significant with increasing voltage. The polarization resistances increase with increasing voltage for all of the flowrates, which is what would be expected for an SOE cell.

One very interesting finding in these results for the seawater is that the overall polarization resistance is much smaller than that of the other cases with different water types. The overall polarization values range between 0.7 and 1 Ohm cm^2. Additionally, the magnitude of the negative imaginary impedance (y-axis) is also significantly smaller for the cases with the seawater than in the previous results. From this preliminary analysis of the cell it does not appear as though the impurities in the seawater negatively impacted the performance. There must be a feature about the operating conditions that led to improved performance over time. It could be that the cell experienced a mechanism that reversed the formation oxygen bubbles in the anode due to the periodic cycling necessary for testing, similar to what Graves et al. discovered in Ref [151]. Graves et al. assessed the ability to reverse degradation of an SOE cell through reversible operation between fuel cell mode and electrolysis. The reversal of degradation relied on ceasing electrolysis polarization to release the “high oxygen pressure” that builds up in closed cavities near the oxygen-electrode/ electrolyte interface and leads to a high oxygen-electrode overpotential [151]. Although Graves et al. briefly discussed the results of their preliminary experiments that suggested that cycling between electrolysis and open circuit voltage did not have the same improvements and degradation prevention mechanisms as cycling with the fuel cell mode, the seawater results may suggest that periodic cycling to open circuit voltages over a

long-term test may lead to a reversal or delay in the degradation mechanisms that typically occur in electrolysis. Further post-mortem analysis may reveal more insights as to the degradation mechanisms. To further analyze the different sources that contribute to the overall polarization resistance, the EIS data was validated using the Kramers-Kronig relations and analyzed using DRT and an equivalent circuit model. This will be discussed in the next section.

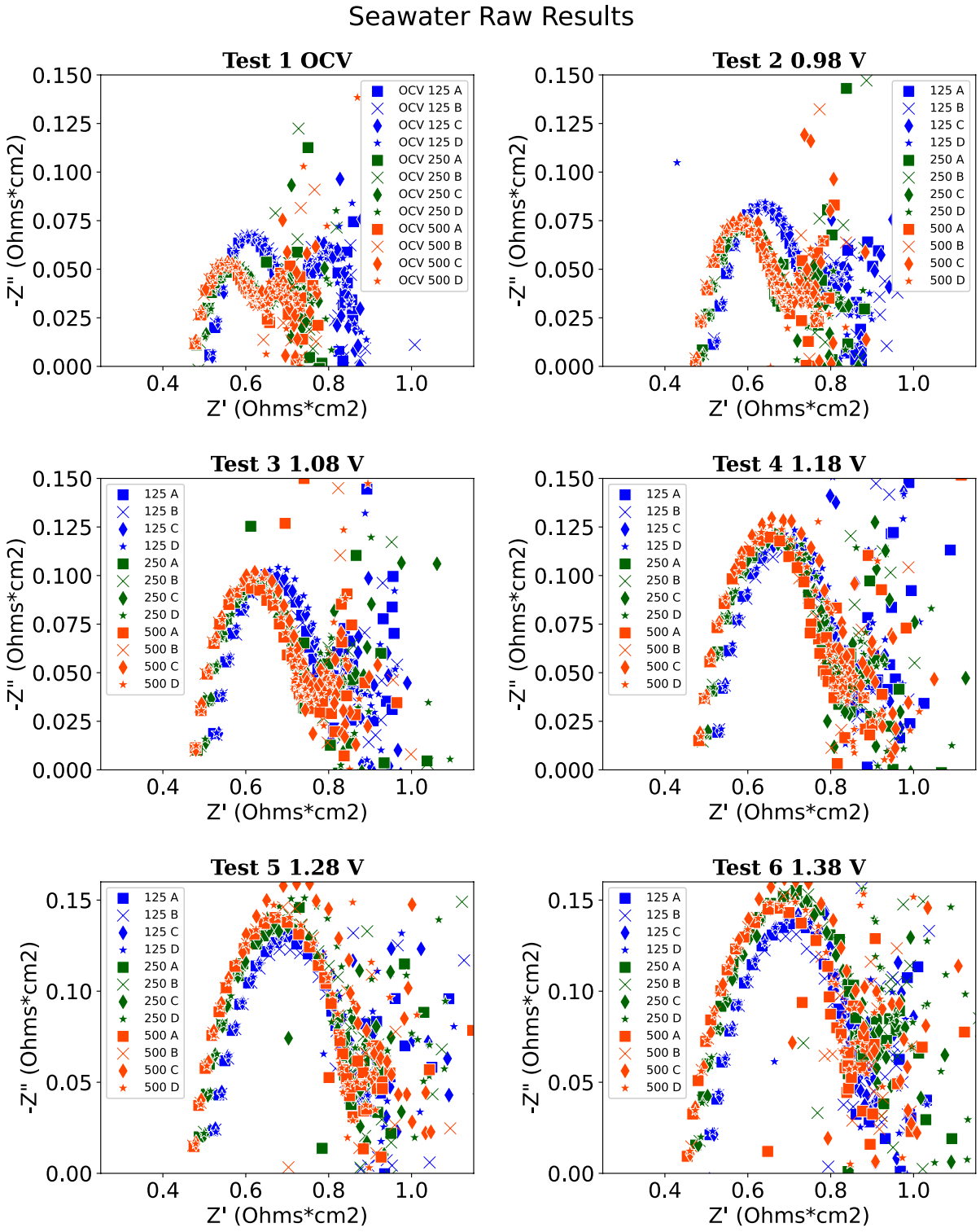

Figure 7-21: Seawater EIS results with the raw data.

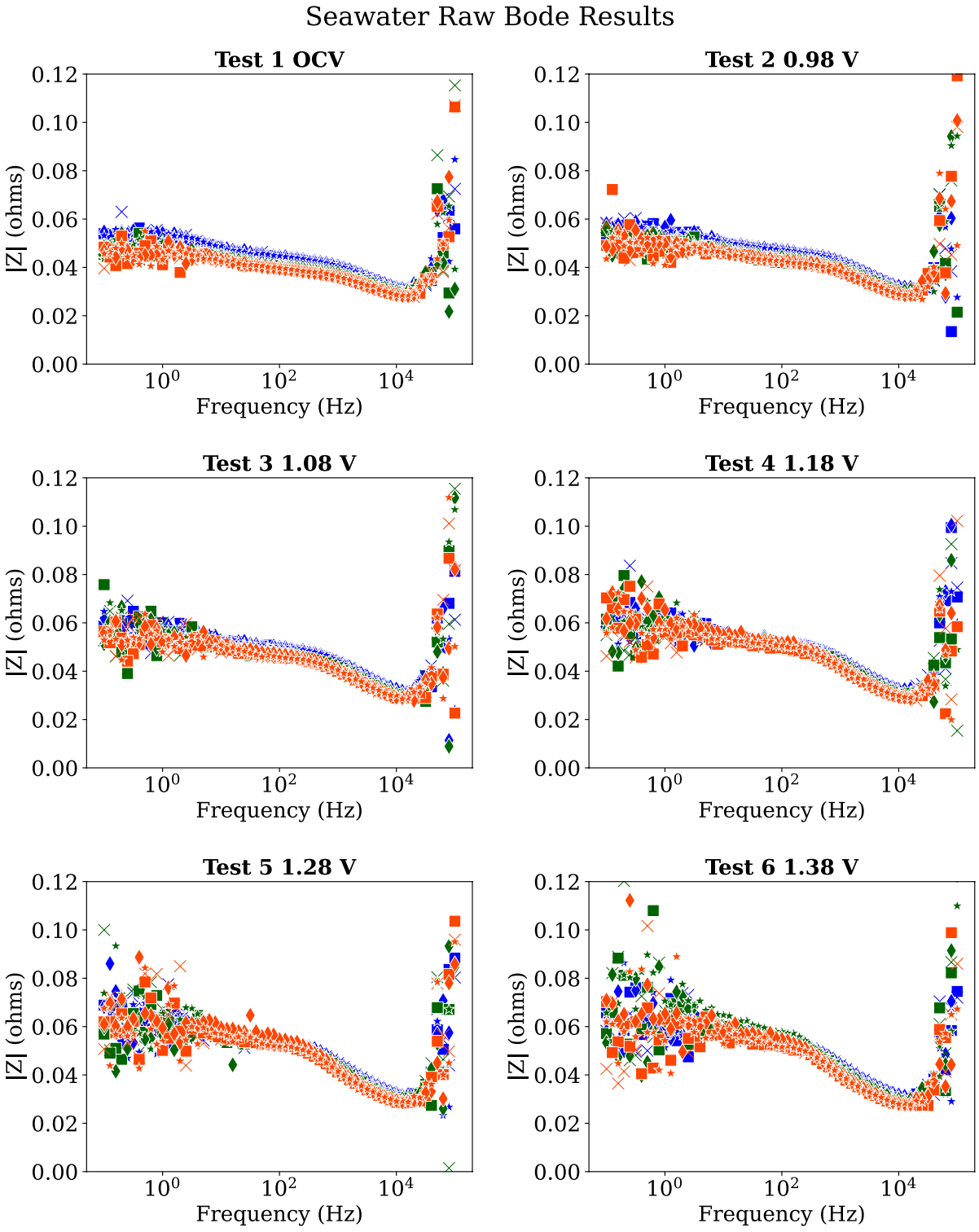

Figure 7-22: Seawater bode results with the raw data.

7.3.3 **EIS Analysis and Modelling**

This section aims to characterize the performance of the cell more closely by using EIS validation tools and modeling. The analyzed data will include 0.125 and 0.25 SLPM for DI water, 0.25 and 0.500 SLPM for tap water, and 0.25 and 0.500 SLPM for seawater, based on the preliminary analysis from the prior section. The analysis will utilize OCV, 1.08V, and 1.38V voltages.

7.3.3.1 Kramers-Kronig

This subsection will present the results from the data validation via the Measurement Model tool that uses the Kramers-Kronig relations. According to Lasia [140], one way to check that a dataset complies with the Kramers-Kronig transform is by comparing with original data with the transformed data to identify significant systematic differences. If the data are very different, then it means the dataset is not compliant with the Kramers-Kronig transform and the data should not be used for further analysis. Following this suggestion, the modelled data and the original data are presented below in Figure 7-23 - Figure 7-27. Every measured spectrum was analyzed by the Measurement Model to assess its compliance with the Kramers Kronig relations. Only the results that were successfully transformed using the Measurement Model tool were plotted. The literature also recommends analyzing the relative residuals between the measured impedance and the model impedance using the following equations [141]:

$$\Delta Re(w) = \frac{Z'(w) - \hat{Z}'(w)}{|Z(w)|} \quad \textbf{(7-8)}$$

$$\Delta Im(w) = \frac{Z'(w) - \hat{Z}'(w)}{|Z(w)|} \quad \textbf{(7-9)}$$

Where Z' and Z'' are the real and imaginary measured impedance, respectively; $\hat{Z}$ is the model impedance; $|Z(w)|$ is the magnitude of the measured impedance, which is a complex number, at a given frequency, w. If the relative residuals are below 1% the impedance data is assumed to fulfill the Kramers-Kronig relations, according to [141].

Figure 7-23 displays the Kramer's Kronig transformed data for the DI water results overlayed with the original data. Unfortunately, a significant drift occurred in the results which is

especially noticeable for the OCV case with 0.125 SLPM. Figure 7-24 displays some of the residuals for the 125 SLPM case, which shows the data has significant errors that lead to residuals that exceed 20%. The results for the 0.25 SLPM scenario are in the appendix. Since DRT requires that the data be validated, and the literature recommends only using data that is successfully represented by the Kramers Kronig transform, most of the data was not compliant with the Kramers Kronig transform. DRT was performed on the Kramers Kronig model results with the smallest residuals. Table x shows the average ohmic resistance, overall polarization, and capacitance for each scenario. The average ohmic resistance, 0.03 Ohms (0.48 Ohms cm^2), is mostly constant for each of the DI water tests analyzed. This ohmic resistance is also consistent with the preliminary analysis of the raw impedance data. The zero-frequency impedance, which is the low frequency intercept that occurs on the x-axis, varies between 0.06 and 0.08 Ohms, which causes the overall polarization impedance to vary. An increase in polarization impedance with voltage should be expected since higher voltage should result in higher current densities and higher concentration polarization losses. The polarization impedance increases with increasing flowrates for all of the voltages tested. This is most likely due to higher concentration losses with the higher flowrates. The capacitance is mostly constant for the 1.08 and 1.38 V cases. It is approximately 0.01 F.

Table 7-3 : Average DI water results from the Kramers Kronig relations

	0.125 OCV	***0.125 1.08V***	***0.125 1.38V***	***0.25 OCV***	***0.25 1.08V***	***0.25 1.38V***
Ohmic Resistance (Ω)	0.0309	0.0310	0.0297	0.0309	0.0320	0.0306
Zero frequency Impedance (Ω)	0.0613	0.0800	0.0763	0.0731	0.0837	0.0796
Polarization Impedance (Ω)	0.0304	0.0490	0.0466	0.0421	0.0518	0.0491
Overall Capacitance (F)	0.0110	0.0075	0.0073	0.0085	0.0074	0.0074

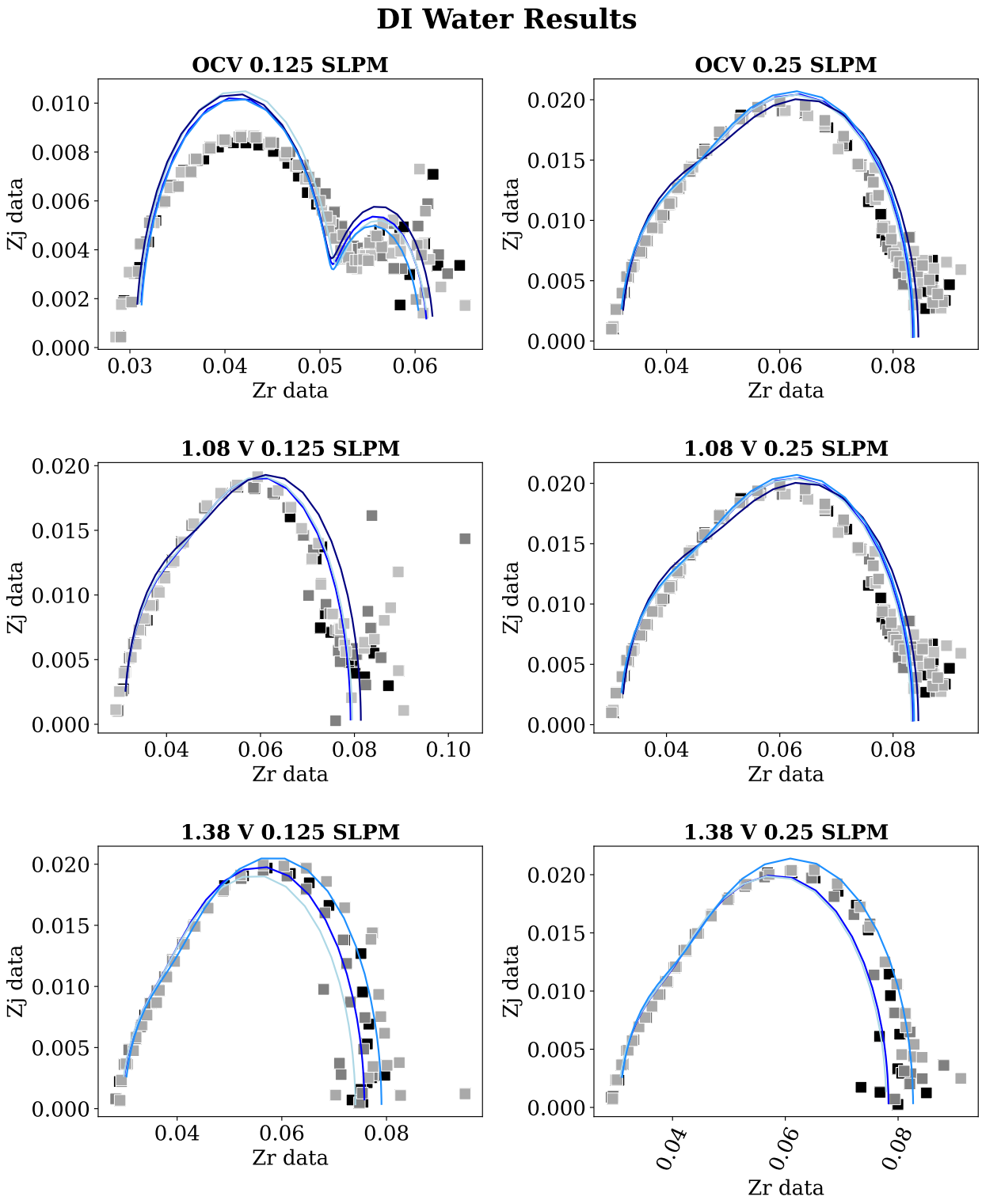

Figure 7-23: DI water Nyquist plot with Kramers Kronig results.

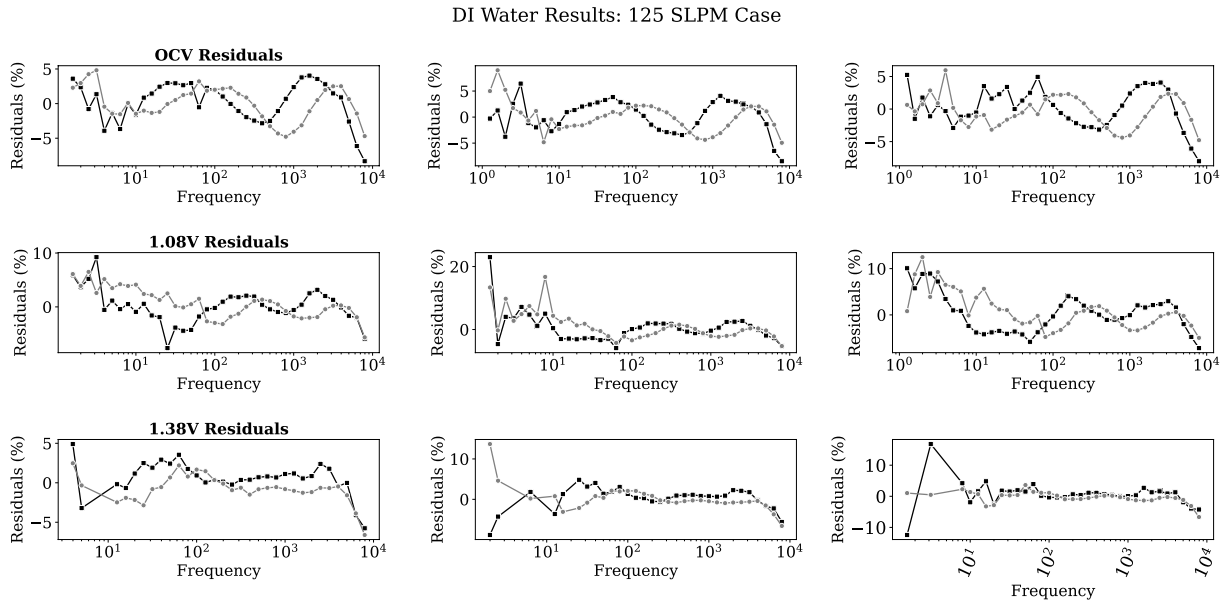

Figure 7-24: DI water residuals from the Kramers Kronig transform.

The tap water results, shown in Figure 7-25, for the Kramers Kronig transform also show a significant drift in the Nyquist plots, particularly for the OCV and the 1.08 V cases. This drift is also reflected in the high residuals in Figure 7-26, which are especially high in the region of high frequency. Unlike the results in Figure 7-23 for the DI tests, there is a more distinct second arc in the results for the tap water case. Table 7-4 shows the average ohmic resistance, overall polarization, and capacitance for each scenario from the Kramers Kronig relations. The average ohmic resistance, 0.03 Ohms (0.48 Ohms cm^2), is constant and consistent with the findings in the DI water tests. The polarization impedance seems to increase for the 0.25 SLPM tests with voltage. It is highest (~ 0.4 Ohms) for the cases with voltage at 1.38V, likely due to increased concentration polarizations. The residuals for the tap water tests are not quite as high as those for the DI water results.

Table 7-4: Average tap water results from the Kramers Kronig relations

	0.25 OCV	***0.25 1.08V***	***0.25 1.38V***	***0.500 OCV***	***0.500 1.08V***	***0.500 1.38V***
Ohmic Resistance	0.0305	0.0310	0.0298	0.0300	0.0313	0.0299
Zero frequency Impedance	0.0518	0.0664	0.0722	0.0693	0.0690	0.0748
Polarization Impedance	0.0213	0.0353	0.0424	0.0393	0.0377	0.0449
Overall Capacitance	0.0105	0.0075	0.0088	0.0089	0.0094	0.0081

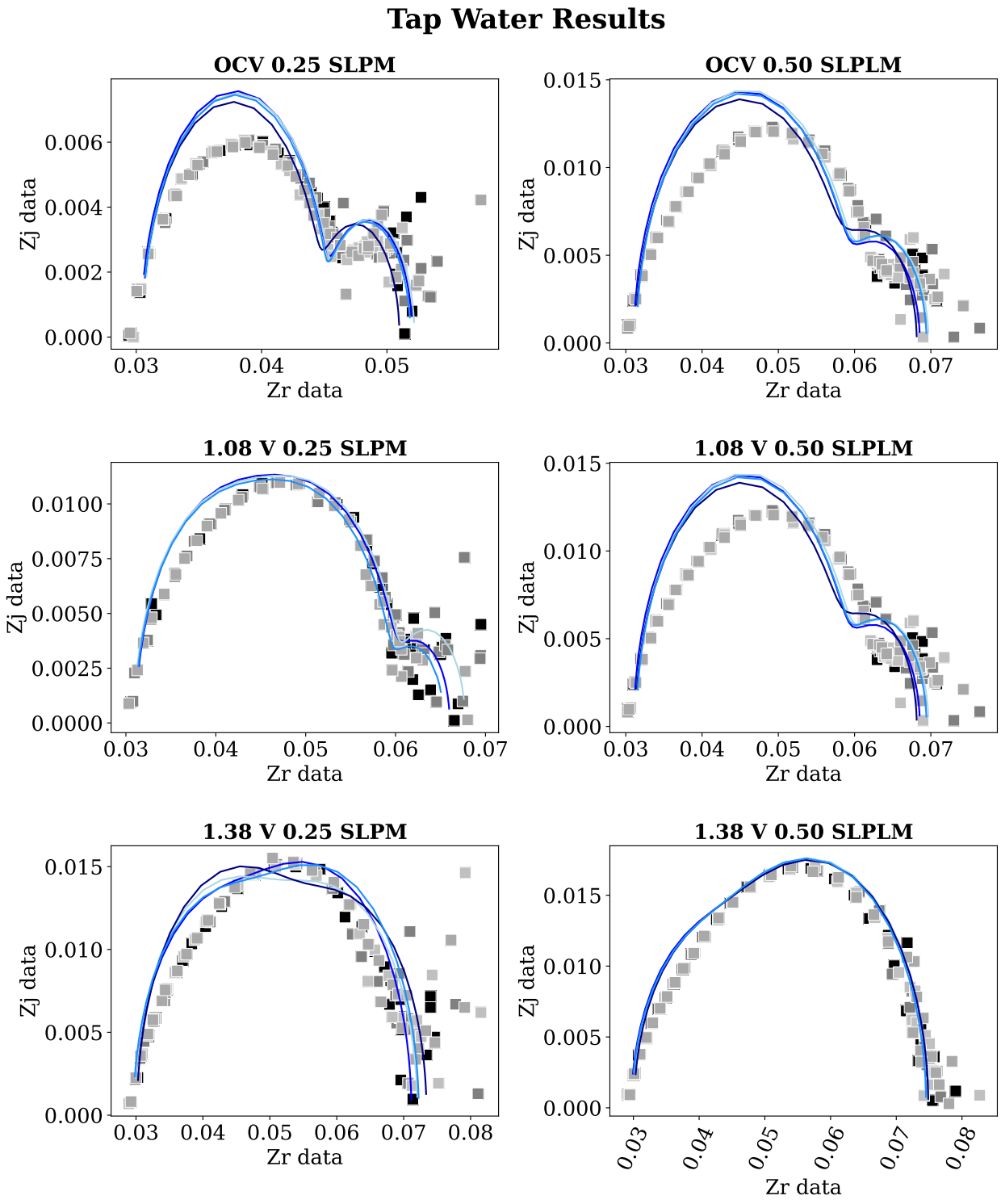

Figure 7-25: Tap water results from Kramers Kronig transform.

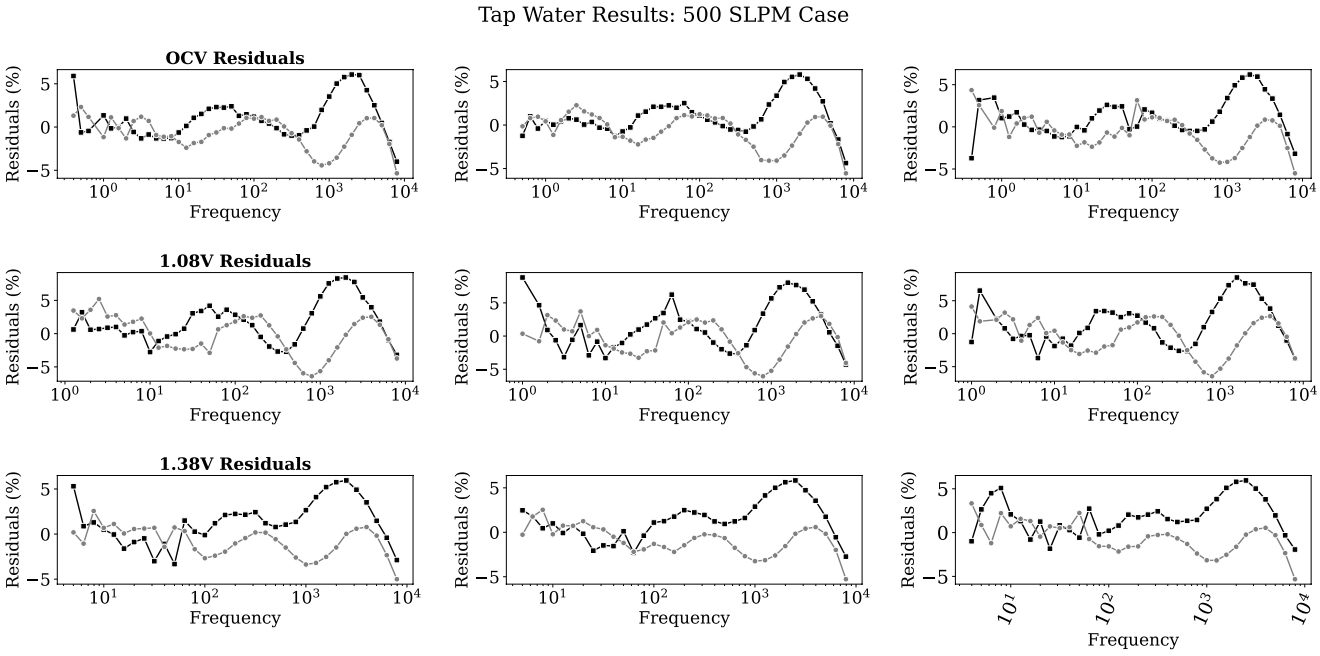

Figure 7-26: Tap water residuals from Kramers Kronig.

The results for the seawater cases are analyzed next. First, there is significant drift that occurs in the data, especially for the OCV cases and the cases at 1.08 V. The residuals are significantly high for the low frequency points. The Ohmic resistance is approximately 0.03 Ohms, and the values lie between 0.0277 and 0.0325 Ohms, which is a range of 4.8 mOhms. and the polarization impedance varies between 0.015 and 0.033 Ohms, which is much smaller than the polarization impedance measured in the previous tests. The seawater results do not seem to suggest that the polarization impedance increases with voltage, although this finding may be due to errors in the data and experimental set up.

Table 7-5: Average seawater results from the Kramers Kronig relations

	0.25 OCV	***0.25 1.08V***	***0.25 1.38V***	***0.500 OCV***	***0.500 1.08V***	***0.500 1.38V***
Ohmic Resistance	0.0316	0.0324	0.0321	0.0278	0.0312	0.0277
Zero frequency Impedance	0.0474	0.0528	0.0653	0.0424	0.0490	0.0441
Polarization Impedance	0.0158	0.0204	0.0332	0.0221	0.0178	0.0239
Overall Capacitance	0.0131	0.0088	0.0093	0.0156	0.0114	0.0149

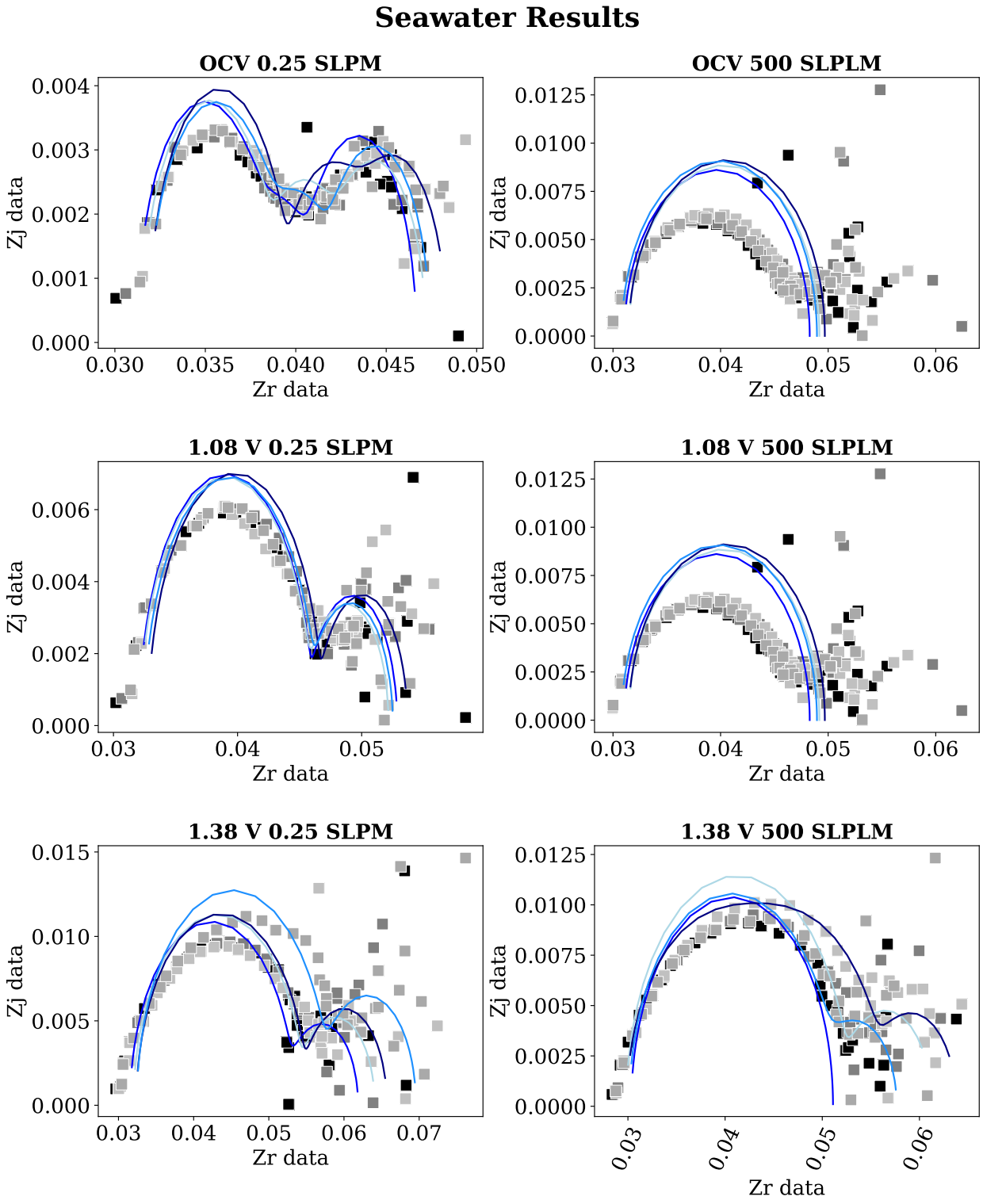

Figure 7-27: Seawater results from Kramers Kronig transform.

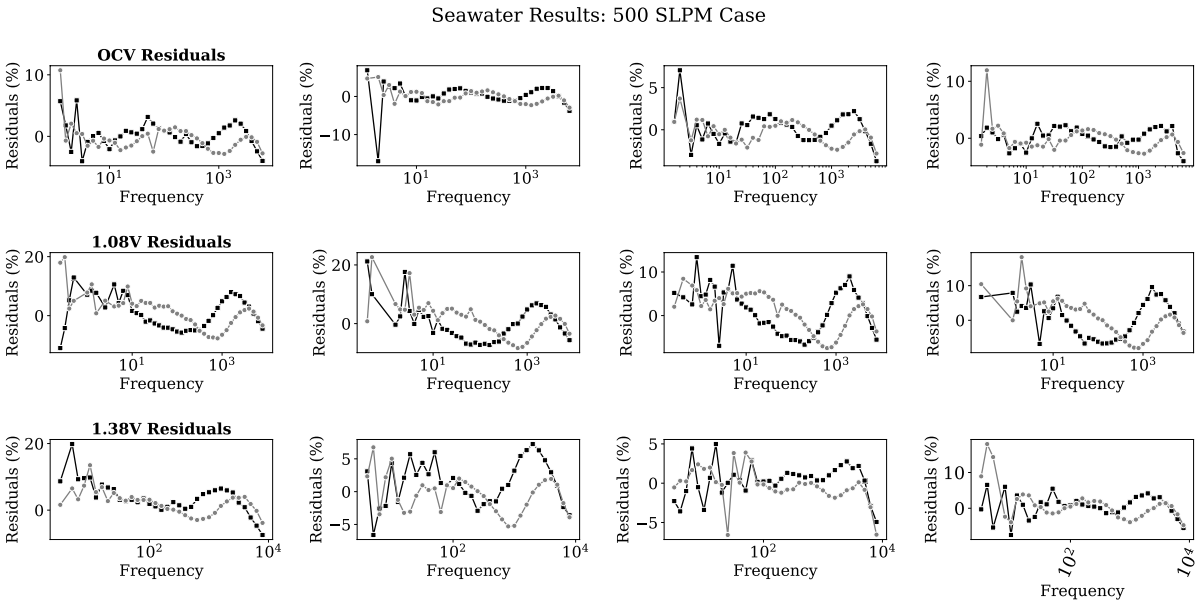

Figure 7-28: Seawater residuals from Kramers Kronig transform.

The Kramers Kronig analysis of the data reveals that there is a significant amount of noise in the data. Although various papers report on the importance of validating EIS data ([136], [140], [141]), this is an underutilized resource in the literature most likely because implementing and understanding the tools to validate data is unclear, variable, and not always accessible. Unfortunately, the Kramers Kronig analysis used in this section suggests that most of the datasets have high residuals, as a result the data did not pass the checks for causality, linearity, and stability. Some possible sources for the errors found in the data include:

- Noise from the potentiostat, which has been found to have poor accuracy at high frequencies [152]
- Cables that introduced noise into the circuit and led to large errors
- Inductive effects from the potentiostat, readings at high frequencies that can lead to an ohmic resistance that is higher than the actual value [152]
- Non equilibrium of input gases, particularly for steam that may lead to fluctuating gas flows
- An insufficient seal that allowed the reactant gasses to react
- Poor electrical contact

Suggestions to reduce the noise include:

- Using galvanostatic perturbation with an alternating current without bias because potentiostatic perturbations may result in high currents for low impedance values especially at high frequencies (1000 Hz) [152]
- Avoiding inappropriately high currents because they may eventually destroy the cell, lead to self-heating that leads to measurement artifacts, or induce large magnetic fields which cause inductive effects [152]
- Using an AC filter to eliminate bias in the voltage signal at high frequencies [152]
- Inserting a delay time of at least three periods (if using 12 points per decade) to ensure the cell has enough time to switch from a harmonic oscillation at one frequency to another [152]
- Selecting a higher data quality option on the EIS options tab
- Using a Frequency Response Analyzer or a device with an accuracy of 1% or better for the measurements and a DC power supply to provide the bias current [152]
- Shield all wires from other electronic devices that may lead [152]
- Avoiding a reference electrode for EIS measurements because it can lead to noise and artifacts [152]
- Reduce the mutual inductance between current lead wires that can deteriorate the quality of impedance measurements at high frequencies by using twisted paired gold wires from the cell to the furnace outlet for probing [153]

7.3.3.2 Distribution of Relaxation Times

This section presents the results from the DRT method. Since the majority of the experiments could not be validated by the Kramers Kronig test, the Nyquist plots were reevaluated by taking the average of the raw results and cleaning the data. This involved deleting imaginary impedance values below the x-axis of the Nyquist plot (negative of the negative imaginary impedance) due to their lack of physical significance. There is a significant amount of datapoints that fell below the x-axis on the Nyquist plot of the negative imaginary impedance in the high frequency region which the literature suggests may be due to inductive effects from the potentiostat [152]. After making these changes, the Nyquist model from the Kramers Kronig transform exhibited an improved representation of the original averaged data (see Figure 7-29 - Figure **7-31**). The ohmic resistance predicted by DRTtools is shown in each graph on the bottom left. Additionally, the

residuals between the Kramers Kronig and the averaged data are notably smaller with the majority falling within the +/- 2% range. Figure **7-32** - Figure **7-33** depicts the residuals. To perform the DRT on the data, a gaussian discretization approach was used on the complex data with a first order regularization derivative and a regularization parameter of $1 * 10^{-3}$. Figure 7-34 shows the DRT spectrums that correspond to the Nyquist plots in Figure 7-29 - Figure **7-31**.

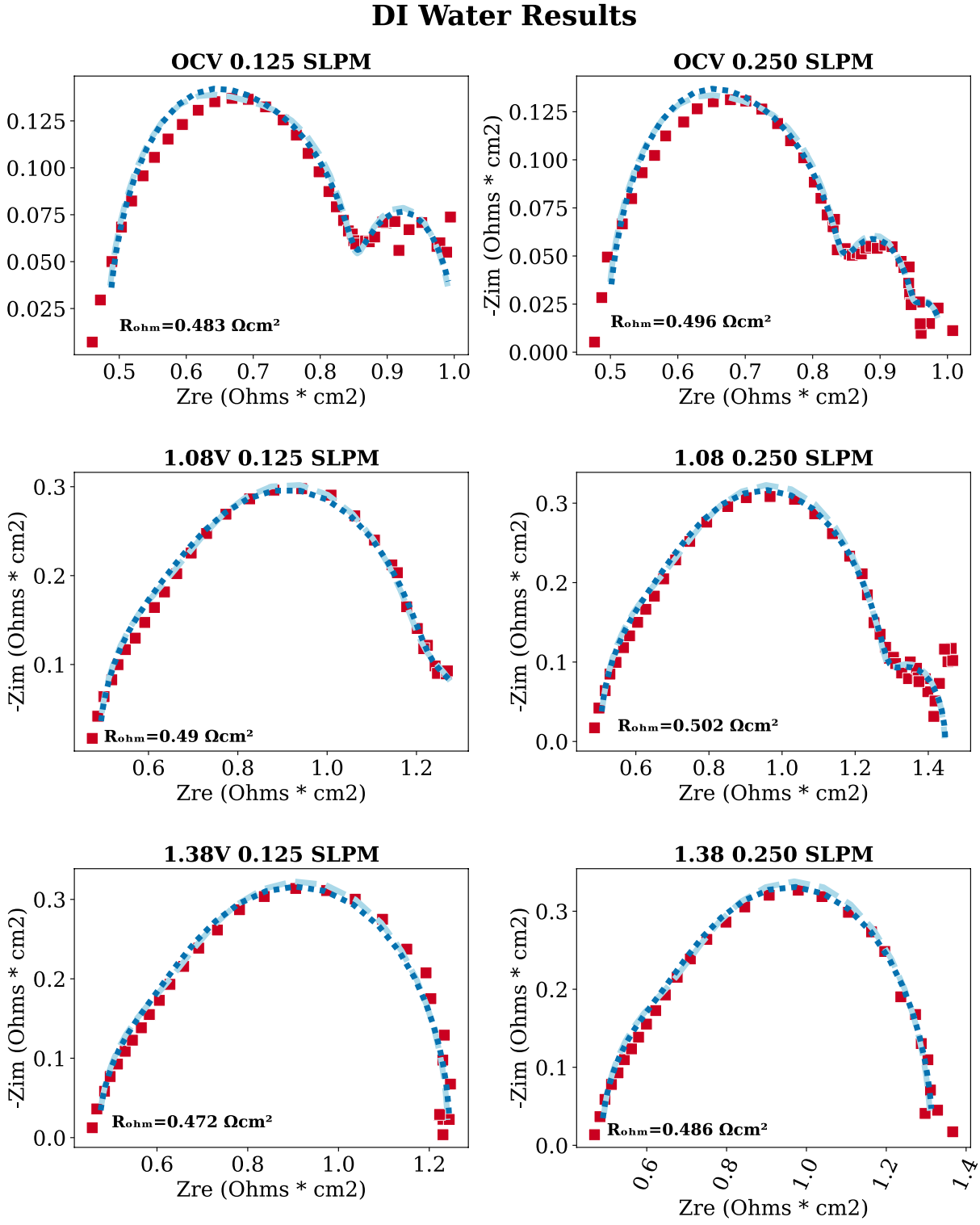

Figure 7-29: Nyquist plot of the averaged data (red squares), Kramers Kronig modelled data (dashed light blue line), and the DRT model (dotted sky blue line) for the DI water cases.

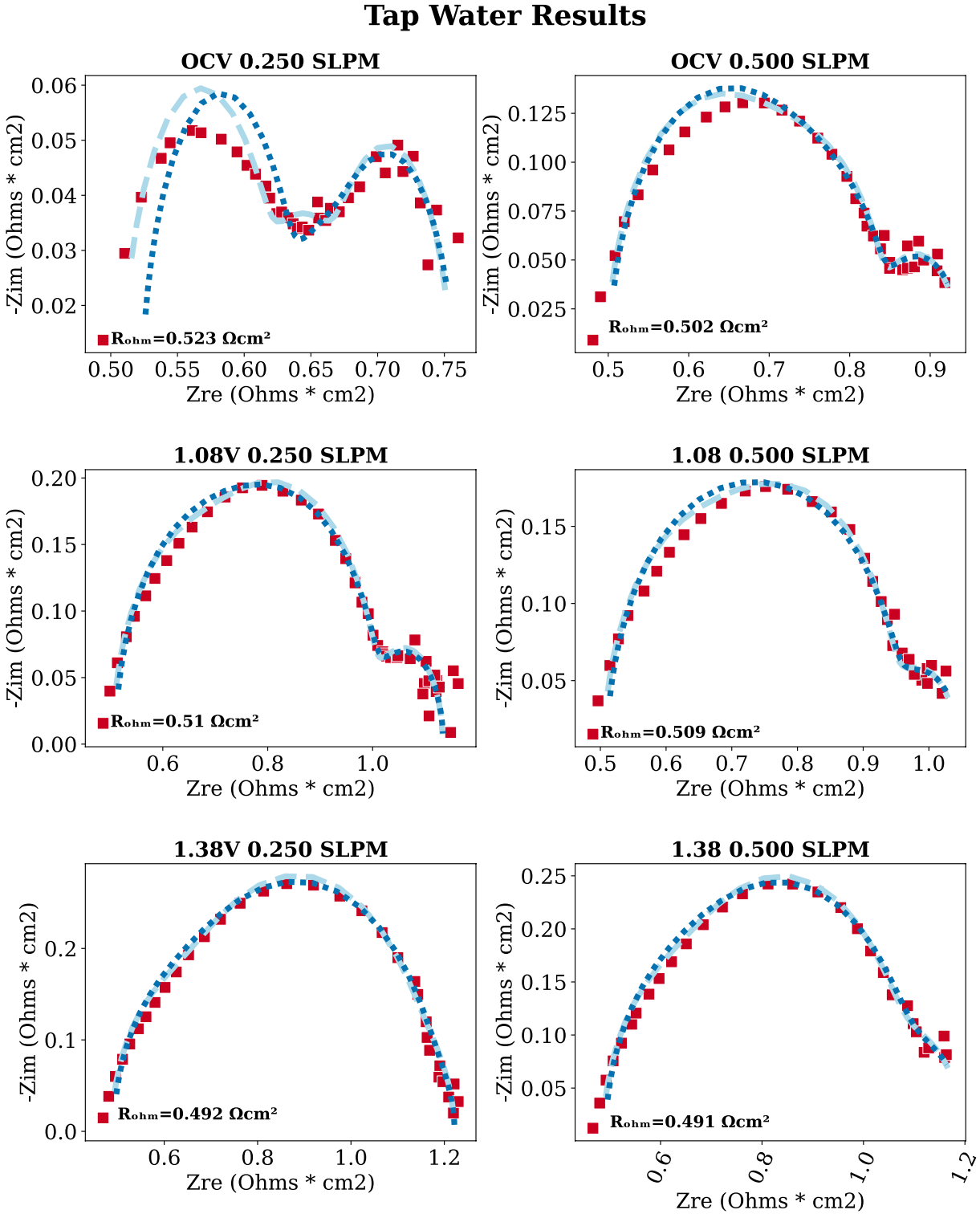

Figure 7-30: Nyquist plot of the averaged data (red squares), Kramers Kronig modelled data (dashed light blue line), and the DRT model (dotted sky blue line) for the tap water cases.

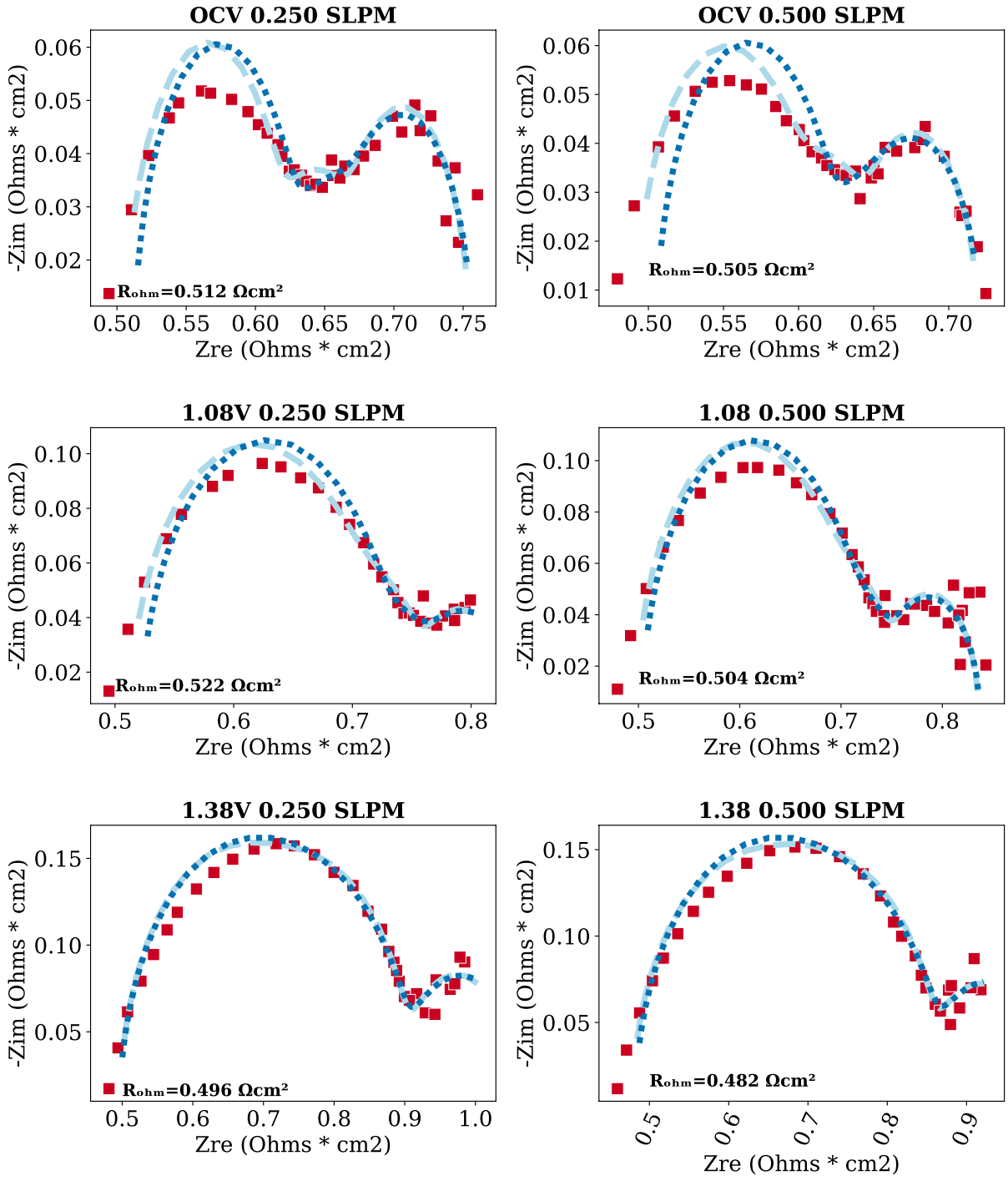

Figure 7-31: Nyquist plot of the averaged data (red squares), Kramers Kronig modelled data (dashed light blue line), and the DRT model (dotted sky blue) for the seawater cases.

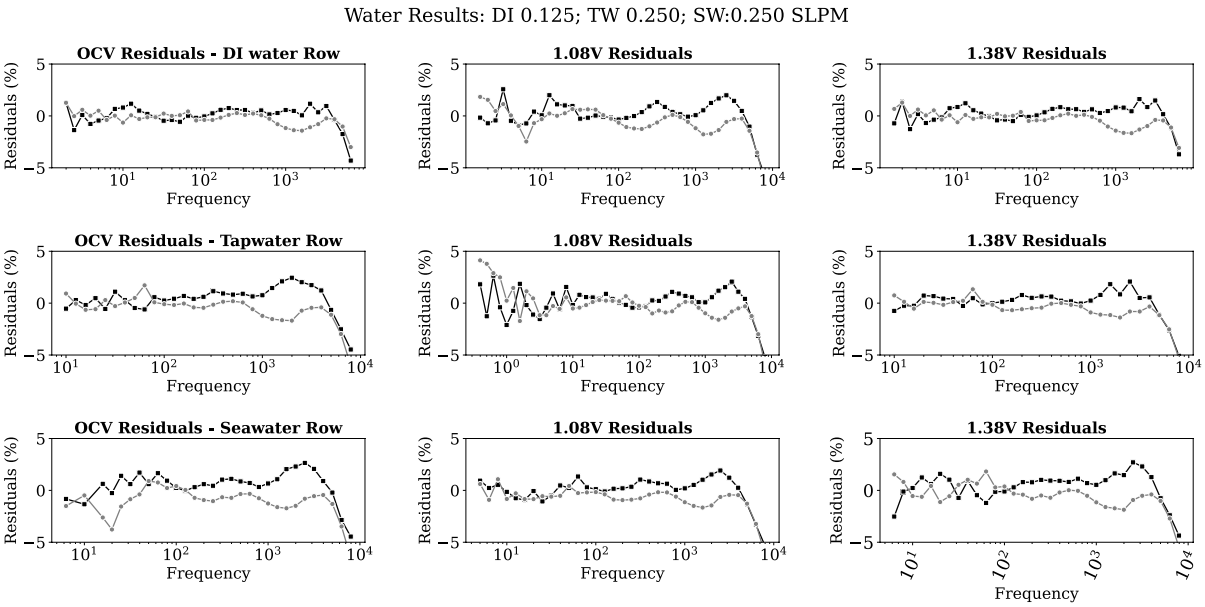

Figure 7-32: Residuals of the averaged data and the Kramers Kronig model. The imaginary residuals are gray circles, and the real residuals are black**.**

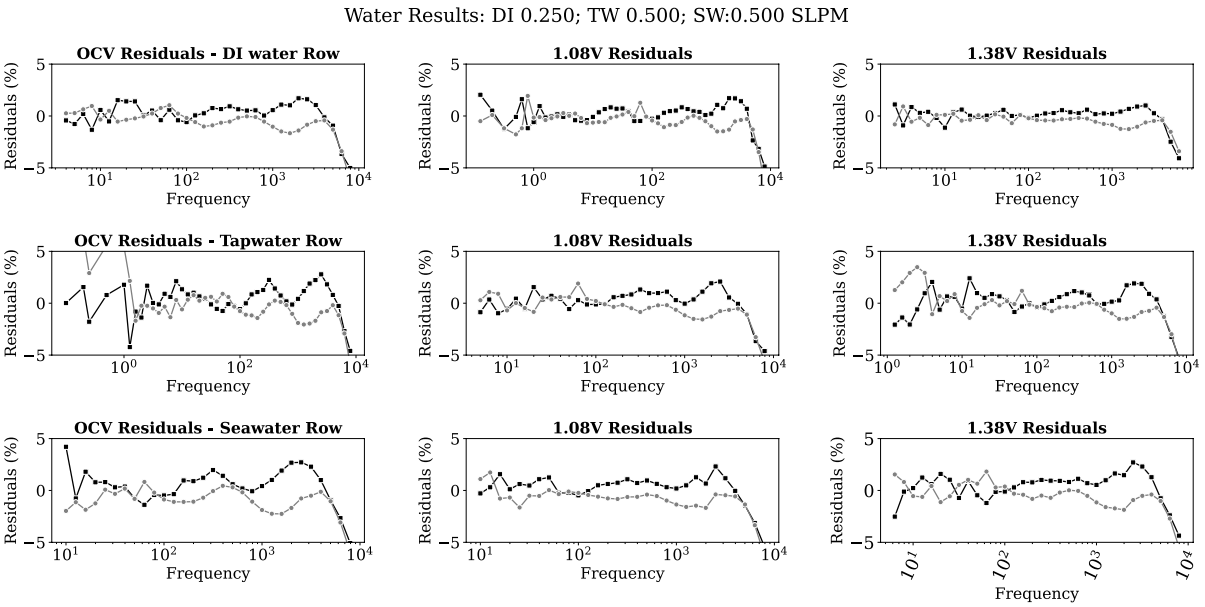

Figure 7-33: Residuals of the averaged data and the Kramers Kronig model. The imaginary residuals are gray circles, and the real residuals are black squares.

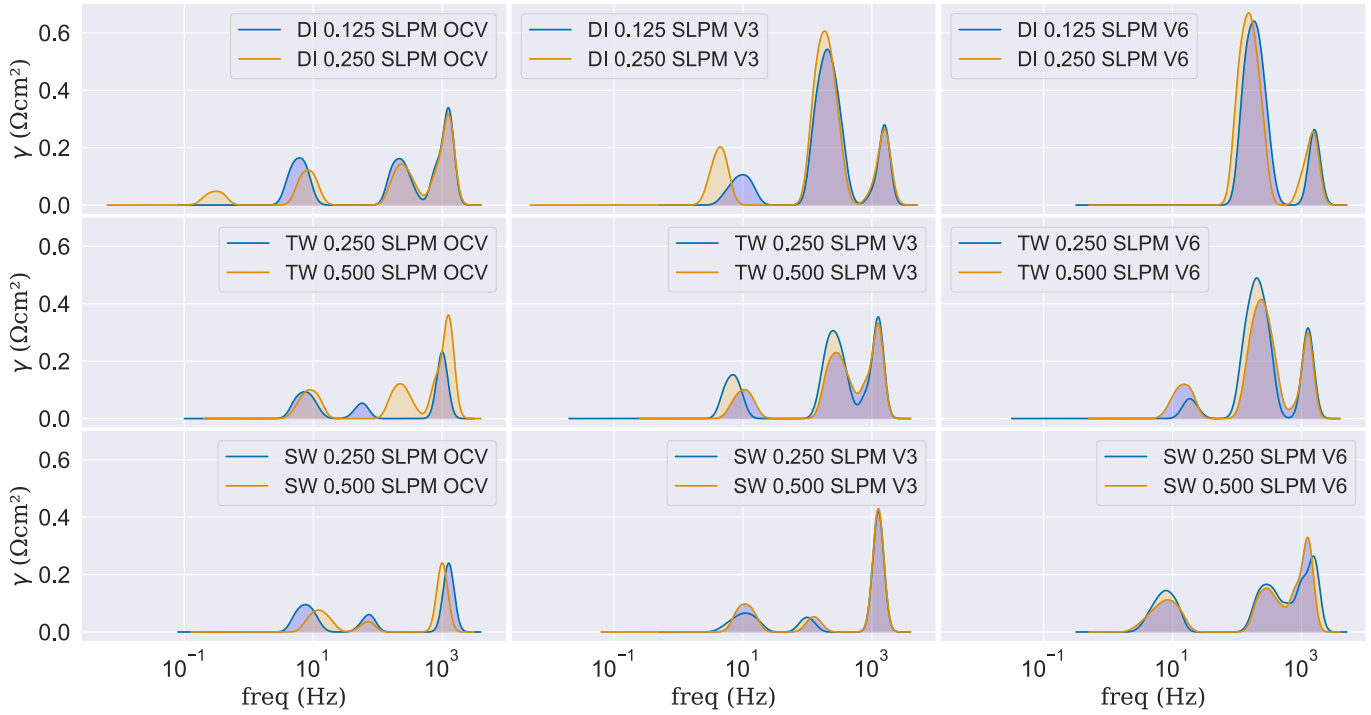

Figure 7-34: DRT Results for the Nyquist plots in Figure 7-29 - Figure 7-31**.**

The DRT results, shown in Figure 7-34, are organized so that each row represents a result for one of the water types. The top row is the DI water results, the middle row is the tap water results, and the bottom row is the seawater results. Each column represents the voltage at which the test was performed. OCV, V3, and V6 correspond to the open circuit voltage, 1.08 V, and 1.38 V, respectively. Beginning the analysis with the OCV results, Figure 7-34, shows that there are three main peaks that stand out in each of the three plots, which indicates there are multiple electrochemical processes with different rate/time constant distributions. The peaks occur at frequencies of approximately 10, 100 and 1000. The peak at 1000 Hz tends to be the most dominant in the results, which, according to the literature, may be attributed to a variety of phenomena or mechanisms including: charge and mass transfer in the air and fuel electrodes, ionic transport in the electrolyte (YSZ), and water reduction at Ni/YSZ TPB [143]. The peak at 10 Hz is the second most pronounced peak at OCV conditions for all of the cases (DI, tap, and salt water), which is likely related to gas diffusion in the hydrogen or oxygen electrode. This is most likely due to oxygen diffusion (mass transport) limitations in this case because the two

electrodes are similar in microstructure and thickness and oxygen is more difficult than hydrogen to diffuse. The third peak at approximately 100 Hz is also likely due to gas diffusion, probably in the hydrogen electrode (again due to faster hydrogen diffusion compared to oxygen diffusion). Comparing the DRT results at OCV between DI water, tap water, and seawater, the intensity of the three peaks is most intense in the DI water results and least intense in the seawater results. This is consistent with the polarization curves which suggest that the seawater polarization is lower, showing improved performance compared to the DI water results. It could be that the cell experienced some chemical (e.g., in-situ nickel reduction) or morphological changes that reduced the initial resistance over this period that led to improved performance. The DRT results of the tap water are consistent with the DI water results in intensity. Although, there is some evidence that the resistance of the tap water case may have decreased in the 10 Hz peak in comparison to the DI water. On the other hand, the 10 Hz peak, indicating mass transport losses, is most persistent in the saltwater cases. This may be due to salt deposition in the electrodes.

The next column of Figure 7-34 shows the results for the scenarios with a voltage of 1.08 V (V3). These results are also characterized by three main peaks with frequencies of approximately 10, 100, and 1000 Hz for the three water types. The peak at the frequency of approximately 10 Hz is most likely due to gas diffusion. Its intensity stays relatively constant across the center column for the three water types. In the DI water scenario, the peak at approximately 100 Hz is the most intense one, which is likely due to overlapping processes, such as oxygen evolution, gas conversion polarization, and gas diffusion. The third peak at 1000 Hz has a lower amplitude and is likely due to the hydrogen electrode processes or charge and mass transfer processes in both electrode-electrolyte interfaces. Notably, the intensity of the peaks decreased in the tap water results and decreases further in the seawater results. The tap water results show the intensity of the peaks at 100 and 1000 Hz is less intense and that there appears to be more overlap between the two peaks. The seawater results at V3 show that the most intense peak occurs at a frequency of 1000 Hz with two smaller peaks at 10 and 100 Hz. The change in intensity of the peaks suggests there may have been changes in the micromorphology of the cell that occurred between the DI water results and the seawater results. These changes may have led to reduced resistances through enhanced gas diffusion, and improved charge and ionic transport processes.

In the final column of Figure 7-34, the results at V6 (1.38V) are shown. In the DI water results, there are only two peaks that appear at approximately 100 and 1000 Hz. The peak at 100 Hz is significantly higher than for any of the other results with DI water. The intensity of the peak at 100 Hz increases with voltage, which suggest that this peak is likely associated with overlapping processes with similar relaxation times like charge and mass transfer near the electrochemical interfaces (TPB) and ionic transport in the fuel and oxygen electrodes. In the next row, the results for tap water are shown at V6. The tap water results are slightly different from the DI water results because there are three defined peaks, and each one is at one of the three previously identified frequencies. The most dominant peak is located at 100 Hz, though it is less intense than the peak at the same frequency for the DI results. In the tap water results, there is a small peak at 10 Hz, which is most likely indicative of gas transport losses. The changes in the DRT results between the DI water and the tap water tests suggests the cell may have started to go through microstructural changes between these two tests (thus, the peak in the mass transport frequency regime). Lastly, the seawater results at V6 also show that there are three dominant peaks with frequencies that align with the previous seawater results at different voltages, and with the tap water results at V6. The seawater results show that the peaks at 100 and 1000 Hz are merging. Consistent with the DRT and EIS results for OCV and at V3, and with the polarization curves, the cell appears to have a lower resistance when it was tested with seawater than with DI water and tap water. This reduction in overall impedance is also coincident with time: the cell was tested with DI water first, then tap water, and finally with seawater. The cell experienced decreased impedance with time.

One possible explanation for these results may be due to a phenomena called “passivation” in the SOE literature [154]. Passivation is used to describe reversible loss of performance in a cell or a temporary degradation in the cell [154]. Cells that passivate can be activated again by operating in fuel cell mode or at constant electrolysis conditions [155]. Prior work has shown that cells may experience short term passivation in the first few hundred hours followed by a period of activation and then long-term degradation [156]. Passivation has previously been attributed to the segregation of impurities from the glass seal [155] and the presence of the electrolyte powder inside the nickel grains and at the nickel/ electrolyte triple phase boundary [157]. According to [157], when impurities build up in the gaseous phase ($Si(OH)_4$), they can block the water from

accessing the triple phase boundary, creating a longer path to the triple phase boundary. Once the impurities crystallize, the triple phase boundary is accessible again, and the cell is "activated" [157]. Activation may occur when the cell is switched from SOEC operation to SOFC operation. The switch in operation changes the water pressure gradient in the fuel electrode and the migration direction of the oxygen ions, which removes impurities from the triple phase boundary and transports them towards the bulk of the fuel electrode [157]. Since the cell manifold uses a sealant for this experiment, it is very likely that the sealant led to initial temporary degradation (passivation) and that by the time the cell was tested with seawater the silica had either crystallized or been transported to the bulk of the fuel electrode.

7.3.4 **Scanning Electron Microscopy**

Scanning electron microscopy (SEM) has been often used for characterization of the microstructures of cells after testing. Previously, ref [158] used SEM to assess the impact of operating temperature on the degradation of cells. The authors used low-voltage SEM micrographs to understand the percolation characteristics of the Nickel phase in the fuel electrode. The authors used carbon to coat the samples for high voltage SEM imaging in which the used an accelerating voltage of 15 kV for imaging and Energy Dispersive X-ray Spectroscopy (EDS) analysis [158]. This section presents the postmortem micromorphology analysis of the cell from the FEI Magellan 400 XHR SEM located at the UC Irvine Materials Research Institute. Prior to imaging, a sputter coater coated the samples 5 nm of iridium. Figure 7-35 - Figure 7-37 show the SEM and EDS results of sections of the fuel and oxygen electrodes and the electrolyte. Surprisingly, unlike the majority of the previous papers that have inspected SO cells for evidence of salt deposition, the results for these tests show very clearly that there is a significant amount of salt (NaCl) on the surface of the cell in the fuel and oxygen electrode. The EIS and polarization curves did not suggest that the cell experienced enhanced resistance during the operation with seawater. It is likely that the salt impurities in the electrode crystallized and as a result they did not significantly inhibit the diffusion of the steam-hydrogen mixture to the triple phase boundary. However, after a long enough test it is highly probable that enough salt would accumulate that it might block the triple phase boundary and quickly degrade the cell. One observation in the SEM/ EDS tests is that the salt was not evenly distributed in the electrodes. There were sections of the fuel electrode where salt was not detected, and no salt was

found in the section of the electrolyte tested. Unlike what prior studies found in their postmortem analysis, this study shows that there is strong evidence of seawater deposition after steam generation. If seawater were to be deployed in the real world, the system would likely require additional water treatment.

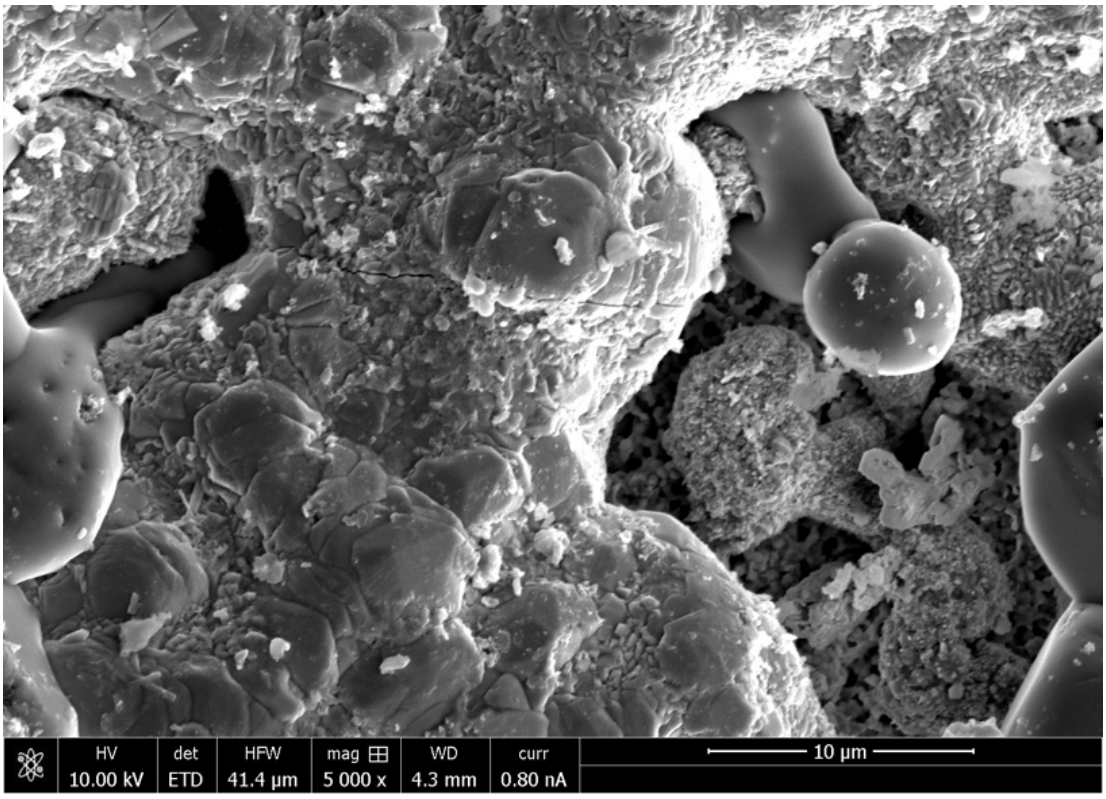

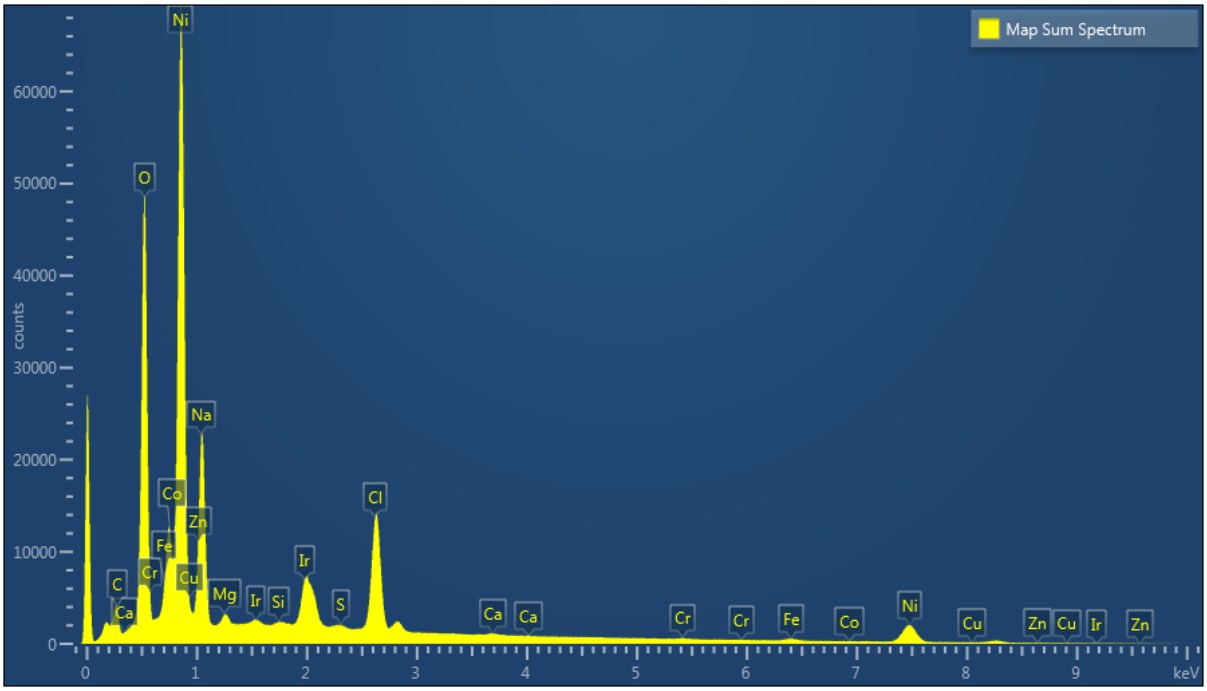

Figure 7-35: (Top) SEM image and (Bottom) EDS results of the fuel electrode.

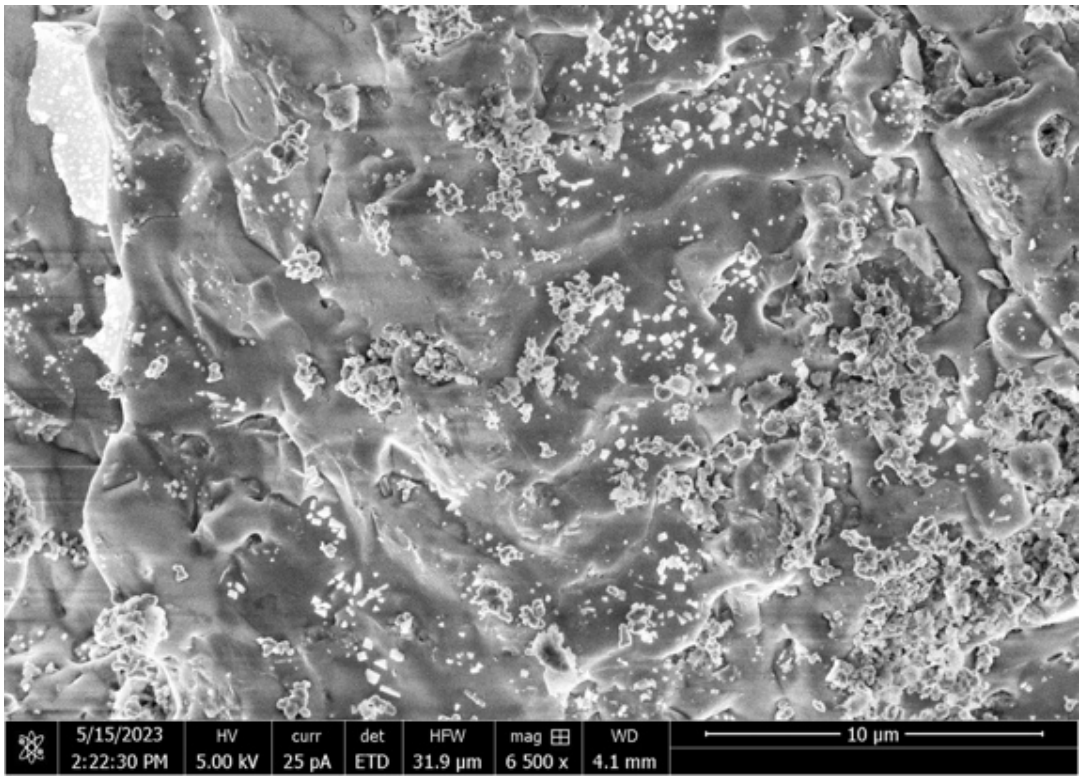

Figure 7-36: (Top) SEM image and (Bottom) EDS results of the oxygen electrode

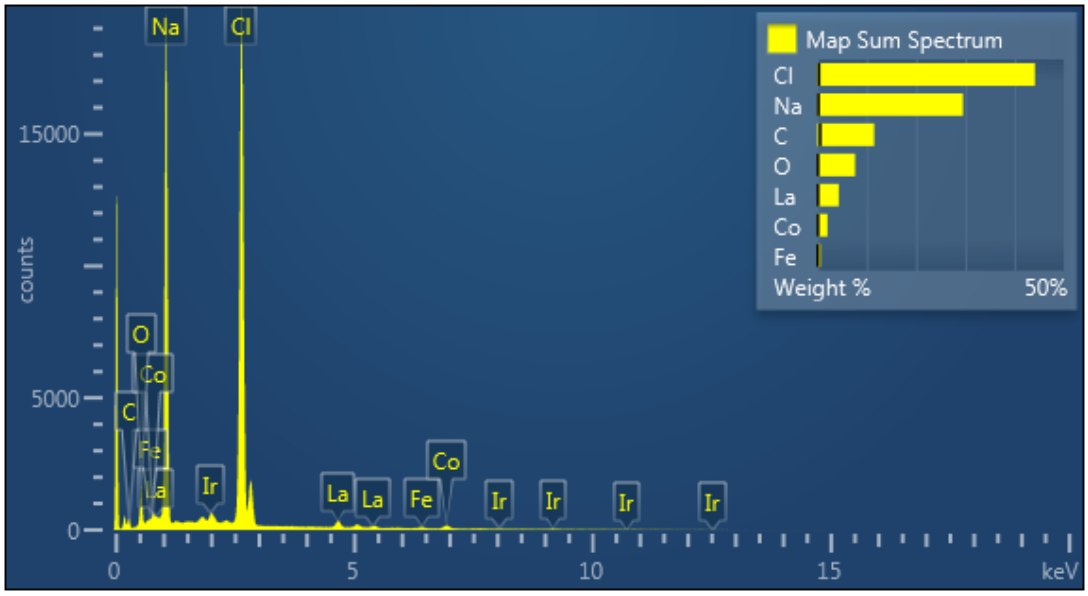

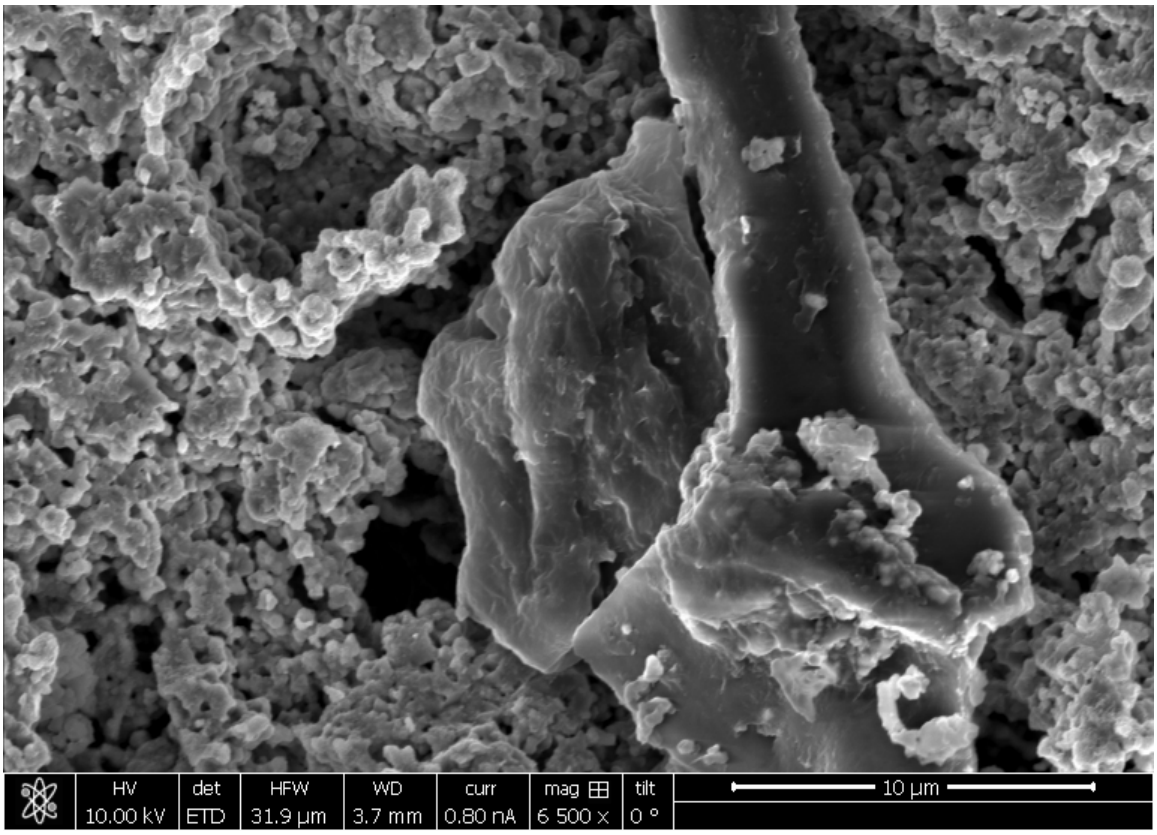

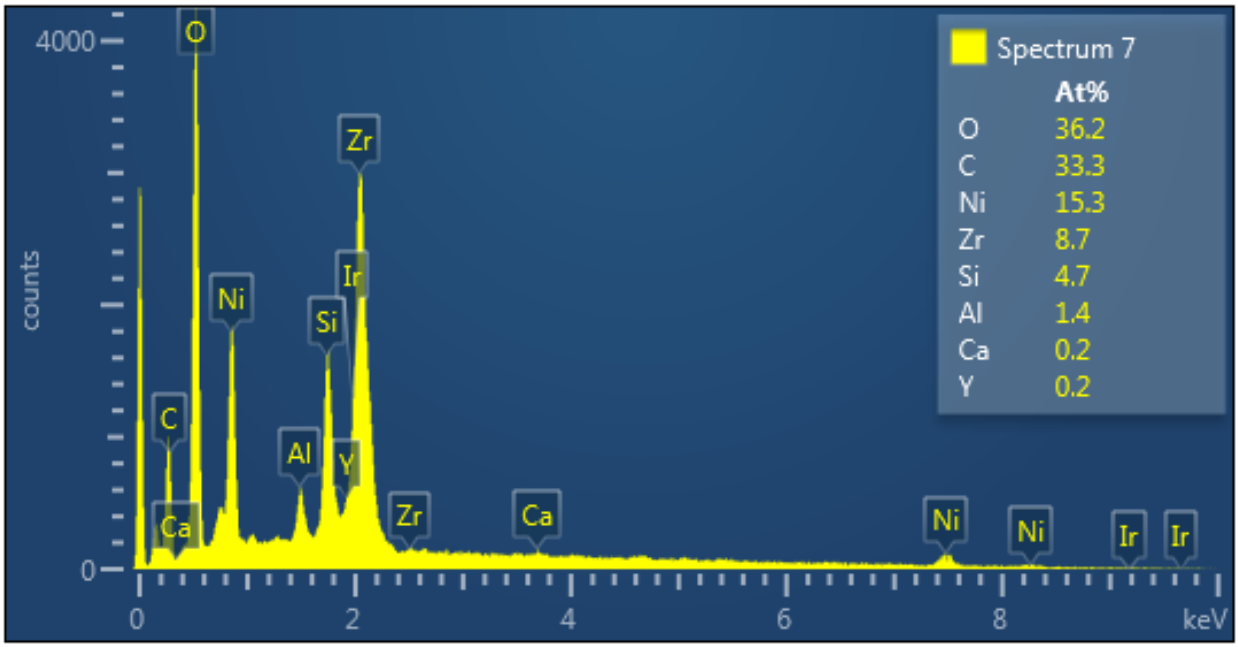

Figure 7-37: (Top) SEM image and (Bottom) EDS results of the electrolyte

7.3.5 **Brine Management**

The final test of the system included measuring the conductivity of the water in the steam generator and at the outlet of the furnace. As the water evaporates from the tank, the concentration of impurities in the water (brine for seawater) will increase with time, which could lead to a higher likelihood of water capturing salt particles and depositing it in the cell or other components. If a high temperature seawater system were to be deployed, this will be a significant consideration from an operational perspective. How will the highly concentrated brine be handled in a way that is sustainable and that mitigates the possibility of damaging the cell?

Table 7-6 lists the expected conductivities of the different water types according to the literature and Figure 7-38 shows the measured conductivities from experiments. We used a conductivity probe (Ohaus AB33EC) to make these measurements. For the DI water results, the average conductivity in the steam generator is identical to the conductivity of the condensate. Note, that the measured conductivity is slightly higher than the expected conductivity in the literature which is likely due to impurities in the piping and infrastructure. The tap water measured an average conductivity of 996 μS/cm in the steam generator and 14.4 μS/cm in the condensate. The tap water condensate value is higher than the DI water which suggests there may have been impurities present in the steam flow through the cell. The simulated seawater had an average conductivity of 48,115 μS/cm in the steam generator and 159.9 μS/cm in the condensate. The condensate conductivity is significantly high and suggests that salt is present in the steam. The original data shows the average conductivity of the seawater condensate increased from 75.06 to 220.14 μS/cm over the time period tested (see Table 10-1 in the appendix). The conductivity of the seawater in the steam generator also shows a similar trend of increasing conductivity from 31.84 mS/cm to 62.31 mS/cm (see Table 10-2 in the appendix). This suggests that increasing the concentration of brine in the steam generator will lead to increasing salt content in the steam, which may damage the cell.

Table 7-6. Expected conductivity in μS/cm (micro Siemens/ centimeter).

Water type	**Expected conductivity (μS)**

DI Water	0.5 – 3 [159]
Tap Water	50 – 800 [159]
Simulated Seawater	30,000 -60,000 [160]
Real Seawater	50, 000 [161]

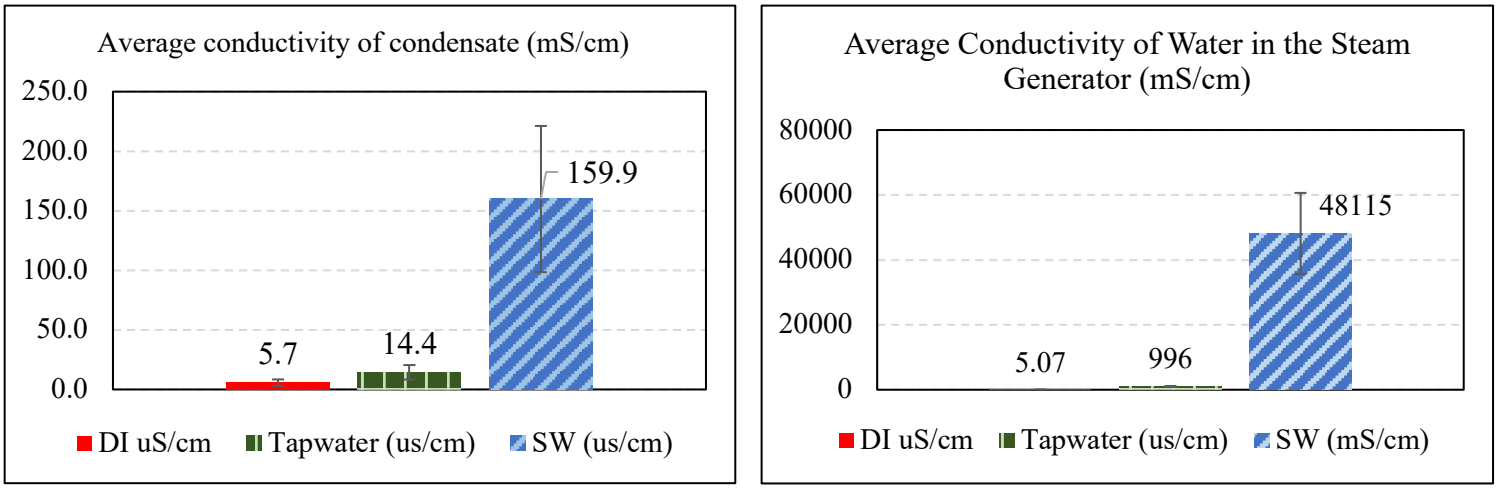

Figure 7-38: Average conductivities of the water in the steam generator and condensate.

7.4 Summary and Conclusions

This chapter addresses Objective 3: Conduct an experiment to understand how impurities in the desalinated water (or seawater) can impact the performance and degradation of SOECs. This section presents first a discussion of the various methods for electrochemical testing, followed by an analysis on the design of the test stand and experiment.

The conclusions of this chapter are the following:

- Steam utilization did not impact the performance of the cell. This is likely due to the low concentration losses of the cell.
- There is some evidence that the cell may be able to operate directly with tap water without degradation.

- The cell showed lower resistance and improved performance with the seawater than with DI water or tap water. One possible explanation for this is that the cell may have experienced passivation, which is the reversal of degradation.
- SEM images and EDS analyses showed that the salt was unevenly deposited on the anode and cathode.
- An analysis on the condensate of the cathode outlet showed significantly higher conductivity measurements that the DI water condensate. This also suggests salt may have evaporated with the steam.
- Although there was evidence of salt deposits on the cell, the cell's performance was not negatively impacted.
- These results suggest additional water treatment methods may be required if a high temperature system is deployed offshore.

8 SUMMARY AND CONCLUSIONS

8.1 Summary

This dissertation examines the potential to use offshore wind energy and hydrogen for renewable energy. The best offshore wind resources in California are located in the northern section, which is remote, is not densely populated, and lacks transmission infrastructure. Complementing offshore wind energy with electrolysis is a key solution the transmission and storage challenges of offshore wind that may enable its use for deep decarbonization via green hydrogen. Chapters 5 – 7 examine offshore wind energy, assess the thermodynamics of offshore wind coupled with seawater electrolysis in solid oxide system, and analyze the feasibility of using seawater in a solid oxide cell. Chapter 5,"Case Study of Offshore Wind Benefits and Challenges in California," used statistical methods to evaluate the coincidence, variability, alignment, and predictability of offshore wind with demand and onshore renewable resources. Chapter 6, "Seawater Solid Oxide Electrolysis Thermodynamic Model" presented a steady state model of an offshore electrolysis platform coupled with offshore wind and seawater purification. Chapter 7, "Experimental Analysis of Seawater Electrolysis," assessed the long-term performance and degradation of a solid oxide electrolysis cell operated with seawater.

8.2 Conclusions

In **Chapter 5** the goal was to investigate the benefits and challenges of deploying offshore wind and to evaluate the dynamics of offshore wind to verify if the advantages of offshore wind previously reported in the literature are true amongst the variety of possible offshore wind resources available in California. The major findings of this study are:

- Across different configurations, the most resilient combination of resources occurs when offshore wind is paired with solar and onshore wind. This is reflected in the firm capacity.
- Onshore wind and solar are the most complementary renewable power generation resources.
- There is no consistent correlation (positive or negative) between the offshore wind sites and the demand, or with solar, or with onshore wind.
- There are some offshore wind sites with a strong positive correlation with each other, but this is not ubiquitous across all the offshore wind sites. This suggests that unlike solar,

offshore wind is not a resource with high predictability and that this resource has a high degree of spatial variability.

- When using a demand-based metric to analyze the value of the different renewable energy resources and the six potential offshore wind sites investigated, we found that offshore wind is the most valuable resource during peak demand hours in the summer and winter in California.
- The value of offshore wind varies spatially and temporally since not all wind sites have uniform patterns.

Chapter 6 presents an offshore wind platform coupled with high temperature hydrogen production to examine the thermodynamics of such a system. Various design point cases are considered with respect to the systems ability to operate in exothermic, thermoneutral, and endothermic thermal regimes. The balance of plant, efficiencies, brine generation and efficiencies are considered in the design. The conclusions of this section are the following:

- The system must use additional equipment to meet its thermal loads even when the stack operates in exothermic mode.
- In both exothermic and endothermic operation, the steam generator represents the largest source of electricity consumption of the balance of plant.
- The amount of brine generated in the steam generator is enormous and will require proper management to prevent pollution.
- With proper controls, offshore wind may have one of the most suitable profiles for high temperature SO electrolysis.
- The ability to couple steam generation and desalination with high temperature electrolysis significantly reduces the net energy demand for offshore hydrogen production.

Chapter 7 presents an experimental analysis of seawater electrolysis using a planar solid oxide cell. The goal of this chapter was to study the impact of seawater on the degradation and performance of a solid oxide cell. The findings are the following:

- The polarization curves did not show a significant influence of the steam utilization. This suggests that concentration losses were largely negligible and that ohmic losses were most likely the dominant polarization.
- There is strong evidence that the cell experienced passivation, which is the reversal of degradation. This explains why the cell showed lower resistance and improved performance with the seawater than with DI water or tap water.
- There is some evidence that the cell may be able to operate directly with tap water without degradation.
- SEM images and EDS analyses showed that the salt was unevenly deposited on the anode and cathode.
- These results suggest additional water treatment methods may be required if a high temperature system is deployed offshore.

8.3 **Future Work**

This dissertation marks the beginning of an investigation of offshore wind and hydrogen production from offshore wind energy. The results from these studies have led to various questions and potential follow-on studies that I'd like to pursue in the future with collaborators.

Offshore Wind Analysis:

- An optimization analysis that determines the most suitable transmission method of offshore wind energy in California and address the question of how much offshore wind energy is most suitable in each of the proposed locations.
- An analysis to determine the optimal transmission and storage strategy of offshore wind.
- A techno economic analysis of deploying offshore wind in various different sites and the cost of transmission (electricity vs hydrogen)

Modelling:

- Develop a technoeconomic analysis that compares the cost of hydrogen production from offshore wind with SO electrolysis and PEM.

- Use or develop a dynamic model that is spatially resolved to evaluate the performance of an SOE system that is directly coupled to variable offshore wind energy.
- Develop a control strategy for coupling offshore wind with solid oxide electrolysis.
- Assess the best end-use of green hydrogen made from offshore wind, considering cost, transmission, and demand.
- Assess the feasibility of generating additional electro fuels, such as methanol, ammonia, and methane from offshore wind.

Experimentation:

- Further experiments and simulations that assess the feasibility of using the pulsing approach described in [125] to operate an SO stack dynamically.
- Long term test to assess the potential degradation mechanisms from seawater. Assess how much salt will affect the performance of the cell.
- Further experimentation to assess if cycling from OCV to electrolysis will result in passivation.
- Further tests to study the phenomena of passivation and how this may be a degradation strategy that is intentionally employed in commercial systems.

9 REFERENCES

[1] J. Bosch, I. Staffell, and A. D. Hawkes, "Global levelised cost of electricity from offshore wind," *Energy*, vol. 189, p. 116357, 2019, doi: 10.1016/j.energy.2019.116357.

[2] S. J. Dundas *et al.*, "Integrating oceans into climate policy: Any green new deal needs a splash of blue," *Conserv. Lett.*, no. February, pp. 1–12, 2020, doi: 10.1111/conl.12716.

[3] S. J. Davis *et al.*, "Net-zero emissions energy systems," *Science (80-.).*, vol. 360, no. 6396, 2018, doi: 10.1126/science.aas9793.

[4] N. Olmer, B. Comer, B. Roy, X. Mao, and D. Rutherford, "Greenhouse Gas Emissions From Global Shipping, 2013-2015," Washington DC, 2017.

[5] R. M. Andrew, "Global CO2 emissions from cement production, 1928-2018," *Earth Syst. Sci. Data*, vol. 11, no. 4, pp. 1675–1710, 2019, doi: 10.5194/essd-11-1675-2019.

[6] B. Graver, K. Zhang, and D. Rutherford, "CO2 emissions from commercial aviation, 2018," 2019.

[7] "California takes bold step to reduce truck pollution," *California Air Resources Board*, 2020. https://ww2.arb.ca.gov/news/california-takes-bold-step-reduce-truck-pollution (accessed Sep. 14, 2020).

[8] S. Horvath, M. Fasihi, and C. Breyer, "Techno-economic analysis of a decarbonized shipping sector: Technology suggestions for a fleet in 2030 and 2040," *Energy Convers. Manag.*, vol. 164, no. November 2017, pp. 230–241, 2018, doi: 10.1016/j.enconman.2018.02.098.

[9] "Decarbonising Shipping: All Hands on Deck."

[10] J. Andrews and B. Shabani, "Re-envisioning the role of hydrogen in a sustainable energy economy," *Int. J. Hydrogen Energy*, vol. 37, no. 2, pp. 1184–1203, 2012, doi: 10.1016/j.ijhydene.2011.09.137.

[11] J. A. Dowling *et al.*, "Role of Long-Duration Energy Storage in Variable Renewable Electricity Systems," *Joule*, 2020, doi: 10.1016/j.joule.2020.07.007.

[12] J. Thorson *et al.*, "Unlocking the Potential of Marine Energy Using Hydrogen Generation Technologies Unlocking the Potential of Marine Energy Using Hydrogen Generation Technologies," no. June, p. 83, 2022.

[13] L. Welder, D. S. Ryberg, L. Kotzur, T. Grube, M. Robinius, and D. Stolten, "Spatio-

temporal optimization of a future energy system for power-to-hydrogen applications in Germany," *Energy*, vol. 158, pp. 1130–1149, 2018, doi: 10.1016/j.energy.2018.05.059.

[14] I. A. Gondal, "Hydrogen integration in power-to-gas networks," *Int. J. Hydrogen Energy*, vol. 44, no. 3, pp. 1803–1815, 2019, doi: 10.1016/j.ijhydene.2018.11.164.

[15] IEA, "Offshore Wind Outlook 2019," Paris, France, 2019.

[16] W. Musial, P. Beiter, S. Tegen, and A. Smith, "Potential Offshore Wind Energy Areas in California: An Assessment of Locations, Technology, and Costs," 2016. doi: http://dx.doi.org/10.1016/j.jpaa.2011.12.005.

[17] R. Wiser *et al.*, "Expert elicitation survey on future wind energy costs," *Nat. Energy*, vol. 1, no. 10, p. 16135, Sep. 2016, doi: 10.1038/nenergy.2016.135.

[18] R. Wiser *et al.*, "Forecasting Wind Energy Costs & Cost Drivers: The Views of the World's Leading Experts," 2016.

[19] R. Collier *et al.*, "California Offshore Wind: Workforce Impacts and Grid Integration," no. September, p. 94, 2019.

[20] K. Eurek, P. Sullivan, M. Gleason, D. Hettinger, D. Heimiller, and A. Lopez, "An improved global wind resource estimate for integrated assessment models," *Energy Econ.*, vol. 64, pp. 552–567, 2017, doi: 10.1016/j.eneco.2016.11.015.

[21] X. Costoya, M. DeCastro, D. Carvalho, and M. Gómez-Gesteira, "On the suitability of offshore wind energy resource in the United States of America for the 21st century," *Appl. Energy*, vol. 262, no. October 2019, p. 114537, 2020, doi: 10.1016/j.apenergy.2020.114537.

[22] W. Musial, D. Heimiller, P. Beiter, G. Scott, and C. Draxl, "2016 Offshore Wind Energy Resource Assessment for the United States," no. September, p. 88, 2016.

[23] S. Hull *et al.*, "The Economic Value of Offshore Wind Power in California," San Francisco, CA, 2019.

[24] M. Junginger, A. Louwen, N. Gomez Tuya, D. de Jager, E. van Zuijlen, and M. Taylor, *Offshore Wind Energy*. Elsevier Inc., 2020.

[25] "Hywind Pilot Park, Aberdeenshire," *Power Technology*. https://www.power-technology.com/projects/hywind-pilot-park-aberdeenshire/ (accessed Jul. 15, 2020).

[26] Y.-H. Wang *et al.*, "Spatial and temporal variation of offshore wind power and its value along the Central California Coast," *Environ. Res. Commun.*, vol. 1, no. 12, p. 121001,

2019, doi: 10.1088/2515-7620/ab4ee1.

[27] "WINDExchange: California Offshore 90-Meter Wind Map and Wind Resource Potential," *Wind Exchange US DOE*. https://windexchange.energy.gov/maps-data/146 (accessed Jul. 13, 2020).

[28] I. A. Gondal, "Offshore renewable energy resources and their potential in a green hydrogen supply chain through power-to-gas," *Sustain. Energy Fuels*, vol. 3, no. 6, pp. 1468–1489, 2019, doi: 10.1039/c8se00544c.

[29] "How Do Wind Turbines Work?," *Department of Energy*. https://www.energy.gov/eere/wind/how-do-wind-turbines-work (accessed Jun. 14, 2021).

[30] R. d'Amore-Domenech, T. J. Leo, and B. G. Pollet, "Bulk power transmission at sea: Life cycle cost comparison of electricity and hydrogen as energy vectors," *Appl. Energy*, vol. 288, no. February, p. 116625, 2021, doi: 10.1016/j.apenergy.2021.116625.

[31] C. Feng, E. K. Chartan, B. M. Hodge, and J. Zhang, "Characterizing time series data diversity for wind forecasting," *BDCAT 2017 - Proc. 4th IEEE/ACM Int. Conf. Big Data Comput. Appl. Technol.*, no. June, pp. 113–119, 2017, doi: 10.1145/3148055.3148065.

[32] P. E. Bett and H. E. Thornton, "The climatological relationships between wind and solar energy supply in Britain," *Renew. Energy*, vol. 87, pp. 96–110, 2016, doi: 10.1016/j.renene.2015.10.006.

[33] J. Widén, "Correlations between large-scale solar and wind power in a future scenario for Sweden," *IEEE Trans. Sustain. Energy*, vol. 2, no. 2, pp. 177–184, 2011, doi: 10.1109/TSTE.2010.2101620.

[34] Y. Li, V. G. Agelidis, and Y. Shrivastava, "Wind-solar resource complementarity and its combined correlation with electricity load demand," *2009 4th IEEE Conf. Ind. Electron. Appl. ICIEA 2009*, pp. 3623–3628, 2009, doi: 10.1109/ICIEA.2009.5138882.

[35] P. Lukhyswara, L. M. Putranto, and D. D. Arianandа, "Solar Irradiation Forecasting Uses Time Series Analysis," *2019 11th Int. Conf. Inf. Technol. Electr. Eng. ICITEE 2019*, vol. 7, 2019, doi: 10.1109/ICITEED.2019.8929990.

[36] A. (Recharge) Lee, "Shell unveils world's largest offshore wind plan to power green hydrogen," *Recharge*, Feb. 27, 2020. https://www.rechargenews.com/wind/shell-unveils-worlds-largest-offshore-wind-plan-to-power-green-hydrogen/2-1-763610 (accessed Jun. 14, 2021).

[37] A. (Recharge) Lee, “World’s largest offshore wind farm to power green hydrogen under UK plan,” *Recharge*, Feb. 18, 2020. https://www.rechargenews.com/transition/worlds-largest-offshore-wind-farm-to-power-green-hydrogen-under-uk-plan/2-1-757976 (accessed Jun. 14, 2021).

[38] “PosHYdon pilot, Dutch North Sea,” *Neptune Energy*. https://www.neptuneenergy.com/esg/new-energy/poshydon-hydrogen-pilot (accessed Jun. 14, 2021).

[39] J. (Green T. M. Parnell, “Ørsted Joins Efforts To Develop Offshore-Wind-to-Green-Hydrogen Tech,” *Greentech Media*, Jan. 11, 2021. https://www.greentechmedia.com/articles/read/rsted-joins-efforts-to-develop-seaworthy-green-hydrogen-tech (accessed Jun. 14, 2021).

[40] J. (Green T. M. Parnell, “Orsted Backs First Major Green Hydrogen Project Focused on Transport Sector | Greentech Media,” *Greentech Media*, May 26, 2020. https://www.greentechmedia.com/articles/read/orsted-to-power-decarbonization-hub-for-land-sea-and-air-transport (accessed Jan. 13, 2021).

[41] R. D’Amore-Domenech and T. J. Leo, “Sustainable Hydrogen Production from Offshore Marine Renewable Farms: Techno-Energetic Insight on Seawater Electrolysis Technologies,” *ACS Sustain. Chem. Eng.*, vol. 7, pp. 8006–8022, 2019, doi: 10.1021/acssuschemeng.8b06779.

[42] K. Meier, “Hydrogen production with sea water electrolysis using Norwegian offshore wind energy potentials,” *Int J Energy Env. Eng*, vol. 5, no. 104, 2014, doi: 10.1007/s40095-014-0104-6.

[43] A. Godula-Jopek, J. Laurencin, J. Mougin, and P. Millet, *Hydrogen Production: Electrolysis*. Berlin: Wiley-VCH Verlag GmbH & Co. KGaA, 2015.

[44] Y. Shi, N. Cai, T. Cao, and J. Zhang, “High-Temperature Electrochemical Energy Conversion and Storage,” in *High-Temperature Electrochemical Energy Conversion and Storage*, 1st ed., Boca Raton: CRC Press, 2017, pp. 41–108.

[45] J. Udagawa, P. Aguiar, and N. P. Brandon, “Hydrogen production through steam electrolysis: Control strategies for a cathode-supported intermediate temperature solid oxide electrolysis cell,” *J. Power Sources*, vol. 180, no. 1, pp. 354–364, 2008, doi: 10.1016/j.jpowsour.2008.01.069.

[46] R. Daneshpour and M. Mehrpooya, “Design and optimization of a combined solar thermophotovoltaic power generation and solid oxide electrolyser for hydrogen production,” *Energy Convers. Manag.*, vol. 176, no. March, pp. 274–286, 2018, doi: 10.1016/j.enconman.2018.09.033.

[47] R. D. Boardman, *High temperature steam electrolysis*. Elsevier B.V., 2021.

[48] A. Saeedmanesh, P. Colombo, D. Mclarty, and J. Brouwer, “Dynamic Behavior of a Solid Oxide Steam Electrolyzer System Using Transient Photovoltaic Generated Power for Renewable Hydrogen Production,” *J. Electrochem. Energy Convers. Storage*, vol. 16, no. 4, p. z, 2019, doi: 10.1115/1.4043340.

[49] W. Sitte and R. Merkle, *High-Temperature Electrolysis From Fundamentals to applications*. IOP Publishing, 2023.

[50] T. F. Fuller and J. N. Harb, *Electrochemical Engineering*, First. Hoboken, NJ: John Wiley & Sons, Inc, 2018.

[51] J. P. Stempien, Q. Liu, M. Ni, Q. Sun, and S. H. Chan, “Physical principles for the calculation of equilibrium potential for co-electrolysis of steam and carbon dioxide in a Solid Oxide Electrolyzer Cell (SOEC),” *Electrochim. Acta*, vol. 147, pp. 490–497, 2014, doi: 10.1016/j.electacta.2014.09.144.

[52] J. S. Newman and Ni. P. Balsara, *Electrochemical Systems*, Fourth. Hoboken, New Jersey: John Wiley & Sons Inc., 2021.

[53] J. Udagawa, P. Aguiar, and N. P. Brandon, “Hydrogen production through steam electrolysis: Model-based steady state performance of a cathode-supported intermediate temperature solid oxide electrolysis cell,” *J. Power Sources*, vol. 166, no. 1, pp. 127–136, 2007, doi: 10.1016/j.jpowsour.2006.12.081.

[54] S. C. Singhal and K. Kendall, Eds., “High-temperature solid oxide fuel cells: fundamentals, design and applications,” Elsevier, 2003.

[55] P. Kazempoor and R. J. Braun, “Model validation and performance analysis of regenerative solid oxide cells: Electrolytic operation,” *Int. J. Hydrogen Energy*, vol. 39, no. 6, pp. 2669–2684, Feb. 2014, doi: 10.1016/J.IJHYDENE.2013.12.010.

[56] W. Tong *et al.*, “Electrolysis of low-grade and saline surface water,” *Nat. Energy*, vol. 5, no. May, pp. 367–377, 2020, doi: 10.1038/s41560-020-0550-8.

[57] S. Dresp, F. Dionigi, M. Klingenhof, and P. Strasser, “Direct Electrolytic Splitting of

Seawater : Opportunities and Challenges," *ACS Energy Lett.*, vol. 4, pp. 932–942, 2019, doi: 10.1021/acsenergylett.9b00220.

[58] C. Kuan, Q. Liu, J. Zhou, Q. Sun, and S. Hwa, "High-temperature electrolysis of synthetic seawater using solid oxide electrolyzer cells," *J. Power Sources*, vol. 342, pp. 79–87, 2017, doi: 10.1016/j.jpowsour.2016.12.019.

[59] K. Kamlungsua, P. C. Su, and S. H. Chan, "Hydrogen Generation Using Solid Oxide Electrolysis Cells," *Fuel Cells*, vol. 20, no. 6, pp. 644–649, 2020, doi: 10.1002/fuce.202070602.

[60] Z. Liu *et al.*, "Efficiency and stability of hydrogen production from seawater using solid oxide electrolysis cells," *Appl. Energy*, vol. 300, no. June, p. 117439, 2021, doi: 10.1016/j.apenergy.2021.117439.

[61] M. Delpisheh, M. A. Haghghi, H. Athari, and M. Mehrpooya, "Desalinated water and hydrogen generation from seawater via a desalination unit and a low temperature electrolysis using a novel solar-based setup," *Int. J. Hydrogen Energy*, vol. 46, no. 10, pp. 7211–7229, 2021, doi: 10.1016/j.ijhydene.2020.11.215.

[62] S. Kumari, R. Turner White, B. Kumar, and J. M. Spurgeon, "Solar hydrogen production from seawater vapor electrolysis," *Energy Environ. Sci.*, vol. 9, no. 5, pp. 1725–1733, 2016, doi: 10.1039/c5ee03568f.

[63] M. Rokni, "Analysis of a polygeneration plant based on solar energy , dual mode solid oxide cells and desalination," *Int. J. Hydrogen Energy*, pp. 1–20, 2018, doi: 10.1016/j.ijhydene.2018.03.147.

[64] A. Saeedmanesh, P. Colombo, and J. Brouwer, "Integration of Solid Oxide Steam Electrolyzer System into the UCI Microgrid to Support High Renewable Use," *ECS Trans.*, vol. 96, no. 1, pp. 71–79, 2020, doi: 10.1149/09601.0071ecst.

[65] N. C. Darre and G. S. Toor, "Desalination of Water: a Review," *Curr. Pollut. Reports*, vol. 4, no. 2, pp. 104–111, 2018, doi: 10.1007/s40726-018-0085-9.

[66] M. H. Sharqawy, M. A. Antar, S. M. Zubair, and A. M. Elbashir, "Optimum thermal design of humidification dehumidification desalination systems," *Desalination*, vol. 349, pp. 10–21, 2014, doi: 10.1016/j.desal.2014.06.016.

[67] D. Brogioli, F. La Mantia, and N. Y. Yip, "Thermodynamic analysis and energy efficiency of thermal desalination processes," *Desalination*, vol. 428, no. July 2017, pp. 29–39,

2018, doi: 10.1016/j.desal.2017.11.010.

[68] M. O. Mavukkandy, C. M. Chabib, I. Mustafa, A. Al Ghaferi, and F. AlMarzooqi, “Brine management in desalination industry: From waste to resources generation,” *Desalination*, vol. 472, no. October, p. 114187, 2019, doi: 10.1016/j.desal.2019.114187.

[69] J. Mustafa, A. A. H. I. Mourad, A. H. Al-Marzouqi, and M. H. El-Naas, “Simultaneous treatment of reject brine and capture of carbon dioxide: A comprehensive review,” *Desalination*, vol. 483, no. March, p. 114386, 2020, doi: 10.1016/j.desal.2020.114386.

[70] B. K. Pramanik, L. Shu, and V. Jegatheesan, “A review of the management and treatment of brine solutions,” *Environ. Sci. Water Res. Technol.*, vol. 3, no. 4, pp. 625–658, 2017, doi: 10.1039/c6ew00339g.

[71] A. Dindi, D. V. Quang, and M. R. M. Abu-Zahra, “Simultaneous carbon dioxide capture and utilization using thermal desalination reject brine,” *Appl. Energy*, vol. 154, pp. 298–308, 2015, doi: 10.1016/j.apenergy.2015.05.010.

[72] S. Manahan, “5.13: Industrial Chemical Reactions - The Solvay Process,” *LibreTexts Chemistry*, Mar. 16, 2021. https://chem.libretexts.org/Bookshelves/Environmental_Chemistry/Green_Chemistry_and_the_Ten_Commandments_of_Sustainability_(Manahan)/05%3A_Chemical_Reactions-_Making_Materials_Safely_and_Sustainable/5.13%3A_Industrial_Chemical_Reactions_-_The_Solvay_Proce (accessed Mar. 27, 2023).

[73] R. I. Macdonald, “Energy Storage in Evaporated Brine.”

[74] R. B. Lakeh, C. Salerno, E. P. Herlim, J. Kiriakos, and S. Delagah, “Repurposing Reverse Osmosis Concentrate as a Low-Cost Thermal Energy Storage Medium,” *J. Clean Energy Technol.*, vol. 8, no. 4, pp. 31–40, 2020, doi: 10.18178/jocet.2020.8.4.522.

[75] L. F. Cabeza *et al.*, “Lithium in thermal energy storage: A state-of-the-art review,” *Renew. Sustain. Energy Rev.*, vol. 42, pp. 1106–1112, 2015, doi: 10.1016/j.rser.2014.10.096.

[76] R. N. Nalbandian *et al.*, “Simulation of an ROC-based thermal energy storage system in charge and discharge cycles,” *Proc. ASME 2021 15th Int. Conf. Energy Sustain. ES 2021*, 2021, doi: 10.1115/ES2021-63930.

[77] J. A. Lee, C. N. Salerno, K. U. Girgis, U. Aguirre, and R. B. Lakeh, “Effect of phase change and buoyancy-driven flows on an ROC-based thermal energy storage system,” *Proc. ASME 2021 15th Int. Conf. Energy Sustain. ES 2021*, pp. 1–10, 2021, doi:

10.1115/ES2021-63938.

[78] B. C. Camey *et al.*, “Techno-Economics of Using Concentrate of Membrane Processes As a Low-Cost Thermal Energy Storage Medium,” *ASME Int. Mech. Eng. Congr. Expo. Proc.*, vol. 8B-2021, pp. 1–9, 2021, doi: 10.1115/IMECE2021-73734.

[79] IRENA, “Offshore renewables: An action agenda for deployment,” Abu Dhabi, 2021.

[80] F. Zhao and J. Lee, “Global Offshore Wind Report 2021,” 2022.

[81] M. Walter *et al.*, “Offshore Wind Market Report: 2021 Edition,” *Dep. Energy*, pp. 0–119, 2021.

[82] P. Bojek, “Wind Power,” Paris, 2021.

[83] H. Díaz and C. Guedes Soares, “Review of the current status, technology and future trends of offshore wind farms,” *Ocean Eng.*, vol. 209, no. January, p. 107381, 2020, doi: 10.1016/j.oceaneng.2020.107381.

[84] C. Dong, G. (Gordon) Huang, and G. Cheng, “Offshore wind can power Canada,” *Energy*, vol. 236, p. 121422, 2021, doi: 10.1016/j.energy.2021.121422.

[85] L. Sommer, “Biden Administration Strikes A Deal To Bring Offshore Wind To California,” *NPR*, 2021. https://www.npr.org/2021/05/25/1000210550/biden-administration-strikes-deal-to-bring-offshore-wind-to-california (accessed Mar. 29, 2022).

[86] “Floating offshore wind in Equinor ,” *equinor.com*, 2021. https://www.equinor.com/en/what-we-do/floating-wind.html (accessed Oct. 12, 2021).

[87] H. Wang, J. Ye, L. Huang, Q. Wang, and H. Zhang, “A multivariable hybrid prediction model of offshore wind power based on multi-stage optimization and reconstruction prediction,” *Energy*, vol. 262, no. PA, p. 125428, 2023, doi: 10.1016/j.energy.2022.125428.

[88] A. J. Headley and D. A. Copp, “Energy storage sizing for grid compatibility of intermittent renewable resources: A California case study,” *Energy*, vol. 198, p. 117310, 2020, doi: 10.1016/j.energy.2020.117310.

[89] J. H. Slusarewicz and D. S. Cohan, “Assessing solar and wind complementarity in Texas,” *Renewables Wind. Water, Sol.*, vol. 5, no. 1, 2018, doi: 10.1186/s40807-018-0054-3.

[90] C. Draxl, A. Clifton, B. M. Hodge, and J. McCaa, “The Wind Integration National Dataset (WIND) Toolkit,” *Appl. Energy*, vol. 151, pp. 355–366, Aug. 2015, doi: 10.1016/J.APENERGY.2015.03.121.

[91] C. Draxl, B.-M. Hodge, A. Clifton, and J. Mccaa, “Overview and Meteorological Validation of the Wind Integration National Dataset Toolkit,” Golden, CO, Apr. 2007.

[92] J. King, R. A. Clifton, and B.-M. Hodge, “Validation of Power Output for the WIND Toolkit,” Golden, CO, Sep. 2014.

[93] “Offshore Wind Turbine SG 14-222 DD ,” *Siemens Gamesa Renewable Energy*. https://www.siemensgamesa.com/products-and-services/offshore/wind-turbine-sg-14-222-dd (accessed Jun. 14, 2021).

[94] T. Ackermann, *Wind Power in Power Systems*. 2005.

[95] Y. H. Wang, R. K. Walter, C. White, M. D. Kehrli, and B. Ruttenberg, “Scenarios for offshore wind power production for Central California Call Areas,” *Wind Energy*, no. April, pp. 1–11, 2021, doi: 10.1002/we.2646.

[96] S. A. Hsu, E. A. Meindle, and D. B. Gilhousen, “Determining the Power-Law Wind Profile Exponent under Near Neutral Stability Conditions at Sea,” *J. Appl. Meteorol. Climatol.*, vol. 33, no. 6, pp. 757–765, 1994, doi: https://doi.org/10.1175/1520-0450(1994)033<0757:DTPLWP>2.0.CO;2.

[97] T. H. Ruggles, D. J. Farnham, D. Tong, and K. Caldeira, “Developing reliable hourly electricity demand data through screening and imputation,” *Sci. Data*, vol. 7, no. 1, pp. 1–14, 2020, doi: 10.1038/s41597-020-0483-x.

[98] “California Solar Energy Statistics and Data.” https://ww2.energy.ca.gov/almanac/renewables_data/solar/index_cms.php (accessed Mar. 29, 2022).

[99] C. L. Archer and M. Z. Jacobson, “Supplying baseload power and reducing transmission requirements by interconnecting wind farms,” *J. Appl. Meteorol. Climatol.*, vol. 46, no. 11, pp. 1701–1717, 2007, doi: 10.1175/2007JAMC1538.1.

[100] I. Jebli, F. Z. Belouadha, M. I. Kabbaj, and A. Tilioua, “Prediction of solar energy guided by pearson correlation using machine learning,” *Energy*, vol. 224, p. 120109, 2021, doi: 10.1016/j.energy.2021.120109.

[101] J. Wu, N. Li, Y. Zhao, and J. Wang, “Usage of correlation analysis and hypothesis test in optimizing the gated recurrent unit network for wind speed forecasting,” *Energy*, vol. 242, 2022, doi: 10.1016/j.energy.2021.122960.

[102] S. C. Edison, “Standard Residential Rate,” 2016.

https://www.sce.com/wps/portal/home/residential/rates/Standard-Residential-Rate-Plan/!ut/p/b1/rVJNc4IwEP0reuCIWQkK9JZWq1Ct3x9wcQIEpIMBIa1tf32j40FnqtaZ5rTJvn15u_uQh5bI4_QjialIMk7T_d1rrhy7ReodXbMHLy0CZDYe9sz5pG6OdQlwJQAuHAKH-rrZIV17AnZn2NDBdowpGIasfzbQAnnIC (accessed Nov. 20, 2016).

[103] L. Akula, "How to add Fourier Terms to your regression & seasonality analysis (using Python & SciPy)," *towards data science*, Oct. 12, 2020. https://towardsdatascience.com/how-to-add-fourier-terms-to-your-regression-seasonality-analysis-using-python-scipy-99a94d3ae51 (accessed Jun. 09, 2021).

[104] A. Collins Jackson and S. Lacey, "The discrete Fourier transformation for seasonality and anomaly detection of an application to rare data," *Data Technol. Appl.*, vol. 54, no. 2, pp. 121–132, 2020, doi: 10.1108/DTA-12-2019-0243.

[105] O. Akgun and T. Cetin Akinci, "Renewable Energy - Resources, Challenges, and Applications," in *Renewable Energy - Resources, Challenges and Applications*, A. Q. Mansour, E. Ahmad, and S. S. Hakan, Eds. IntechOpen, 2020.

[106] E. Dokur, N. Erdogan, M. E. Salari, C. Karakuzu, and J. Murphy, "Offshore wind speed short-term forecasting based on a hybrid method: Swarm decomposition and meta-extreme learning machine," *Energy*, vol. 248, p. 123595, 2022, doi: 10.1016/j.energy.2022.123595.

[107] F. Pedregosa *et al.*, "Scikit-learn: Machine Learning in Python ," *J. Mach. Learn. Res.*, vol. 12, pp. 2825–2830, Oct. 2011.

[108] S. H. Jensen, P. H. Larsen, and M. Mogensen, "Hydrogen and synthetic fuel production from renewable energy sources," *Int. J. Hydrogen Energy*, vol. 32, no. 15 SPEC. ISS., pp. 3253–3257, 2007, doi: 10.1016/j.ijhydene.2007.04.042.

[109] A. A. AlZahrani and I. Dincer, "Thermodynamic and electrochemical analyses of a solid oxide electrolyzer for hydrogen production," *Int. J. Hydrogen Energy*, vol. 42, no. 33, pp. 21404–21413, 2017, doi: 10.1016/j.ijhydene.2017.03.186.

[110] L. Mastropasqua, I. Pecenati, A. Giostri, and S. Campanari, "Solar hydrogen production: Techno-economic analysis of a parabolic dish-supported high-temperature electrolysis system," *Appl. Energy*, vol. 261, no. September 2019, p. 114392, 2020, doi: 10.1016/j.apenergy.2019.114392.

[111] H. Zhu, R. J. Kee, V. M. Janardhanan, O. Deutschmann, and D. G. Goodwin, "Modeling

Elementary Heterogeneous Chemistry and Electrochemistry in Solid-Oxide Fuel Cells," *J. Electrochem. Soc.*, vol. 152, no. 12, p. A2427, 2005, doi: 10.1149/1.2116607.

[112] P. Mottaghizadeh, M. Fardadi, F. Jabbari, and J. Brouwer, "Dynamics and control of a thermally self-sustaining energy storage system using integrated solid oxide cells for an islanded building," *Int. J. Hydrogen Energy*, vol. 46, no. 49, pp. 24891–24908, 2021, doi: 10.1016/j.ijhydene.2021.03.136.

[113] P. Holtappels, H. Mehling, S. Roehlich, S. S. Liebermann, and U. Stimming, "SOFC system operating strategies for mobile applications," *Fuel Cells*, vol. 5, no. 4, pp. 499–508, 2005, doi: 10.1002/fuce.200400088.

[114] L. Ba *et al.*, "A study on solid oxide electrolyzer stack and system performance based on alternative mapping models," *Int. J. Hydrogen Energy*, vol. 47, no. 25, pp. 12469–12486, 2022, doi: 10.1016/j.ijhydene.2022.01.253.

[115] V. Menon, V. M. Janardhanan, and O. Deutschmann, "A mathematical model to analyze solid oxide electrolyzer cells (SOECs) for hydrogen production," *Chem. Eng. Sci.*, vol. 110, pp. 83–93, 2014, doi: 10.1016/j.ces.2013.10.025.

[116] T. L. Bergman, A. S. Lavine, F. P. Incropera, and D. P. Dewitt, *Fundamentals of Heat and Mass Transfer*, 7th ed. John Wiley & Sons Inc., 2011.

[117] T. L. Bergman, A. S. Lavine, F. P. Incropera, and D. P. Dewitt, *Fundamentals of Heat and Mass Transfer*, 7th ed., no. c. John Wiley & Sons Inc., 2011.

[118] "National Centers for Environmental Information," *National Oceanic and Atmospheric Administration*. https://www.ncei.noaa.gov/access/coastal-water-temperature-guide/all_table.html#npac.

[119] V. Liso, A. C. Olesen, M. P. Nielsen, and S. K. Kær, "Performance comparison between partial oxidation and methane steam reforming processes for solid oxide fuel cell (SOFC) micro combined heat and power (CHP) system," *Energy*, vol. 36, no. 7, pp. 4216–4226, 2011, doi: 10.1016/j.energy.2011.04.022.

[120] G. Xiao, A. Sun, H. Liu, M. Ni, and H. Xu, "Thermal management of reversible solid oxide cells in the dynamic mode switching," *Appl. Energy*, vol. 331, no. November 2022, p. 120383, 2023, doi: 10.1016/j.apenergy.2022.120383.

[121] F. Salomone, E. Giglio, D. Ferrero, M. Santarelli, R. Pirone, and S. Bensaid, "Techno-economic modelling of a Power-to-Gas system based on SOEC electrolysis and CO2

methanation in a RES-based electric grid," *Chem. Eng. J.*, vol. 377, no. October 2018, p. 120233, 2019, doi: 10.1016/j.cej.2018.10.170.

[122] H. Shimada *et al.*, "Nanocomposite electrodes for high current density over 3 A cm−2 in solid oxide electrolysis cells," *Nat. Commun.*, vol. 10, no. 1, pp. 1–10, 2019, doi: 10.1038/s41467-019-13426-5.

[123] M. Tucker *et al.*, "HydroGEN: High Temperature Electrolysis (HTE) Hydrogen Production," *2018 Annual Meri Review, DC*, 2018. https://www.hydrogen.energy.gov/pdfs/review18/pd148_boardman_2018_o.pdf.

[124] Hydrogen and Fuel Cell Technologies Office, "Technical Targets for High Temperature Electrolysis," *Office of ENERGY EFFICIENCY & RENEWABLE ENERGY*. https://www.energy.gov/eere/fuelcells/technical-targets-high-temperature-electrolysis.

[125] T. L. Skafte *et al.*, "Electrothermally balanced operation of solid oxide electrolysis cells," *J. Power Sources*, vol. 523, 2022, doi: 10.1016/j.jpowsour.2022.231040.

[126] M. Carmo, D. L. Fritz, J. Mergel, and D. Stolten, "A comprehensive review on PEM water electrolysis," *Int. J. Hydrogen Energy*, vol. 38, no. 12, pp. 4901–4934, 2013, doi: 10.1016/j.ijhydene.2013.01.151.

[127] N. Ghaffour, S. Lattemann, T. Missimer, K. C. Ng, S. Sinha, and G. Amy, "Renewable energy-driven innovative energy-efficient desalination technologies," *Appl. Energy*, vol. 136, pp. 1155–1165, 2014, doi: 10.1016/j.apenergy.2014.03.033.

[128] M. Bonanno, K. Müller, B. Bensmann, R. Hanke-Rauschenbach, R. Peach, and S. Thiele, "Evaluation of the Efficiency of an Elevated Temperature Proton Exchange Membrane Water Electrolysis System," *J. Electrochem. Soc.*, vol. 168, no. 9, p. 094504, 2021, doi: 10.1149/1945-7111/ac2188.

[129] H. R. Corti, "Polymer electrolytes for low and high temperature PEM electrolyzers," *Curr. Opin. Electrochem.*, vol. 36, p. 101109, 2022, doi: 10.1016/j.coelec.2022.101109.

[130] J. O. Jensen, C. Chatzichristodoulou, E. Christensen, N. J. Bjerrum, and Q. Li, "Intermediate Temperature Electrolysers," no. 25, pp. 253–285.

[131] S. Fukuzumi, Y. M. Lee, and W. Nam, "Fuel Production from Seawater and Fuel Cells Using Seawater," *ChemSusChem*, vol. 10, no. 22, pp. 4264–4276, 2017, doi: 10.1002/cssc.201701381.

[132] Y. Wang, B. Marchetti, and X. D. Zhou, "Call attention to using DRT and EIS to quantify

the contributions of solid oxide cell components to the total impedance," *Int. J. Hydrogen Energy*, no. xxxx, pp. 1–12, 2022, doi: 10.1016/j.ijhydene.2022.08.093.

[133] M. E. Orazem and B. Tribollet, *Electrochemical impedance spectroscopy*, 2nd Editio., vol. 1, no. 1. Hoboken, New Jersey: John Wiley & Sons Inc., 2017.

[134] Q. Fang, L. Blum, and N. H. Menzler, "Performance and Degradation of Solid Oxide Electrolysis Cells in Stack," *J. Electrochem. Soc.*, vol. 162, no. 8, pp. F907–F912, 2015, doi: 10.1149/2.0941508jes.

[135] T. P. Holme, R. Pornprasertsuk, and F. B. Prinz, "Interpretation of Low Temperature Solid Oxide Fuel Cell Electrochemical Impedance Spectra," *J. Electrochem. Soc.*, vol. 157, no. 1, p. B64, 2010, doi: 10.1149/1.3251291.

[136] V. Vivier and M. E. Orazem, "Impedance Analysis of Electrochemical Systems," *Chem. Rev.*, vol. 122, no. 12, pp. 11131–11168, 2022, doi: 10.1021/acs.chemrev.1c00876.

[137] W. G. Bessler and S. Gewies, "Gas Concentration Impedance of Solid Oxide Fuel Cell Anodes," *J. Electrochem. Soc.*, vol. 154, no. 6, p. B548, 2007, doi: 10.1149/1.2720639.

[138] G. Nusev, B. Morel, J. Mougin, Đ. Juričić, and P. Boškoski, "Condition monitoring of solid oxide fuel cells by fast electrochemical impedance spectroscopy: A case example of detecting deficiencies in fuel supply," *J. Power Sources*, vol. 489, no. January, p. 229491, 2021, doi: 10.1016/j.jpowsour.2021.229491.

[139] V. Subotić, B. Stoeckl, V. Lawlor, J. Strasser, H. Schroettner, and C. Hochenauer, "Towards a practical tool for online monitoring of solid oxide fuel cell operation: An experimental study and application of advanced data analysis approaches," *Appl. Energy*, vol. 222, no. November 2017, pp. 748–761, 2018, doi: 10.1016/j.apenergy.2018.03.182.

[140] A. Lasia, *Electrochemical impedance spectroscopy and its applications*, vol. 9781461489. 2014.

[141] A. Weiß, S. Schindler, S. Galbiati, M. A. Danzer, and R. Zeis, "Distribution of Relaxation Times Analysis of High-Temperature PEM Fuel Cell Impedance Spectra," *Electrochim. Acta*, vol. 230, pp. 391–398, 2017, doi: 10.1016/j.electacta.2017.02.011.

[142] T. H. Wan, M. Saccoccio, C. Chen, and F. Ciucci, "Influence of the Discretization Methods on the Distribution of Relaxation Times Deconvolution: Implementing Radial Basis Functions with DRTtools," *Electrochim. Acta*, vol. 184, pp. 483–499, 2015, doi: 10.1016/j.electacta.2015.09.097.

[143] V. Subotić and C. Hochenauer, “Analysis of solid oxide fuel and electrolysis cells operated in a real-system environment: State-of-the-health diagnostic, failure modes, degradation mitigation and performance regeneration,” *Prog. Energy Combust. Sci.*, vol. 93, no. March, 2022, doi: 10.1016/j.pecs.2022.101011.

[144] V. Subotić *et al.*, “Detailed insight into processes of reversible solid oxide cells and stacks using DRT analysis,” *Energy Convers. Manag.*, vol. 226, no. September, 2020, doi: 10.1016/j.enconman.2020.113509.

[145] Z. Liu *et al.*, “Reversible cycling performance of a flat-tube solid oxide cell for seawater electrolysis,” *Energy Convers. Manag.*, vol. 258, no. January, p. 115543, 2022, doi: 10.1016/j.enconman.2022.115543.

[146] “Anode Supported Planar Cell.” https://fuelcellmaterials.com/products/cells/anode-supported-cells/anode-supported-planar-cell/ (accessed Mar. 18, 2022).

[147] J. Huang, “A simple accurate formula for calculating saturation vapor pressure of water and ice,” *J. Appl. Meteorol. Climatol.*, vol. 57, no. 6, pp. 1265–1272, 2018, doi: 10.1175/JAMC-D-17-0334.1.

[148] “Sea Water,” *National Weather Service*. https://www.weather.gov/jetstream/seawater (accessed Mar. 17, 2022).

[149] L. Mastropasqua, S. Campanari, and J. Brouwer, “Solid oxide fuel cell short stack performance testing - Part A: Experimental analysis and M-combined heat and power unit comparison,” *J. Power Sources*, vol. 371, pp. 225–237, 2017, doi: 10.1016/j.jpowsour.2017.10.028.

[150] W. Watson and M. E. Orazem, “EIS: Measurement Model Program,” 2020. .

[151] C. Graves, S. D. Ebbesen, S. H. Jensen, S. B. Simonsen, and M. B. Mogensen, “Eliminating degradation in solid oxide electrochemical cells by reversible operation,” *Nat. Mater.*, vol. 14, no. 2, pp. 239–244, 2015, doi: 10.1038/nmat4165.

[152] D. Klotz, A. Weber, and E. Ivers-Tiffée, “Practical Guidelines for Reliable Electrochemical Characterization of Solid Oxide Fuel Cells,” *Electrochim. Acta*, vol. 227, pp. 110–126, 2017, doi: 10.1016/j.electacta.2016.12.148.

[153] G. Jeanmonod, S. Diethelm, and J. Van herle, “Poisoning effects of chlorine on a solid oxide cell operated in co-electrolysis,” *J. Power Sources*, vol. 506, no. July, p. 230247, 2021, doi: 10.1016/j.jpowsour.2021.230247.

[154] A. Nechache, M. Cassir, and A. Ringuedé, “Solid oxide electrolysis cell analysis by means of electrochemical impedance spectroscopy: A review,” *J. Power Sources*, vol. 258, pp. 164–181, 2014, doi: 10.1016/j.jpowsour.2014.01.110.

[155] A. Hauch, S. D. Ebbesen, S. H. Jensen, and M. Mogensen, “Solid Oxide Electrolysis Cells: Microstructure and Degradation of the Ni/Yttria-Stabilized Zirconia Electrode,” *J. Electrochem. Soc.*, vol. 155, no. 11, p. B1184, 2008, doi: 10.1149/1.2967331.

[156] A. Hauch, *Solid oxide electrolysis cells - Performance and durability*, vol. 37, no. October. 2007.

[157] P. Moçoteguy and A. Brisse, “A review and comprehensive analysis of degradation mechanisms of solid oxide electrolysis cells,” *Int. J. Hydrogen Energy*, vol. 38, no. 36, pp. 15887–15902, 2013, doi: 10.1016/j.ijhydene.2013.09.045.

[158] Y. Yang *et al.*, “Study of solid oxide electrolysis cells operated in potentiostatic mode: Effect of operating temperature on durability,” *Chem. Eng. J.*, vol. 417, no. November 2020, p. 129260, 2021, doi: 10.1016/j.cej.2021.129260.

[159] “Electrical Conductivity/Salinity Fact Sheet,” Sacramento, CA, 2004.

[160] Z. Zheng, Y. Fu, K. Liu, R. Xiao, X. Wang, and H. Shi, “Three-stage vertical distribution of seawater conductivity,” *Sci. Reports 2018 81*, vol. 8, no. 1, pp. 1–10, Jul. 2018, doi: 10.1038/s41598-018-27931-y.

[161] “Water quality standards.” https://mrccc.org.au/wp-content/uploads/2013/10/Water-Quality-Salinity-Standards.pdf (accessed Mar. 17, 2022).

10 APPENDIX

10.1 Appendix A

10.1.1 Raw EIS data from the DI water tests:

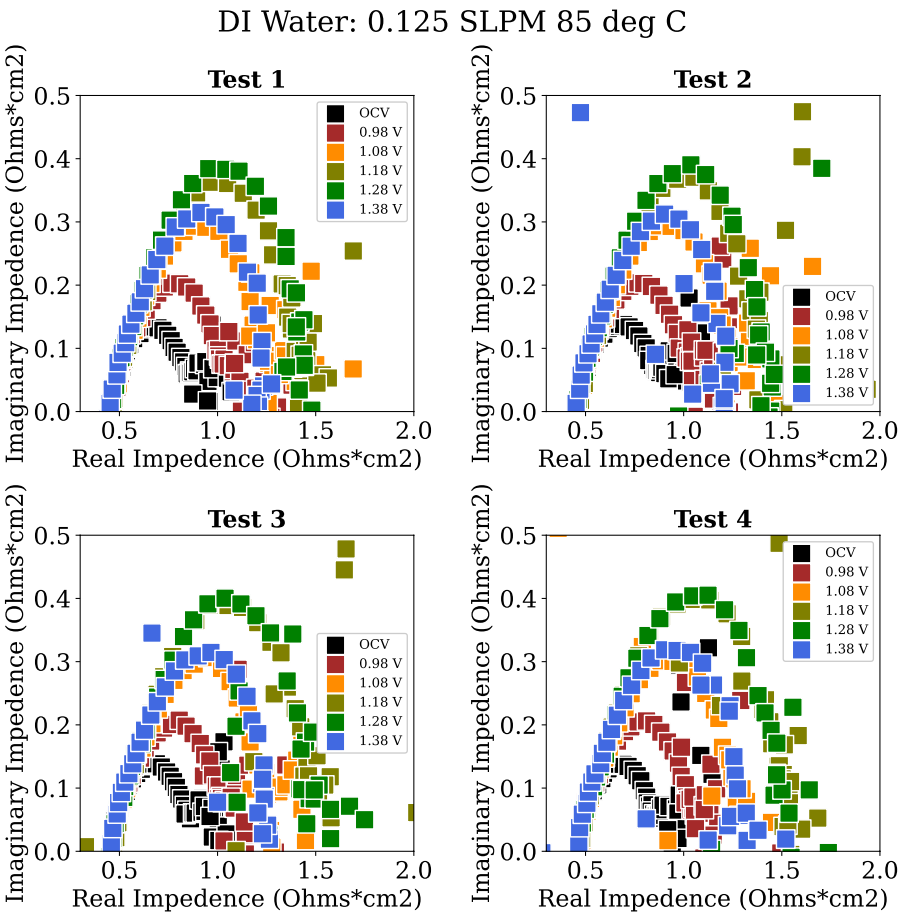
DI Water: 0.125 SLPM 85 deg C
Test 1
Test 2
Test 3
Test 4
Imaginary Impedence (Ohms*cm2)
Real Impedence (Ohms*cm2)
OCV
0.98 V
1.08 V
1.18 V
1.28 V
1.38 V
0.0
0.1
0.2
0.3
0.4
0.5
0.5
1.0
1.5
2.0

DI Water: 0.25 SLPM 85 deg C

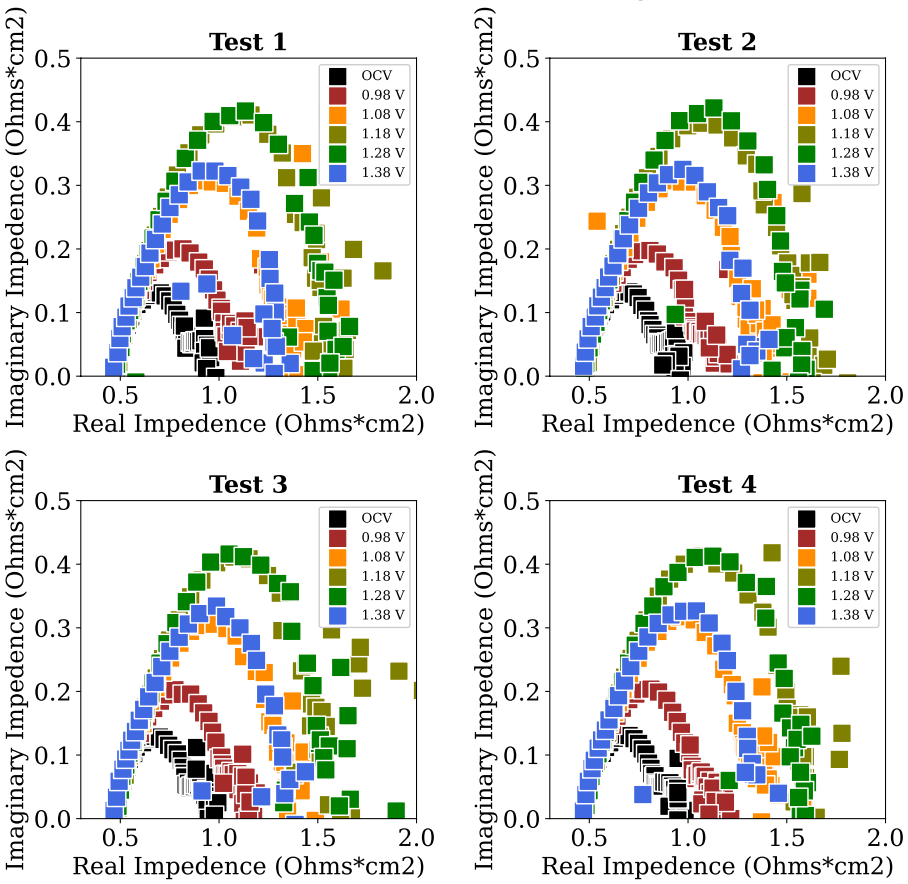

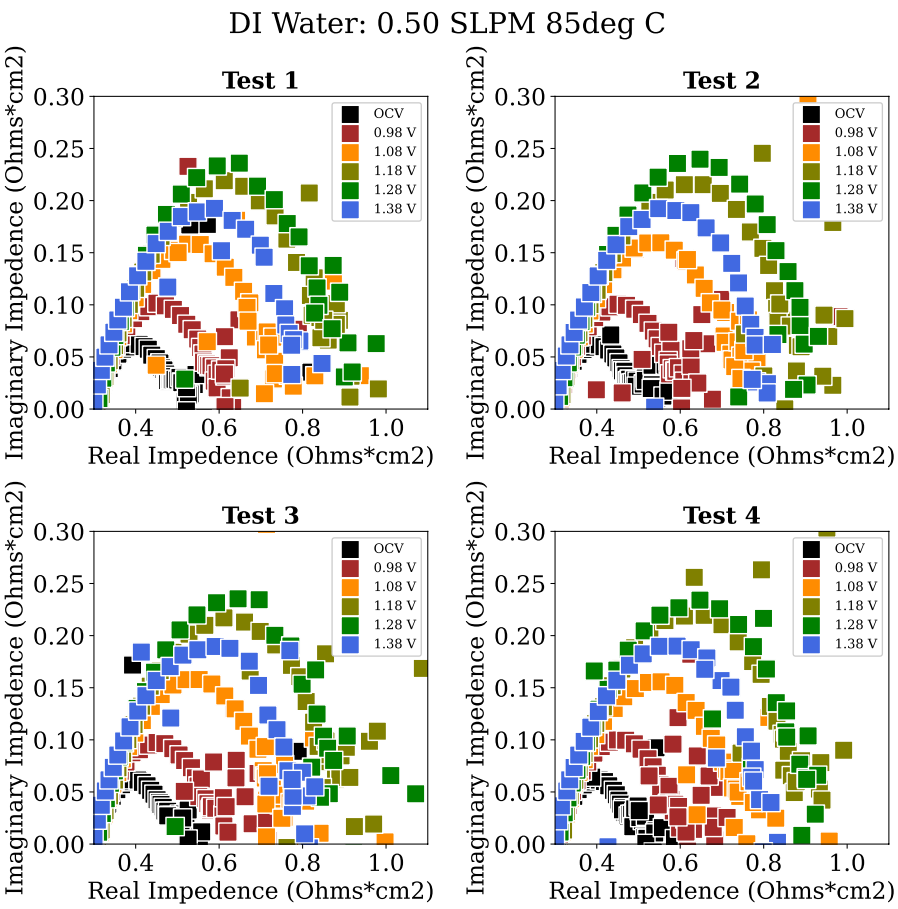
DI Water: 0.50 SLPM 85deg C
Test 1
Test 2
Test 3
Test 4
Imaginary Impedence (Ohms*cm2)
Real Impedence (Ohms*cm2)
OCV
0.98 V
1.08 V
1.18 V
1.28 V
1.38 V
0.00
0.05
0.10
0.15
0.20
0.25
0.30
0.4
0.6
0.8
1.0

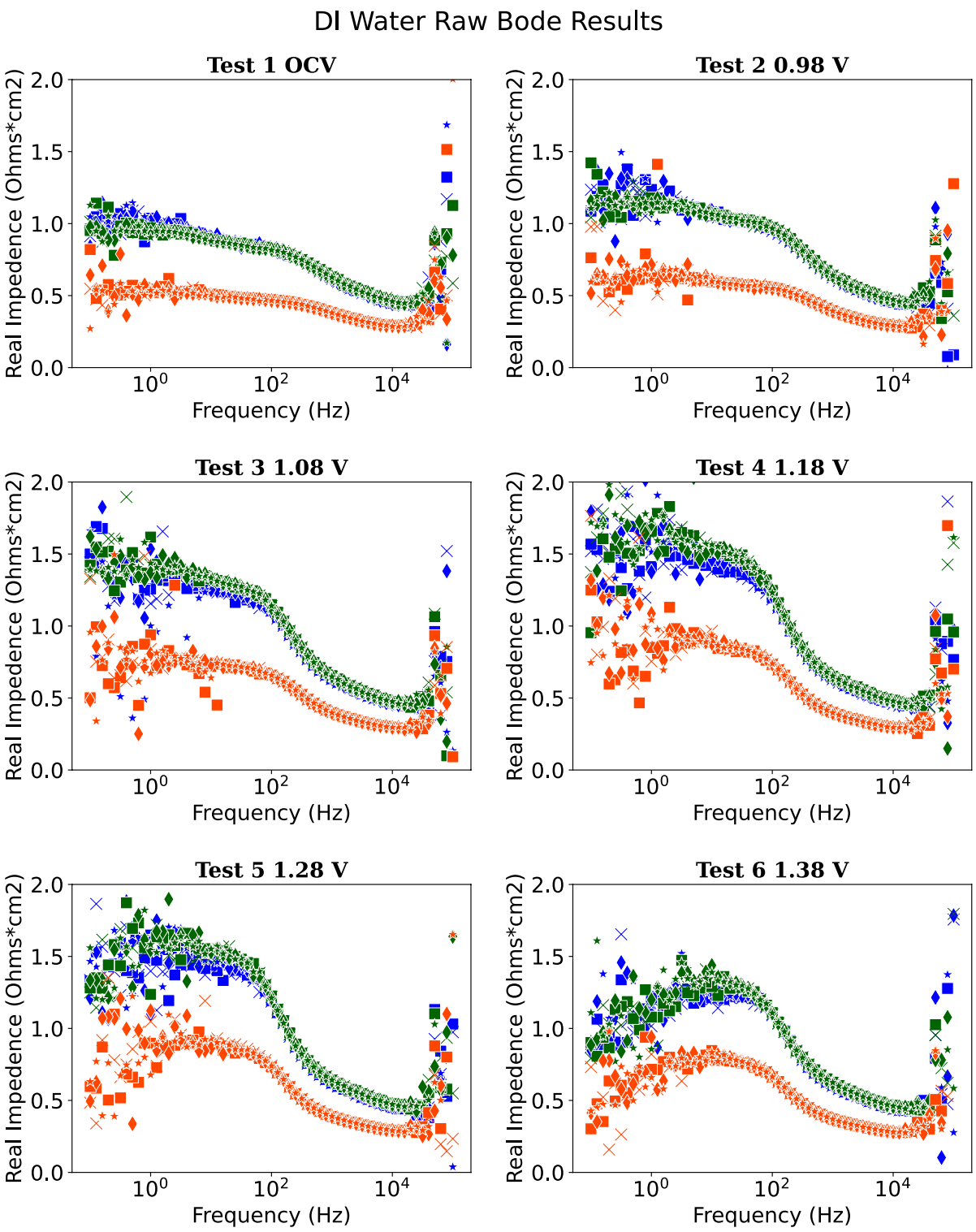
DI Water Raw Bode Results
Test 1 OCV
Test 2 0.98 V
Test 3 1.08 V
Test 4 1.18 V
Test 5 1.28 V
Test 6 1.38 V
Real Impedence (Ohms*cm2)
Frequency (Hz)
0.0
0.5
1.0
1.5
2.0
10^0
10^2
10^4

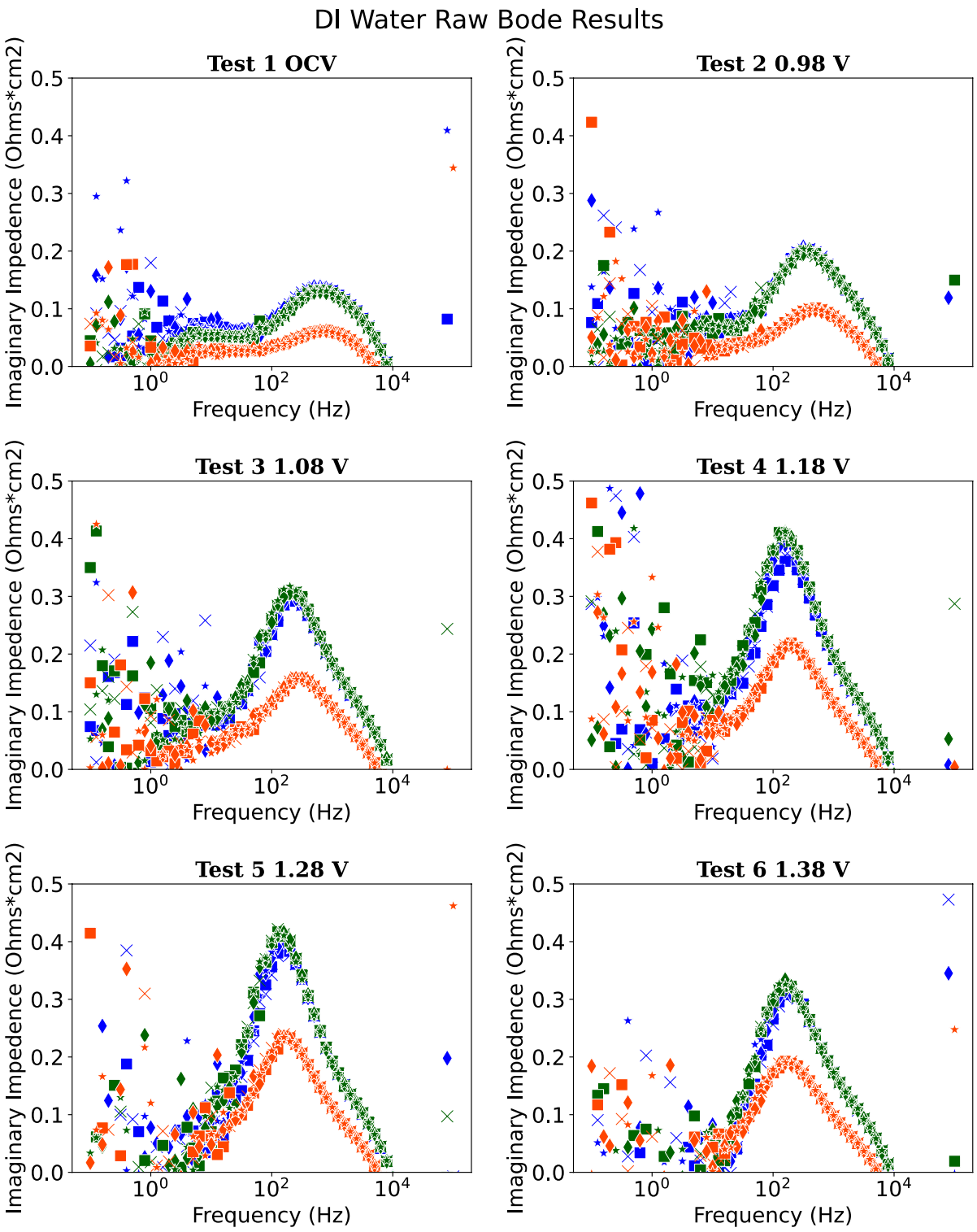
DI Water Raw Bode Results
Test 1 OCV
Test 2 0.98 V
Test 3 1.08 V
Test 4 1.18 V
Test 5 1.28 V
Test 6 1.38 V
Imaginary Impedence (Ohms*cm2)
Frequency (Hz)
0.0
0.1
0.2
0.3
0.4
0.5
10^0
10^2
10^4

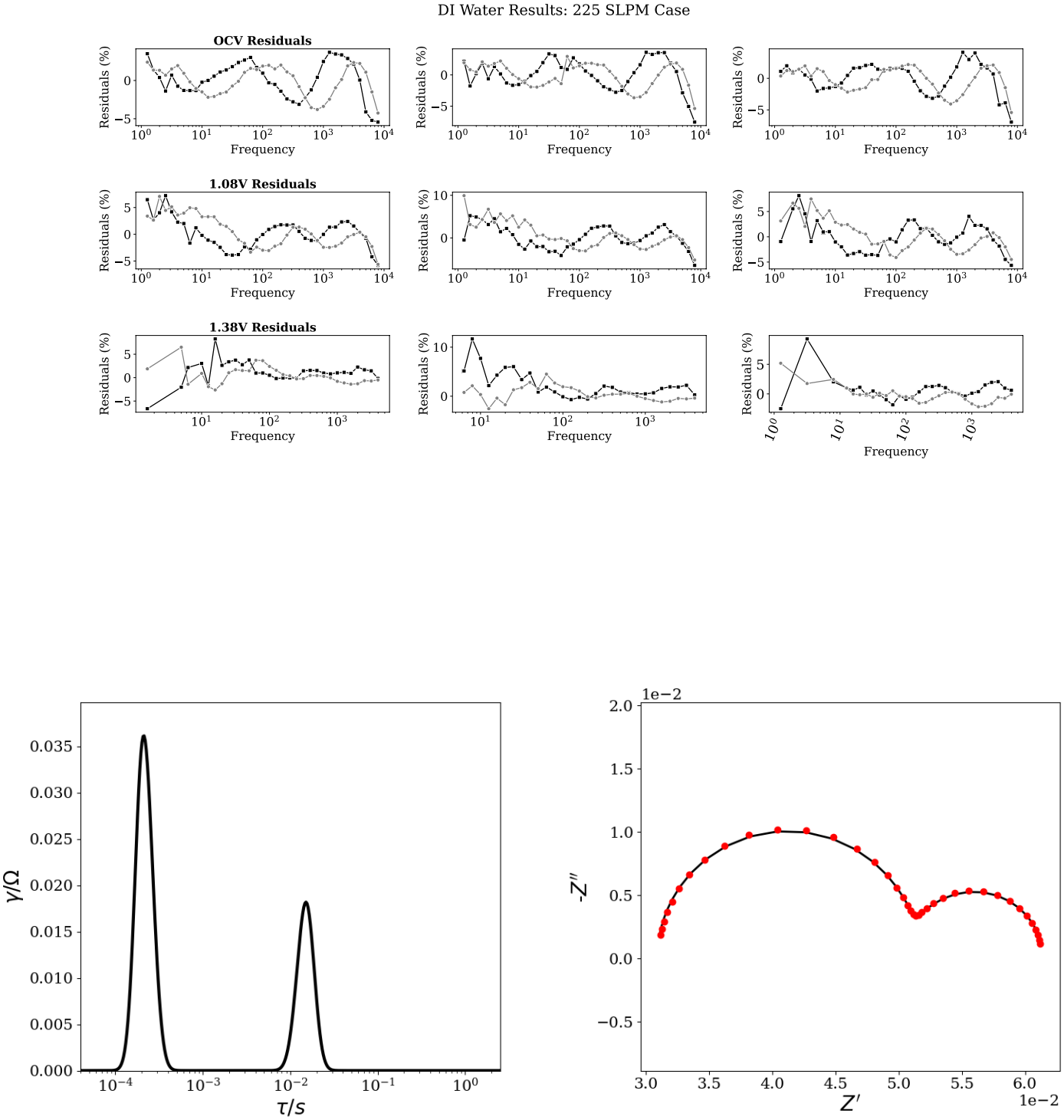

Figure 10-1: DRT Results for the DI water case at OCV with 0.125 SLPM

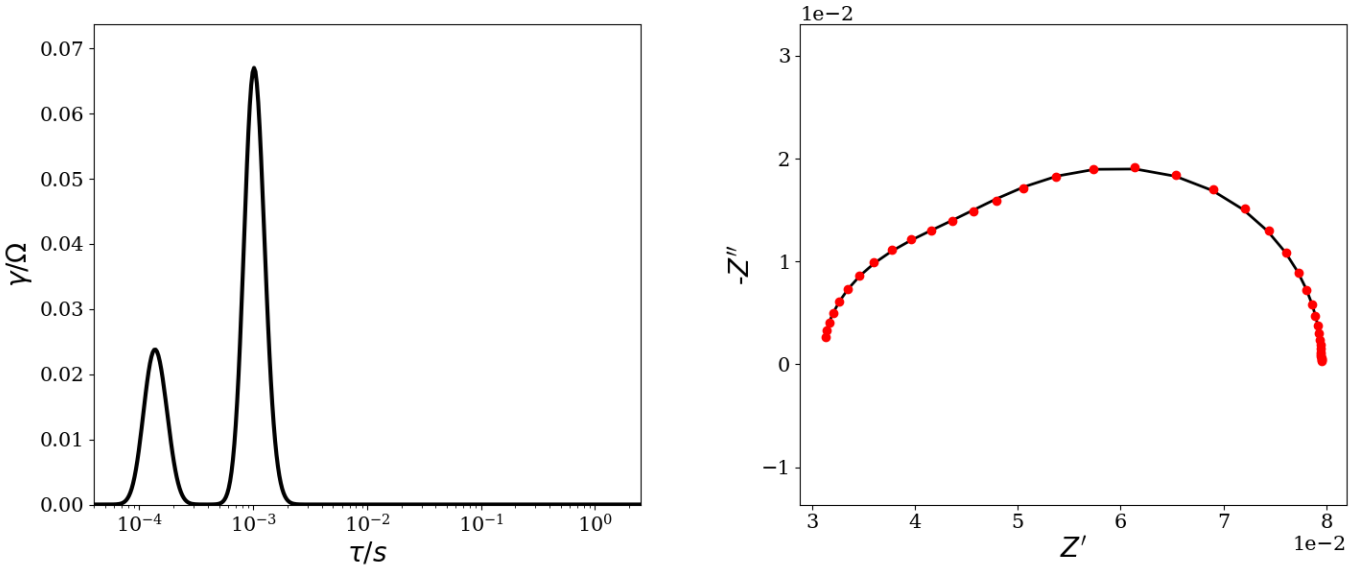

Figure 10-2: DRT result for DI water 0.125 SLPM 1.08V

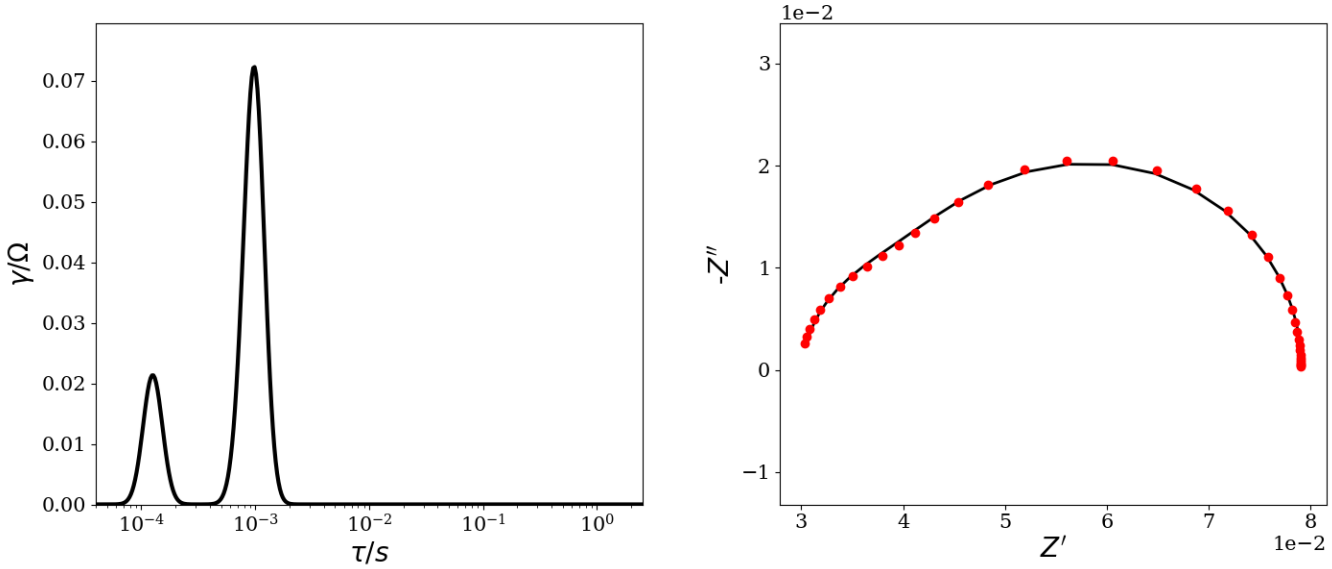

Figure 10-3: DRT result for DI water with 0.125 SLPM at 1.38 V

10.1.2 **Raw EIS data from Tap Water:**

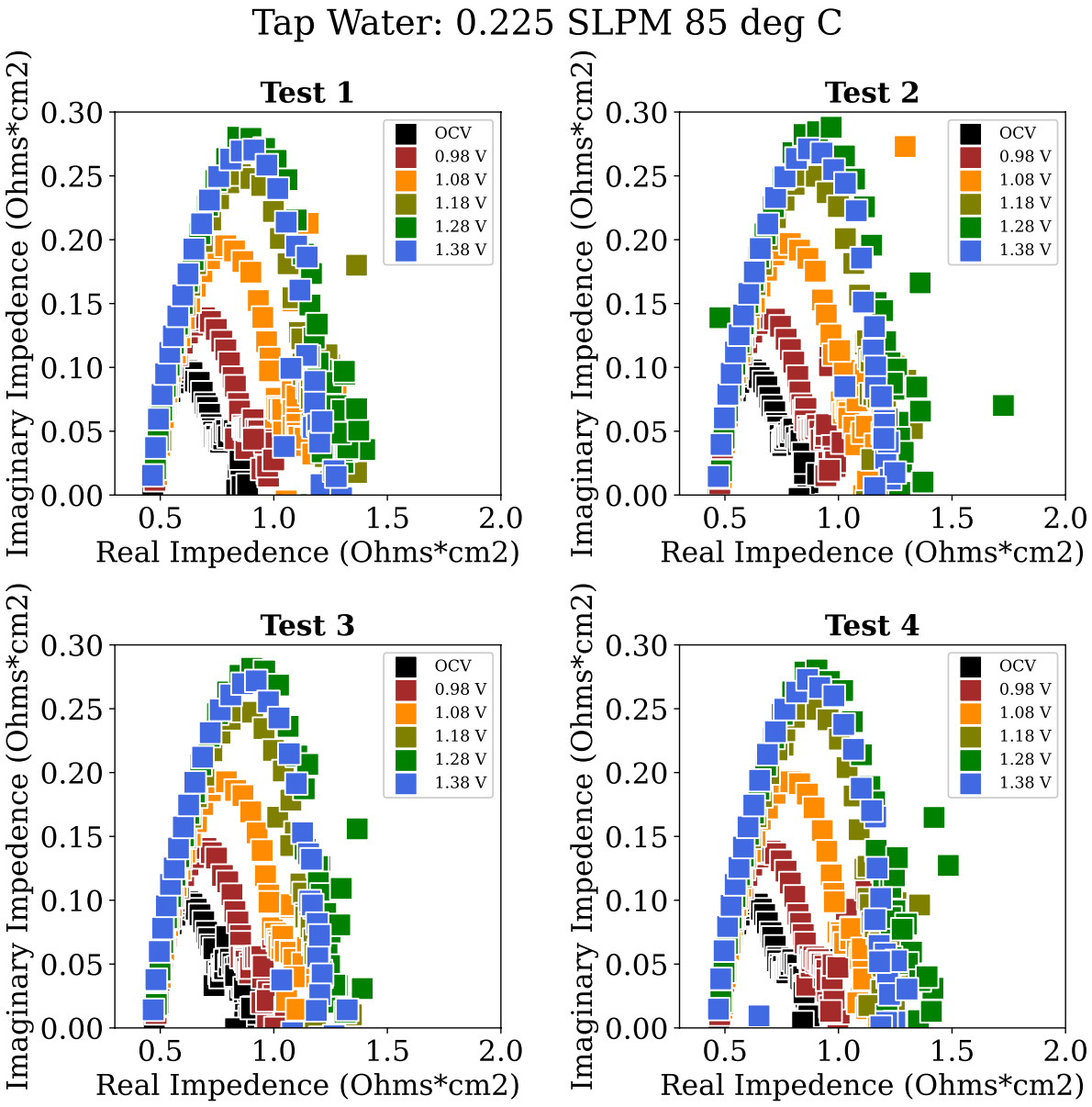
Tap Water: 0.225 SLPM 85 deg C
Test 1
Test 2
Test 3
Test 4
Imaginary Impedence (Ohms*cm2)
Real Impedence (Ohms*cm2)
0.00
0.05
0.10
0.15
0.20
0.25
0.30
0.5
1.0
1.5
2.0
OCV
0.98 V
1.08 V
1.18 V
1.28 V
1.38 V

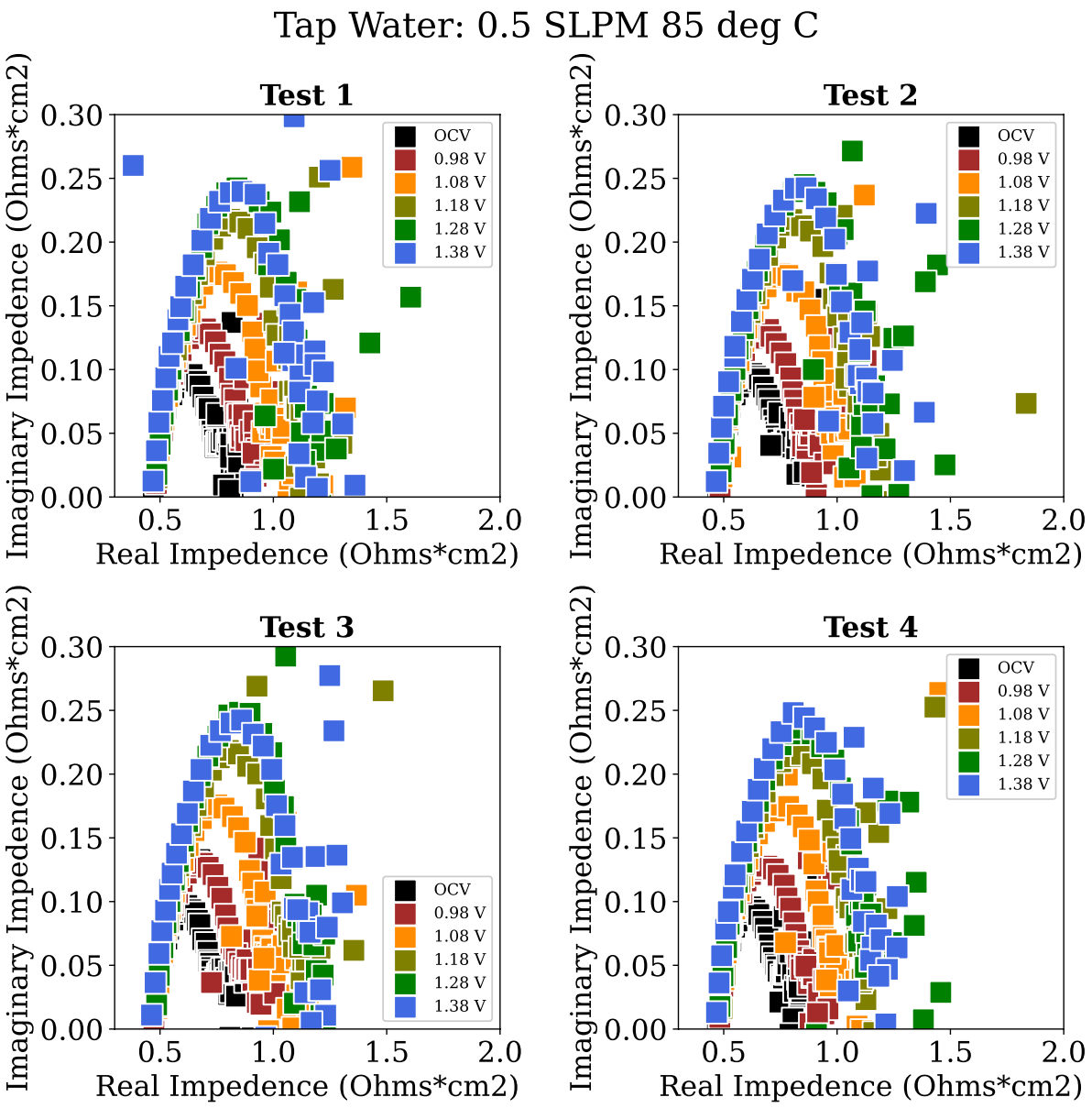
Tap Water: 0.5 SLPM 85 deg C
Test 1
Test 2
Test 3
Test 4
Imaginary Impedence (Ohms*cm2)
Real Impedence (Ohms*cm2)
0.00
0.05
0.10
0.15
0.20
0.25
0.30
0.5
1.0
1.5
2.0
OCV
0.98 V
1.08 V
1.18 V
1.28 V
1.38 V

Tap Water Raw Bode Results

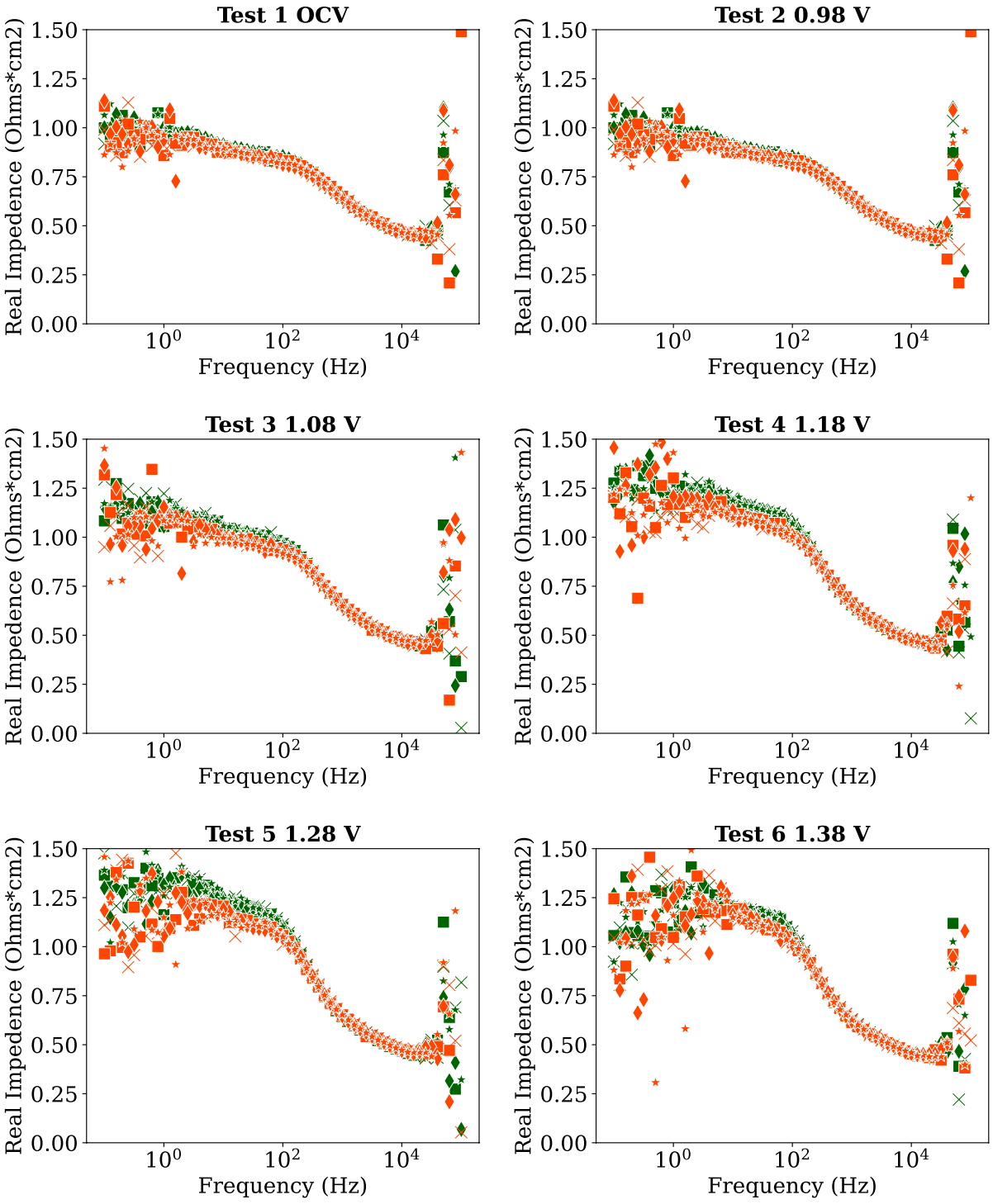

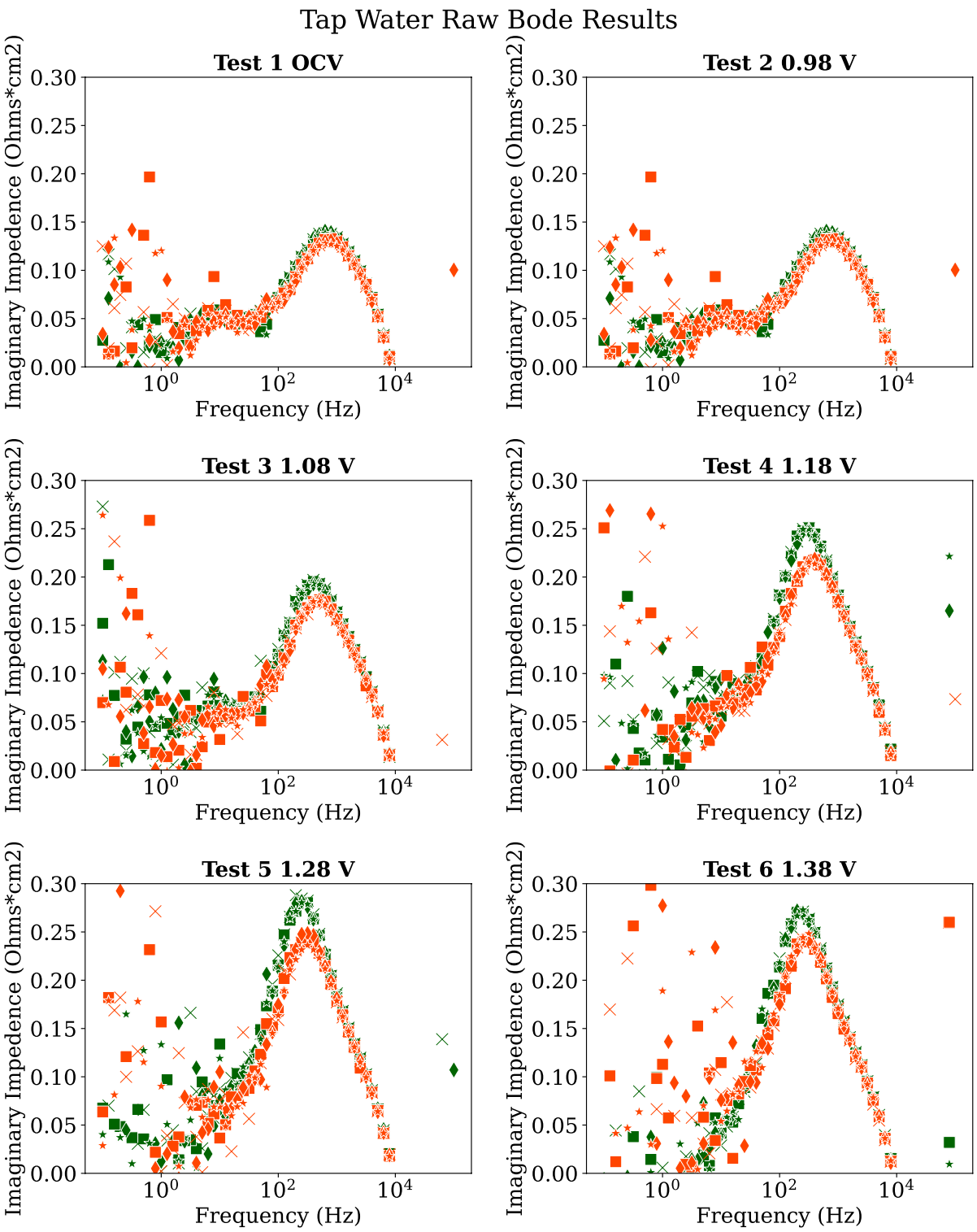
Tap Water Raw Bode Results
Test 1 OCV
Test 2 0.98 V
Test 3 1.08 V
Test 4 1.18 V
Test 5 1.28 V
Test 6 1.38 V
Imaginary Impedence (Ohms*cm2)
Frequency (Hz)
0.00
0.05
0.10
0.15
0.20
0.25
0.30
10^0
10^2
10^4

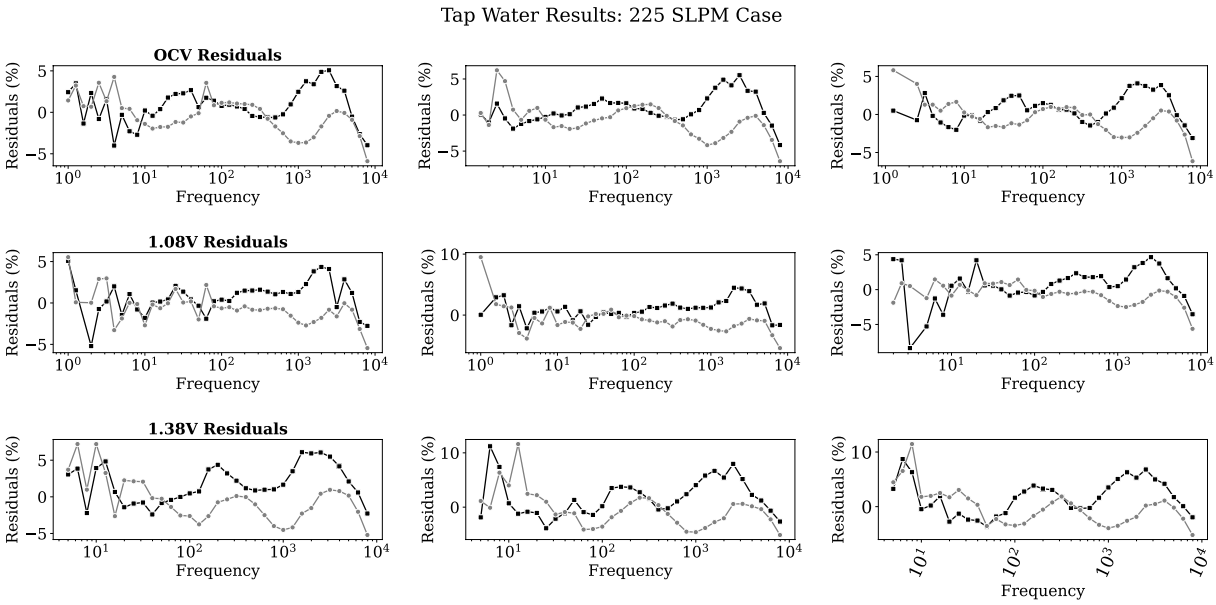

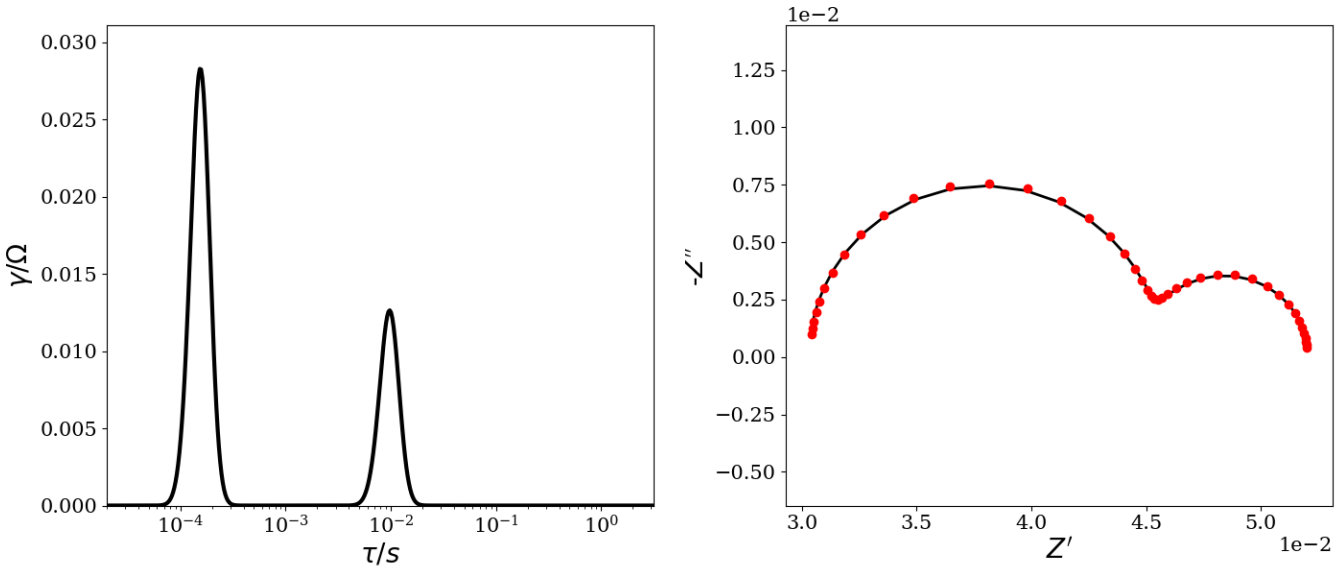

Figure 10-4: DRT Tapwater 225 OCV

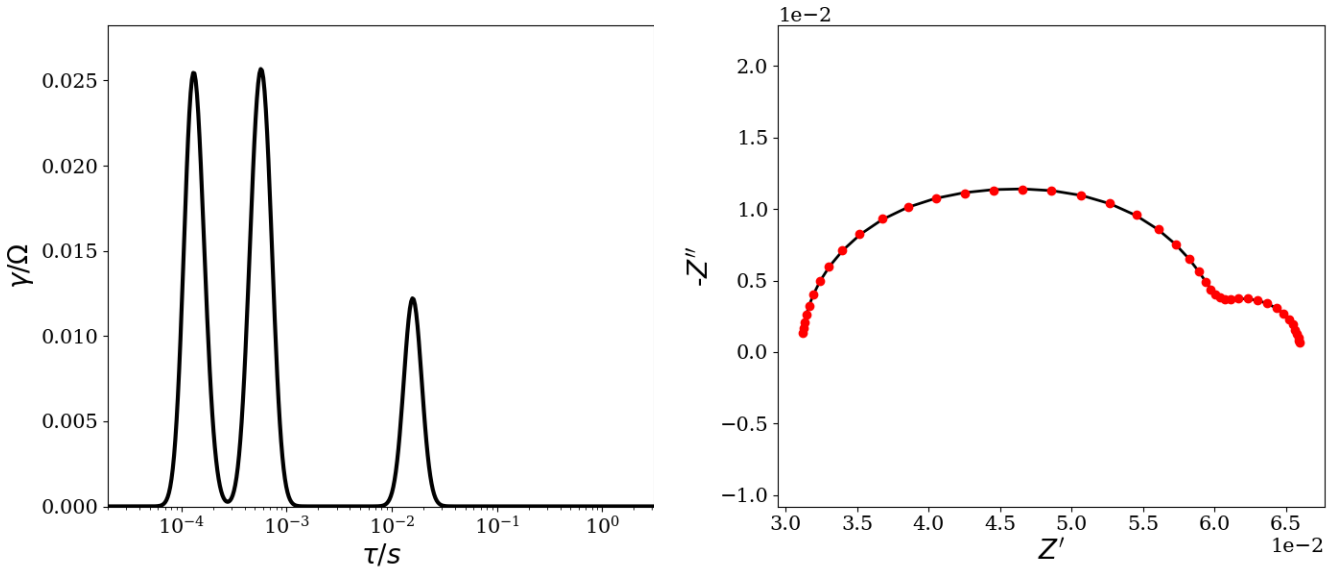

Figure 10-5: Tap water 0.25 SLPM 1.08 V

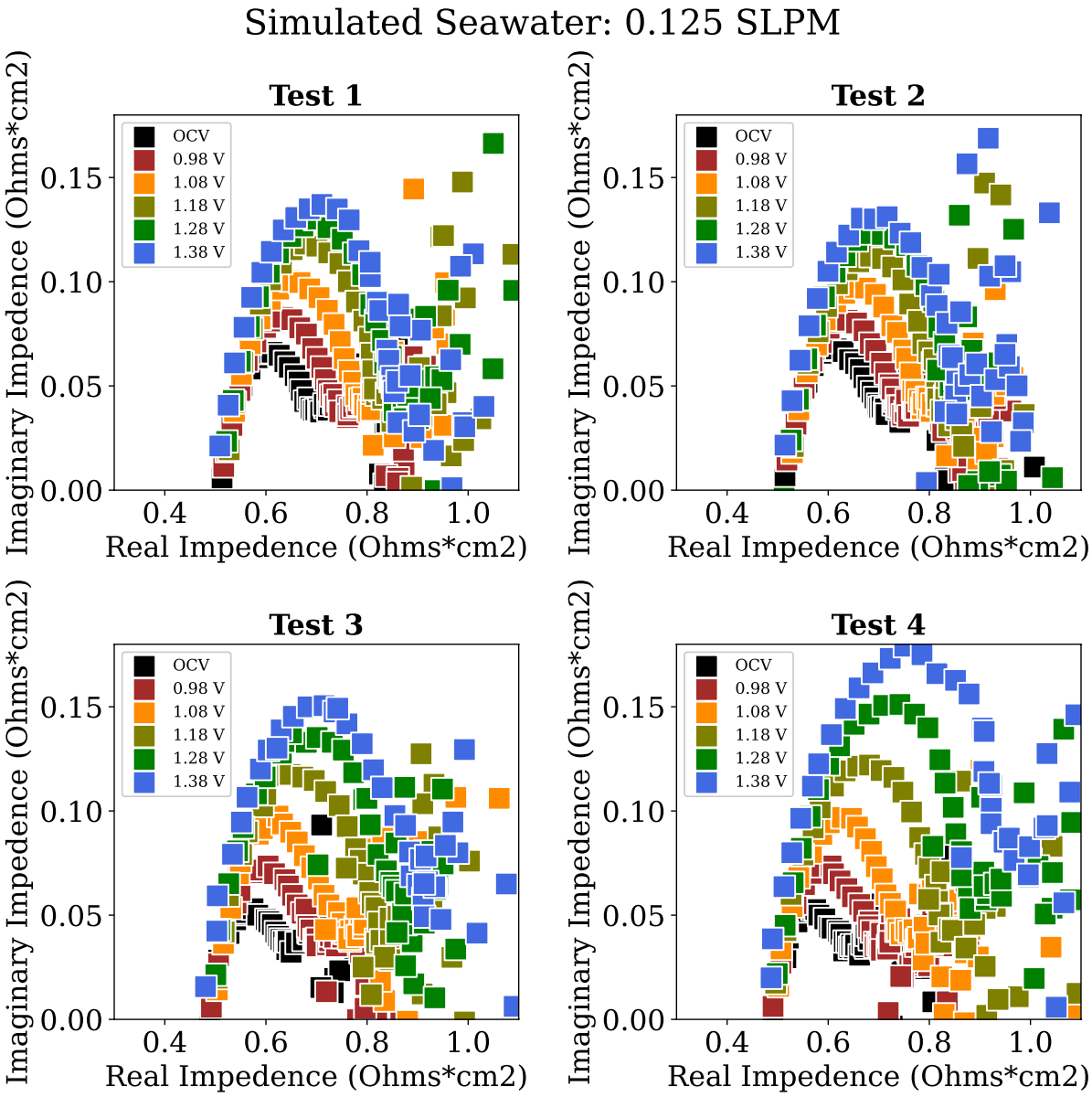
Simulated Seawater: 0.125 SLPM
Test 1
Test 2
Test 3
Test 4
OCV
0.98 V
1.08 V
1.18 V
1.28 V
1.38 V
Imaginary Impedence (Ohms*cm2)
Real Impedence (Ohms*cm2)
0.00
0.05
0.10
0.15
0.4
0.6
0.8
1.0

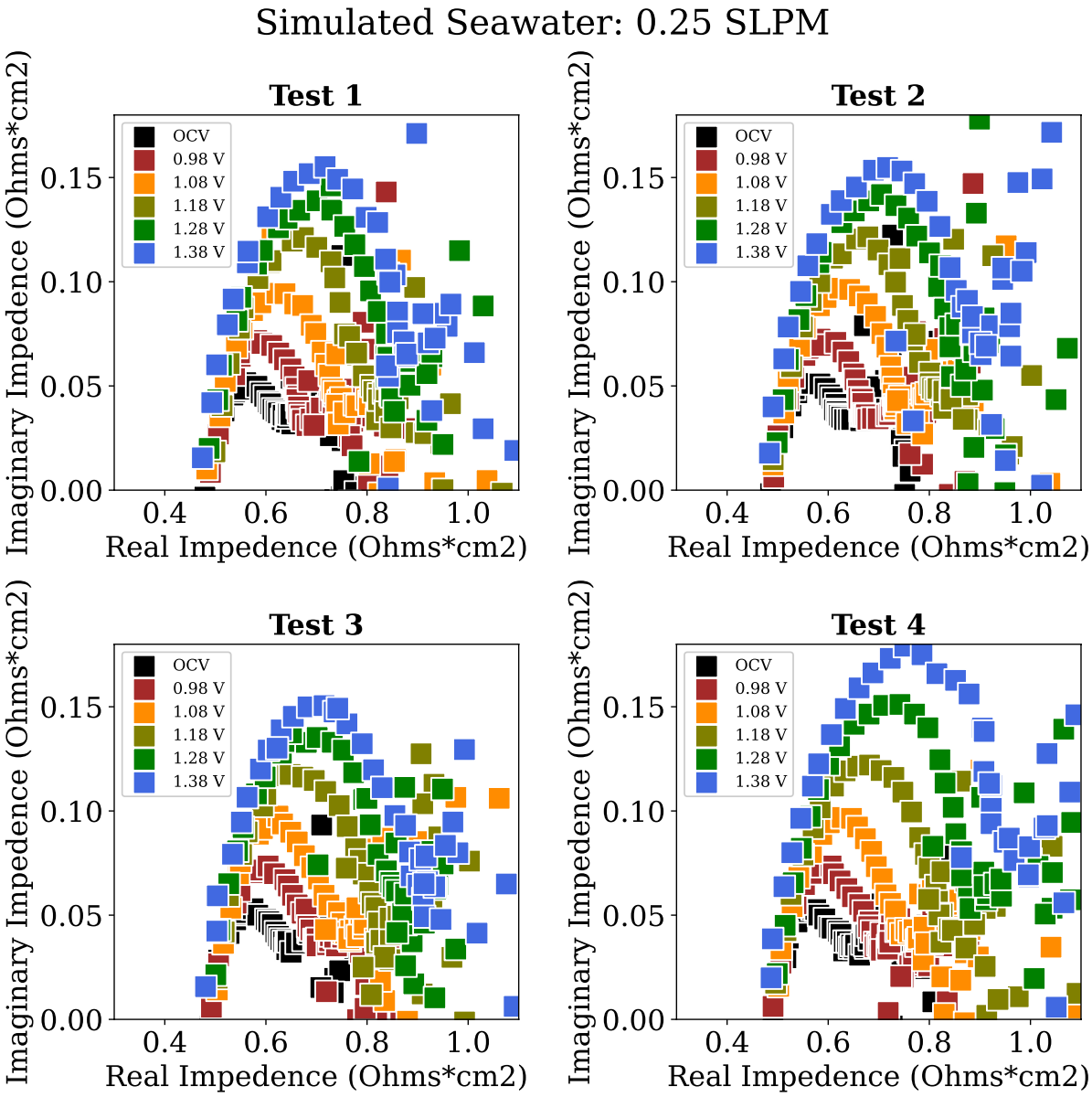
Simulated Seawater: 0.25 SLPM
Test 1
Test 2
Test 3
Test 4
OCV
0.98 V
1.08 V
1.18 V
1.28 V
1.38 V
Imaginary Impedence (Ohms*cm2)
Real Impedence (Ohms*cm2)
0.00
0.05
0.10
0.15
0.4
0.6
0.8
1.0

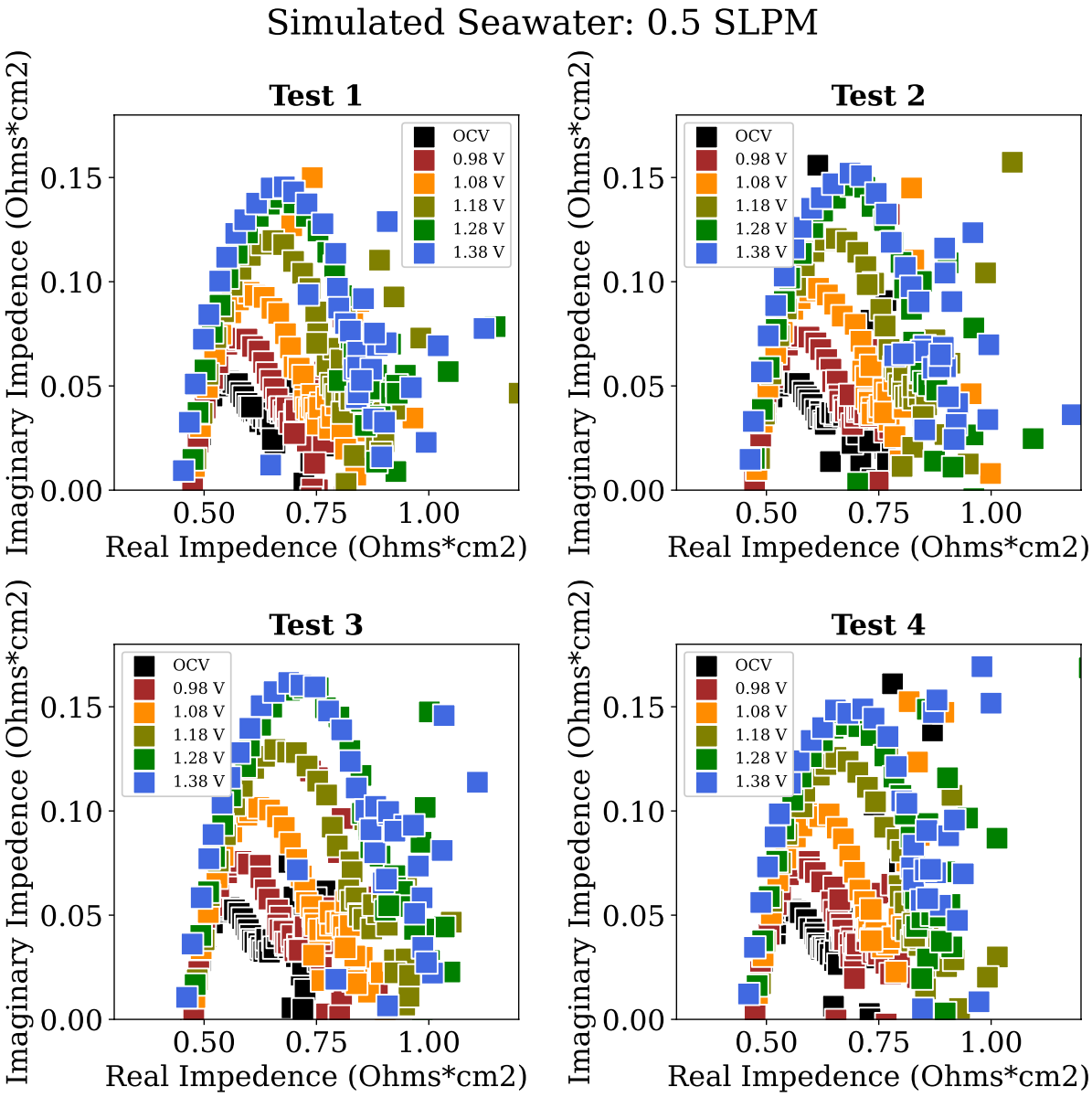
Simulated Seawater: 0.5 SLPM
Test 1
Test 2
Test 3
Test 4
OCV
0.98 V
1.08 V
1.18 V
1.28 V
1.38 V
Imaginary Impedence (Ohms*cm2)
Real Impedence (Ohms*cm2)
0.00
0.05
0.10
0.15
0.50
0.75
1.00

Seawater Raw Bode Results

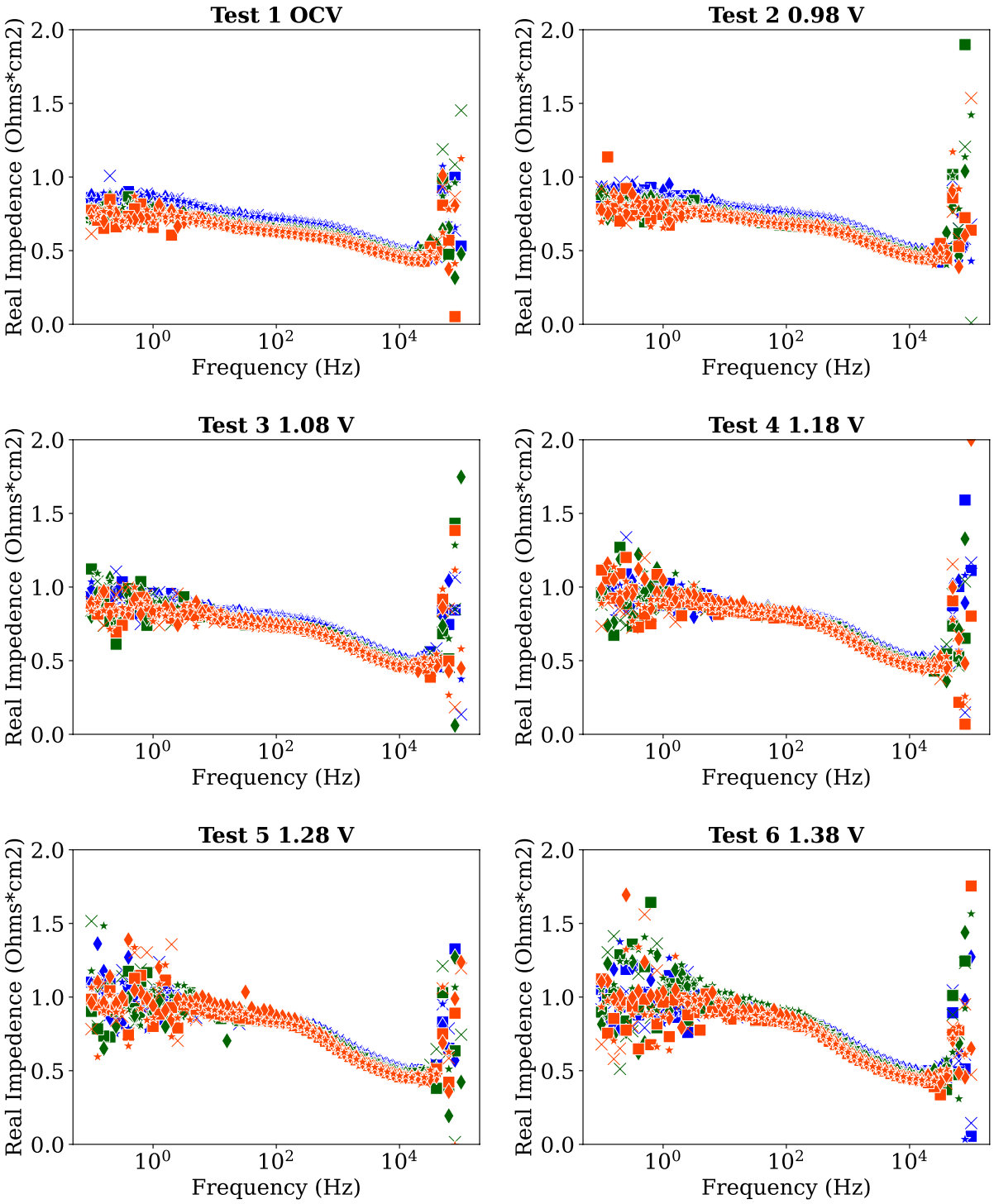

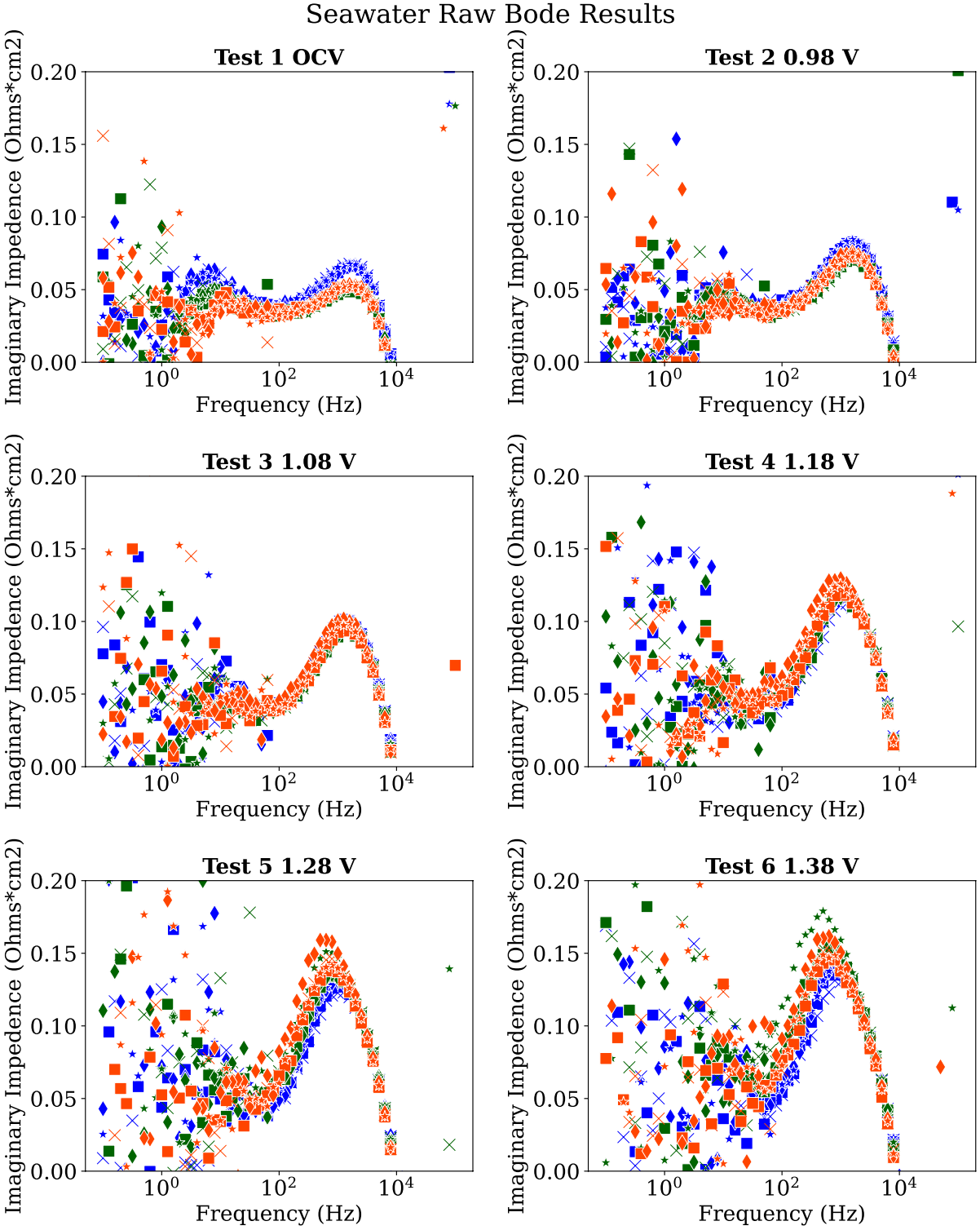
Seawater Raw Bode Results
Test 1 OCV
Test 2 0.98 V
Test 3 1.08 V
Test 4 1.18 V
Test 5 1.28 V
Test 6 1.38 V
Imaginary Impedence (Ohms*cm2)
Frequency (Hz)
0.00
0.05
0.10
0.15
0.20
10^0
10^2
10^4

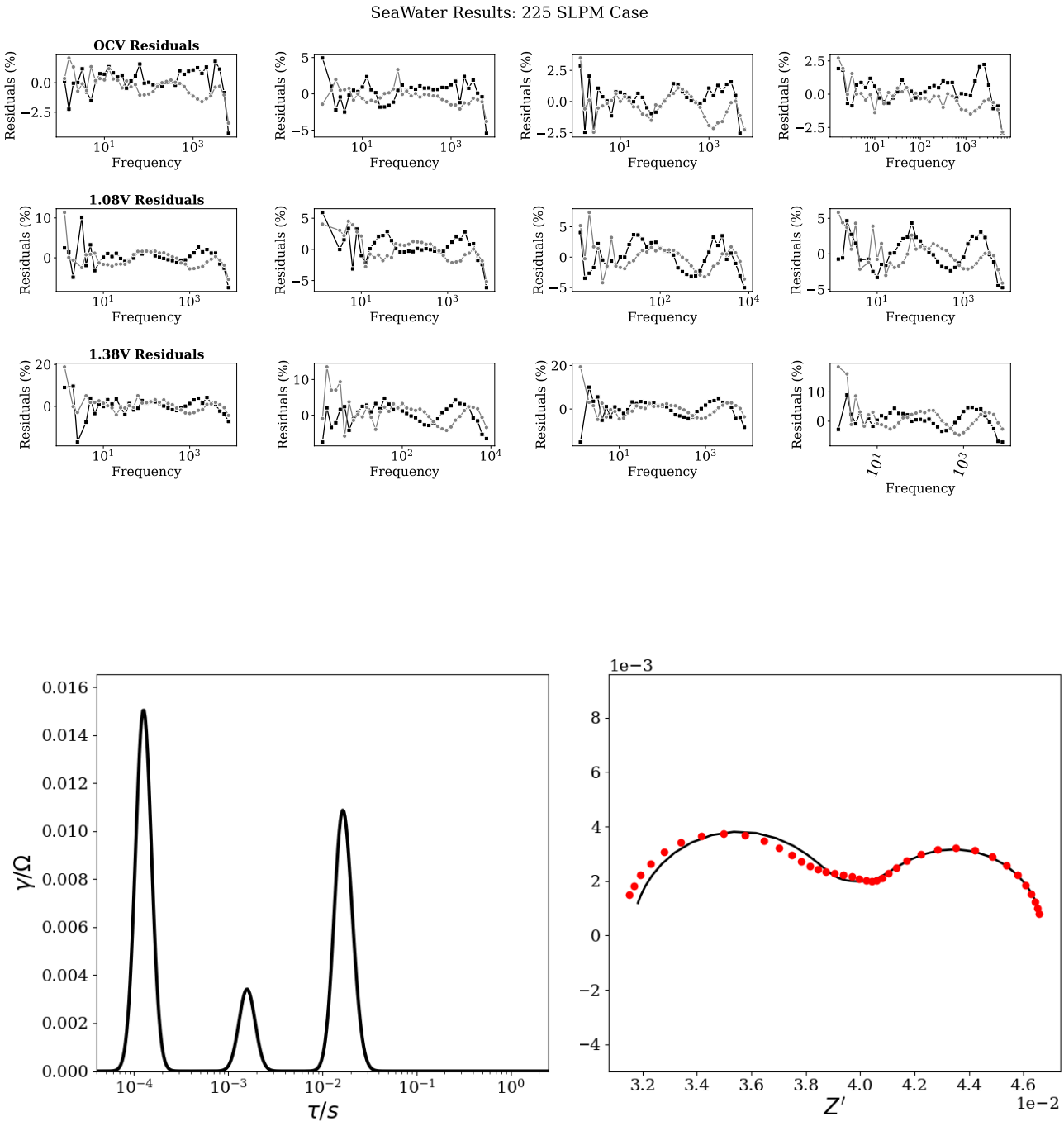

Figure 10-6: DRT Result for Seawater at OCV with 0.25 SLPM

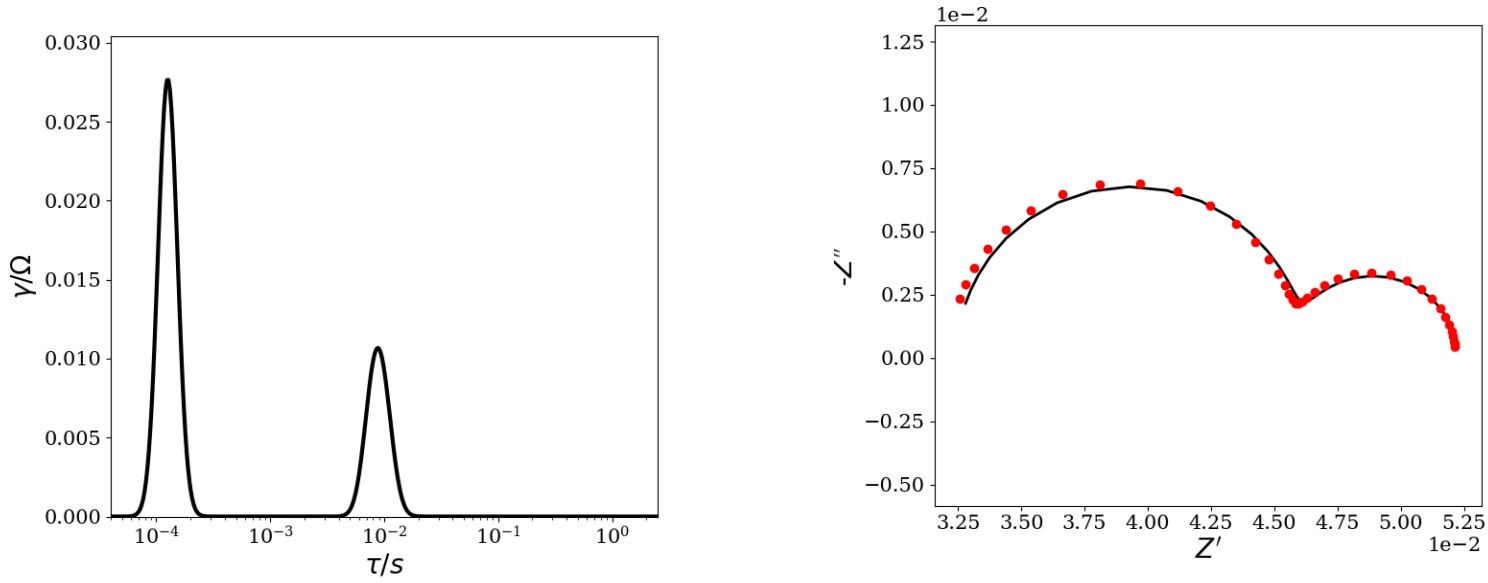

Figure 10-7: DRT Result for seawater at 1.08V with 0.25 SLPM

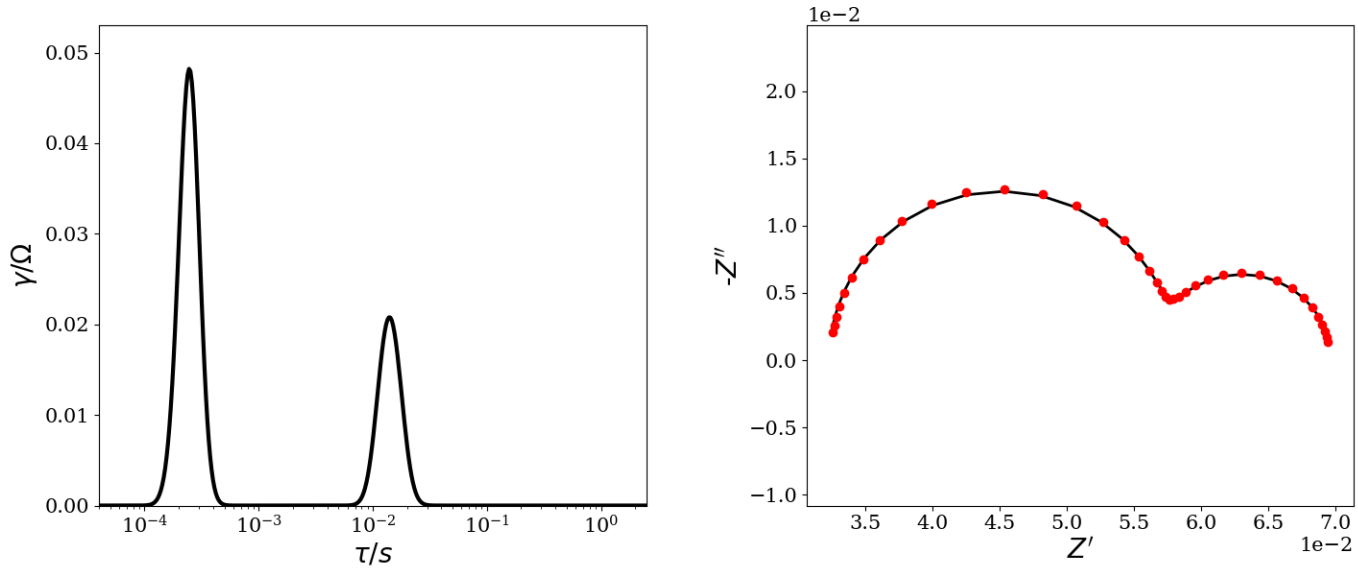

Figure 10-8:Results for seawater at 1.38V with 0.25 SLPM

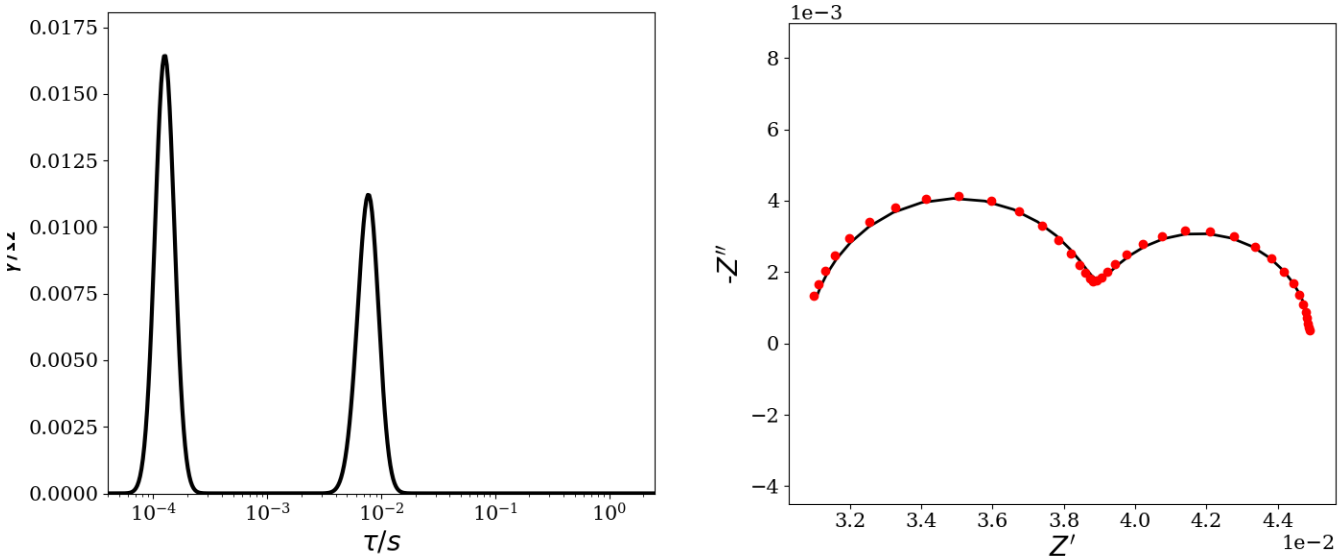

Figure 10-9: Seawater OCV with 0.500 SLPM

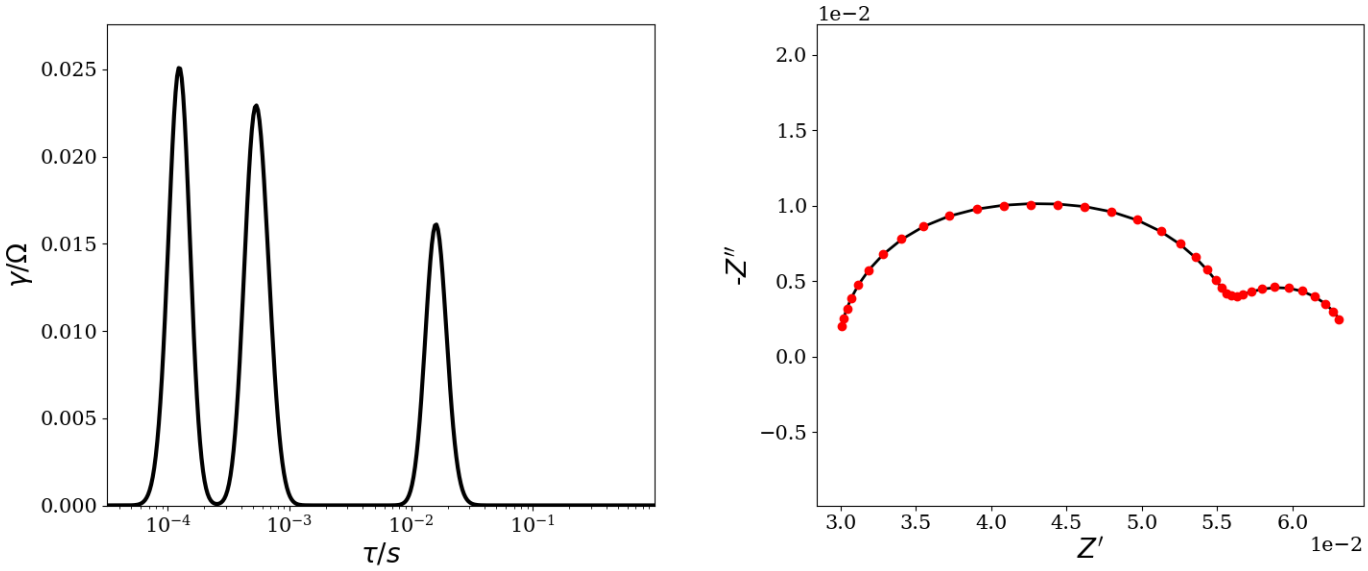

Figure 10-10: Seawater 1.08V with 0.500 SLPM

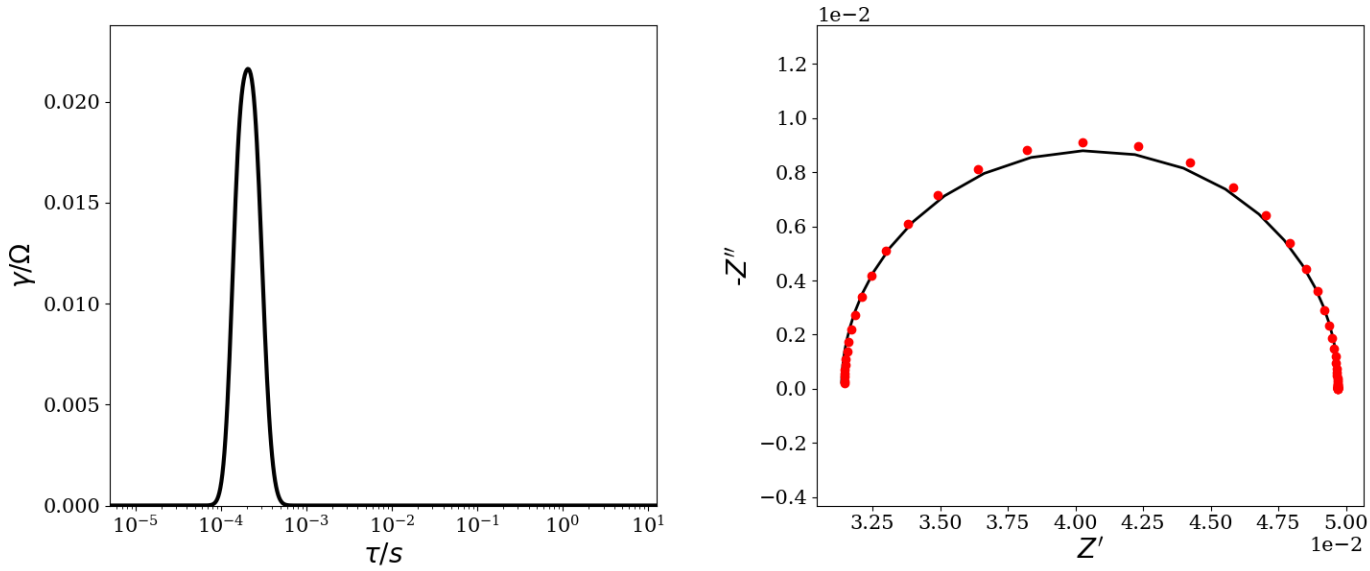

Figure 10-11: Seawater at 1.38V with 0.500 SLPM

10.2 Appendix B

Table 10-1: Conductivity of condensate

DI uS/cm	Tapwater (us/cm)	Seawater (us/cm)
2.764	22.13	75.06
2.189	16.3	162.8
3.54	10.39	181.41
7.39	8.832	220.14
7.569		
8.525		
7.891		

Table 10-2: Conductivity of steam generator data

DI uS/cm	Tapwater (us/cm)	SW (mS/cm)

3.953	918.5	31.84
5.457	960.8	33.01
3.627	948.6	35.05
5.647	1045	33.5066667
6.257	1053	35.4233333
5.782	960.2	47.43
5.649	1083	55.3
4.756		59.53
5.076		52.23
4.888		59.17
4.677		57.18
		63.51
		62.31